UNIVERSITY OF OKLAHOMA

GRADUATE COLLEGE

CARBON-BASED COMPLEX STRUCTURE AND MODEL DEVELOPMENT

A DISSERTATION

SUBMITTED TO THE GRADUATE FACULTY

In partial fulfillment of the requirements for the

Degree of

DOCTOR OF PHILOSOPHY

By

Qi Qiao

Norman, Oklahoma

2020

CARBON-BASED COMPLEX STRUCTURE AND MODEL DEVELOPMENT

A DISSERTATION APPROVED FOR THE

SCHOOL OF CHEMICAL, BIOLOGICAL, AND MATERIALS ENGINEERING

By

Dr. Liangliang Huang, Chair

Dr. Brian P. Grady

Dr. Jeffrey H. Harwell

Dr. Wang Bin

Dr. Lloyd Bumm

Acknowledgements

I would like to thank my advisor, Dr. Liangliang "Paul" Huang, for his supervision, guidance and support for the past five years at University of Oklahoma. He has always listened to my ideas openly and encouraged me to think independently, and he would always help guide me to think about "telling a story with narrative logic" for my research. His insights and constant encouragement to pursue creative ideas and fundamental understandings have made my doctoral study an enjoyable experience. He always encourages me to attend conferences, meetings, and workshops worldwide, and creates opportunities for me to visit other research groups in pursuing my scientific interest. I have been also benefiting from the teaching assistant experience with Paul. I am deeply touched by his patience, enthusiasm and carefulness in teaching. Also, I am very grateful to his kindness and support to my professional career development. I am a leaf of his academic tree, and continue to grow under his guidance.

I would also like to thank my committee members, Professor Brian P. Grady, Professor Jeffrey H. Harwell, Professor Wang Bin and Professor Lloyd Bumm for their patience and insightful comments on the examinations and my research projects.

Many thanks go to thank Professor Zhen Yang at Jiangxi Normal University, for his kindness and inspiring guidance on the fundamental understanding of molecular dynamics simulation and coding.

I thank Professor Wei Gao and her research groups at North Carolina State University. I have enjoyed my three-month stay at Raleigh in May 2017, and have learnt a lot about the synthesis and characterization of graphene oxide experimentally.

I also want to thank Professor Chang Liu at Nanjing University of Technology, and Professor Xiaobao Li at Nanjing Forestry University, for introducing the exciting experimental results and the publications we have put together. Also, the encouragement from Professor Xiaohua Lu and Professor Xin Feng at Nanjing University of Technology, China, is greatly appreciated.

I thank past and present members of the Huang group: Guobing “Kevin” Zhou, currently a PhD student advised by Dr. Huang, for his help on molecular dynamics simulations, especially the model setup, radial distribution function calculation, Linux shell scripts, supercomputer usage and many others; Tarrett Tow and Trevor Fisher for the interesting discussions of my research.

I would like to thank my friends, Huiyu “Hailey” Wang, Wen Yang, Monica Chidurala, and Tong Mou for their hospitality, company, and friendship over the four years of my PhD’s program. We were all working on our own master’s and PhD’s research concurrently, and getting to share that experience with them provided me with the motivation and enthusiasm needed to finish strong.

Lastly, I would like to thank my family, especially my parents, Jujie Cai and Yanbo Qiao, for looking after me all these years to help me become the person I am today. Their love and devotion to me ultimately inspired me to keep pushing my own limits and live a life of continued learning and self-improvement.

Table of Contents

List of Tables

List of Figures

Abstract

Growing concerns about the environment and energy crisis prompt a search for effective carbon-based materials due to their low cost, renewability, sustainability, easy accessibility and excellent properties. We study the model development, structure and properties of graphene oxide, cellulose and their nanocomposites in order to obtain a better fundamental understanding of carbon complex materials and construct a structure-property relationship via reactive molecular dynamics simulations.

In chapter 3, the model development of GO is studied. Theoretical GO models developed so far present a good description of its chemical structure. However, when it comes to the structural properties, such as the size and distribution of vacancy defects, the curvature (or roughness), there exist significant gaps between computational models and experimentally synthesized GO materials. We carry out reactive molecular dynamics simulations and use experimental characteristics to fine tune theoretical GO models. Attentions have been paid to the vacancy defects, the distribution and hybridization of carbon atoms, and the overall C/O ratio of GO. The GO models proposed in this work have been significantly improved to represent quantitative structural details of GO materials synthesized via the modified Hummers method. The temperature-programmed protocol and the computational post analyses of Fourier-transform infrared spectroscopy, X-ray photoelectron spectroscopy, vacancy size and curvature distribution, are of general interest to a broad audience working on GO structures from other synthesis methods and other two-dimensional materials and their composites.

In Chapter 4, we outline the state-of-the-art understanding of cellulose structures, and discuss in details cellulose interactions, dissolutions and decompositions via computational methods of molecular dynamics (MD) and reactive molecular dynamics (RxMD) simulations. In

addition, cellulose characterizations, beneficial to validate and support computational results, are also briefly summarized. Such a state-of-the-art account of atomistic computational studies could inspire interdisciplinary collaborations, optimize process design, promote cellulose-based materials for emerging important applications and shed a light on fundamental understandings of similar systems of biomolecules, polymers and surfactants.

In Chapter 5, we investigate the fundamental mechanism of how cellulose structure transforms under pyrolysis conditions and the practical guideline of how cellulose properties are fined tuned accordingly. A series of reactive molecular dynamics calculations has been designed to reveal the structural evolution of crystalline cellulose under pyrolysis treatments. Through the detailed analysis of cellulose configuration change, hydrogen bonding network variation, reaction and redistribution of carbon, oxygen and hydrogen elements, and Young's modulus, a molecule level insight of crystalline cellulose and its structural evolution under pyrolysis conditions has been constructed via reactive molecular dynamics simulations. We anticipate those theoretical results could effectively promote the design, the manufacture, and the optimization of cellulose based materials for relevant emerging applications.

In Chapter 6, we combined the results from previous chapters and explore a new composite material that incorporating amorphous cellulose chains on GO surface, which is barely reported by recent publications. A series of RxMD simulations have been carried out to reveal the mechanical properties of pure GO and cellulose-GO nanocomposites. Two different cellulose-GO composites are constructed, namely, cellulose (monolayer)-GO model and cellulose (multilayer)-GO model. The tensile deformation, Young's modulus and mechanical strength of GO and cellulose-GO composites have been recorded and calculated under the temperature of 300, 500 800 K, with two strain rates of 10^{-4}/fs and 10^{-5}/fs. We hope the GO model with the simultaneously

description to both structural and chemical properties can provide a new fundamental understanding of the mechanical performance of GO and cellulose-GO composites, and could add some advancement to existing knowledge of carbon-based materials.

Chapter 1: Introduction

1.1 Carbon-Based Material Model Development

Carbon-based materials consist a large family of diverse structures of solid carbon and carbides have been attracting more and more interest worldwide [1]. Several thousands of studies have been published since the twentieth century with searching topics “carbon materials”. The versatility of carbon-based materials is due to their excellent physical and chemical properties, and the easy accessibility to bond with many other materials. Therefore, carbon-based materials have shown a variety of structures with remarkable properties such as high mechanical strength, high thermal stability, high surface area and great electrical conductivity, *etc*. [2, 3]. Their excellent properties lead to a diversity of applications in catalysis [4, 5], separation [6-8], sensor [9-11], degradation of organic pollutants [5, 12, 13], biomedical engineering [14-16], and clean energy-related fields [17-20].

For example, graphene, with exotic electronic properties and excellent mechanical strength of ~1 TPa [21], is widely used in sensing, separation, catalysis, and energy-related applications [21-25]. Additionally, the polymer-functionalized graphene showed great enhancement in the mechanical, thermal, electrical and optical properties [26-29]. The graphene precursor, graphene oxide (GO) derivatives, has been considered as a promising candidate in polymer nanocomposites due to the accessibility of macro-scale production, interfacial modification, and better dispersibility [30-34]. The extensive applications of GO include composites [35], separation [36-38], catalysis [39, 40], sensing [41, 42], electronics [43, 44], energy storage [45, 46], biological and drug delivery [47-50]. With the increasing global demand, carbon-based catalysts, such as GO, carbon nanotubes and metal-free porous graphitic carbon nitride (g-C_5N_2), provide alternative way

for green and renewable processes to generate H_2O_2 in aqueous conditions [17, 51, 52]. Furthermore, cellulose, as the most abundant carbon-based materials to civilization, has an annual production of about 700 billion tons. Owing to properties such as renewability, sustainability, low cost, tunable mechanical strength, high biodegradability and excellent biocompatibility, cellulose has been widely used in biofuel productions [53, 54], energy related applications [55-58], biomedical engineering [59-67], paper and construction industry [68-72].

Despite these encouraging progresses and applications of carbon-based materials, detailed fundamental understandings at atomistic level are still incomplete. The challenges in the theoretical study of carbon-based materials are: (1) lack of representative models that includes both structural and chemistry properties compared with realistic materials; (2) lack of a structure-properties -process relationship that could benefit both experiment and simulation studies. In this thesis, we choose GO, cellulose and cellulose-GO nanocomposites as the carbon-based material representatives, and carry out computational studies (1) to investigate the model development, the structural and mechanical properties of these materials; (2) to bridge the connection between experiments and simulation via various characterization techniques; and (3) to understand from the atomistic levels that how the properties of these materials can be fine-tuned via the manipulation of structures. Those molecular level understandings can provide a new fundamental understanding of carbon-based materials and add advancement to existing carbon-based materials knowledge. And such understandings could also shed a light on the construction of a structure-property relationship and further inspire interdisciplinary collaborations, optimize process design, and promote carbon-based materials for emerging important applications.

1.2 Graphene Oxide

Two-dimensional (2D) nanomaterials typically refer to flat or slightly corrugated sheets with nanometer thicknesses and infinite lateral dimensions, such as graphene, single-layer boron nitride (BN), molybdenum disulfide (MoS_2) and so on (Figure 1). The quantum confinement on the thickness direction results in exotic electronic properties and enhanced surface effects that can be useful in sensing, separation, catalysis, energy-related applications, *etc*. [25]. In 2005, Geim's group obtained the first real piece of graphene, and experimentally observed the quantum hall effect on the sample at room temperature [73, 74]. Soon after that, a storm of graphene research dominated the world of carbon nanomaterial research. Recently, 2D materails have attracted tremendous attention, since they belong to a major category in nanomaterials that has not yet been well explored.

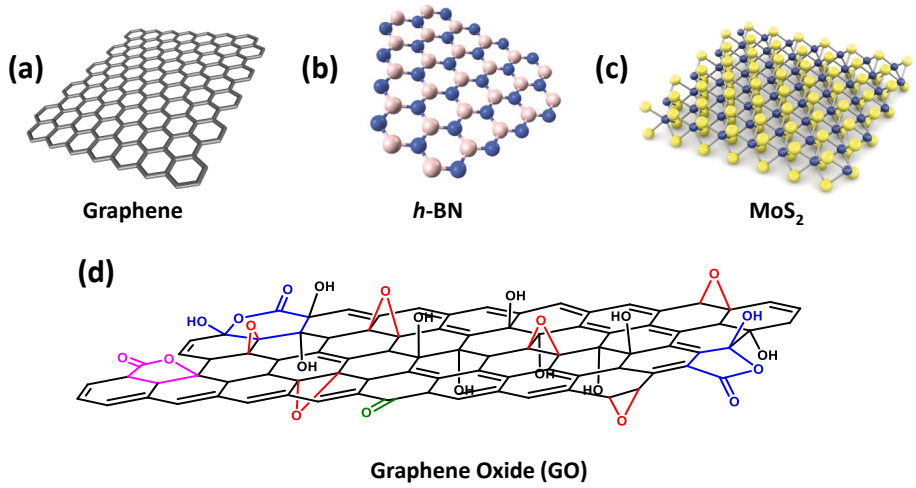

Figure 1. Schematic of single-atomic-layer structure of (a) graphene; (b) h-BN, with blue spheres representing boron atoms and pink spheres representing nitrogen atoms; (c) MoS_2, with blue spheres as Mo atoms and yellow spheres as sulfur atoms; (d) graphene oxide (GO), with epoxy

(red), hydroxyl (black), ketone (green), lactol (blue), and ester (pink) functionalities highlighted in different colors [75].

One of the biggest challenges in graphene research was the large-scale production of graphene. The original method Geim's group adapted, named as mechanical exfoliation of highly oriented pyrolytic graphite (HOPG) [73, 74], was both time consuming and extremely low in yield. Different strategies have been introduced for graphene production, including metal ion intercalation[76], liquid phase exfoliation of graphite [25, 77], chemical vapor deposition (CVD) growth[78], vacuum graphitization of silicon carbide (SiC) [79], bottom up organic synthesis of large polycyclic aromatic hydrocarbons(PAHs) [80-82], and most importantly, chemical reduction of graphene oxide (GO) [83, 84]. Pros and cons exist for each strategy; nevertheless, GO was believed to be one of the most promising pathways to the mass production of graphene, mainly due to its wet-chemical processability, large-scale availability in monolayers, and relatively low cost as compared to that of graphene (either CVD grown or mechanically exfolicated). In addition, GO and its derivatives have shown several promising applications in catalysis, composites, energy storage, sensing, water purification, electronics, *etc*. Therefore, GO has been established as an important and technologically relevant material during the past decade. There now exists an extensive literature regarding the synthesis, chemical structure, reactivity, properties of GO, as well as its use in multiple applications. However, GO has recently been reported to degrade after about a month of synthesis at room temperature [85]. Loss of epoxy groups is believed to be the major structural change during the degradation process of GO. This structural change presents a significant challenge for all potential applications of GO. Therefore, a better understanding of GO, especially regarding its structural stability and chemical reactivity, via the intertwined experimental and theoretical studies. Understanding these fundamental concepts is key to the development of all the GO-based applications, such as catalysis and separation.

Experimentally, one of the most widely used GO models in literature is from Lerf and Klinowski, where hydroxyl and epoxy groups exist mainly on the basal plane and carboxyl groups are located at edges [86-88]. With the advance of modern characterization techniques, Gao and co-workers proposed a more detailed GO model that has large vacancy defects, and other quantitative features, such as the overall carbon/oxygen (C/O) ratio (2.44); the relative ratio of major functional groups, namely, 115 (hydroxyl and epoxide): 3 (lactol O–C–O): 63 (graphitic sp^2 carbon): 10 (lactol + ester + acid carbonyl): 9 (ketone carbonyl) [89]. Since GO material is sensitive to the synthesis protocols (temperature and oxidants), a static GO structure with a 'dynamic structure' which constantly evolves with its environment has been proposed.[90] In addition, the experimental results also indicate that a good GO model shall capture both structural (i.e. vacancy defects, curvature) and chemical information (i.e. C/O ratio, major functional groups, *etc*.).

From the computational point of view, efforts have been made via *ab initio* density functional theory (DFT) method to study GO materials and their properties [91-94]. Using the knowledge from DFT calculations, more attempts have been made to develop GO models *via* molecular dynamics (MD) simulations.[95-104] Theoretical GO models developed so far present a good description of its chemical structure. However, when it comes to the structural properties, such as the size and distribution of vacancy defects, the curvature (or roughness), there exist significant gaps between computational models and experimentally synthesized GO materials. The GO models proposed in this thesis inherit both structural and chemistry information of previous GO models but have significantly improved to represent quantitative structural details of experimentally synthesized GO materials.

1.3 Cellulose

Cellulose is a polysaccharide that consisting linear chains of hundreds of β-1,4-linker glucose units. As a primary component of cell walls of plants, algae, bacteria and other natural biomaterials, cellulose is the most abundant and widespread natural resource with an annual production of about 700 billion tons. Due to its renewability, sustainability, low cost, tunable mechanical strength, high biodegradability and excellent biocompatibility, cellulose has been widely used in biofuel productions [53, 54], energy related applications [55-58], biomedical engineering [59-67], paper and construction industry [68-72].

Remarkable studies have been published for the cellulose dissolution/interactions [105, 106], cellulose degradation/conversion via enzymes [107, 108], catalysis [109-114], hydrolysis [111, 115-117] and pyrolysis processes [116, 118], as well as numerous cellulose applications in experiments [55, 56, 67, 119-129]. As for theoretical efforts, reports are available regarding model developments of cellulose microfibril and plant cell wall [130], mathematical models for cellulose plant growth [131], computational studies of the decomposition of lignocellulosic materials (cellulose, hemicellulose and lignin) via catalyzes, enzyme, pyrolysis and dissolution methods [132, 133], and computational NMR predictions of carbohydrate materials [134].

It is accepted that the utilization of cellulose is highly dependent on the effective and selective modification of the 1,4-β glycosidic linkages and the inter/intra hydrogen bonding networks. In order to effectively convert natural cellulose into processable advanced functional materials, various treatments have been proposed in industrial such as mechanical treatment [135-139], chemical treatments [139-148], hydrolysis treatments [140, 149-169] and pyrolysis treatments [170-174]. More recently, a new strategy that maintaining inherent structural features and manipulating subtle properties have brought applications of cellulose-based materials to a new

horizon [142, 175-178]. For example, Song et al. [141] proposed a subtle two-step treatment to obtain advanced materials from cellulose resources. They processed natural wood to firstly remove lignin and hemicellulose, followed by a mechanical compressing to fine-tune properties of the remaining cellulose. The transformed wood, mostly the structurally manipulated cellulose, is mechanically more than 10 times stronger than steel.

For the theoretical understanding, *ab initio* and classical MD simulations were used to simulate the surface of cellulose Iβ and its interactions and dissolution with water [179] and ILs [180-182]. Recently, the computational study of cellulose pyrolysis has attracted more and more interest [183-185]. BergenstråhleLars et al. [183] reported that cellulose Iβ crystal changed its structure when the temperature was above 450 K via classical MD simulations. Zheng and co-workers [186] studied the pyrolysis process of amorphous cellulose at temperatures from 500 to 1400 K via RxMD, and their pyrolysis products is consistent with available experiments. Paajanen et al. [187] also studied the amorphous cellulose decomposition from 1400 to 2000 K. They observed that the breaking of 1-4-β bonds eventually leads to the cellulose decomposition, and that the decomposition products are mainly glycolaldehyde, water, formaldehyde and formic acid, which agreed with experimental results. Although numerous efforts have been made experimentally and theoretically, a molecular level understanding of how cellulose structure transforms under different treatments and how its property could be fine-tuned accordingly, is still incomplete. In this thesis we have focused on the crystalline cellulose and its structural evolution under pyrolysis conditions

1.4 The Mechanical Properties of GO and Cellulose-GO Composite

As aforementioned, GO has become one of the most widely utilized two-dimensional (2D) nanomaterials during the past decade [73, 74, 83, 188, 189]. The extensive applications of GO include composites [35], separation [36-38], catalysis [39, 40], sensing [41, 42], electronics [43, 44], energy storage [45, 46], biological and drug delivery [47-50]. Due to the accessibility of macro-scale production, interfacial modification, and good dispersibility, GO and its derivatives, has been considered as a promising candidate in polymer nanocomposites recently [30-34]. And the prediction of mechanical properties is one of the important parts for the investigation of the incorporated composites.

Since GO generated by different synthesis method showed different concentration and distribution of functional groups (mainly hydroxyl, epoxide and carboxyl) [86-89, 189], and defects located on GO surface. The mechanical and fracture studies of GO itself is still ambiguous and conflicting. Both the structural (defect, curvature) and chemical (functional groups) properties of GO significantly affect the mechanical behavior of GO. Experimentally, Gao and co-workers [190] reported that the grip pressure, length and loading rate highly affect the measurement of GO mechanical properties. Sakorikar et al. [191] demonstrated that the thickness of reduced graphene oxide (rGO) determines the crack propagation process of rGO films. An increasing thickness results in the decrease of the crack density and the increase of crack width. Similarly, Cao et al. [192] found that the random distribution of functional groups between GO multiple layers prevents the growth of preexisting crack. In theoretical studies, Cao et al. [193] studied mechanical properties of the monolayer GO membranes with 20% degree of oxidation via DFT and found that the brittle failure of GO occurred along the connecting oxidized carbon atoms on GO surface. On the contrary, Wei and co-workers [194] observed ductile behavior for 70% oxidization monolayer

GO via density functional-based tight binding (DFTB). Their reported elastic modulus (256.4 ± 28.2 GPa) is lower than the value (384 ± 31 GPa) proposed from Cao et al. [193], which indicated that the increasing of oxidation of GO might lead to the decrease of elastic modulus. It is reported that the hydroxyl groups cause the brittle behavior, whereas the ductile failure occurred when the transformation of epoxide-to-ether groups is dominated on GO surface [195, 196]. Using reactive force field (ReaxFF), Verma et al. [197] proposed that the spatial distribution and concentration of hydroxyl and epoxide groups are critical for the ductile behavior of GO. Although the functionalized GO materials demonstrate unique anisotropic mechanical, electrical and many other properties, which could bring the research and utilization of 2D nanomaterial to a next level, a better fundamental understanding of GO mechanical properties at atomistic level is still required.

Cellulose and its derivatives have been used to functionalize GO for GO/cellulose nanocomposites due to its excellent mechanical strength. Effort has been made experimentally in order to evaluate the properties and applications of GO/cellulose composites [198, 199]. The Young's modulus was reported to be improved by ~30% for GO/cellulose [200, 201]. Li et al. [202] incorporated GO with nanofibrillated cellulose (NFC) fibers and reported that this hybrid fibers are stronger than the pure GO and NFC due to the synergistic effect of bonds between NFC fibers and GO sheets. Peng and co-worker [203] proposed a cellulose/rGO paper with tunable mechanical properties and high biocompatibility, which could be used in biomaterial scaffolds for biomedical and tissue engineering. A potential electrochemical film consisting of nanocrystalline cellulose acetate (NCCA) and GO showed not only the enhancement of 61.92% in tensile strength compared with pure NCCA, but the electrical properties are greatly improved as well.[204]

Theoretically, RxMD was carried out to study the mechanical properties of multilayered GO composite paper [96, 205]. It is reported that the HBs network and water molecules influence the

mechanical behavior of multilayered GO composite. The control of structural and mechanical properties of the GO composite can be achieved by adjusting the amounts of functional groups, adding extra H-bonding favorable polymers (e.g. polyvinyl alcohol) and changing the concentration of water between GO layers. Zhang and Jiang [206] found that a large number of functional groups between graphene/GO layers increases the overall stiffness by increasing the number of HBs in the graphene/GO paper composite. While the elastic modulus of single GO sheet decreased with more functional groups in the surface. Rahman et al. [207] reported that the Young's modulus of graphene/cellulose composites with 5% graphene are 100% higher than pure cellulose resin system. Despite of the plenty computational studies aforementioned, there is barely no published work comparing the mechanical performance of monolayer GO and new cellulose-GO nanocomposites after incorporating amorphous cellulose chains on GO surface. In this thesis, the tensile deformation, Young's modulus and yield strength of GO and cellulose-GO composites will be studied.

1.5 Reach Approach

Despite of the progressing studies and applications of carbon-based materials, fundamental understanding of the structure and properties of these materials is far from complete. Form the view of computational studies, the challenge is due to the absence of representative models that could contain both structural and chemistry of carbon-based materials. And the mechanism of how structure changes affect the properties of these materials at atomistic level is still remain unclear. In this thesis, we use GO, cellulose and cellulose-GO composites to investigate the model development via reactive molecular dynamics simulations. And multiple calculated characterization techniques are carried out in order to construct a structure-property relationship

and bridge the connection between experiment and simulations. The thesis is organized as follows: In Chapter 2, a brief introduction of quantum mechanics (QM), molecular mechanics (MM) and reactive force field (ReaxFF) method is given. The calculation methods of some commonly used characterization techniques are also introduced in this chapter. Chapter 3 discusses the model development of GO. Chapter 4 summarized the recent atomistic studies about the structure, properties and process of cellulose. The studies of cellulose via simulation method of MM and MD based on ReaxFF are reviewed. Based on Chapter 4, we investigate the structural evolution of crystalline cellulose under the isolated pyrolysis process in Chapter 5. The pyrolysis temperature, the change of cellulose crystallinity, the variation of inter/intra HB networks, the reaction and distribution of C, O and H elements and mechanical properties of cellulose crystal have been analyzed. In Chapter 6, we combined the results from Chapter 3 (GO) and Chapter 5 (cellulose) to propose a cellulose-GO nanocomposite model. The model development and mechanical behavior of pure GO and cellulose-GO nanocomposites are investigated. Finally, the results we obtained are conclude in Chapter 7, and future research plans about carbon-based material model development and properties studies has been given.

1.6 Reference

1. Inagaki, M., *CHAPTER 1 - Old but New Materials: "Carbons"*, in *New Carbons - Control of Structure and Functions*, M. Inagaki, Editor. 2000, Elsevier Science: Oxford. p. 1-29.
2. Cazorla-Amorós, D., *Grand Challenges in Carbon-Based Materials Research.* Frontiers in Materials, 2014. **1**(6).
3. Walker, P.L., *Carbon: An old but new material revisited.* Carbon, 1990. **28**(2): p. 261-279.
4. Hu, C. and L. Dai, *Carbon-Based Metal-Free Catalysts for Electrocatalysis beyond the ORR.* Angewandte Chemie International Edition, 2016. **55**(39): p. 11736-11758.
5. Ribeiro, R.S., et al., *Catalytic wet peroxide oxidation: a route towards the application of hybrid magnetic carbon nanocomposites for the degradation of organic pollutants. A review.* Applied Catalysis B: Environmental, 2016. **187**: p. 428-460.

6. Bahamon, D., M.R.M. Abu-Zahra, and L.F. Vega, *Molecular simulations of carbon-based materials for selected CO2 separation and water treatment processes.* Fluid Phase Equilibria, 2019. **492**: p. 10-25.
7. Steel, K.M. and W.J. Koros, *Investigation of porosity of carbon materials and related effects on gas separation properties.* Carbon, 2003. **41**(2): p. 253-266.
8. Steel, K.M. and W.J. Koros, *An investigation of the effects of pyrolysis parameters on gas separation properties of carbon materials.* Carbon, 2005. **43**(9): p. 1843-1856.
9. Meyyappan, M., *Carbon Nanotube-Based Chemical Sensors.* Small, 2016. **12**(16): p. 2118-2129.
10. Venkatesan, B.M. and R. Bashir, *Nanopore sensors for nucleic acid analysis.* Nature Nanotechnology, 2011. **6**(10): p. 615-624.
11. Shao, Y., et al., *Graphene Based Electrochemical Sensors and Biosensors: A Review.* Electroanalysis, 2010. **22**(10): p. 1027-1036.
12. Herney-Ramirez, J., M.A. Vicente, and L.M. Madeira, *Heterogeneous photo-Fenton oxidation with pillared clay-based catalysts for wastewater treatment: A review.* Applied Catalysis B: Environmental, 2010. **98**(1): p. 10-26.
13. Assumpção, M.H.M.T., et al., *Low content cerium oxide nanoparticles on carbon for hydrogen peroxide electrosynthesis.* Applied Catalysis A: General, 2012. **411-412**: p. 1-6.
14. Wang, Z., L. Colombi Ciacchi, and G. Wei, *Recent Advances in the Synthesis of Graphene-Based Nanomaterials for Controlled Drug Delivery.* Applied Sciences, 2017. **7**(11).
15. Cha, C., et al., *Carbon-Based Nanomaterials: Multifunctional Materials for Biomedical Engineering.* ACS Nano, 2013. **7**(4): p. 2891-2897.
16. Roy, R.K. and K.-R. Lee, *Biomedical applications of diamond-like carbon coatings: A review.* Journal of Biomedical Materials Research Part B: Applied Biomaterials, 2007. **83B**(1): p. 72-84.
17. Cao, Y., et al., *Hydrogen peroxide synthesis on porous graphitic carbon nitride using water as a hydrogen source.* Journal of Materials Chemistry A, 2020. **8**(1): p. 124-137.
18. Wang, D.-W. and D. Su, *Heterogeneous nanocarbon materials for oxygen reduction reaction.* Energy & Environmental Science, 2014. **7**(2): p. 576-591.
19. Hu, Q., et al., *Origin of the improved photocatalytic activity of Cu incorporated TiO2 for hydrogen generation from water.* Applied Surface Science, 2016. **382**: p. 170-177.
20. Xiang, Q., B. Cheng, and J. Yu, *Graphene-Based Photocatalysts for Solar-Fuel Generation.* Angewandte Chemie International Edition, 2015. **54**(39): p. 11350-11366.
21. Lee, C., et al., *Measurement of the Elastic Properties and Intrinsic Strength of Monolayer Graphene.* Science, 2008. **321**(5887): p. 385.
22. Geim, A.K. and K.S. Novoselov, *The rise of graphene.* Nature Materials, 2007. **6**(3): p. 183-191.
23. Geim, A.K., *Graphene: Status and Prospects.* Science, 2009. **324**(5934): p. 1530.
24. Palermo, V., et al., *Nanoscale Mechanics of Graphene and Graphene Oxide in Composites: A Scientific and Technological Perspective.* Advanced Materials, 2016. **28**(29): p. 6232-6238.
25. Coleman, J.N., et al., *Two-Dimensional Nanosheets Produced by Liquid Exfoliation of Layered Materials.* Science, 2011. **331**(6017): p. 568-571.
26. Potts, J.R., et al., *Graphene-based polymer nanocomposites.* Polymer, 2011. **52**(1): p. 5-25.

27. Rafiee, M.A., et al., *Enhanced Mechanical Properties of Nanocomposites at Low Graphene Content.* ACS Nano, 2009. **3**(12): p. 3884-3890.
28. Song, W.-L., et al., *Polymeric nanocomposites with graphene sheets – Materials and device for superior thermal transport properties.* Polymer, 2012. **53**(18): p. 3910-3916.
29. Wu, J., et al., *Enhanced mechanical and gas barrier properties of rubber nanocomposites with surface functionalized graphene oxide at low content.* Polymer, 2013. **54**(7): p. 1930-1937.
30. Kim, J., L.J. Cote, and J. Huang, *Two Dimensional Soft Material: New Faces of Graphene Oxide.* Accounts of Chemical Research, 2012. **45**(8): p. 1356-1364.
31. Du, J. and H.-M. Cheng, *The Fabrication, Properties, and Uses of Graphene/Polymer Composites.* Macromolecular Chemistry and Physics, 2012. **213**(10-11): p. 1060-1077.
32. Young, R.J., et al., *The mechanics of graphene nanocomposites: A review.* Composites Science and Technology, 2012. **72**(12): p. 1459-1476.
33. Zhang, Y., et al., *What factors control the mechanical properties of poly (dimethylsiloxane) reinforced with nanosheets of 3-aminopropyltriethoxysilane modified graphene oxide?* Polymer, 2013. **54**(14): p. 3605-3611.
34. Li, Z., et al., *Control of the functionality of graphene oxide for its application in epoxy nanocomposites.* Polymer, 2013. **54**(23): p. 6437-6446.
35. Stankovich, S., et al., *Graphene-based composite materials.* Nature, 2006. **442**(7100): p. 282-286.
36. Joshi, R.K., et al., *Precise and Ultrafast Molecular Sieving Through Graphene Oxide Membranes.* Science, 2014. **343**(6172): p. 752-754.
37. Li, H., et al., *Ultrathin, Molecular-Sieving Graphene Oxide Membranes for Selective Hydrogen Separation.* Science, 2013. **342**(6154): p. 95-98.
38. Gao, W., et al., *Engineered Graphite Oxide Materials for Application in Water Purification.* Acs Applied Materials & Interfaces, 2011. **3**(6): p. 1821-1826.
39. Gao, W., et al., *Is reduced graphene oxide favorable for nonprecious metal oxygen-reduction catalysts?* Carbon, 2016. **102**: p. 346-356.
40. Song, Y.J., et al., *Graphene Oxide: Intrinsic Peroxidase Catalytic Activity and Its Application to Glucose Detection.* Advanced Materials, 2010. **22**(19): p. 2206-2210.
41. Zhou, M., Y.M. Zhai, and S.J. Dong, *Electrochemical Sensing and Biosensing Platform Based on Chemically Reduced Graphene Oxide.* Analytical Chemistry, 2009. **81**(14): p. 5603-5613.
42. Robinson, J.T., et al., *Reduced Graphene Oxide Molecular Sensors.* Nano Letters, 2008. **8**(10): p. 3137-3140.
43. Eda, G. and M. Chhowalla, *Chemically Derived Graphene Oxide: Towards Large-Area Thin-Film Electronics and Optoelectronics.* Advanced Materials, 2010. **22**(22): p. 2392-2415.
44. Eda, G., G. Fanchini, and M. Chhowalla, *Large-area ultrathin films of reduced graphene oxide as a transparent and flexible electronic material.* Nature Nanotechnology, 2008. **3**(5): p. 270-274.
45. Gao, W., et al., *Direct laser writing of micro-supercapacitors on hydrated graphite oxide films.* Nature Nanotechnology, 2011. **6**(8): p. 496-500.
46. Gao, W., et al., *Ozonated Graphene Oxide Film as a Proton-Exchange Membrane.* Angewandte Chemie-International Edition, 2014. **53**(14): p. 3588-3593.

47. Liu, Z., et al., *PEGylated nanographene oxide for delivery of water-insoluble cancer drugs.* Journal of the American Chemical Society, 2008. **130**(33): p. 10876-+.
48. Zhang, L.M., et al., *Functional Graphene Oxide as a Nanocarrier for Controlled Loading and Targeted Delivery of Mixed Anticancer Drugs.* Small, 2010. **6**(4): p. 537-544.
49. Rahmani, F., et al., *Molecular simulation insights on the in vacuo adsorption of amino acids on graphene oxide surfaces with varying surface oxygen densities.* Journal of Nanoparticle Research, 2016. **18**(11): p. 320.
50. Mahdavi, M., F. Rahmani, and S. Nouranian, *Molecular simulation of pH-dependent diffusion, loading, and release of doxorubicin in graphene and graphene oxide drug delivery systems.* Journal of Materials Chemistry B, 2016. **4**(46): p. 7441-7451.
51. Lu, Z., et al., *High-efficiency oxygen reduction to hydrogen peroxide catalysed by oxidized carbon materials.* Nature Catalysis, 2018. **1**(2): p. 156-162.
52. Kim, H.W., et al., *Efficient hydrogen peroxide generation using reduced graphene oxide-based oxygen reduction electrocatalysts.* Nature Catalysis, 2018. **1**(4): p. 282-290.
53. Rubin, E.M., *Genomics of cellulosic biofuels.* Nature, 2008. **454**(7206): p. 841-845.
54. Hill, J., et al., *Environmental, economic, and energetic costs and benefits of biodiesel and ethanol biofuels.* Proceedings of the National Academy of Sciences, 2006. **103**(30): p. 11206.
55. Thomas, B., et al., *Nanocellulose, a Versatile Green Platform: From Biosources to Materials and Their Applications.* Chemical Reviews, 2018. **118**(24): p. 11575-11625.
56. Zhu, H., et al., *Wood-Derived Materials for Green Electronics, Biological Devices, and Energy Applications.* Chemical Reviews, 2016. **116**(16): p. 9305-9374.
57. Muhd Julkapli, N. and S. Bagheri, *Nanocellulose as a green and sustainable emerging material in energy applications: a review.* Polymers for Advanced Technologies, 2017. **28**(12): p. 1583-1594.
58. Chen, H., et al., *Exploring Chemical, Mechanical, and Electrical Functionalities of Binders for Advanced Energy-Storage Devices.* Chemical Reviews, 2018. **118**(18): p. 8936-8982.
59. Jacob, J., et al., *Biopolymer based nanomaterials in drug delivery systems: A review.* Materials Today Chemistry, 2018. **9**: p. 43-55.
60. Löbmann, K. and A.J. Svagan, *Cellulose nanofibers as excipient for the delivery of poorly soluble drugs.* International Journal of Pharmaceutics, 2017. **533**(1): p. 285-297.
61. Chin, S.F., F.B. Jimmy, and S.C. Pang, *Size controlled fabrication of cellulose nanoparticles for drug delivery applications.* Journal of Drug Delivery Science and Technology, 2018. **43**: p. 262-266.
62. Treesuppharat, W., et al., *Synthesis and characterization of bacterial cellulose and gelatin-based hydrogel composites for drug-delivery systems.* Biotechnology Reports, 2017. **15**: p. 84-91.
63. Luo, H., et al., *Bacterial cellulose/graphene oxide nanocomposite as a novel drug delivery system.* Current Applied Physics, 2017. **17**(2): p. 249-254.
64. Abo-Elseoud, W.S., et al., *Chitosan nanoparticles/cellulose nanocrystals nanocomposites as a carrier system for the controlled release of repaglinide.* International Journal of Biological Macromolecules, 2018. **111**: p. 604-613.
65. Rahimi, M., et al., *Biocompatible magnetic tris(2-aminoethyl)amine functionalized nanocrystalline cellulose as a novel nanocarrier for anticancer drug delivery of methotrexate.* New Journal of Chemistry, 2017. **41**(5): p. 2160-2168.

66. Madhusudana Rao, K., A. Kumar, and S.S. Han, *Polysaccharide based bionanocomposite hydrogels reinforced with cellulose nanocrystals: Drug release and biocompatibility analyses.* International Journal of Biological Macromolecules, 2017. **101**: p. 165-171.
67. Sheikhi, A., et al., *Recent advances in nanoengineering cellulose for cargo delivery.* Journal of Controlled Release, 2019. **294**: p. 53-76.
68. Nogi, M., et al., *High thermal stability of optical transparency in cellulose nanofiber paper.* Applied Physics Letters, 2013. **102**(18): p. 181911.
69. Salajkova, M., et al., *Tough nanopaper structures based on cellulose nanofibers and carbon nanotubes.* Composites Science and Technology, 2013. **87**: p. 103-110.
70. Sun, X., et al., *Cellulose Nanofibers as a Modifier for Rheology, Curing and Mechanical Performance of Oil Well Cement.* Scientific Reports, 2016. **6**(1): p. 31654.
71. Li, F., E. Mascheroni, and L. Piergiovanni, *The Potential of NanoCellulose in the Packaging Field: A Review.* Packaging Technology and Science, 2015. **28**(6): p. 475-508.
72. Juntaro, J., et al., *Nanocellulose enhanced interfaces in truly green unidirectional fibre reinforced composites.* Composite Interfaces, 2007. **14**(7-9): p. 753-762.
73. Novoselov, K.S., et al., *Electric Field Effect in Atomically Thin Carbon Films.* Science, 2004. **306**(5696): p. 666-669.
74. Novoselov, K.S., et al., *Two-dimensional gas of massless Dirac fermions in graphene.* Nature, 2005. **438**(7065): p. 197-200.
75. Gao, W., et al., *New insights into the structure and reduction of graphite oxide.* Nat Chem, 2009. **1**(5): p. 403-408.
76. Viculis, L.M., J.J. Mack, and R.B. Kaner, *A Chemical Route to Carbon Nanoscrolls.* Science, 2003. **299**(5611): p. 1361.
77. Hernandez, Y., et al., *High-yield production of graphene by liquid-phase exfoliation of graphite.* Nat Nano, 2008. **3**(9): p. 563-568.
78. Li, X., et al., *Large-Area Synthesis of High-Quality and Uniform Graphene Films on Copper Foils.* Science, 2009. **324**(5932): p. 1312-1314.
79. Berger, C., et al., *Electronic Confinement and Coherence in Patterned Epitaxial Graphene.* Science, 2006. **312**(5777): p. 1191-1196.
80. Cai, J., et al., *Atomically precise bottom-up fabrication of graphene nanoribbons.* Nature, 2010. **466**(7305): p. 470-473.
81. Tomović, Ž., M.D. Watson, and K. Müllen, *Superphenalene-Based Columnar Liquid Crystals.* Angewandte Chemie International Edition, 2004. **43**(6): p. 755-758.
82. Treier, M., et al., *Surface-assisted cyclodehydrogenation provides a synthetic route towards easily processable and chemically tailored nanographenes.* Nat Chem, 2011. **3**(1): p. 61-67.
83. Gilje, S., et al., *A Chemical Route to Graphene for Device Applications.* Nano Letters, 2007. **7**(11): p. 3394-3398.
84. Stankovich, S., et al., *Synthesis of graphene-based nanosheets via chemical reduction of exfoliated graphite oxide.* Carbon, 2007. **45**(7): p. 1558-1565.
85. Kim, S., et al., *Room-temperature metastability of multilayer graphene oxide films.* Nat Mater, 2012. **11**(6): p. 544-549.
86. A. Lerf, H.H., T. Riedl, M. Forster and J. Klinowski, *Solid State Ionics*. Vol. 101-103. 1997. 857-862.
87. He, H.Y., et al., *Solid-state NMR studies of the structure of graphite oxide.* Journal of Physical Chemistry, 1996. **100**(51): p. 19954-19958.

88. Lerf, A., et al., *Structure of graphite oxide revisited.* Journal of Physical Chemistry B, 1998. **102**(23): p. 4477-4482.
89. Gao, W., et al., *New insights into the structure and reduction of graphite oxide.* Nature Chemistry, 2009. **1**(5): p. 403-408.
90. Chua, C.K. and M. Pumera, *Chemical reduction of graphene oxide: a synthetic chemistry viewpoint.* Chemical Society Reviews, 2014. **43**(1): p. 291-312.
91. Boukhvalov, D.W., et al., *A Computational Investigation of the Catalytic Properties of Graphene Oxide: Exploring Mechanisms by using DFT Methods.* Chemcatchem, 2012. **4**(11): p. 1844-1849.
92. Wang, X.X., Z.S. Chen, and S.B. Yang, *Application of graphene oxides for the removal of Pb(II) ions from aqueous solutions: Experimental and DFT calculation.* Journal of Molecular Liquids, 2015. **211**: p. 957-964.
93. Zhao, W.H., et al., *The strong effect of substituents on the carbonyl reduction in graphene oxide: A DFT study.* Computational and Theoretical Chemistry, 2015. **1068**: p. 1-7.
94. Larijani, H.T., M.D. Ganji, and M. Jahanshahi, *Trends of amino acid adsorption onto graphene and graphene oxide surfaces: a dispersion corrected DFT study.* Rsc Advances, 2015. **5**(113): p. 92843-92857.
95. Rui, X., et al., *Wrapping Nanocellulose Nets around Graphene Oxide Sheets.* Angewandte Chemie, 2018. **0**(0).
96. Medhekar, N.V., et al., *Hydrogen Bond Networks in Graphene Oxide Composite Paper: Structure and Mechanical Properties.* Acs Nano, 2010. **4**(4): p. 2300-2306.
97. Sun, X.T., et al., *Mechanism of Graphene Oxide as an Enzyme Inhibitor from Molecular Dynamics Simulations.* Acs Applied Materials & Interfaces, 2014. **6**(10): p. 7153-7163.
98. Raghav, N., S. Chakraborty, and P.K. Maiti, *Molecular mechanism of water permeation in a helium impermeable graphene and graphene oxide membrane.* Physical Chemistry Chemical Physics, 2015. **17**(32): p. 20557-20562.
99. Tang, H., et al., *Molecular Dynamics Study of the Aggregation Process of Graphene Oxide in Water.* Journal of Physical Chemistry C, 2015. **119**(47): p. 26712-26718.
100. Devanathan, R., et al., *Molecular Dynamics Simulations Reveal that Water Diffusion between Graphene Oxide Layers is Slow.* Scientific Reports, 2016. **6**: p. 8.
101. Willcox, J.K.L. and H.J. Kim, *Molecular Dynamics Study of Water Flow across Multiple Layers of Pristine, Oxidized, and Mixed Regions of Graphene Oxide.* Acs Nano, 2017. **11**(2): p. 2187-2193.
102. Rahmani, F., et al., *Confinement effects on the thermal stability of poly(ethylene oxide)/graphene nanocomposites: A reactive molecular dynamics simulation study.* Journal of Polymer Science Part B: Polymer Physics, 2017. **55**(13): p. 1026-1035.
103. Rahmani, F., et al., *Reactive Molecular Simulation of the Damage Mitigation Efficacy of POSS-, Graphene-, and Carbon Nanotube-Loaded Polyimide Coatings Exposed to Atomic Oxygen Bombardment.* ACS Applied Materials & Interfaces, 2017. **9**(14): p. 12802-12811.
104. Akarsh, V. and P. Avinash, *Molecular dynamics based simulations to study the fracture strength of monolayer graphene oxide.* Nanotechnology, 2018. **29**(11): p. 115706.
105. Pinkert, A., et al., *Ionic Liquids and Their Interaction with Cellulose.* Chemical Reviews, 2009. **109**(12): p. 6712-6728.
106. Wang, H., G. Gurau, and R.D. Rogers, *Ionic liquid processing of cellulose.* Chemical Society Reviews, 2012. **41**(4): p. 1519-1537.

107. Schwarz, W., *The cellulosome and cellulose degradation by anaerobic bacteria.* Applied Microbiology and Biotechnology, 2001. **56**(5): p. 634-649.
108. Pérez, J., et al., *Biodegradation and biological treatments of cellulose, hemicellulose and lignin: an overview.* International Microbiology, 2002. **5**(2): p. 53-63.
109. Wang, A. and T. Zhang, *One-Pot Conversion of Cellulose to Ethylene Glycol with Multifunctional Tungsten-Based Catalysts.* Accounts of Chemical Research, 2013. **46**(7): p. 1377-1386.
110. Barta, K. and P.C. Ford, *Catalytic Conversion of Nonfood Woody Biomass Solids to Organic Liquids.* Accounts of Chemical Research, 2014. **47**(5): p. 1503-1512.
111. Esposito, D. and M. Antonietti, *Redefining biorefinery: the search for unconventional building blocks for materials.* Chemical Society Reviews, 2015. **44**(16): p. 5821-5835.
112. Zhang, X., K. Wilson, and A.F. Lee, *Heterogeneously Catalyzed Hydrothermal Processing of C5–C6 Sugars.* Chemical Reviews, 2016. **116**(19): p. 12328-12368.
113. Zhang, Z., J. Song, and B. Han, *Catalytic Transformation of Lignocellulose into Chemicals and Fuel Products in Ionic Liquids.* Chemical Reviews, 2017. **117**(10): p. 6834-6880.
114. Shrotri, A., H. Kobayashi, and A. Fukuoka, *Cellulose Depolymerization over Heterogeneous Catalysts.* Accounts of Chemical Research, 2018. **51**(3): p. 761-768.
115. Lynd, L.R., et al., *Microbial Cellulose Utilization: Fundamentals and Biotechnology.* Microbiology and Molecular Biology Reviews, 2002. **66**(3): p. 506.
116. Kumar, P., et al., *Methods for Pretreatment of Lignocellulosic Biomass for Efficient Hydrolysis and Biofuel Production.* Industrial & Engineering Chemistry Research, 2009. **48**(8): p. 3713-3729.
117. Chen, H., et al., *A review on the pretreatment of lignocellulose for high-value chemicals.* Fuel Processing Technology, 2017. **160**: p. 196-206.
118. Liu, C., et al., *Catalytic fast pyrolysis of lignocellulosic biomass.* Chemical Society Reviews, 2014. **43**(22): p. 7594-7623.
119. Arora, P. and Z. Zhang, *Battery Separators.* Chemical Reviews, 2004. **104**(10): p. 4419-4462.
120. Kontturi, E., T. Tammelin, and M. Österberg, *Cellulose—model films and the fundamental approach.* Chemical Society Reviews, 2006. **35**(12): p. 1287-1304.
121. Roy, D., et al., *Cellulose modification by polymer grafting: a review.* Chemical Society Reviews, 2009. **38**(7): p. 2046-2064.
122. Joubert, F., et al., *The preparation of graft copolymers of cellulose and cellulose derivatives using ATRP under homogeneous reaction conditions.* Chemical Society Reviews, 2014. **43**(20): p. 7217-7235.
123. Gericke, M., J. Trygg, and P. Fardim, *Functional Cellulose Beads: Preparation, Characterization, and Applications.* Chemical Reviews, 2013. **113**(7): p. 4812-4836.
124. Ummartyotin, S. and H. Manuspiya, *A critical review on cellulose: From fundamental to an approach on sensor technology.* Renewable and Sustainable Energy Reviews, 2015. **41**: p. 402-412.
125. Wu, Z.-Y., et al., *Bacterial Cellulose: A Robust Platform for Design of Three Dimensional Carbon-Based Functional Nanomaterials.* Accounts of Chemical Research, 2016. **49**(1): p. 96-105.
126. Lavoine, N. and L. Bergström, *Nanocellulose-based foams and aerogels: processing, properties, and applications.* Journal of Materials Chemistry A, 2017. **5**(31): p. 16105-16117.

127. Chen, W., et al., *Nanocellulose: a promising nanomaterial for advanced electrochemical energy storage.* Chemical Society Reviews, 2018. **47**(8): p. 2837-2872.
128. Chen, C. and L. Hu, *Nanocellulose toward Advanced Energy Storage Devices: Structure and Electrochemistry.* Accounts of Chemical Research, 2018. **51**(12): p. 3154-3165.
129. Zhou, S., et al., *Cladophora Cellulose: Unique Biopolymer Nanofibrils for Emerging Energy, Environmental, and Life Science Applications.* Accounts of Chemical Research, 2019. **52**(8): p. 2232-2243.
130. Cosgrove, D.J., *Re-constructing our models of cellulose and primary cell wall assembly.* Current Opinion in Plant Biology, 2014. **22**: p. 122-131.
131. Smithers, E.T., J.X. Luo, and R.J. Dyson, *Mathematical principles and models of plant growth mechanics: from cell wall dynamics to tissue morphogenesis.* Journal of Experimental Botany, 2019. **70**(14): p. 3587-3599.
132. Zhang, Y.Q., et al., *Recent progress in theoretical and computational studies on the utilization of lignocellulosic materials.* Green Chemistry, 2019. **21**(1): p. 9-35.
133. Beckham, G.T., et al., *Towards a molecular-level theory of carbohydrate processivity in glycoside hydrolases.* Current Opinion in Biotechnology, 2014. **27**: p. 96-106.
134. Toukach, F.V. and V.P. Ananikov, *Recent advances in computational predictions of NMR parameters for the structure elucidation of carbohydrates: methods and limitations.* Chemical Society Reviews, 2013. **42**(21): p. 8376-8415.
135. Millett, M.A., A.J. Baker, and L.D. Satter, *Physical And Chemical Pretreatments For Enhancing Cellulose Saccharification.* Biotechnology and Bioengineering, 1976(6): p. 125-153.
136. Iwamoto, S., A.N. Nakagaito, and H. Yano, *Nano-fibrillation of pulp fibers for the processing of transparent nanocomposites.* Applied Physics A, 2007. **89**(2): p. 461-466.
137. Zimmermann, T., N. Bordeanu, and E. Strub, *Properties of nanofibrillated cellulose from different raw materials and its reinforcement potential.* Carbohydrate Polymers, 2010. **79**(4): p. 1086-1093.
138. Dufresne, A., J.-Y. Cavaillé, and M.R. Vignon, *Mechanical behavior of sheets prepared from sugar beet cellulose microfibrils.* Journal of Applied Polymer Science, 1997. **64**(6): p. 1185-1194.
139. Johnson, R.K., et al., *A new bio-based nanocomposite: fibrillated TEMPO-oxidized celluloses in hydroxypropylcellulose matrix.* Cellulose, 2009. **16**(2): p. 227-238.
140. Dong, X.M., J.-F. Revol, and D.G. Gray, *Effect of microcrystallite preparation conditions on the formation of colloid crystals of cellulose.* Cellulose, 1998. **5**(1): p. 19-32.
141. Song, J., et al., *Processing bulk natural wood into a high-performance structural material.* Nature, 2018. **554**(7691): p. 224-228.
142. Chen, C., et al., *Scalable and Sustainable Approach toward Highly Compressible, Anisotropic, Lamellar Carbon Sponge.* Chem, 2018. **4**(3): p. 544-554.
143. Trifol, J., et al., *Chemically extracted nanocellulose from sisal fibres by a simple and industrially relevant process.* Cellulose, 2017. **24**(1): p. 107-118.
144. Bhatnagar, A. and M. Sain, *Processing of Cellulose Nanofiber-reinforced Composites.* Journal of Reinforced Plastics and Composites, 2005. **24**(12): p. 1259-1268.
145. Rånby, B.G., *Fibrous macromolecular systems. Cellulose and muscle. The colloidal properties of cellulose micelles.* Discussions of the Faraday Society, 1951. **11**(0): p. 158-164.

146. Saito, T., et al., *Homogeneous Suspensions of Individualized Microfibrils from TEMPO-Catalyzed Oxidation of Native Cellulose.* Biomacromolecules, 2006. **7**(6): p. 1687-1691.
147. Saito, T., et al., *Individualization of Nano-Sized Plant Cellulose Fibrils by Direct Surface Carboxylation Using TEMPO Catalyst under Neutral Conditions.* Biomacromolecules, 2009. **10**(7): p. 1992-1996.
148. Wu, Q., et al., *A High Strength Nanocomposite Based on Microcrystalline Cellulose and Polyurethane.* Biomacromolecules, 2007. **8**(12): p. 3687-3692.
149. Broder, J.D., et al., *Biofuels system economics.* World Resource Review, 1995. **7**(4): p. 560-569.
150. Iranmahboob, J., F. Nadim, and S. Monemi, *Optimizing acid-hydrolysis: a critical step for production of ethanol from mixed wood chips.* Biomass and Bioenergy, 2002. **22**(5): p. 401-404.
151. Hubbe, M.A., et al., *Cellulosic Nanocomposites: A Review.* Bioresources, 2008. **3**(3): p. 929-980.
152. Habibi, Y., L.A. Lucia, and O.J. Rojas, *Cellulose Nanocrystals: Chemistry, Self-Assembly, and Applications.* Chemical Reviews, 2010. **110**(6): p. 3479-3500.
153. Wang, B. and M. Sain, *Isolation of nanofibers from soybean source and their reinforcing capability on synthetic polymers.* Composites Science and Technology, 2007. **67**(11): p. 2521-2527.
154. Filson, P.B. and B.E. Dawson-Andoh, *Sono-chemical preparation of cellulose nanocrystals from lignocellulose derived materials.* Bioresource Technology, 2009. **100**(7): p. 2259-2264.
155. Elazzouzi-Hafraoui, S., et al., *The Shape and Size Distribution of Crystalline Nanoparticles Prepared by Acid Hydrolysis of Native Cellulose.* Biomacromolecules, 2008. **9**(1): p. 57-65.
156. Beck-Candanedo, S., M. Roman, and D.G. Gray, *Effect of Reaction Conditions on the Properties and Behavior of Wood Cellulose Nanocrystal Suspensions.* Biomacromolecules, 2005. **6**(2): p. 1048-1054.
157. Bondeson, D., A. Mathew, and K. Oksman, *Optimization of the isolation of nanocrystals from microcrystalline celluloseby acid hydrolysis.* Cellulose, 2006. **13**(2): p. 171.
158. Karim, Z., et al., *Necessity of enzymatic hydrolysis for production and functionalization of nanocelluloses.* Critical Reviews in Biotechnology, 2017. **37**(3): p. 355-370.
159. Henriksson, M., et al., *An environmentally friendly method for enzyme-assisted preparation of microfibrillated cellulose (MFC) nanofibers.* European Polymer Journal, 2007. **43**(8): p. 3434-3441.
160. Pääkkö, M., et al., *Enzymatic Hydrolysis Combined with Mechanical Shearing and High-Pressure Homogenization for Nanoscale Cellulose Fibrils and Strong Gels.* Biomacromolecules, 2007. **8**(6): p. 1934-1941.
161. Tibolla, H., F.M. Pelissari, and F.C. Menegalli, *Cellulose nanofibers produced from banana peel by chemical and enzymatic treatment.* LWT - Food Science and Technology, 2014. **59**(2, Part 2): p. 1311-1318.
162. Chung, D., et al., *Cellulosic ethanol production via consolidated bioprocessing at 75 °C by engineered Caldicellulosiruptor bescii.* Biotechnology for Biofuels, 2015. **8**(1): p. 163.
163. Yarbrough, J.M., et al., *Multifunctional Cellulolytic Enzymes Outperform Processive Fungal Cellulases for Coproduction of Nanocellulose and Biofuels.* ACS Nano, 2017. **11**(3): p. 3101-3109.

164. Camarero Espinosa, S., et al., *Isolation of Thermally Stable Cellulose Nanocrystals by Phosphoric Acid Hydrolysis.* Biomacromolecules, 2013. **14**(4): p. 1223-1230.
165. Reid, M.S., M. Villalobos, and E.D. Cranston, *Benchmarking Cellulose Nanocrystals: From the Laboratory to Industrial Production.* Langmuir, 2017. **33**(7): p. 1583-1598.
166. Battista, O.A., *Hydrolysis and Crystallization of Cellulose.* Industrial & Engineering Chemistry, 1950. **42**(3): p. 502-507.
167. Lee, S.-Y., et al., *Nanocellulose reinforced PVA composite films: Effects of acid treatment and filler loading.* Fibers and Polymers, 2009. **10**(1): p. 77-82.
168. Filpponen, I. and D.S. Argyropoulos, *Regular Linking of Cellulose Nanocrystals via Click Chemistry: Synthesis and Formation of Cellulose Nanoplatelet Gels.* Biomacromolecules, 2010. **11**(4): p. 1060-1066.
169. Liu, D., et al., *Starch composites reinforced by bamboo cellulosic crystals.* Bioresource Technology, 2010. **101**(7): p. 2529-2536.
170. Chen, L., et al., *Unveiling Mesopore Evolution in Carbonized Wood: Interfacial Separation, Migration, and Degradation of Lignin Phase.* ACS Sustainable Chemistry & Engineering, 2015. **3**(10): p. 2489-2495.
171. Shafizadeh, F. and A.G.W. Bradbury, *Thermal degradation of cellulose in air and nitrogen at low temperatures.* Journal of Applied Polymer Science, 1979. **23**(5): p. 1431-1442.
172. Melo, E. and J.F. Kennedy, *Cellulose hydrolysis (biotechnology monographs, Vol. 3) edited by L.-T. Fan, M. M. Gharpuray and Y.-H. Lee, Springer-Verlag, Berlin, Heidelberg, New York, London, Paris and Tokyo, 1987. pp. viii + 198, price DM168.00. ISBN 3-540-17671-3.* British Polymer Journal, 1988. **20**(6): p. 532-532.
173. Kilzer, F.J. and A. Broido, *Speculations on the nature of cellulose pyrolysis.* Pyrodynamics, 1965. **2**: p. 151-163.
174. Zwart, R.W.R., H. Boerrigter, and A. van der Drift, *The Impact of Biomass Pretreatment on the Feasibility of Overseas Biomass Conversion to Fischer−Tropsch Products.* Energy & Fuels, 2006. **20**(5): p. 2192-2197.
175. Guan, H., Z. Cheng, and X. Wang, *Highly Compressible Wood Sponges with a Spring-like Lamellar Structure as Effective and Reusable Oil Absorbents.* ACS Nano, 2018. **12**(10): p. 10365-10373.
176. Fu, Q., et al., *Wood Nanotechnology for Strong, Mesoporous, and Hydrophobic Biocomposites for Selective Separation of Oil/Water Mixtures.* ACS Nano, 2018. **12**(3): p. 2222-2230.
177. Vidiella del Blanco, M., E.J. Fischer, and E. Cabane, *Underwater Superoleophobic Wood Cross Sections for Efficient Oil/Water Separation.* Advanced Materials Interfaces, 2017. **4**(21): p. 1700584.
178. Keplinger, T., X. Wang, and I. Burgert, *Nanofibrillated cellulose composites and wood derived scaffolds for functional materials.* Journal of Materials Chemistry A, 2019. **7**(7): p. 2981-2992.
179. Mazeau, K. and A. Rivet, *Wetting the (110) and (100) Surfaces of Iβ Cellulose Studied by Molecular Dynamics.* Biomacromolecules, 2008. **9**(4): p. 1352-1354.
180. Zhao, Y.L., et al., *Effects of Cationic Structure on Cellulose Dissolution in Ionic Liquids: A Molecular Dynamics Study.* Chemphyschem, 2012. **13**(13): p. 3126-3133.
181. Zhao, Y., et al., *Effects of anionic structure on the dissolution of cellulose in ionic liquids revealed by molecular simulation.* Carbohydrate Polymers, 2013. **94**(2): p. 723-730.

182. Rabideau, B.D., A. Agarwal, and A.E. Ismail, *Observed Mechanism for the Breakup of Small Bundles of Cellulose I alpha and I beta in Ionic Liquids from Molecular Dynamics Simulations.* Journal of Physical Chemistry B, 2013. **117**(13): p. 3469-3479.
183. Bergenstråhle, M., L.A. Berglund, and K. Mazeau, *Thermal Response in Crystalline Iβ Cellulose: A Molecular Dynamics Study.* The Journal of Physical Chemistry B, 2007. **111**(30): p. 9138-9145.
184. Mayes, H.B. and L.J. Broadbelt, *Unraveling the Reactions that Unravel Cellulose.* Journal of Physical Chemistry A, 2012. **116**(26): p. 7098-7106.
185. Agarwal, V., et al., *Ab Initio Dynamics of Cellulose Pyrolysis: Nascent Decomposition Pathways at 327 and 600 degrees C.* Journal of the American Chemical Society, 2012. **134**(36): p. 14958-14972.
186. Zheng, M., et al., *Initial reaction mechanisms of cellulose pyrolysis revealed by ReaxFF molecular dynamics.* Fuel, 2016. **177**: p. 130-141.
187. Paajanen, A. and J. Vaari, *High-temperature decomposition of the cellulose molecule: a stochastic molecular dynamics study.* Cellulose, 2017. **24**(7): p. 2713-2725.
188. Gao, W., *Graphene oxide: Reduction recipes, spectroscopy, and applications*. 2015: Springer International Publishing. 1-147.
189. Ayrat M. Dimiev, S.E., *Graphene Oxide: Fundamentals and Applications*. 2017, Chichester, West Sussex: John Wiley & Sons, Inc.
190. Gao, E., et al., *Intrinsic mechanical properties of graphene oxide films: Strain characterization and the gripping effects.* Carbon, 2017. **118**: p. 467-474.
191. Sakorikar, T., et al., *Thickness-dependent Crack Propagation in Uniaxially Strained Conducting Graphene Oxide Films on Flexible Substrates.* Scientific Reports, 2017. **7**(1): p. 2598.
192. Cao, C., et al., *Nonlinear fracture toughness measurement and crack propagation resistance of functionalized graphene multilayers.* Science Advances, 2018. **4**(4): p. eaao7202.
193. Cao, C., et al., *High strength measurement of monolayer graphene oxide.* Carbon, 2015. **81**: p. 497-504.
194. Wei, X., et al., *Plasticity and ductility in graphene oxide through a mechanochemically induced damage tolerance mechanism.* Nature Communications, 2015. **6**(1): p. 8029.
195. Soler-Crespo, R.A., et al., *Engineering the Mechanical Properties of Monolayer Graphene Oxide at the Atomic Level.* The Journal of Physical Chemistry Letters, 2016. **7**(14): p. 2702-2707.
196. Verma, A., A. Parashar, and M. Packirisamy, *Tailoring the failure morphology of 2D bicrystalline graphene oxide.* Journal of Applied Physics, 2018. **124**(1): p. 015102.
197. Verma, A. and A. Parashar, *Molecular dynamics based simulations to study the fracture strength of monolayer graphene oxide.* Nanotechnology, 2018. **29**(11): p. 115706.
198. Shi, Y., et al., *Preparation of graphene oxide–cellulose acetate nanocomposite membrane for high-flux desalination.* Journal of Materials Science, 2017. **52**(22): p. 13296-13306.
199. Uddin, M.E., et al., *Preparation and enhanced mechanical properties of non-covalently-functionalized graphene oxide/cellulose acetate nanocomposites.* Composites Part B: Engineering, 2016. **90**: p. 223-231.
200. Kim, C.-J., et al., *Graphene oxide/cellulose composite using NMMO monohydrate.* Carbohydrate Polymers, 2011. **86**(2): p. 903-909.

201. Luo, H., et al., *Layer-by-Layer Assembled Bacterial Cellulose/Graphene Oxide Hydrogels with Extremely Enhanced Mechanical Properties.* Nano-Micro Letters, 2018. **10**(3): p. 42.
202. Li, Y.Y., et al., *Hybridizing wood cellulose and graphene oxide toward high-performance fibers.* Npg Asia Materials, 2015. **7**: p. 10.
203. Peng, H., et al., *Simultaneous Reduction and Surface Functionalization of Graphene Oxide by Natural Cellulose with the Assistance of the Ionic Liquid.* The Journal of Physical Chemistry C, 2012. **116**(30): p. 16294-16299.
204. Kabiri, R. and H. Namazi, *Nanocrystalline cellulose acetate (NCCA)/graphene oxide (GO) nanocomposites with enhanced mechanical properties and barrier against water vapor.* Cellulose, 2014. **21**(5): p. 3527-3539.
205. Compton, O.C., et al., *Tuning the Mechanical Properties of Graphene Oxide Paper and Its Associated Polymer Nanocomposites by Controlling Cooperative Intersheet Hydrogen Bonding.* ACS Nano, 2012. **6**(3): p. 2008-2019.
206. Zhang, J. and D. Jiang, *Molecular dynamics simulation of mechanical performance of graphene/graphene oxide paper based polymer composites.* Carbon, 2014. **67**: p. 784-791.
207. Rahman, R., J.T. Foster, and A. Haque, *Molecular Dynamics Simulation and Characterization of Graphene-Cellulose Nanocomposites.* Journal of Physical Chemistry A, 2013. **117**(25): p. 5344-5353.

Chapter 2: Simulation Methodology

2.1 Quantum Mechanics

Quantum mechanics (QM) has been used to study the electron and chemistry of materials at subatomic level over decades [1, 2]. Instead of describing the motion of a particle by position and momentum, a wavefunction is used to specify the state of motion in QM. Generally, the time-dependent Schrödinger's wave equation is the form of

$$\frac{-\hbar^2}{2m}\nabla^2\Psi(\mathbf{r}) + V(\mathbf{r})\Psi(\mathbf{r}) = E\Psi(\mathbf{r}) \quad (2\text{-}1)$$

Where $\hbar$ is the reduced Planck constant, m is the electrion mass, ∇ is the Laplacian operator, Ψ is the wave function, V is the potential energy, E is the energy eigenvalue and $(\mathbf{r})$ represents the quantities are functions of spherical polar coordinates (r, θ, φ).

In principle, solving the Schrödinger equation exactly will increase the accuracy in the prediction of atoms and molecules, whereas in practice it is only possible to get the exact solution for one electron systems. Therefore, numerous methods have been developed to approximately calculate the electronic energy, electron density and other properties for multi-electron system[3-8] including: (1) ab initio, (2) density functional theory (DFT), (3) semi-empirical methods.

The ability of describing electronic structures makes QM the most accurate predictive method compared with other simulation approaches. Because of this supreme accuracy and predictability of QM method, it is widely used to evaluate and verify the structural and electronic properties of carbon-based materials and compared with experimental results. For example, with the reported unit cell parameters from experiments, QM is able to perform optimizations in material geometry and regenerate optimal lattice parameters based on the energy calculations of QM method. Similarly, QM method can be used to determine the most energetically favorable

bond lengths, bond angle and HBs patterns inside materials and offer useful information in the manipulation of advanced materials. Furthermore, QM is commonly used to interpret the interactions, adsorptions and dissolution mechanism associated with experiments. When considering the calculation of some mechanical properties, technically QM method could be able to provide correct predictions. However, due to the limitations of system size and simulation time, the small representative model used in QM might result in the lack of description of synergetic effects belongs to complex bulk structures, as well as the description of macroscopic structures and properties. Several possible ways to solve this problem are to: (1) make more approximations (which might conflict with the accuracy of QM method); (2) allow the combination of QM and other (MM or COSMO-RS) methods; (3) develop methods or hardware that can highly promote the QM calculations.

2.2 Molecular Mechanics

Force field based computational methods, such as molecular mechanics (MM), molecular dynamics (MD) simulations and Monte Carlo (MC) calculations have been applied in a large variety of scientific fields [9, 10]. MD is one of the mostly used MM methods which generate the trajectory of atom positions, velocities and accelerations by calculating the motions based on classical Newtonian equation under a time evolution at finite temperatures [11-13]

$$F = m \cdot a = m \cdot \frac{dv}{dt} = m \cdot \frac{d^2\mathbf{x}}{dt^2} \tag{2-2}$$

Where F is the force exerted on particle, m is the mass of the particle, a is the acceleration of particle and $\mathbf{x}$ is the cartesian vector of the system.

The calculation of total energy (E_{tot}) in MM includes bonded terms (E_{bonded}) that are interactions involved with atoms linked by covalent bonds and nonbonded terms ($E_{nonbonded}$) that

related with long-range electrostatic and van der Waals forces. Although the detailed equation varies depends on different force fields, a general for E_{tot} could be describe as:

$$E_{tot} = E_{bonded} + E_{nonbonded} \tag{2-3}$$

With

$$E_{bonded} = E_{bond} + E_{angle} + E_{dihedral} \tag{2-4}$$

$$E_{nonbonded} = E_{electrostatic} + E_{van\ der\ Waals} \tag{2-5}$$

The ability of simulating large system with ~500,000 atoms in the system makes MD a proper tools in the studies of molecular structures and properties predictions [9, 10, 14], drug design [15, 16] and complex protein and DNA system [17, 18]. Although these advantages allow the wide applications of MD methods, the limitation of MD is obvious. The accuracy and predictability of MD method are highly dependent on refinement of force field parameters. The relatively long equilibrium time (over a microsecond in time scale) for large systems is another challenging problem need to be solved for MD method. Also, the bonds and angles of atoms are fixed without any breaking, which is opposites from the realistic molecules. Another widely used MM method is energy minimization to obtain the most stable conformers of molecules with force fields as the criterion. It is widely used in the calculations of elastic modulus of cellulose, and a detailed discussion will be found in session 8. Different from MD methods, MC method compute the properties of molecules as long as it has a probabilistic interpretation (such as the free energy) without out the involvement of time [19].The MC method is widely used in the studies of molecular conformations [20, 21], adsorptions [22-24], diffusions [25-27] and estimation of kinetic parameters [28-30]. Several popular force fields for MM studies are GROMOS [31-33], CHARMM [34-36], COMPASS [37], AMBER [38-41], GLYCAM06 [42], OPLS-AA [43-46], PCFF [37], UFF [47], CVFF [48], DREIDING [49], MM2 [50], MM3 [51], MM4 [52].

2.3 QM/MM method and Ab Initio Molecular Dynamics

However, QM method is not capable to describe large system, especially with protein or enzyme in the model, due to its limitation in simulating systems within 1-10 nm. To address this issue, a combination QM/MM method is developed to contain both accuracy (QM) and speed (MM) [53]. The QM region calculates the molecules that involved with bonds formations and breaking, while MM part contains large molecules such as protein residues or solution elements via classical force fields. This advantage allows QM/MM method to widely used for the calculations of chemical reactions in solutions, biological systems, and other complex systems.

Despite the success of MD method in describing both equilibrium and dynamical properties of systems, it still has limitations because of the force fields. The accuracy of MD method highly depends on the force fields. Additionally, classical MD method cannot allow bonds formation and breaking during the simulations. In order to address these problems, ab initio molecular dynamics (AIMD) method has been developed and successfully combined finite temperature dynamics with on-the-fly force that based on the accurate electronic structure calculations. Based on Schrödinger equation, classical, Ehrenfest, Born-Oppenheimer and Car-Parrinello molecular dynamics (CPMD) has been derived via separating the nuclear and electronic degrees of freedom [54]. The utilization of electronic structure calculation not only allows AIMD to represent bonds forming and breaking, but also make it possible to describe system with unusual chemical bonds and reactions as well. Therefore, AIMD is widely applied in the calculations including the structure, dynamic and proton transport in aqueous solutions, cluster and ice system [55-66],complex polymer and protein system [67-70] and surface catalysis [71, 72]. However, AIMD is only capable of describing small system with up to hundreds of atoms and timescale (tens of picoseconds) compared with MD method

because of the expensive electronic calculations. Similar to MD method, the accuracy of AIMD is dependent on the electronic structure method used. More details of AIMD can be find in the reference and reviews [54, 73-80].

2.4 Reactive Force Field Method

Due to the advantage that electronic/reaction details and large time/space scale computations can be achieved simultaneously, molecule dynamics based on reactive force field (ReaxFF) has gained more and more attention from the cellulose community recently. ReaxFF has been developed by van Duin in 2001 [81] with a bond-order concept adopted from Tersoff [82] to develop a reactive empirical force field (ReaxFF) for hydrocarbon systems. In the ReaxFF description, the bond order BO'_{ij} for a pair of atoms can be obtained directly from the interatomic distance r_{ij}, as illustrated in Eq. (2-6)

$$\begin{aligned} BO'_{ij} &= BO'^{\sigma}_{ij} + BO'^{\pi}_{ij} + BO'^{\pi\pi}_{ij} \\ &= \exp\left[p_{bo1} \cdot \left(\frac{r_{ij}}{r_o^{\sigma}} \right)^{P_{bo2}} \right] + \exp\left[p_{bo3} \cdot \left(\frac{r_{ij}}{r_o^{\pi}} \right)^{P_{bo4}} \right] + \exp\left[p_{bo5} \cdot \left(\frac{r_{ij}}{r_o^{\pi\pi}} \right)^{P_{bo6}} \right] \end{aligned} \quad (2\text{-}6)$$

Where the p_{bo1}, p_{bo2}, p_{bo3}, p_{bo4}, p_{bo5} and p_{bo6} are used to describe the σ, π and $\pi\pi$ bonds, respectively. Eq. (2-6) is defined so that the value of the three exponentials is unity below a threshold interatomic distance and zero at longer distances.

The assumption of the bond orders BO'_{ij} concept allows the spontaneous bond breaking or forming while keeping the energy and force continuous during the simulation. The bond order values need to be updated at each MD step in order to determine the total energy of the system. Generally, the total energy for ReaxFF is in the form of

$$E_{tot} = E_{bond} + E_{lp} + E_{over} + E_{under} + E_{val} + E_{pen} + E_{coa} + E_{C2} + E_{triple} + E_{tors} + E_{conj} + E_{H-bond} + E_{vdWaals} + E_{Coulomb} \quad (2\text{-}7)$$

For instance, the bond energy E_{bond} is calculated from the bond order BO'_{ij} as:

$$E_{bond} = -D_e^{\sigma} \cdot BO_{ij}^{\sigma} \cdot \exp\left[p_{be1}\left(1 - BO_{ij}^{\sigma}\right)^{p_{be2}} \right] - D_e^{\pi} \cdot BO_{ij}^{\pi} - D_e^{\pi\pi} \cdot BO_{ij}^{\pi\pi} \quad (2\text{-}8)$$

where D_e^{σ}, D_e^{π}, $D_e^{\pi\pi}$, p_{be1} and p_{be2} are the bond parameters, BO_{ij}^{σ}, BO_{ij}^{π} and $BO_{ij}^{\pi\pi}$ are the corrected bond orders for the σ, π and $\pi\pi$ bonds, respectively. Similarly, in order to describe the connectivity, the nonbonded van der Waals and Coulomb interactions are also calculated between every atom pair at each MD step. In addition, the electronegativity equalization method (EEM) [83] is applied to dynamically derive the atomic charges for the polarization effects. More detailed descriptions of specific energy terms in Eq. (2-7) and the algorithms for the nonbonded calculation can be found from the ReaxFF manual [84] and publications [81, 85, 86]. It is worth noting that to ensure a smooth transition of the energy and the force for the ReaxFF calculations, the bond order and the energy terms for the bond, the angle and the dihedral angle are zero when considering the dissociation of this bond.

ReaxFF has been successfully used in describing complex and large-scale reactive systems that contained many hundreds to several thousands of atoms such as protein/DNA [87, 88], membrane fuel cell systems [89], and very complex coal structure and properties [90, 91]. Because of the bond-order concept, ReaxFF is able to widely used in the study of adsorption, dissociation, complicated reactions [92-94] and specialized in predicting structural evolution, tracing intermediates, and analyzing final products [95-98]. Although ReaxFF is generally an order slower than nonreactive force fields, because of the expensive charge calculations via the electronegativity equalization method (EEM) [99-101], a time scale of microseconds trajectory could be archived

with the help of parallel calculations. More details of ReaxFF are available from recent reviews [86, 102, 103].

2.5 Simulation Methodology and Computational Characterizations

2.5.1 The Temperature-Programmed RxMD Simulation

A temperature-programmed RxMD simulation process is used to generate GO in order to to overcome reaction energy barriers in our research.[96, 97] A detailed description of the simulation protocol is provided in Figure 2. For each RxMD simulation, we start with the isothermal–isobaric ensemble for 100 ps at low temperature and 5 ns for annealing process at 1 atm and T_{tri}, where the number of atoms (N), the pressure (P) and the temperature (T) are fixed. This is to relax the initial structure to an appropriate volume and reduce stresses from the basal plane. After this annealing process, another 5 ns of RxMD simulation at room temperature (300K) with canonical (NVT) ensemble is carried out for post-analyses. For the annealing parts, 5 ns is enough to allow the energy of the system and the productions of side products reach equilibrium. All generated GO structures are further relaxed at room temperature (300 K) for 5ns with the same criteria to reach stable structures. A timestep of 0.25 fs is used throughout the calculations. The Berendsen method with the damping constant 100 fs is applied to maintain the temperature of the system. Initial velocity is generated by the Boltzmann distribution.

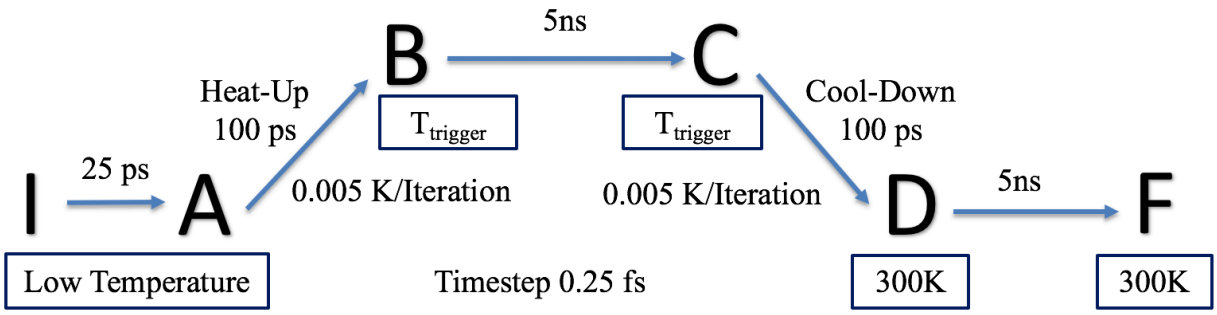

Figure 2. The temperature-programmed RxMD simulation process. I and F represent initial and final stage of the GO model; A, B, C, D are the intermediate GO structures. A timestep of 0.25 fs is used in the RxMD simulations.

2.5.2 Computational Characterizations

In experiments, Fourier-transform infrared spectroscopy (FTIR), X-ray photoelectron spectroscopy (XPS) and X-ray powder diffraction (XRD) are commonly used for carbon-based material characterization. The calculation of these methods can be carried out via MD simulations, numerical calculations and commercial software.

2.5.2.1 Fourier-transform infrared spectroscopy (FTIR)

FTIR provides a fast and easy way to gain the bonding information *via* characteristic vibration spectra. For the computational FTIR analysis, one has to be careful with noise peaks. This is due to a rich number of functional groups in materials. In the trajectory of RxMD simulation, functional groups are flexible and can interact with each other or with the basal plane, producing ambiguous peaks and overlaps in the FTIR fingerprint region.

The principles of FTIR are based on the facts that electromagnetic radiation of the wavenumber range from 400-4000 cm^{-1} can be absorbed by materials. Characteristic peaks are distinguishable due to different functional groups and their unique vibrational spectra. In this work, the FTIR spectrum calculation is summarized as the following: firstly, the dipole moment of the system is collected from the RxMD trajectory.

$$\bar{\mu} = \sum_i q_i(\bar{r}_i - \bar{r}_0) \tag{2-9}$$

Secondly, the autocorrelation function of dipole moment is calculated *via* the equation below[104-108],

$$R_x(\tau) = E[x(t)x(t+\tau)] = \lim_{T\to\infty} \frac{1}{T}\int_0^T x(t)x(t+\tau)dt \tag{2-10}$$

Finally, fast Fourier transform is applied to process the calculated autocorrelation function and generate the IR spectra. We adopted the python script template provided by Efrem Braun[109], and modified it to our cases. Benchmark calculations and FTIR analyses have been performed to systems of liquids (bulk water and bulk ethanol) and solids (metal-organic framework, MOF-5). Those benchmark FTIR calculations agree well with corresponding FTIR experiments.

We carried out several benchmark calculations about water systems to validate the accuracy and predictivity of their methods as well. Figure 3 showed the comparison of calculated FTIR between different force fields and systems. A single water molecule system calculated with Lennard-Jones (LJ) potential and ReaxFF are compared in Figure 3 (a) and (b). Both force fields can qualitatively reproduce main characteristic peaks compared with colored region of experimental value. Figure 3 (c) and (d) showed the bulk water system calculated with LJ potential and ReaxFF. Although the peak of O-H stretch is not large compared with results based on LJ

potential, ReaxFF is able to generate correct characteristic peaks for water. The peak intensity is commonly used to quantitively calculate the concentration of the target functional groups on materials. In the simulation, the peak intensity can be adjusted via parameters in the python code if possible.

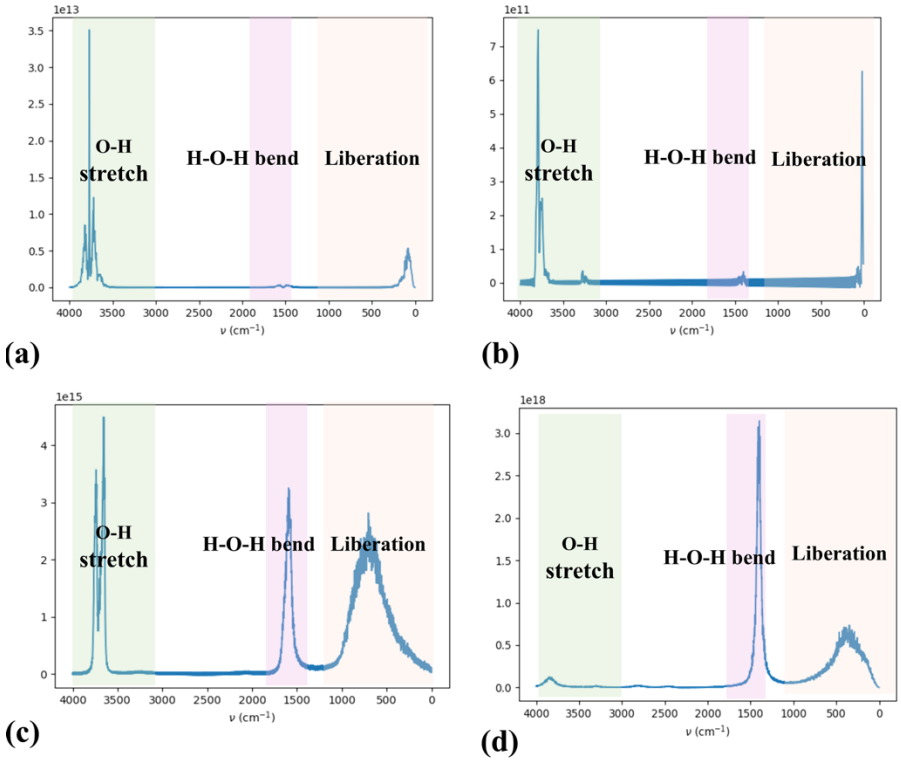

Figure 3. Calculated FITR of a single water molecule via (a) LJ potential; (b) ReaxFF; Calculated FITR of bulk water system via (c) LJ potential and (d) ReaxFF. Experimental data is provided in colored regions in each plot. Green, pink and orange regions represent peaks generated by O-H stretch peak, H-O-H bend and liberation, respectively.

2.5.2.2 X-ray photoelectron spectroscopy (XPS)

XPS provides quantitative information of element percentage analysis. In this work, we used the experimental XPS data from Ganguly [110], Mariana and co-workers [111], and compared

with the calculated hybridization and distribution of carbon atoms of GO. Figure 4 provides GO structures analysis outline for hybridization of carbon atoms and their distribution analysis. The bond connections can be obtained from the bond order output via LAMMPS. Fortran codes were carried out for the corresponding post-analysis of hybridization.

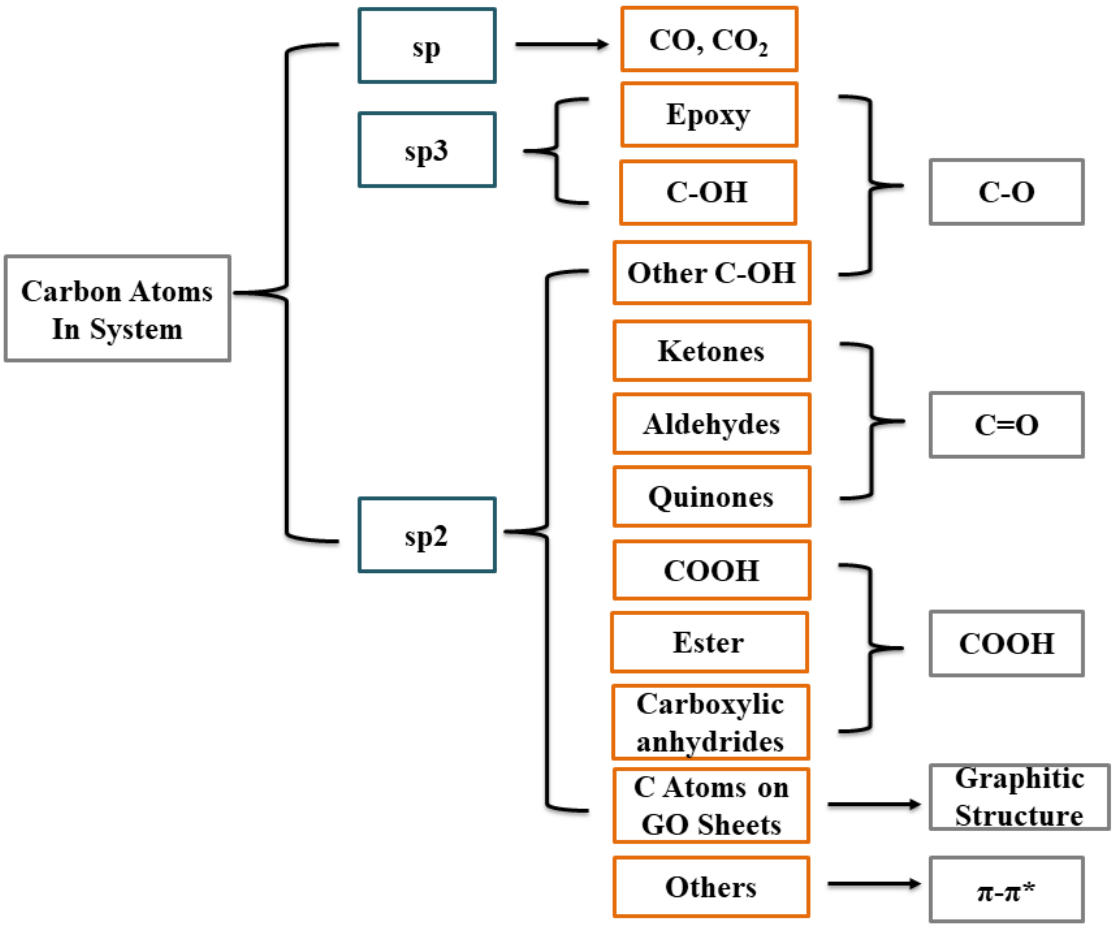

Figure 4. GO structures analysis outline for hybridization of carbon atoms and their distribution analysis.

2.5.2.3 X-ray powder diffraction (XRD)

X-ray diffraction (XRD) patterns are capable of determining the orientation of a single crystal or grain since they are sensitive to spacings between layers or rows of atoms. For the past decades, XRD has been utilized to identify crystal structures, measure the size, shape and internal stress of small crystalline regions. It is also a primary tool for determination of nano-crystallite orientation in polymers. In this thesis XRD plots were calculated to monitor the structural evolution of crystalline cellulose: the peak positions are determined by the lattice parameters, while the peak intensities are from the motif. XRD calculations were carried out by the Mercury and Diamond software, more information is available from the software manual [112, 113].

2.6 Reference

1. Friedrich, H., *Theoretical Atomic Physics*. 2006: Springer, Berlin, Heidelberg.
2. Neese, F., et al., *Chemistry and Quantum Mechanics in 2019: Give Us Insight and Numbers.* Journal of the American Chemical Society, 2019. **141**(7): p. 2814-2824.
3. Friesner, R.A., *Ab initio quantum chemistry: Methodology and applications.* Proceedings of the National Academy of Sciences of the United States of America, 2005. **102**(19): p. 6648.
4. Christensen, A.S., et al., *Semiempirical Quantum Mechanical Methods for Noncovalent Interactions for Chemical and Biochemical Applications.* Chemical Reviews, 2016. **116**(9): p. 5301-5337.
5. Johansson, M.P., V.R.I. Kaila, and D. Sundholm, *Ab Initio, Density Functional Theory, and Semi-Empirical Calculations*, in *Biomolecular Simulations: Methods and Protocols*, L. Monticelli and E. Salonen, Editors. 2013, Humana Press: Totowa, NJ. p. 3-27.
6. Capelle, K., *A bird's-eye view of density-functional theory.* Brazilian Journal of Physics, 2006. **36**: p. 1318-1343.
7. Jones, R.O., *Density functional theory: Its origins, rise to prominence, and future.* Reviews of Modern Physics, 2015. **87**(3): p. 897-923.
8. Becke, A.D., *Perspective: Fifty years of density-functional theory in chemical physics.* The Journal of Chemical Physics, 2014. **140**(18): p. 18A301.
9. van Gunsteren, W.F. and H.J.C. Berendsen, *Computer Simulation of Molecular Dynamics: Methodology, Applications, and Perspectives in Chemistry.* Angewandte Chemie International Edition in English, 1990. **29**(9): p. 992-1023.

10. Vangunsteren, W.F., et al., *MOLECULAR MECHANICS IN BIOLOGY - FROM STRUCTURE TO FUNCTION, TAKING ACCOUNT OF SOLVATION.* Annual Review of Biophysics and Biomolecular Structure, 1994. **23**: p. 847-863.
11. Frenkel, D. and B. Smit, *Chapter 4 - Molecular Dynamics Simulations*, in *Understanding Molecular Simulation (Second Edition)*, D. Frenkel and B. Smit, Editors. 2002, Academic Press: San Diego. p. 63-107.
12. Rapaport, D.C., *The Art of Molecular Dynamics Simulation*. 2 ed. 2004, Cambridge: Cambridge University Press.
13. Alavi, S., *Statistical Mechanics: Theory and Molecular Simulation. By Mark E. Tuckerman.* Angewandte Chemie International Edition, 2011. **50**(51): p. 12138-12139.
14. Allen, M.P., *Introduction to Molecular Dynamics Simulation*, in *Computational Soft Matter: From Synthetic Polymers to Proteins, Lecture Notes*, K.B. Norbert Attig, Helmut Grubmu¨ller, Kurt Kremer, Editor. 2004, John von Neumann Institute for Computing: Ju¨lich.
15. Durrant, J.D. and J.A. McCammon, *Molecular dynamics simulations and drug discovery.* BMC Biology, 2011. **9**(1): p. 71.
16. De Vivo, M., et al., *Role of Molecular Dynamics and Related Methods in Drug Discovery.* Journal of Medicinal Chemistry, 2016. **59**(9): p. 4035-4061.
17. Hospital, A., et al., *Molecular dynamics simulations: advances and applications.* Advances and applications in bioinformatics and chemistry : AABC, 2015. **8**: p. 37-47.
18. Pérez, A., F.J. Luque, and M. Orozco, *Frontiers in Molecular Dynamics Simulations of DNA.* Accounts of Chemical Research, 2012. **45**(2): p. 196-205.
19. Dubbeldam, D., A. Torres-Knoop, and K.S. Walton, *On the inner workings of Monte Carlo codes.* Molecular Simulation, 2013. **39**(14-15): p. 1253-1292.
20. Pillardy, J., et al., *Conformation-family Monte Carlo: A new method for crystal structure prediction.* Proceedings of the National Academy of Sciences, 2001. **98**(22): p. 12351.
21. Wang, J.M., et al., *Conformational analysis of peptides using Monte Carlo simulations combined with the genetic algorithm.* Chemometrics and Intelligent Laboratory Systems, 1999. **45**(1-2): p. 347-351.
22. Kierlik, E. and M.L. Rosinberg, *Free-energy density functional for the inhomogeneous hard-sphere fluid: Application to interfacial adsorption.* Physical Review A, 1990. **42**(6): p. 3382-3387.
23. Düren, T., Y.-S. Bae, and R.Q. Snurr, *Using molecular simulation to characterise metal–organic frameworks for adsorption applications.* Chemical Society Reviews, 2009. **38**(5): p. 1237-1247.
24. Jiang, J. and S.I. Sandler, *Monte Carlo Simulation for the Adsorption and Separation of Linear and Branched Alkanes in IRMOF-1.* Langmuir, 2006. **22**(13): p. 5702-5707.
25. Biagi, S.F., *Monte Carlo simulation of electron drift and diffusion in counting gases under the influence of electric and magnetic fields.* Nuclear Instruments and Methods in Physics Research Section A: Accelerators, Spectrometers, Detectors and Associated Equipment, 1999. **421**(1): p. 234-240.
26. Jones, D.K., *The effect of gradient sampling schemes on measures derived from diffusion tensor MRI: A Monte Carlo study†.* Magnetic Resonance in Medicine, 2004. **51**(4): p. 807-815.
27. Umrigar, C.J., M.P. Nightingale, and K.J. Runge, *A diffusion Monte Carlo algorithm with very small time-step errors.* The Journal of Chemical Physics, 1993. **99**(4): p. 2865-2890.

28. Chatterjee, A. and D.G. Vlachos, *An overview of spatial microscopic and accelerated kinetic Monte Carlo methods.* Journal of Computer-Aided Materials Design, 2007. **14**(2): p. 253-308.
29. Voter, A.F. *INTRODUCTION TO THE KINETIC MONTE CARLO METHOD*. in *Radiation Effects in Solids*. 2007. Dordrecht: Springer Netherlands.
30. Henkelman, G. and H. Jónsson, *Long time scale kinetic Monte Carlo simulations without lattice approximation and predefined event table.* The Journal of Chemical Physics, 2001. **115**(21): p. 9657-9666.
31. Hermans, J., et al., *A consistent empirical potential for water–protein interactions.* Biopolymers, 1984. **23**(8): p. 1513-1518.
32. Ott, K.-H. and B. Meyer, *Parametrization of GROMOS force field for oligosaccharides and assessment of efficiency of molecular dynamics simulations.* Journal of Computational Chemistry, 1996. **17**(8): p. 1068-1084.
33. *GROMOS Force Field*, in *Encyclopedia of Computational Chemistry*.
34. MacKerell, A.D., et al., *All-Atom Empirical Potential for Molecular Modeling and Dynamics Studies of Proteins.* The Journal of Physical Chemistry B, 1998. **102**(18): p. 3586-3616.
35. Momany, F.A. and R. Rone, *Validation of the general purpose QUANTA ®3.2/CHARMm® force field.* Journal of Computational Chemistry, 1992. **13**(7): p. 888-900.
36. Pavelites, J.J., et al., *A molecular mechanics force field for NAD+ NADH, and the pyrophosphate groups of nucleotides.* Journal of Computational Chemistry, 1997. **18**(2): p. 221-239.
37. Sun, H., P. Ren, and J.R. Fried, *The COMPASS force field: parameterization and validation for phosphazenes.* Computational and Theoretical Polymer Science, 1998. **8**(1): p. 229-246.
38. Cornell, W.D., et al., *A Second Generation Force Field for the Simulation of Proteins, Nucleic Acids, and Organic Molecules.* Journal of the American Chemical Society, 1995. **117**(19): p. 5179-5197.
39. Weiner, P.K. and P.A. Kollman, *AMBER: Assisted model building with energy refinement. A general program for modeling molecules and their interactions.* Journal of Computational Chemistry, 1981. **2**(3): p. 287-303.
40. Weiner, S.J., et al., *A new force field for molecular mechanical simulation of nucleic acids and proteins.* Journal of the American Chemical Society, 1984. **106**(3): p. 765-784.
41. Weiner, S.J., et al., *An all atom force field for simulations of proteins and nucleic acids.* Journal of Computational Chemistry, 1986. **7**(2): p. 230-252.
42. Kirschner, K.N., et al., *GLYCAM06: A generalizable Biomolecular force field. Carbohydrates.* Journal of Computational Chemistry, 2008. **29**(4): p. 622-655.
43. Jorgensen, W.L., J.D. Madura, and C.J. Swenson, *Optimized intermolecular potential functions for liquid hydrocarbons.* Journal of the American Chemical Society, 1984. **106**(22): p. 6638-6646.
44. Jorgensen, W.L. and C.J. Swenson, *Optimized intermolecular potential functions for amides and peptides. Structure and properties of liquid amides.* Journal of the American Chemical Society, 1985. **107**(3): p. 569-578.
45. Jorgensen, W.L., *Intermolecular potential functions and Monte Carlo simulations for liquid sulfur compounds.* The Journal of Physical Chemistry, 1986. **90**(23): p. 6379-6388.

46. Jorgensen, W.L., *Optimized intermolecular potential functions for liquid alcohols.* The Journal of Physical Chemistry, 1986. **90**(7): p. 1276-1284.
47. Rappe, A.K., et al., *UFF, a full periodic table force field for molecular mechanics and molecular dynamics simulations.* Journal of the American Chemical Society, 1992. **114**(25): p. 10024-10035.
48. Dauber-Osguthorpe, P., et al., *Structure and energetics of ligand binding to proteins: Escherichia coli dihydrofolate reductase-trimethoprim, a drug-receptor system.* Proteins: Structure, Function, and Bioinformatics, 1988. **4**(1): p. 31-47.
49. Mayo, S.L., B.D. Olafson, and W.A. Goddard, *DREIDING: a generic force field for molecular simulations.* The Journal of Physical Chemistry, 1990. **94**(26): p. 8897-8909.
50. Allinger, N.L., *Conformational analysis. 130. MM2. A hydrocarbon force field utilizing V1 and V2 torsional terms.* Journal of the American Chemical Society, 1977. **99**(25): p. 8127-8134.
51. Lii, J.-H. and N.L. Allinger, *The MM3 force field for amides, polypeptides and proteins.* Journal of Computational Chemistry, 1991. **12**(2): p. 186-199.
52. Allinger, N.L., K. Chen, and J.-H. Lii, *An improved force field (MM4) for saturated hydrocarbons.* Journal of Computational Chemistry, 1996. **17**(5-6): p. 642-668.
53. Warshel, A. and M. Levitt, *Theoretical studies of enzymic reactions: Dielectric, electrostatic and steric stabilization of the carbonium ion in the reaction of lysozyme.* Journal of Molecular Biology, 1976. **103**(2): p. 227-249.
54. Hutter, D.M.a.J., *Ab initio molecular dynamics: Theory and Implementation*, in *Modern Methods and Algorithms of Quantum Chemistry*, J. Grotendorst, Editor. 2000, John von Neumann Institute for Computing, Julich, NIC Series. p. pp. 301-449.
55. Geissler, P.L., et al., *Autoionization in liquid water.* Science, 2001. **291**(5511): p. 2121-2124.
56. Pfrommer, B.G., F. Mauri, and S.G. Louie, *NMR Chemical Shifts of Ice and Liquid Water: The Effects of Condensation.* Journal of the American Chemical Society, 2000. **122**(1): p. 123-129.
57. Morrone, J.A. and M.E. Tuckerman, *Ab initio molecular dynamics study of proton mobility in liquid methanol.* The Journal of Chemical Physics, 2002. **117**(9): p. 4403-4413.
58. Diraison, M., G.J. Martyna, and M.E. Tuckerman, *Simulation studies of liquid ammonia by classical ab initio, classical, and path-integral molecular dynamics.* The Journal of Chemical Physics, 1999. **111**(3): p. 1096-1103.
59. Meijer, E.J. and M. Sprik, *Ab Initio Molecular Dynamics Study of the Reaction of Water with Formaldehyde in Sulfuric Acid Solution.* Journal of the American Chemical Society, 1998. **120**(25): p. 6345-6355.
60. Kim, D. and M.L. Klein, *Ab Initio Molecular Dynamics Study of the Superacid System SbF5/HF Solution.* The Journal of Physical Chemistry B, 2000. **104**(43): p. 10074-10079.
61. Zhu, Z. and M.E. Tuckerman, *Ab Initio Molecular Dynamics Investigation of the Concentration Dependence of Charged Defect Transport in Basic Solutions via Calculation of the Infrared Spectrum.* The Journal of Physical Chemistry B, 2002. **106**(33): p. 8009-8018.
62. Chen, B., et al., *First-Principles Study of Aqueous Hydroxide Solutions.* Journal of the American Chemical Society, 2002. **124**(29): p. 8534-8535.
63. Tuckerman, M.E., et al., *On the Quantum Nature of the Shared Proton in Hydrogen Bonds.* Science, 1997. **275**(5301): p. 817.

64. Benoit, M., D. Marx, and M. Parrinello, *Tunnelling and zero-point motion in high-pressure ice.* Nature, 1998. **392**(6673): p. 258-261.
65. Marx, D., et al., *The nature of the hydrated excess proton in water.* Nature, 1999. **397**(6720): p. 601-604.
66. Tuckerman, M.E., D. Marx, and M. Parrinello, *The nature and transport mechanism of hydrated hydroxide ions in aqueous solution.* Nature, 2002. **417**(6892): p. 925-929.
67. Saitta, A.M., et al., *Influence of a knot on the strength of a polymer strand.* Nature, 1999. **399**(6731): p. 46-48.
68. Piana, S., et al., *Ab Initio Molecular Dynamics-Based Assignment of the Protonation State of Pepstatin A/HIV-1 Protease Cleavage Site.* Journal of the American Chemical Society, 2001. **123**(36): p. 8730-8737.
69. Rothlisberger, U. and P. Carloni, *Ab initio molecular dynamics studies of a synthetic biomimetic model of galactose oxidase.* International Journal of Quantum Chemistry, 1999. **73**(2): p. 209-218.
70. Andreoni, W., A. Curioni, and T. Mordasini, *DFT-based molecular dynamics as a new tool for computational biology: First applications and perspective.* IBM Journal of Research and Development, 2001. **45**(3.4): p. 397-407.
71. Hass, K.C., et al., *The Chemistry of Water on Alumina Surfaces: Reaction Dynamics from First Principles.* Science, 1998. **282**(5387): p. 265.
72. Kroes, G.-J., et al., *Quantum Theory of Dissociative Chemisorption on Metal Surfaces.* Accounts of Chemical Research, 2002. **35**(3): p. 193-200.
73. Car, R. and M. Parrinello, *UNIFIED APPROACH FOR MOLECULAR-DYNAMICS AND DENSITY-FUNCTIONAL THEORY.* Physical Review Letters, 1985. **55**(22): p. 2471-2474.
74. Remler, D.K. and P.A. Madden, *MOLECULAR-DYNAMICS WITHOUT EFFECTIVE POTENTIALS VIA THE CAR-PARRINELLO APPROACH.* Molecular Physics, 1990. **70**(6): p. 921-966.
75. Payne, M.C., et al., *ITERATIVE MINIMIZATION TECHNIQUES FOR ABINITIO TOTAL-ENERGY CALCULATIONS - MOLECULAR-DYNAMICS AND CONJUGATE GRADIENTS.* Reviews of Modern Physics, 1992. **64**(4): p. 1045-1097.
76. Galli, G. and A. Pasquarello, *First-principles Molecular Dynamics*, in *Computer Simulation in Chemical Physics*, M.P. Allen and D.J. Tildesley, Editors. 1993, Springer Netherlands: Dordrecht. p. 261-313.
77. Tuckerman, M.E., et al., *Ab initio molecular dynamics simulations.* Journal of Physical Chemistry, 1996. **100**(31): p. 12878-12887.
78. Tuckerman, M.E., *Ab initio molecular dynamics: basic concepts, current trends and novel applications.* Journal of Physics-Condensed Matter, 2002. **14**(50): p. R1297-R1355.
79. Gillan, M.J., *The virtual matter laboratory.* Contemporary Physics, 1997. **38**(2): p. 115-130.
80. Parrinello, M., *From silicon to RNA: The coming of age of ab initio molecular dynamics.* Solid State Communications, 1997. **102**(2-3): p. 107-120.
81. van Duin, A.C.T., et al., *ReaxFF: A reactive force field for hydrocarbons.* Journal of Physical Chemistry A, 2001. **105**(41): p. 9396-9409.
82. Tersoff, J., *Chemical order in amorphous silicon carbide.* Physical Review B, 1994. **49**(23): p. 16349-16352.

83. Mortier, W.J., K. Vangenechten, and J. Gasteiger, *ELECTRONEGATIVITY EQUALIZATION - APPLICATION AND PARAMETRIZATION.* Journal of the American Chemical Society, 1985. **107**(4): p. 829-835.
84. Zhang, L.M., et al., *Janus graphene from asymmetric two-dimensional chemistry.* Nature Communications, 2013. **4**.
85. Cheung, S., et al., *ReaxFF(MgH) reactive force field for magnesium hydride systems.* Journal of Physical Chemistry A, 2005. **109**(5): p. 851-859.
86. Chenoweth, K., A.C.T. van Duin, and W.A. Goddard, III, *ReaxFF reactive force field for molecular dynamics simulations of hydrocarbon oxidation.* Journal of Physical Chemistry A, 2008. **112**(5): p. 1040-1053.
87. Monti, S., et al., *Exploring the conformational and reactive dynamics of biomolecules in solution using an extended version of the glycine reactive force field.* Physical Chemistry Chemical Physics, 2013. **15**(36): p. 15062-15077.
88. Zhang, W.W. and A.C.T. van Duin, *Improvement of the ReaxFF Description for Functionalized Hydrocarbon/Water Weak Interactions in the Condensed Phase.* Journal of Physical Chemistry B, 2018. **122**(14): p. 4083-4092.
89. Zhang, W.W. and A.C.T. van Duin, *ReaxFF Reactive Molecular Dynamics Simulation of Functionalized Poly(phenylene oxide) Anion Exchange Membrane.* Journal of Physical Chemistry C, 2015. **119**(49): p. 27727-27736.
90. Castro-Marcano, F., et al., *Combustion of an Illinois No. 6 coal char simulated using an atomistic char representation and the ReaxFF reactive force field.* Combustion and Flame, 2012. **159**(3): p. 1272-1285.
91. Zhang, J.L., et al., *The effect of supercritical water on coal pyrolysis and hydrogen production: A combined ReaxFF and DFT study.* Fuel, 2013. **108**: p. 682-690.
92. Senftle, T.P., et al., *The ReaxFF reactive force-field: development, applications and future directions.* 2016. **2**: p. 15011.
93. Liang, T., et al., *Reactive Potentials for Advanced Atomistic Simulations.* Annual Review of Materials Research, Vol 43, 2013. **43**: p. 109-129.
94. Li, P. and K.M. Merz, *Metal Ion Modeling Using Classical Mechanics.* Chemical Reviews, 2017. **117**(3): p. 1564-1686.
95. Qiao, Q., X. Li, and L. Huang, *Crystalline Cellulose under Pyrolysis Conditions: The Structure–Property Evolution via Reactive Molecular Dynamics Simulations.* Journal of Chemical & Engineering Data, 2019.
96. Qiao, Q., et al., *Graphene oxide model with desirable structural and chemical properties.* Carbon, 2019. **143**: p. 566-577.
97. Huang, L.L., et al., *Controllable atomistic graphene oxide model and its application in hydrogen sulfide removal.* Journal of Chemical Physics, 2013. **139**(19).
98. Bagri, A., et al., *Structural evolution during the reduction of chemically derived graphene oxide.* Nature Chemistry, 2010. **2**(7): p. 581-587.
99. Russo, M.F. and A.C.T. van Duin, *Atomistic-scale simulations of chemical reactions: Bridging from quantum chemistry to engineering.* Nuclear Instruments & Methods in Physics Research Section B-Beam Interactions with Materials and Atoms, 2011. **269**(14): p. 1549-1554.
100. Mortier, W.J., S.K. Ghosh, and S. Shankar, *Electronegativity equalization method for the calculation of atomic charges in molecules.* Journal of the American Chemical Society, 1986. **108**(15): p. 4315-4320.

101. Janssens, G.O.A., et al., *COMPARISON OF CLUSTER AND INFINITE CRYSTAL CALCULATIONS ON ZEOLITES WITH THE ELECTRONEGATIVITY EQUALIZATION METHOD (EEM).* Journal of Physical Chemistry, 1995. **99**(10): p. 3251-3258.
102. Agrawalla, S. and A.C.T. van Duin, *Development and Application of a ReaxFF Reactive Force Field for Hydrogen Combustion.* Journal of Physical Chemistry A, 2011. **115**(6): p. 960-972.
103. Chenoweth, K., et al., *Development and application of a ReaxFF reactive force field for oxidative dehydrogenation on vanadium oxide catalysts.* Journal of Physical Chemistry C, 2008. **112**(37): p. 14645-14654.
104. Berens, P.H. and K.R. Wilson, *MOLECULAR-DYNAMICS AND SPECTRA .1. DIATOMIC ROTATION AND VIBRATION.* Journal of Chemical Physics, 1981. **74**(9): p. 4872-4882.
105. Guillot, B., *A MOLECULAR-DYNAMICS STUDY OF THE FAR INFRARED-SPECTRUM OF LIQUID WATER.* Journal of Chemical Physics, 1991. **95**(3): p. 1543-1551.
106. Bornhauser, P. and D. Bougeard, *Intensities of the vibrational spectra of siliceous zeolites by molecular dynamics calculations. I. Infrared spectra.* Journal of Physical Chemistry B, 2001. **105**(1): p. 36-41.
107. Gaigeot, M.P. and M. Sprik, *Ab initio molecular dynamics computation of the infrared spectrum of aqueous uracil.* Journal of Physical Chemistry B, 2003. **107**(38): p. 10344-10358.
108. Thomas, M., et al., *Computing vibrational spectra from ab initio molecular dynamics.* Physical Chemistry Chemical Physics, 2013. **15**(18): p. 6608-6622.
109. Braun, E. *Open Source Code: Calculating an IR Spectra from a LAMMPS Simulation*. 2016 [cited 2018 Oct. 25, 2018]; Available from: https://zenodo.org/record/154672#.W9HlQ6fMwlK.
110. Ganguly, A., et al., *Probing the Thermal Deoxygenation of Graphene Oxide Using High-Resolution In Situ X-ray-Based Spectroscopies.* The Journal of Physical Chemistry C, 2011. **115**(34): p. 17009-17019.
111. Araujo, M.P., et al., *Tuning the surface chemistry of graphene flakes: new strategies for selective oxidation.* Rsc Advances, 2017. **7**(23): p. 14290-14301.
112. Mercury. *Mercury User Guide and Tutorials*. 2019 [cited 2019 Aug/25/2019]; Available from: https://www.ccdc.cam.ac.uk/support-and-resources/CCDCResources/Mercury_UserGuide.pdf.
113. Diamond. *Diamond, Crystal and Molecular Structure Visualization*. 2019 [cited 2019 Aug/25/2019]; Available from: https://www.crystalimpact.com/download/diamond/tutorial.pdf.

Chapter 3: Graphene Oxide Model with Desirable Structural and Chemical Properties*

3.1 Introduction

Graphene oxide (GO) has been one of the most widely studied and utilized two-dimensional (2D) nanomaterials during the last decade[1-4]. As a promising precursor for graphene mass production, GO has unusual electronic properties and other features such as wet-chemical processability, large-scale availability as monolayers, and much lower cost as compared to that of chemical vapor deposition (CVD) or mechanical exfoliation products[5]. In addition, GO and its derivatives have shown promising applications in catalysis[6, 7], composites[8], energy storage[9, 10], sensing[11, 12], separation[13-15], electronics[16, 17], biological and drug delivery,[18-21] *etc*.. GO has been established as an important and technologically relevant material in the past decade, and there now exist a large number of literatures about GO synthesis, some of which dated back to 150 years ago. However, GO structure with molecular level details remains inaccessible. On the other hand, despite the lack of structural details, many renovated GO applications[22-29] are indeed based on the tunability of GO properties, through the structural and surface chemistry control of defects and oxygen-containing functional groups. The functionalized GO materials demonstrate unique anisotropic electrical, magnetic, and optical properties, which could lead the research and application of 2D nanomaterial to the next level, and in turn require a better fundamental understanding of atomic GO structures.

Historically, the first widely accepted GO model from experiments was proposed by Hofmann and Holst, with repeating units of 1,2-epoxides[30]. Later, Ruess deduced a new model

*Qiao, Q., Liu, C, Huang, L., *Graphene oxide model with desirable structural and chemical properties.* Carbon, 2019. **143**: p. 566-577.

based on sp^3 hybridized graphene basal planes[31]. Scholz and Boehm proposed a GO model in 1969 that only contains hydroxyl and ketone groups[32]. Dekany and co-workers proposed another model, which has trans-linked cyclohexane chairs and corrugated hexagon ribbons[33]. One of the most widely used GO models in literature is from Lerf and Klinowski, where hydroxyl and epoxy groups exist mainly on the basal plane and carboxyl groups are located at edges[34-36]. With the advance of modern characterization techniques, more quantitative features have been revealed. For example, through X-ray photoelectron spectroscopy (XPS) and solid-state magnetic resonance (ssNMR) analyses, Gao and co-workers proposed a GO model that has large vacancy defects, and other quantitative features, such as the overall carbon/oxygen (C/O) ratio (2.44); the relative ratio of major functional groups, namely, 115 (hydroxyl and epoxide): 3(lactol O–C–O): 63 (graphitic sp^2 carbon): 10 (lactol + ester + acid carbonyl): 9 (ketone carbonyl)[37]. The reported lactol groups was also interpreted as hydrates of ketones groups (geminal diols)[38]. It is worth noting that GO material is sensitive to the synthesis protocols, such as temperature and oxidants used. Experimentally synthesized GO materials are generally amorphous and will degrade even under ambient conditions. A static GO structure with definitive functional groups probably does not exist, one has to treat GO as a 'dynamic structure' which constantly evolves with its environment[39]. In addition, the experimental results also indicate that a good GO model shall capture both structural (i.e. vacancy defects, curvature) and chemical information (i.e. C/O ratio, major functional groups, *etc*.).

As for GO models proposed by theoretical efforts, early studies were from *ab initio* quantum mechanics methods[40-43]. Despite the accuracy, quantum mechanics calculations typically deal with small systems, on the order of tens of atoms. Such system size limitation prevents a simultaneous description of defects, functional groups and their correlations. *Ab initio*

density functional theory (DFT) method has been also widely applied to study GO materials and their properties[44-47]. But it is still challenging to use *ab initio* DFT method to develop a dynamic GO structure at finite temperatures. The expensive computational cost also prevents studies involving multiple phases and multiple reacting species during GO synthesis. This explains why for most *ab initio* DFT studies, usually one feature of GO is studied. Using the knowledge from DFT calculations, more attempts have been made to develop GO models *via* molecular dynamics (MD) simulations[48-57]. Among those efforts, the reactive force field (ReaxFF) based molecular dynamics (RxMD) method is promising for GO model development.

Previously, we proposed a protocol to perform temperature-programmed RxMD simulations[58] and controllably generate GO structures with different functional groups and defects. The produced GO models capture critical chemical characteristics of GO, agreeing with the results from *ab initio* quantum calculations and having been further validated with reactive adsorption experiments for H_2S removal. Also using a ReaxFF force field, Bagri *et al.* studied the residual oxygen distribution and structural evolution of reduced GO (rGO) *via* a thermal annealing process[59]. The rGO structures received from their calculations agree with Fourier-transform infrared spectroscopy (FTIR) and XPS characterizations,[60-62] which further demonstrates that ReaxFF based RxMD simulations can accurately describe GO structures at finite temperature and pressure conditions. Medhekar and co-workers applied RxMD to investigate humidity effect on GO materials[49]. According to their study, ReaxFF is able to describe both GO models and hydrogen bond network formed between GO and water molecules at the GO interlays. Srinivasan *et al.* adopted RxMD simulations to study hyperthermal collisions of atomic oxygens with graphene,[63] and generated GO models with defects and epoxide functional groups. ReaxFF-based RxMD simulations were also carried out to investigate mechanical properties of polyvinyl

alcohol-graphene oxide nanocomposite by Compton and co-workers[64]. In their study, the GO models have the same stoichiometry of $C_6O_3H_1$ but differ in the distribution of hydroxyl and epoxy groups. The behavior of water in GO and GO nanocomposites was elucidated and agreed well with experimental results.

Most theoretical models developed so far have archived a good description of chemical properties of GO. But for the structural properties, such as the size and distribution of vacancy defects, the curvature (or roughness) dependence on temperature and pressure conditions, no systematic understanding has been achieved. Considering the great potential of GO-based materials in drug delivery[65-67], separation and storage applications[68-73], there is a strong need of theoretical efforts in GO model development, capable of predicting both structural and chemical properties of GO, and correlating structure-property-application relationships. In this work, using experimental GO characteristics mainly from modified Hummers method[4, 37, 38, 74-76], we reevaluate critical controlling parameters to GO model development. Specific attentions have been paid to the vacancy defects, the distribution and hybridization of carbon atoms, and the overall C/O ratio of GO. Morphology of defects in GO models are compared with lattice defects in both graphene[77, 78] and graphene oxide[4, 79]. Chemical properties are discussed with related experimental results and characterization methods (FTIR, XPS). The GO models proposed in this work inherit both structural and chemistry information of previous GO models but have significantly improved to represent quantitative structural details of experimentally synthesized GO materials. It is worth noting that the structural and chemistry properties of GO are intrinsically coupled at the atomic level. A change of the C/O ratio will potentially affect the number and the size of vacancy defects. In return, the defects will stabilize a different combination of functional groups, as well as the overall C/O ratio. We hope the revisit to GO model

development, especially the simultaneously description to both structural and chemical properties, will provide a new fundamental understanding of GO model and add advancement to existing GO knowledge. The article is organized as follows: Section 2 presents a brief introduction to the ReaxFF reactive force, a discussion of the simulation method and calculation setup, and a list of experimental characterizations. In the Results and Discussion of Section 3, we summarize in order the three tunable parameters for GO model, the chemistry and structural characteristics, and the comparison between theoretical calculations and experiments. Conclusions are presented in Section 4.

3.2 Methods and Simulation Details

3.2.1 ReaxFF Reactive Force Field

ReaxFF reactive force field was developed in 2001 by van Duin and co-workers to study chemical reactions of hydrocarbon systems[80]. Over the development of the last fifteen years, ReaxFF potential has become a powerful computational tool to explore, develop and optimize material properties. It is widely used in disciplines of science and engineering for multi-scale fundamental studies involving chemisorption and reactions of complex systems[81-83]. Instead of explicitly defining molecular topology (such as bonds, angles and dihedrals) like traditional non-reactive force fields, ReaxFF uses the concept of bond order[84-88] to calculate and update atomic pair connections, structural details, potential chemisorption and reactions. This allows a continuous structural evolution and enables the bond breaking or formation along the interaction pathway[80]. During the RxMD simulation, atomic charge information is fitted *via* the electronegativity equalization method (EEM) of Mortier and co-workers[89, 90], which is also the most computationally expensive part of the RxMD simulations[91]. Compared with non-reactive

MD simulations, RxMD *via* ReaxFF reactive force field is generally one order slower. However, RxMD simulations are capable of describing systems composed of hundreds of thousands of atoms. With the advance of hardware and efficient parallel computations, RxMD simulation can archive a trajectory to the time sale of microseconds[82]. To date, under the framework of ReaxFF, force fields have been developed for more than 40 elements of the periodic table, capable of describing systems like hydrocarbon reactions, alkoxysilane gelation, transition-metal-catalyzed nanotube formation, and high-energy materials. More details of ReaxFF force field are available from the website of the developers[92] as well as recent review papers[93-95]. The ReaxFF force field used in this work has been developed and used extensively for GO systems[49, 55-59, 63, 64, 96-98].

3.2.2 RxMD Simulation Setup

Similar to our previous study[58], the temperature-programmed protocol has been adopted for RxMD simulations in this work. A pristine zigzag graphene of size 8.8 nm × 8.9 nm is randomly functionalized by a mixture of hydroxyl and epoxy groups. We generate a serial of GO structures by tuning three key parameters: the initial functionalization density, that is, the fraction of functionalized carbon atoms over the total number of carbon atoms of the pristine graphene; the ratio of hydroxyl/epoxy groups; the annealing trigger temperature (T_{tri}). We note that those RxMD simulations are not designed to mimic experimental synthesis conditions. Instead, we try to combine and tune the aforementioned three parameters, until the produced GO structures share the same characteristics as those from experiments. Here, the comparison is focused on the overall carbon/oxygen ratio, the carbon hybridization, and the vacancy defects. With regard to previous calculations[58], in this work, we use higher T_{tri}, 1500 K (cf. 1000 K), a larger initial functionalization density, 70 % (cf. 30%), and three different ratios of hydroxyl and epoxy, namely,

1:1, 1:10, 10:1 (cf. 1:1). Those changes are justified based on our iterative calculations, as illustrated in Figure 1. The resulted GO structures have C/O ratios closer to the experimental values. The higher T_{tri} and the variation of hydroxyl/epoxy ratios will significantly affect vacancy defects, pores and channels of GO models. More specific, a higher concentration of epoxy groups will result in a GO structure with more defects. This is because epoxy groups are more reactive than hydroxyl, therefore interacting much easily with basal carbon atoms to produce vacancies.

The calculations are carried out by the LAMMPS software package with the ReaxFF implemented as an external library[99]. For each RxMD simulation, we start with the isothermal–isobaric ensemble for 100 ps at low temperature and 5 ns for annealing process at 1 atm and T_{tri}, where the number of atoms (N), the pressure (P) and the temperature(T) are fixed. This is to relax the initial structure to an appropriate volume and reduce stresses from the basal plane. After this annealing process, another 5 ns of RxMD simulation at room temperature (300K) with canonical (NVT) ensemble is carried out for post-analyses. A timestep of 0.25 fs is used throughout the calculations. The Berendsen method with the damping constant 100 fs is applied to maintain the temperature of the system. Initial velocity is generated by the Boltzmann distribution. Similar to our previous work[58], a temperature-programmed protocol is applied to overcome reaction energy barriers. For the annealing parts, 5 ns is enough to allow the energy of the system and the productions of side products reach equilibrium. All generated GO structures are further relaxed at room temperature (300 K) for 5ns with the same criteria to reach stable structures. We then perform post-analyses and compare with experimental results if applicable. A detailed description of the simulation protocol and a set of calculation files are provided in the supplementary material, including the ReaxFF force field file, the data and control files for the RxMD simulation *via* LAMMPS.

3.2.3 Computational FTIR, XPS Characterizations

In experiments, nuclear magnetic resonance spectroscopy (NMR), FTIR, Raman spectroscopy and XPS are commonly used for GO characterization. FTIR provides a fast and easy way to gain the bonding information *via* characteristic vibration spectra. For the computational FTIR analysis, one has to be careful with noise peaks. This is due to a rich number of functional groups of GO. In the trajectory of RxMD simulation, functional groups are flexible and can interact with each other or with the basal plane, producing ambiguous peaks and overlaps in the FTIR fingerprint region.

The principles of FTIR are based on the facts that electromagnetic radiations of the wavenumber range from 400-4000 cm^{-1} can be absorbed by materials. Characteristic peaks are distinguishable due to different functional groups and their unique vibrational spectra. In this work, the FTIR spectrum calculation is summarized as the following: firstly, the dipole moment of the system is collected from the RxMD trajectory.

$$\bar{\mu} = \sum_i q_i(\bar{r}_i - \bar{r}_0)$$

This is performed when those generated GO structures have been fully relaxed at room temperature (300K). Also, gas-phase reaction products (CO, CO_2, H_2O, *etc*.) have been removed prior to the FTIR analysis. Secondly, the autocorrelation function of dipole moment is calculated *via* the equation below[100-104],

$$R_x(\tau) = E[x(t)x(t+\tau)] = \lim_{T\to\infty} \frac{1}{T}\int_0^T x(t)x(t+\tau)dt$$

Finally, fast Fourier transform is applied to process the calculated autocorrelation function and generate the IR spectra. We adopted the python script template provided by Efrem Braun[105], and modified it to our cases. Benchmark calculations and FTIR analyses have been performed to systems of liquids (bulk water and bulk ethanol) and solids (metal-organic framework, MOF-5). Those benchmark FTIR calculations agree well with corresponding FTIR experiments. XPS provides quantitative information of element percentage analysis. In this work, we used the experimental XPS data from Ganguly[75], Mariana and co-workers[106], and compared with the calculated hybridization and distribution of carbon atoms of GO.

It is worth noting that the GO size of theoretical models is much smaller than the actual GO samples from experiments. However, in the MD simulations, the GO model is described as a periodic model along the X and Y directions. Therefore, we can consider the initial GO structure is an infinitely large 2-D structure. Therefore, the comparisons between simulation and experiment on FTIR and XPS are mainly for the surface chemistry, which is an intensive property of GO materials, not depending on the amount or the size of the GO sample. We compare the calculated FTIR with the experimental results, because GO has a plenty of surface functional groups, such as OH, epoxy, COOH, C-O and C=O groups. All those functional groups can be identified as characteristic peaks of FTIR results. For that purpose, we use calculated FTIR to determine functional groups of those generated GO models. Regardless GO structure size, micron or sub-nanometer, the characteristic FTIR peaks shall have same peak positions. Similarly, we performed XPS analysis to identify the elements and their oxidation states, and the calculation results are not dependent of the GO structure size.

3.3 Results and Discussions

3.3.1 Three Tunable Parameters to GO Model

For the initial GO structure, once the density of functional group and the hydroxyl/epoxy ratio have been pre-determined, we applied a Monte Carlo algorithm to randomly attach hydroxyl and epoxy groups on both sides of the zigzag graphene sheet. Those functional groups are added with a 3.0 Å overlap criterion, so that no functional groups are too close to each other[58]. Periodic boundary conditions have been applied on all three directions, with the box size of the Z direction 10 nm. As shown in Figure 5, by tuning the density of initial functionalization, the ratio of hydroxyl/epoxy, the T_{tri}, reactions from hydroxyl, epoxy and carbons of the basal plane shall define the final generated GO structure. By comparing the structural information (computational FTIR, XPS, pore size, *etc*.) between the GO model and the experimental GO sample from modified Hummers method[37, 38, 74, 75], we then fine tune those parameters and iterate the calculations until an agreement has been achieved satisfactorily.

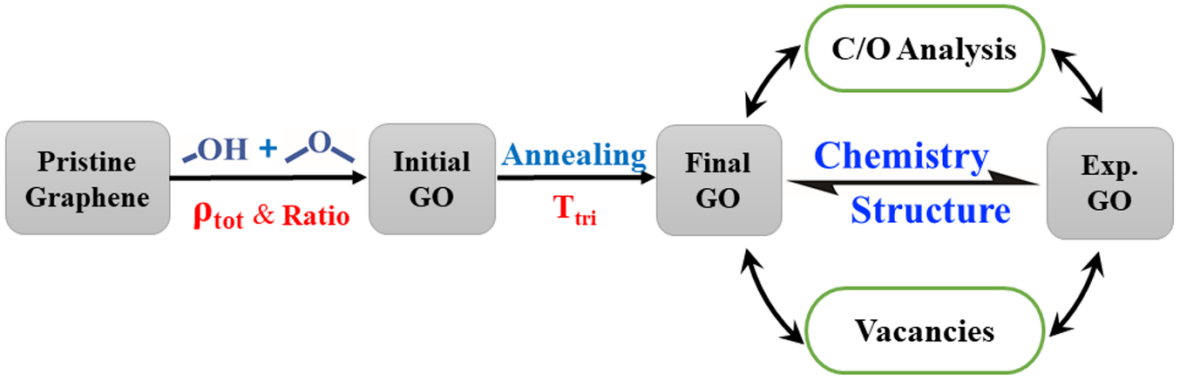

Figure 5. Scheme of the process of generating and comparing GO models with experiments GO samples: the density of functionalization, the ratio of hydroxyl/epoxy, and the T_{tri} are three tunable parameters for the GO model development.

To briefly summarize, a total of 27 RxMD simulations has been carried out in this work: three initial functionalization densities, 70%, 50% and 30%; three ratios of hydroxyl to epoxy groups, namely, 1:1, 10:1, and 1:10; and three T_{tri}, 700, 1000 and 1500 K. It is worth adding that calculations have been performed for other combinations of the three parameters, but the chosen 27 cases present the trend we have revealed from those calculations. It is also important to note that the studied concentrations (30%, 50%, 70%) are the initial density of the functional groups. After the RxMD simulation, the final GO structures shall have a different density of functional groups, which is listed in Table 1 and discussed in the following session.

Table 1. Final functionalization density of generated GO structures.

	Final Functionalization Density								
	70% GO			50% GO			30% GO		
	OH:CO			OH:CO			OH:CO		
T_{tri}	1:1	10:1	1:10	1:1	10:1	1:10	1:1	10:1	1:10
1500K	48.40%	38.65%	– [a]	27.22%	16.86%	34.15%	9.24%	3.67%	10.69%
1000K	53.60%	42.14%	61.69%	30.08%	19.00%	35.44%	11.17%	4.58%	11.03%
700K	54.43%	44.12%	63.86%	30.92%	18.98%	35.88%	11.51%	5.30%	11.12%

[a] The complete combustion was observed for this system.

3.3.1.1 Annealing Trigger Temperature, T_{tri}

Temperature is an important parameter for RxMD simulations, describing the balance between stability and reactivity. It is also a descriptor of the reaction energy barrier. A higher temperature indicates that molecules and structures of the system have larger kinetics energies and can overcome energy barriers more easily to interact with each other. As long as the reaction mechanism and reaction pathway are not altered, elevated temperatures can allow us to sample the potential energy surface as much as possible for a typical nanosecond time scale of RxMD

simulations. We also want to point out that the temperatures used in the simulations do not correspond directly to the experimental temperature conditions. For example, GO is reported to be thermally stable up to 200 °C[4]. But as shown in this work, in the RxMD simulations, GO models could remain stable at 1500 K.

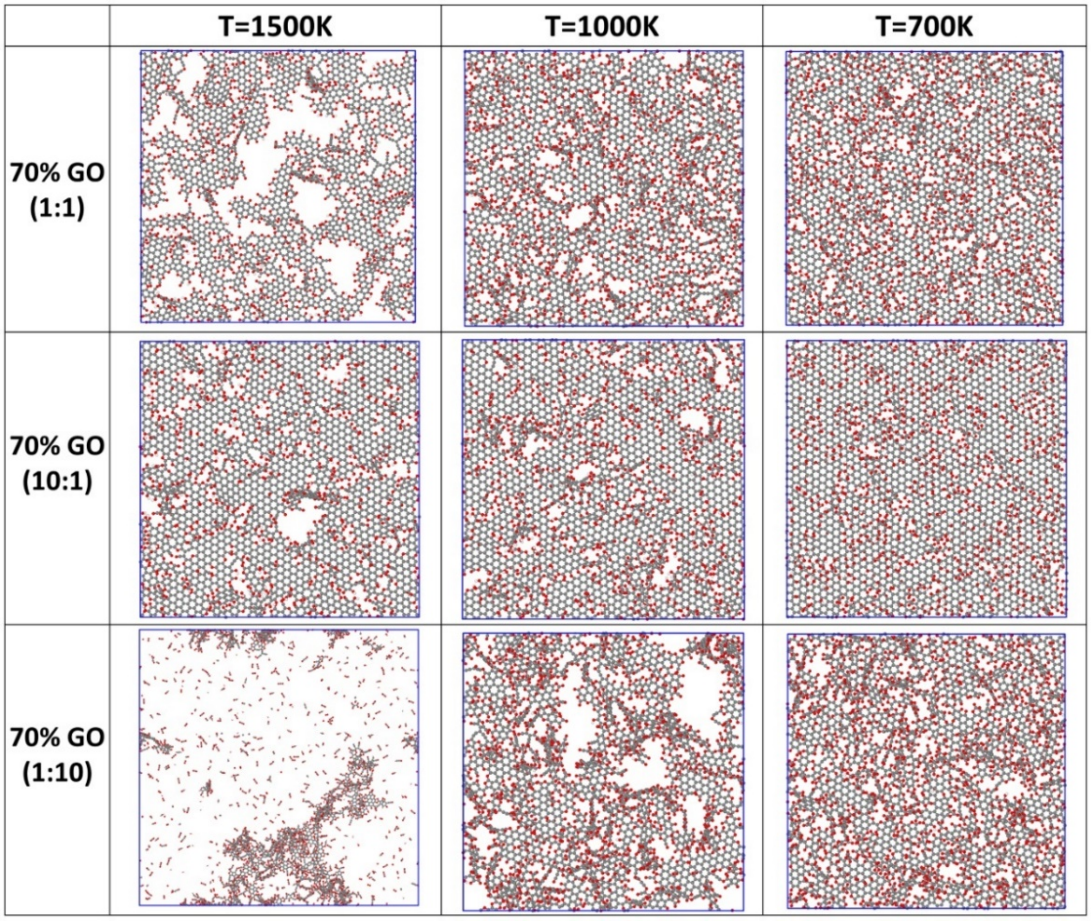

Figure 6. Final GO structures from RxMD simulations where the 70% initial functionalization density has been applied: the hydroxyl/epoxy ratios of 1:1, 10:1 and 1:10, and the T_{tri} of 1500, 1000 and 700 K were combined to investigate the overall effect.

The snapshots in Figure 6 illustrate the temperature effect to GO model development. For the 70% functionalization density, the combination of temperature and hydroxyl/epoxy ratio will produce different final GO structures. For the 1:1 ratio of hydroxyl/epoxy groups, when the T_{tri} is 1500 K, nearly all hydroxyl groups are released from the surface as water molecules. At such high temperature, many epoxy groups react with sp^2 carbon atoms of the graphene basal plane. Reaction products, such as CO and CO_2, will be released from the surface. In return, vacancies, pores or channels will be generated in the final GO models. As T_{tri} decreases to 1000 K and 700 K, more hydroxyl groups will remain stable on the final GO models, which agrees with the previous study that hydroxyl groups are relatively stable at lower temperatures[107]. A lower T_{tri} will also reduce the reactions among other species, therefore the final GO structures have less defects and their sizes are smaller. When the ratio of hydroxyl/epoxy changes from 1:1 to 1:10 and 10:1, the temperature imposes a similar effect. However, it is interesting to emphasize that more epoxy groups can lead to an almost complete combustion of the initial structure, see the case, 70% GO (1:10). As demonstrated by those calculations, the size of defects, the remaining functional groups, as well as their concentrations, are sensitive to all three studied parameters. In general, when the initial functionalization density increases, tuning the T_{tri} can effectively change the number of defects and their sizes.

3.3.1.2 Ratio of Hydroxyl/Epoxy Groups

As shown in Figure 6, when hydroxyl groups dominate, such as the three GO structures of the (10:1) ratio, the defect size is smaller than the ones from the other two ratios. This indicates that -OH groups would interact more strongly among functional groups, rather than interacting

with carbon atoms of the basal plane. On the contrary, it is much more difficult for GO to hold a planar structure when there are more epoxy groups, see the (1:10) cases. At the high T_{tri} of 1500 K, the GO (1:10) structure is completely combusted, producing CO, CO_2, H_2O and small GO segments as reaction products. The sizes and shapes of vacancies for the GO (1:10) model at 1000 K are similar to those from the (1:1) GO model produced at T=1500 K. Those calculation results suggest that epoxy groups react with basal carbon atoms, and that the amount of epoxy groups has a significant impact on the vacancies of GO.

3.3.1.3 Initial Functionalization Density, ρ_{tot}

In literature, experimental results[37] revealed a lower C/O ratio 2.44 in GO generated of modified Hummers method than what we observed in previous calculations[58] (~ 4.17). Here for the 70% (1:1) GO model at 1500 K, during the annealing process, nearly all hydroxyl groups are released from the surface as H_2O molecules. Most epoxy groups react with basal carbon atoms, being released as CO and CO_2 from the surface. Thus, among the three GO models, 70% (1:1), 50% (1:1) and 30% (1:1), the T_{tri} 1500 K assists the reactions between epoxy and basal carbon atoms. Therefore, the final 70% (1:1) GO structure has a smaller C/O ration than those of the 50% (1:1) and 30% (1:1) GO structures, which is accepted as a better model to the GO of modified Hummers method experiments[37]. For the other two T_{tri} (1000 K, and 700 K), regardless the initial hydroxyl/epoxy ratios, most functional groups interact with each other, eventually being released from the surface. Therefore, the final C/O ratios are larger than those from experiments. Similarly, having more epoxy groups is likely to remove more basal carbon atoms during the

annealing process. Thus, the final C/O ratio is lower than the GO structures from the (1:1) and (10:1) group.

3.3.2 Representative Localized Morphologies

Several representative localized morphologies that generated by the reactions of carbon, hydroxyl and epoxy groups are shown in Figure 7 in the final GO models : (a) and (b) are sp^3 carbon atoms with hydroxyl groups and isolated epoxy groups, respectively. The two structural patents are identified from all 70%, 50% and 30% GO models. Although carboxyl groups are usually located at the edges of GO structures, in our calculations, we observe carboxylic acids at vacancy sites, as shown in Figure 7 (c). Due to the nature of the thermal annealing protocol, there is no liquid phase in those studied cases. Therefore, most carboxyl groups are in the deprotonated form, as shown in Figure 7 (d). Figure 7 (e) and (f) are observed from the 70% and 50% GO structures, where esters are around defect edges; hydroxyl groups exist as phenols, and oxygen atoms can substitute carbons to form pentagon and hexagon structures. Oxygen substitution has been observed from all final GO structures. Figure 7 (g) shows a basal plane with defects of oxygen substitutions. This type of localized morphology has been observed in all 70% and 50% GO structures, and in the 30% GOs when the T_{tri} is 1500 K. Figure 7 (h), (i) and (j) demonstrates common defects observed in the 50% and70% GOs at T_{tri} about 1000K and 1500K. Unlike the 70% models, defects from the 30% and 50% GOs are generally small vacancies. Ketones, phenols or oxygen rings are identified along edges of defects, pores or channels, and carbon hexagonal rings distorted to pentagonal and heptagonal rings along the edge of defects in Figure 7 (i) and (j), similar as the lattice defects and distortions in graphene sheet[77]. Figure 7 (k) shows a defect of carbon

rings rearrangement from hexagonal rings to an octagonal ring with adjacent pairs of pentagonal rings, this type of defects could be observed in both 50% and 70% GOs with T_{tri} of 1000K. Figure 7 (l) shows a single missing carbon atom with an oxygen substitution and a Jahn-Teller distortion, this kind of single defects is observed in all 50% GOs and some 70% GOs with more hydroxyl groups in the initial setup. Defects structures shown in Figure 7 (g) ~ (l) are also reported in both experiments and DFT calculations in graphene and graphene oxide[4, 77-79].

It is worth noting that for the 30% GOs, similar to our previous study[58], only few defects could form, and the defect density is quite low. Phenols and ketones have been observed at the T_{tri} of 1500 K. But in general, no large pores or channels could form at this low initial functionalization density.

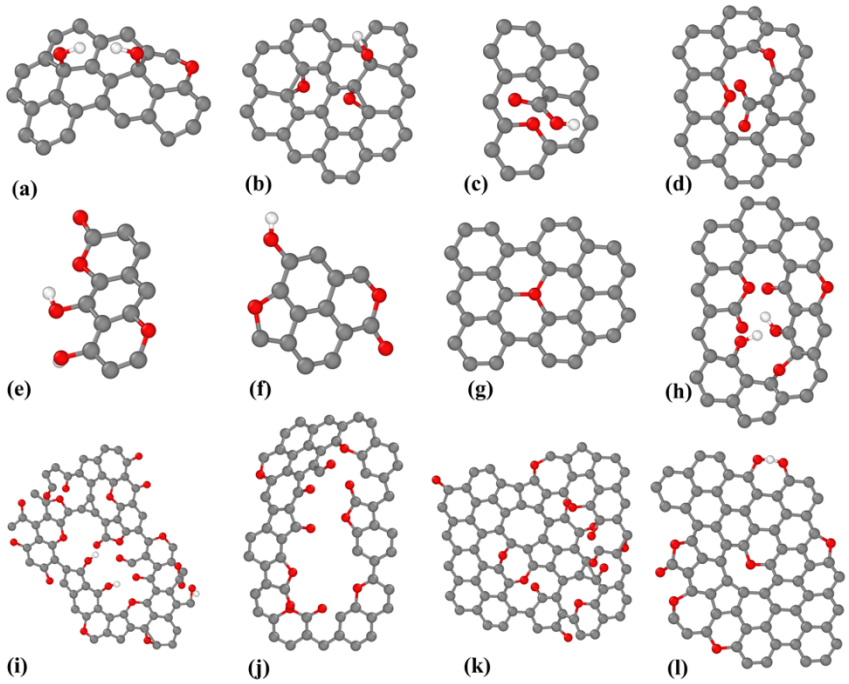

Figure 7. Representative morphologies of final GO models with the (1:1) hydroxyl/epoxy ratio. (a) sp^3 carbon with hydroxyl groups; (b) Isolated epoxy group and hydroxyl groups; (c) Carboxylic acid group; (d) Deprotonated carboxylic acid group; (e) Phenol and ester on the edges of GO; (f)

Phenol, oxygen substituted pentagon and hexagon structures; (g) Oxygen substitution structure; (h) Defects with multiple oxidized groups in 50% GO; (i) Defects with multiple oxidized groups and carbon rings distortion in 50% GO; (j) Large multiple vacancy defects on 70% GO surface; (k) Carbon rings distortion on GO surface; (l) Similar single defects with carbon rings distortion.

3.3.3 Thermal Annealing vs. Hydrothermal Protocols

GO structures and their stability depend closely on the environment. Dimiev and co-workers proposed to treat GO by dynamic models[4, 108]. They argued that even for a specific GO model, it exhibits different structures when in a solid state or in aqueous solutions. In addition, they suggested that there shall be enols in dynamic GO models, which leads to the acidity of GO solutions. On the other hand, when GO is in the solid state, those enols will be transformed and remain as ketones. Despite the difference between the thermal annealing protocol applied in our calculations and the experimental hydrothermal conditions, our GO models have same structural features as what Dimiev[108] and Gao[37] observed in their experiments. For example, Figure 8 (a) shows enol and conjugation of vinylogous carboxylic acids with graphene domain, indicated by the black arrow. The rectangle box in Figure 8 (b) illustrates the 1,3-dihydroxyxanthone structure reported from hydrothermal experiments[37]. As Kumar *et al.* reported[109], oxygen functional groups have the potential to aggregate and form oxygen and non-oxygen zones. This asymmetric nature has been also observed in our calculated GO structures, as shown in Figure 6.

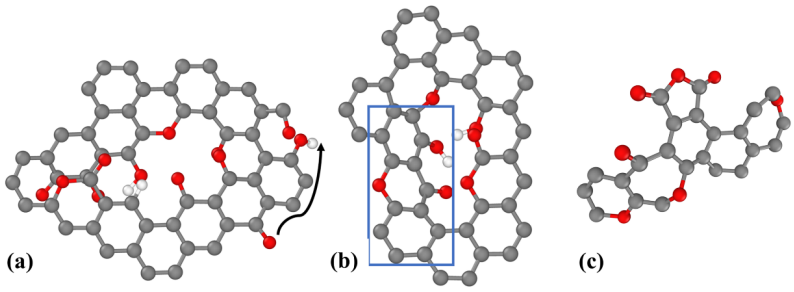

Figure 8. Characteristic structural patents observed both in hydrothermal experiments and thermal annealing process of this work: (a) Enols and the conjugation of vinylogous acids; (b) the 1,3-dihydroxyxanthone structure; (c) the phthalic anhydride structure.

3.3.4 Chemical Details of GO Models

3.3.4.1 C/O Ratio

XPS experiments are widely used to characterize the C/O ratio of synthesized GO materials. The ratio is sensitive to the synthesis methods and adopted oxidants. For instance, GO is reported to be highly oxidized via the modified Hummers method[37]: the C/O ratio could be as low as 2.44. The C/O ratios to GO models of this work are listed in Table 2.

From the table, the 70% (1:1) GOs have C/O ratios very similar to experimental values of modified Hummers method[37], from 2.26 to 2.93. For the 70% (10:1) GOs, initially having more hydroxyl groups, the C/O ratios are also closer to the experiments for the 700 K and 1000 K cases. At 1500 K, more functional groups are released from the surface, in the form of CO, CO_2 and H_2O, which results in the increase of C/O ratio, up to 3.36. On the other hand, if there are more initial epoxy groups, they interact strongly with the basal plane, leading to the decrease of C/O ratio. This is witnessed by the GO (1:10) structures in Figure 6: more defects, vacancies, pores and drastic

changes to the basal planes are evidenced. Initially having more epoxy groups is equivalent to use stronger oxidants in the GO synthesis experiments.

Table 2. The C/O ratios to GO models in this work.

	Initial Functionalization Density								
	70% GO			50% GO			30% GO		
	OH:CO			OH:CO			OH:CO		
T_{tri}	1:1	10:1	1:10	1:1	10:1	1:10	1:1	10:1	1:10
1500K	2.93	3.36	– [a]	5.55	9.59	4.34	18.05	49.18	15.25
1000K	2.36	2.77	1.99	4.47	6.67	3.61	12.67	28.67	12.84
700K	2.26	2.47	1.86	4.01	6.09	3.33	11.47	24.76	10.92

[a] The complete combustion was observed for this system.

Table 3. Relative atomic percentages of carbon-based functional groups presented in the XPS high resolution C1s spectra[75, 106]

GO Sample	Oxidation Method	C/O	Percentage of carbon-based functional groups, %				
			C-O	C=O	COOH	Graphitic Structure	π-π*
1	Pure G	30.1	5.8	5.4	1.9	71.4	15.5
2[a]	Modified Hummers	2.1	25.0	20.0	15.0	40.0	0.0
3	HNO_3	21.2	4.4	4.4	2.6	79.8	8.8
4[b]	O_3_disp	9.8	6.4	5.3	0.5	76.4	11.4
5[c]	O_3_gas	9.8	13.8	6.6	1.1	67.6	10.8
6	$KMnO_4$	4.9	19.2	10.0	1.5	64.9	4.5
7[d]	m-CPBA	7.8	6.3	4.9	0.4	76.8	11.6
8[e]	m-CPBA	13.0	6.6	5.25	0.4	75.2	12.6

[a] Sample 2 was prepared by modified Hummers method, data from Ref. 75.
[b] Sample 4 was prepared by bubbling O_3 gas passing through graphene dispersions, Ref. 106.
[c] Sample 5 was prepared by bubbling O_3 gas passing through graphene solid phase, Ref. 106.
[d] Sample 7 was prepared by 0.1M 3-chloroperbenzoic acid (m-CPBA) solution, Ref. 106.
[e] Sample 8 was prepared by 0.01M m-CPBA solution, Ref. 106.

Similarly, the C/O ratio of 50% GO (1:10) is smaller than that from 50% GO (1:1) and 50% GO (10:1). As for the 30% GOs, the initial functionalization density is lower, and the final C/O ratio, depending on the T_{tri}, varies from 10 to 49. Such a high C/O ratio was not observed in

experiments of the modified Hummers method[37, 38, 75, 76]. But it is possible if one uses weak oxidants to synthesize GO[106]. For example, in Table 3 graphene flakes oxidized by $KMnO_4$ will produce GO with the C/O ratio of 4.9, which is similar to the 50% GO (1:1) in our calculation. GO produced by 0.01M m-CPBA has a similar C/O ratio to the 30% (1:1) and 30% (1:10) GOs. The pure graphene flakes with a C/O ratio of 30.1 is close to the 30% GO (10:1) with T_{tri} = 1500 K.

3.3.4.2 Carbon Hybridization

By calculating the bond orders of final GO structures, we are able to get carbon hybridization information and compare it with XPS experiments. As shown in Figure 9, each column represents the carbon hybridization analysis of one GO model. Figure 9 (a) summarizes GO samples from different syntheses, while Figure 9 (b) to (d) present GO models from the three studied hydroxyl/epoxy ratios. For the (1:1) hydroxyl/epoxy ratio in Figure 9 (b), about 7~15% of carbon atoms exist as C-O bonds. Those C-O bonds are from hydroxyls, phenols and epoxy groups. For the 70% (1:1) GOs from 1500 K and 1000 K, most C-O bonds are phenols at the edge of vacancy defects. At lower T_{tri} and lower initial functionalization density, there are C-O bonds from sp^3 carbons bonded with OH groups, which is observed from the 70% (1:1) GO from 700 K, and the 50% (1:1) GO from both 700 and 1000 K. For the 70% (1:1) GOs, there are about 5% O-C=O bonds, which is attributed to carboxylic acids, carboxylic anhydrides and esters. For all (1:1) GO models, less than 4% carbons exist as C=O groups. This implies that those GO models have a low concentration of ketones, aldehydes or quinones. In addition, there are π–π^* and sp^2 hybridized carbons. Generally speaking, high T_{tri} or high initial functionalization density will lead to a larger

degree of oxidation. Therefore, the final structures will have more vacancy defects, and more oxygen substitutions, such as five or seven oxygen-containing ring structures.

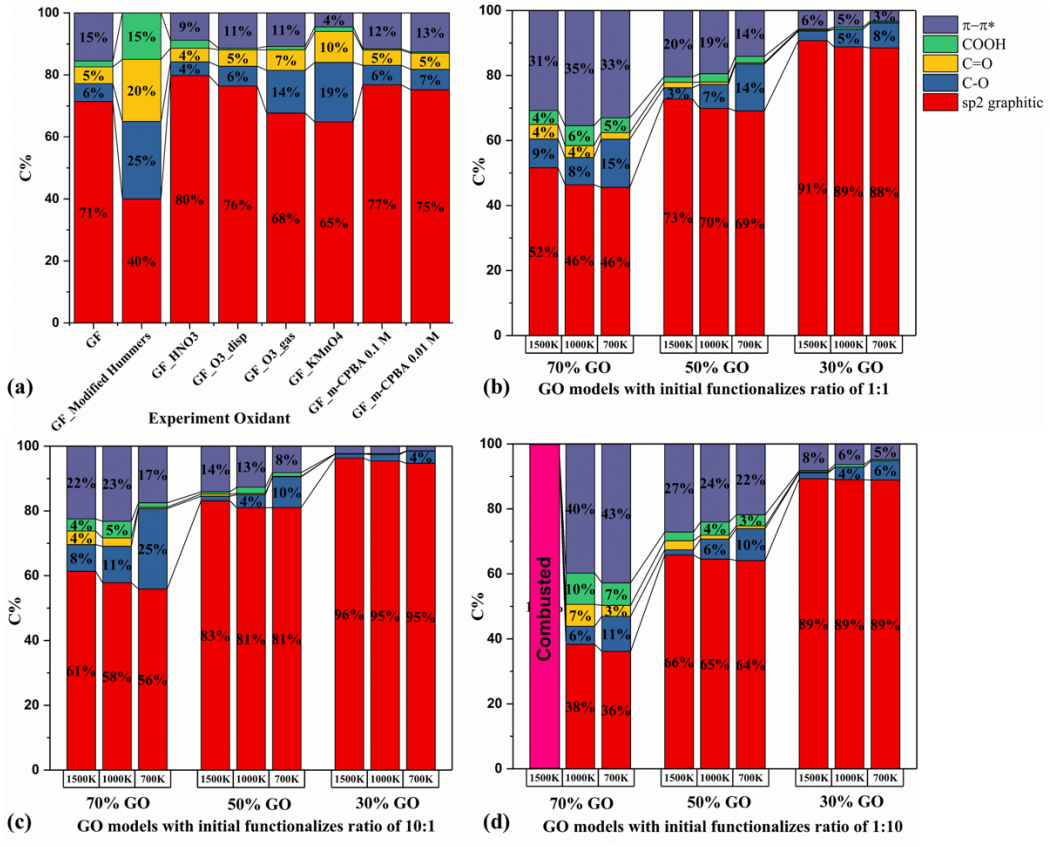

Figure 9. Hybridization of carbon atoms and its distribution analysis: (a) XPS results for experimental GOs[75, 106] by different oxidation treatments; (b) GO models, hydroxyl/epoxy ratio is 1:1; (c) GO models, hydroxyl/epoxy ratio is 10:1; (d) GO models, hydroxyl/epoxy ratio is 1:10.

For the (10:1) GOs, as shown in Figure 9 (c), most OH groups will be released from the surface for the three studied temperatures. While there are not many epoxy groups interacting with basal carbon atoms, a small percentage of π-π* carbon atoms are observed for this group. For the

50% and 30% initial functionalization densities, those GO models have a higher concentration of sp^2 carbons. For the (1:10) GOs in Figure 9 (d), because there are more reactive epoxy groups, more reactions will occur during the annealing process. Higher percentages of C-O, O-C=O and C=O have been identified in those GO models. For the 70% (1:10) GO from 1500 K, the structure is completely combusted.

Compared with experimental XPS results, the 70% (1:1) GOs from three studied temperature and the 70% (10:1) GOs from 700 and 1000 K share a similar carbon hybridization, and they are very similar to GO samples synthesized by the modified Hummers method[75] shown in Figure 9 (a), which is characterized by a low C/O ratio and a high degree of oxidation.

3.3.4.3 Computational FTIR Analysis

Considering the C/O ratio and the carbon hybridization, we conclude that the 70% (1:1) and 70% (1:10) GO models can better represent experimental GO samples of modified Hummers method[37, 75]. In Figure 10, we compared the absorption bands between the 70% (1:1), 70% (1:10) final GO models and the GO sample synthesized by the modified Hummers method[37, 75]. For the 70% (1:1) 1500 K GO model and the experimental GO, the band at around 3600-2400 cm^{-1} corresponds to the O-H stretching modes. Other characteristic adsorption bands have been also observed. For example, the bands at 1734-1719 cm^{-1} (yellow region) is from the stretching of C=O of carboxylic groups. The peak around 1850 cm^{-1} is due to multiple acid anhydrides, which has been identified in our calculations, as shown in Figure 8 (c). It is interesting to note that the band around 1626-1615 cm^{-1} (blue region), which has been observed from the experimental GO sample.

Most literatures assign the band to the stretching of C=C bonds. However, Dimiev argued[4] this band is from the bending modes of water molecules in the GO systems. By using deuterated water in the GO experiments, Dimiev reported that this peak will disappear[33, 108, 110]. For our FTIR analysis, all gas-phase reaction produces, including CO, CO_2, and H_2O, have been removed prior to the analysis. This is why we did not observe this peak from our calculated GO models. It is worth noting that in the 70% (1:10) from T=1000K, we could observe this peak around 1626-1615 cm^{-1} (blue region). This is attributed to intermediate structures where distorted epoxy groups are interacting with the basal plane.

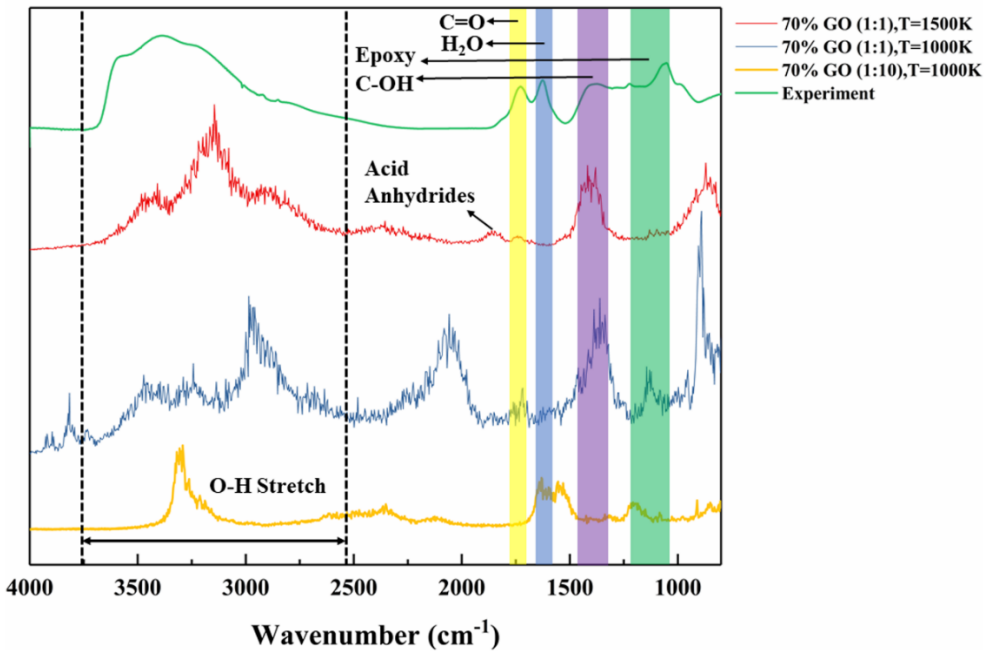

Figure 10. FTIR calculation and the comparison between experiment and simulation: FTIR of GO sample by the modified Hummers method[37]. The models from simulation are the 70% (1:1) GO from1500 K, 70% (1:1) GO from 1000 K and 70% (1:10) GO from 1000 K, respectively.

The peak around 1420-1368 cm^{-1} (purple region) is assigned to the bending of C-OH groups, which is also observed in the 70% (1:1) GO from 1500 K. Another intense peak is around 1040-1060 cm^{-1} (green region), which is characteristic of epoxy groups. However, some literature[4] argued that the epoxy group spectra are around 1250 cm^{-1}. For the 70% (1:1) GO from 1500 K, despite the total amount of 10% C-O bonds, as discussed in Figure 9, only 0.3% are epoxy groups. Therefore, we argue that the weak peak around 1040-1060 cm^{-1} in the 70% (1:1) GO from 1500 K model might due to the small amount of epoxy groups. In summary, the IR calculation of 70% (1:1) GO from 1500 K model agrees well with the experimental FTIR result. Considering the C/O ratio analysis in Figure 9, we conclude the 70% (1:1) GO from 1500 K is the best model to represent experimental GO samples from modified Hummers method[37, 38, 74-76].

3.3.4.4 Vacancy Properties of GO Models

Since the 70% GO models better represent experimental samples from modified Hummers method[37, 38, 74-76], the vacancy analysis is only carried out for them. The defect is characterized by two parameters, namely, the pore size and the vacancy density. Here, the vacancy density is defined as the percentage of carbon atoms that have been removed from the basal plane during the process. Generally speaking, more removed carbon atoms correspond to more (or larger) defects. Figure 11 shows a schematic illustration of how the pore size was determined. A Monte Carlo algorithm was adopted to determine the maximum inscribed sphere, whose diameter is considered as the pore size of the defect. It is worth noting that the GO models do not have regular defects, but the probe using inscribed sphere can provide a reasonable estimation of the defect size. Table 4 lists the pore size and vacancy density of the 70% GO models. For the 70% (1:1) GO from

1500 K, pores are connected to form channels, therefore the diffusion of molecules is easier in this model. In addition, for this GO model, the averaged pore size is around 1nm, which agrees with experiments HRSTEM values[3, 4, 37, 79] of vacancies with diameters about 1nm and usually under 5 nm^2 from modified Hummers method. It also has the highest vacancy density of the three 70% GO models.

Table 4. Pore size and vacancy density of 70% GO models.

		Initial Functionalization Density		
		70% GO		
		OH:CO		
T_{tri}		1:1	10:1	1:10
1500K	Vacancy Density	17.94%	7.94%	– [a]
	Pore Size	0.7-1.7 nm	0.3-1.1 nm	– [a]
1000K	Vacancy Density	5.66%	3.77%	9.80%
	Pore Size	0.4-0.9 nm	0.4-0.6 nm	0.6-1.5 nm
700K	Vacancy Density	3.59%	1.00%	4.82%
	Pore Size	0.2-0.4 nm	0.2-0.4 nm	0.5-0.7 nm

[a] The complete combustion was observed for this system.

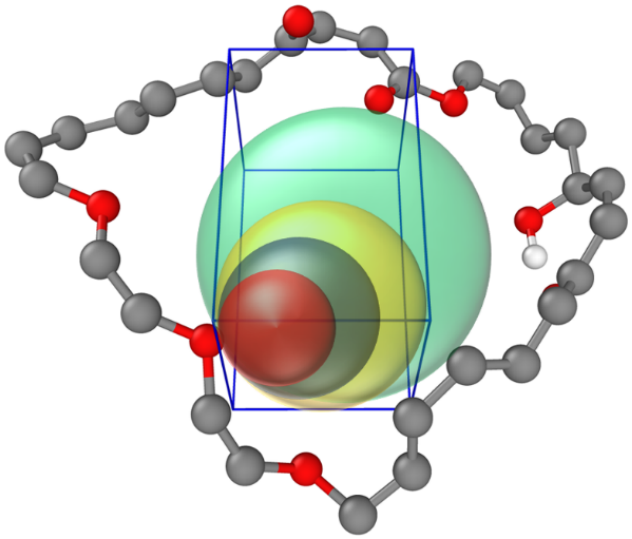

Figure 11. A schematic illustration of pore size calculation: A Monte Carlo algorithm is adopted to determine the maximum inscribed sphere, whose diameter is considered as the pore size of the defect.

Even with a larger initial density of functional groups, the pore size of the 70% (10:1) GO from different T_{tri} is still much smaller than that of the 70% (1:1) GOs. This is probably because of the high concentration of hydroxyl groups, which do not interact actively with the basal carbon atoms. On the other hand, the 70% (1:10) GOs, which have higher concentrations of epoxy groups, have more and larger defects, due to the interactions between epoxy and basal carbons. Figure 12 shows the curvature analysis of the 70% (1:1) GOs from different T_{tri}. Interestingly, a higher T_{tri} does not necessarily result in a drastic curvature. As shown in Figure 12 (b), the 70% (1:1) GO from 1500 K has a fitted curvature of 0.9427 nm compared to AFM values of 0.8-1.2nm for GO samples from modified Hummers method[3, 4, 37]. It is 1.0471 nm and 0.9420 nm respectively for the 70% (1:1) GOs from 1000 K and 700 K. The 50% GOs also show a similar trend: both pore size and vacancy density will decrease when T_{tri} decreases from 1500 K to 700 K. Because of the high initial concentration of epoxy, the 50% (1:10) GOs have larger pores, and their vacancy densities are also larger than those of 50% (1:1) GOs. Due to the low initial density of functional groups, all 30% GOs have fewer and smaller defects.

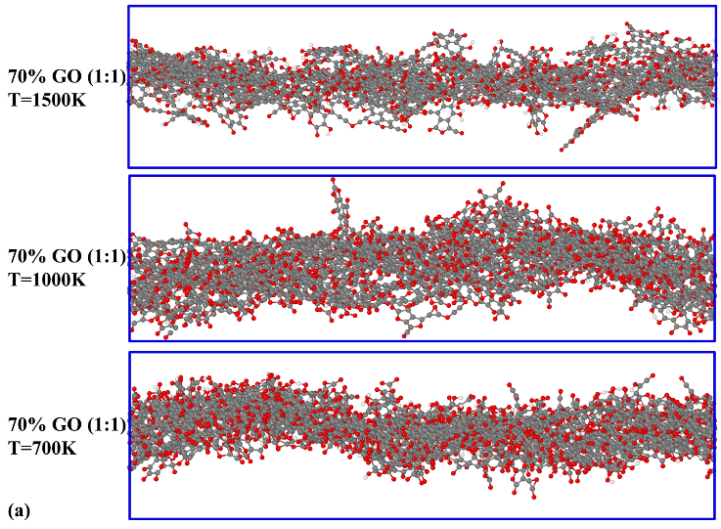

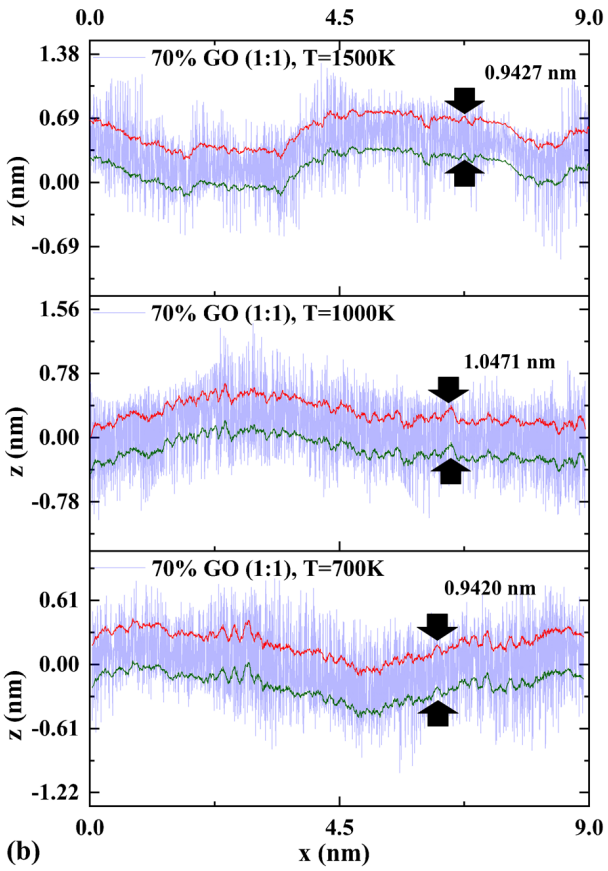

Figure 12. Curvature analysis of 70% (1:1) GO models: (a) snapshots of the structures; (b) the fitted curvature of the GO models.

3.4 Conclusion

Temperature-programmed RxMD simulations have been carried out to study structural and chemistry properties of GO models. Three critical controlling parameters, namely, the initial functionalization density, the ratio of hydroxyl/epoxy groups, the trigger annealing temperature T_{tri}, are investigated systematically. FTIR, XPS, vacancy defects and curvature properties have been computed and compared with available experimental results. GO models proposed this work have an overall C/O ratio in the range of 1.86 to 18.05, and vacancy defects as large as 1.7 nm. By comparing with GO sample from the modified Hummers method, the 70% GO (1:1) model from

T=1500K is considered to be the best GO model, final model has a final functionalization density of 48.40%, C/O value about 2.93, curvature for 0.9427 nm and vacancy sizes around 0.7-1.7 nm with a good agreement for both FTIR and XPS characteristics. A structure file of 70% GO (1:1) with T_{tri} = 1500K model is provided in the supplementary material. While GO structures are very sensitive to experimental synthesis conditions, the studies in this work could provide a general protocol to generate atomic GO structures representative of experimental samples. The theoretical FTIR and XPS calculations are useful tools for GO model characterization, and can be adopted for computational studies of other two-dimensional materials and their composites.

3.5 Reference

1. Novoselov, K.S., et al., *Electric field effect in atomically thin carbon films.* Science, 2004. **306**(5696): p. 666-669.
2. Novoselov, K.S., et al., *Two-dimensional gas of massless Dirac fermions in graphene.* Nature, 2005. **438**(7065): p. 197-200.
3. Gao, W., *Graphene oxide: Reduction recipes, spectroscopy, and applications*. 2015: Springer International Publishing. 1-147.
4. Ayrat M. Dimiev, S.E., *Graphene Oxide: Fundamentals and Applications*. 2017, Chichester, West Sussex: John Wiley & Sons, Inc.
5. Gilje, S., et al., *A chemical route to graphene for device applications.* Nano Letters, 2007. **7**(11): p. 3394-3398.
6. Gao, W., et al., *Is reduced graphene oxide favorable for nonprecious metal oxygen-reduction catalysts?* Carbon, 2016. **102**: p. 346-356.
7. Song, Y.J., et al., *Graphene Oxide: Intrinsic Peroxidase Catalytic Activity and Its Application to Glucose Detection.* Advanced Materials, 2010. **22**(19): p. 2206-2210.
8. Stankovich, S., et al., *Graphene-based composite materials.* Nature, 2006. **442**(7100): p. 282-286.
9. Gao, W., et al., *Direct laser writing of micro-supercapacitors on hydrated graphite oxide films.* Nature Nanotechnology, 2011. **6**(8): p. 496-500.
10. Gao, W., et al., *Ozonated Graphene Oxide Film as a Proton-Exchange Membrane.* Angewandte Chemie-International Edition, 2014. **53**(14): p. 3588-3593.
11. Zhou, M., Y.M. Zhai, and S.J. Dong, *Electrochemical Sensing and Biosensing Platform Based on Chemically Reduced Graphene Oxide.* Analytical Chemistry, 2009. **81**(14): p. 5603-5613.

12. Robinson, J.T., et al., *Reduced Graphene Oxide Molecular Sensors.* Nano Letters, 2008. **8**(10): p. 3137-3140.
13. Joshi, R.K., et al., *Precise and Ultrafast Molecular Sieving Through Graphene Oxide Membranes.* Science, 2014. **343**(6172): p. 752-754.
14. Li, H., et al., *Ultrathin, Molecular-Sieving Graphene Oxide Membranes for Selective Hydrogen Separation.* Science, 2013. **342**(6154): p. 95-98.
15. Gao, W., et al., *Engineered Graphite Oxide Materials for Application in Water Purification.* Acs Applied Materials & Interfaces, 2011. **3**(6): p. 1821-1826.
16. Eda, G. and M. Chhowalla, *Chemically Derived Graphene Oxide: Towards Large-Area Thin-Film Electronics and Optoelectronics.* Advanced Materials, 2010. **22**(22): p. 2392-2415.
17. Eda, G., G. Fanchini, and M. Chhowalla, *Large-area ultrathin films of reduced graphene oxide as a transparent and flexible electronic material.* Nature Nanotechnology, 2008. **3**(5): p. 270-274.
18. Liu, Z., et al., *PEGylated nanographene oxide for delivery of water-insoluble cancer drugs.* Journal of the American Chemical Society, 2008. **130**(33): p. 10876-+.
19. Zhang, L.M., et al., *Functional Graphene Oxide as a Nanocarrier for Controlled Loading and Targeted Delivery of Mixed Anticancer Drugs.* Small, 2010. **6**(4): p. 537-544.
20. Rahmani, F., et al., *Molecular simulation insights on the in vacuo adsorption of amino acids on graphene oxide surfaces with varying surface oxygen densities.* Journal of Nanoparticle Research, 2016. **18**(11): p. 320.
21. Mahdavi, M., F. Rahmani, and S. Nouranian, *Molecular simulation of pH-dependent diffusion, loading, and release of doxorubicin in graphene and graphene oxide drug delivery systems.* Journal of Materials Chemistry B, 2016. **4**(46): p. 7441-7451.
22. Zhang, L., et al., *Magnetic-mesoporous Janus nanoparticles.* Chemical Communications, 2011. **47**(4): p. 1225-1227.
23. Li, C., et al., *A facile fabrication of amphiphilic Janus and hollow latex particles by controlling multistage emulsion polymerization.* Journal of Colloid and Interface Science, 2014. **426**: p. 39-43.
24. Chao, Y.C., et al., *Assembly and Manipulation of Fe3O4/Coumarin Bifunctionalized Submicrometer Janus Particles.* Acs Applied Materials & Interfaces, 2014. **6**(6): p. 4338-4345.
25. Zhao, Z.X., et al., *Self-assembled film of hydrophobins on gold surfaces and its application to electrochemical biosensing.* Colloids and Surfaces B-Biointerfaces, 2009. **71**(1): p. 102-106.
26. Yang, H.L., et al., *Responsive Janus Composite Nanosheets.* Macromolecules, 2013. **46**(7): p. 2754-2759.
27. Cheng, L., et al., *Efficient Synthesis of Unimolecular Polymeric Janus Nanoparticles and Their Unique Self-Assembly Behavior in a Common Solvent.* Macromolecules, 2008. **41**(21): p. 8159-8166.
28. Lattuada, M. and T.A. Hatton, *Synthesis, properties and applications of Janus nanoparticles.* Nano Today, 2011. **6**(3): p. 286-308.
29. Liu, J.H., et al., *Synthesis and Self-Assembly of Amphiphilic Janus Laponite Disks.* Macromolecules, 2013. **46**(15): p. 5974-5984.
30. Hofmann, U. and R. Holst, *Über die Säurenatur und die Methylierung von Graphitoxyd.* Berichte der deutschen chemischen Gesellschaft (A and B Series), 1939. **72**(4): p. 754-771.

31. Ruess, G., *Über das Graphitoxyhydroxyd (Graphitoxyd).* Monatshefte für Chemie und verwandte Teile anderer Wissenschaften, 1947. **76**(3): p. 381-417.
32. Scholz, W. and H.P. Boehm, *Untersuchungen am Graphitoxid. VI. Betrachtungen zur Struktur des Graphitoxids.* Zeitschrift für anorganische und allgemeine Chemie, 1969. **369**(3-6): p. 327-340.
33. Szabo, T., et al., *Evolution of surface functional groups in a series of progressively oxidized graphite oxides.* Chemistry of Materials, 2006. **18**(11): p. 2740-2749.
34. A. Lerf, H.H., T. Riedl, M. Forster and J. Klinowski, *Solid State Ionics*. Vol. 101-103. 1997. 857-862.
35. He, H.Y., et al., *Solid-state NMR studies of the structure of graphite oxide.* Journal of Physical Chemistry, 1996. **100**(51): p. 19954-19958.
36. Lerf, A., et al., *Structure of graphite oxide revisited.* Journal of Physical Chemistry B, 1998. **102**(23): p. 4477-4482.
37. Gao, W., et al., *New insights into the structure and reduction of graphite oxide.* Nature Chemistry, 2009. **1**(5): p. 403-408.
38. Hummers, W.S. and R.E. Offeman, *PREPARATION OF GRAPHITIC OXIDE.* Journal of the American Chemical Society, 1958. **80**(6): p. 1339-1339.
39. Chua, C.K. and M. Pumera, *Chemical reduction of graphene oxide: a synthetic chemistry viewpoint.* Chemical Society Reviews, 2014. **43**(1): p. 291-312.
40. Saikia, N. and R.C. Deka, *Ab initio study on the noncovalent adsorption of camptothecin anticancer drug onto graphene, defect modified graphene and graphene oxide.* Journal of Computer-Aided Molecular Design, 2013. **27**(9): p. 807-821.
41. Wang, L., et al., *Characteristics of Raman spectra for graphene oxide from ab initio simulations.* Journal of Chemical Physics, 2011. **135**(18).
42. Paulla, K.K. and A.A. Farajian, *Concentration Effects of Carbon Oxides on Sensing by Graphene Nanoribbons: Ab Initio Modeling.* Journal of Physical Chemistry C, 2013. **117**(24): p. 12815-12825.
43. Zhang, H. and Y. Miyamoto, *Graphene production by laser shot on graphene oxide: An ab initio prediction.* Physical Review B, 2012. **85**(3).
44. Boukhvalov, D.W., et al., *A Computational Investigation of the Catalytic Properties of Graphene Oxide: Exploring Mechanisms by using DFT Methods.* Chemcatchem, 2012. **4**(11): p. 1844-1849.
45. Wang, X.X., Z.S. Chen, and S.B. Yang, *Application of graphene oxides for the removal of Pb(II) ions from aqueous solutions: Experimental and DFT calculation.* Journal of Molecular Liquids, 2015. **211**: p. 957-964.
46. Zhao, W.H., et al., *The strong effect of substituents on the carbonyl reduction in graphene oxide: A DFT study.* Computational and Theoretical Chemistry, 2015. **1068**: p. 1-7.
47. Larijani, H.T., M.D. Ganji, and M. Jahanshahi, *Trends of amino acid adsorption onto graphene and graphene oxide surfaces: a dispersion corrected DFT study.* Rsc Advances, 2015. **5**(113): p. 92843-92857.
48. Rui, X., et al., *Wrapping Nanocellulose Nets around Graphene Oxide Sheets.* Angewandte Chemie, 2018. **0**(0).
49. Medhekar, N.V., et al., *Hydrogen Bond Networks in Graphene Oxide Composite Paper: Structure and Mechanical Properties.* Acs Nano, 2010. **4**(4): p. 2300-2306.
50. Sun, X.T., et al., *Mechanism of Graphene Oxide as an Enzyme Inhibitor from Molecular Dynamics Simulations.* Acs Applied Materials & Interfaces, 2014. **6**(10): p. 7153-7163.

51. Raghav, N., S. Chakraborty, and P.K. Maiti, *Molecular mechanism of water permeation in a helium impermeable graphene and graphene oxide membrane.* Physical Chemistry Chemical Physics, 2015. **17**(32): p. 20557-20562.
52. Tang, H., et al., *Molecular Dynamics Study of the Aggregation Process of Graphene Oxide in Water.* Journal of Physical Chemistry C, 2015. **119**(47): p. 26712-26718.
53. Devanathan, R., et al., *Molecular Dynamics Simulations Reveal that Water Diffusion between Graphene Oxide Layers is Slow.* Scientific Reports, 2016. **6**: p. 8.
54. Willcox, J.K.L. and H.J. Kim, *Molecular Dynamics Study of Water Flow across Multiple Layers of Pristine, Oxidized, and Mixed Regions of Graphene Oxide.* Acs Nano, 2017. **11**(2): p. 2187-2193.
55. Rahmani, F., et al., *Confinement effects on the thermal stability of poly(ethylene oxide)/graphene nanocomposites: A reactive molecular dynamics simulation study.* Journal of Polymer Science Part B: Polymer Physics, 2017. **55**(13): p. 1026-1035.
56. Rahmani, F., et al., *Reactive Molecular Simulation of the Damage Mitigation Efficacy of POSS-, Graphene-, and Carbon Nanotube-Loaded Polyimide Coatings Exposed to Atomic Oxygen Bombardment.* ACS Applied Materials & Interfaces, 2017. **9**(14): p. 12802-12811.
57. Akarsh, V. and P. Avinash, *Molecular dynamics based simulations to study the fracture strength of monolayer graphene oxide.* Nanotechnology, 2018. **29**(11): p. 115706.
58. Huang, L.L., et al., *Controllable atomistic graphene oxide model and its application in hydrogen sulfide removal.* Journal of Chemical Physics, 2013. **139**(19).
59. Bagri, A., et al., *Structural evolution during the reduction of chemically derived graphene oxide.* Nature Chemistry, 2010. **2**: p. 581.
60. Cassagneau, T., F. Guérin, and J.H. Fendler, *Preparation and Characterization of Ultrathin Films Layer-by-Layer Self-Assembled from Graphite Oxide Nanoplatelets and Polymers.* Langmuir, 2000. **16**(18): p. 7318-7324.
61. Szabó, T., et al., *Enhanced acidity and pH-dependent surface charge characterization of successively oxidized graphite oxides.* Carbon, 2006. **44**(3): p. 537-545.
62. Cai, W., et al., *Synthesis and Solid-State NMR Structural Characterization of ¹³C-Labeled Graphite Oxide.* Science, 2008. **321**(5897): p. 1815-1817.
63. Goverapet Srinivasan, S. and A.C.T. van Duin, *Molecular-Dynamics-Based Study of the Collisions of Hyperthermal Atomic Oxygen with Graphene Using the ReaxFF Reactive Force Field.* The Journal of Physical Chemistry A, 2011. **115**(46): p. 13269-13280.
64. Compton, O.C., et al., *Tuning the Mechanical Properties of Graphene Oxide Paper and Its Associated Polymer Nanocomposites by Controlling Cooperative Intersheet Hydrogen Bonding.* ACS Nano, 2012. **6**(3): p. 2008-2019.
65. Bao, H., et al., *Chitosan-Functionalized Graphene Oxide as a Nanocarrier for Drug and Gene Delivery.* Small, 2011. **7**(11): p. 1569-1578.
66. Liu, J.Q., L. Cui, and D. Losic, *Graphene and graphene oxide as new nanocarriers for drug delivery applications.* Acta Biomaterialia, 2013. **9**(12): p. 9243-9257.
67. Zhang, L., et al., *Enhanced Chemotherapy Efficacy by Sequential Delivery of siRNA and Anticancer Drugs Using PEI-Grafted Graphene Oxide.* Small, 2011. **7**(4): p. 460-464.
68. Yang, S.B., et al., *Fabrication of Graphene-Encapsulated Oxide Nanoparticles: Towards High-Performance Anode Materials for Lithium Storage.* Angewandte Chemie-International Edition, 2010. **49**(45): p. 8408-8411.
69. Chen, C.M., et al., *Self-Assembled Free-Standing Graphite Oxide Membrane (vol 21, pg 3007, 2009).* Advanced Materials, 2009. **21**(35): p. 3541-3541.

70. Chen, L., et al., *Ion sieving in graphene oxide membranes via cationic control of interlayer spacing.* Nature, 2017. **550**(7676): p. 415-418.
71. Liu, G.P., W.Q. Jin, and N.P. Xu, *Graphene-based membranes.* Chemical Society Reviews, 2015. **44**(15): p. 5016-5030.
72. Zhang, L.L., R. Zhou, and X.S. Zhao, *Graphene-based materials as supercapacitor electrodes.* Journal of Materials Chemistry, 2010. **20**(29): p. 5983-5992.
73. Sun, Y.Q., Q.O. Wu, and G.Q. Shi, *Graphene based new energy materials.* Energy & Environmental Science, 2011. **4**(4): p. 1113-1132.
74. Kovtyukhova, N.I., et al., *Layer-by-Layer Assembly of Ultrathin Composite Films from Micron-Sized Graphite Oxide Sheets and Polycations.* Chemistry of Materials, 1999. **11**(3): p. 771-778.
75. Ganguly, A., et al., *Probing the Thermal Deoxygenation of Graphene Oxide Using High-Resolution In Situ X-ray-Based Spectroscopies.* The Journal of Physical Chemistry C, 2011. **115**(34): p. 17009-17019.
76. Marcano, D.C., et al., *Improved Synthesis of Graphene Oxide.* Acs Nano, 2010. **4**(8): p. 4806-4814.
77. Tian, W., et al., *A Review on Lattice Defects in Graphene: Types, Generation, Effects and Regulation.* Micromachines, 2017. **8**(5): p. 163.
78. Banhart, F., J. Kotakoski, and A.V. Krasheninnikov, *Structural Defects in Graphene.* ACS Nano, 2011. **5**(1): p. 26-41.
79. Erickson, K., et al., *Determination of the Local Chemical Structure of Graphene Oxide and Reduced Graphene Oxide.* Advanced Materials, 2010. **22**(40): p. 4467-4472.
80. van Duin, A.C.T., et al., *ReaxFF: A reactive force field for hydrocarbons.* Journal of Physical Chemistry A, 2001. **105**(41): p. 9396-9409.
81. Senftle, T.P., et al., *The ReaxFF reactive force-field: development, applications and future directions.* Npj Computational Materials, 2016. **2**: p. 15011.
82. Liang, T., et al., *Reactive Potentials for Advanced Atomistic Simulations.* Annual Review of Materials Research, Vol 43, 2013. **43**: p. 109-129.
83. Li, P. and K.M. Merz, *Metal Ion Modeling Using Classical Mechanics.* Chemical Reviews, 2017. **117**(3): p. 1564-1686.
84. Abell, G.C., *Empirical chemical pseudopotential theory of molecular and metallic bonding.* Physical Review B, 1985. **31**(10): p. 6184-6196.
85. Tersoff, J., *New empirical model for the structural properties of silicon.* Physical Review Letters, 1986. **56**(6): p. 632-635.
86. Tersoff, J., *New empirical approach for the structure and energy of covalent systems.* Physical Review B, 1988. **37**(12): p. 6991-7000.
87. Tersoff, J., *Empirical Interatomic Potential for Carbon, with Applications to Amorphous Carbon.* Physical Review Letters, 1988. **61**(25): p. 2879-2882.
88. Tersoff, J., *Modeling solid-state chemistry: Interatomic potentials for multicomponent systems.* Physical Review B, 1989. **39**(8): p. 5566-5568.
89. Russo, M.F. and A.C.T. van Duin, *Atomistic-scale simulations of chemical reactions: Bridging from quantum chemistry to engineering.* Nuclear Instruments & Methods in Physics Research Section B-Beam Interactions with Materials and Atoms, 2011. **269**(14): p. 1549-1554.

90. Mortier, W.J., S.K. Ghosh, and S. Shankar, *Electronegativity equalization method for the calculation of atomic charges in molecules.* Journal of the American Chemical Society, 1986. **108**(15): p. 4315-4320.
91. Janssens, G.O.A., et al., *Comparison of cluster and infinite crystal calculations on zeolites with electronegativity equalization method (EEM).* Journal of Physical Chemistry, 1995. **99**(10): p. 3251-3258.
92. Duin, A.v. *Home - Dr. Adri van Duin*. 2018 [cited 2018 Oct. 25, 2018]; Available from: http://www.engr.psu.edu/adri/
93. Agrawalla, S. and A.C.T. van Duin, *Development and Application of a ReaxFF Reactive Force Field for Hydrogen Combustion.* Journal of Physical Chemistry A, 2011. **115**(6): p. 960-972.
94. Chenoweth, K., et al., *Development and application of a ReaxFF reactive force field for oxidative dehydrogenation on vanadium oxide catalysts.* Journal of Physical Chemistry C, 2008. **112**(37): p. 14645-14654.
95. Chenoweth, K., A.C.T. van Duin, and W.A. Goddard, *ReaxFF reactive force field for molecular dynamics simulations of hydrocarbon oxidation.* Journal of Physical Chemistry A, 2008. **112**(5): p. 1040-1053.
96. Zandiatashbar, A., et al., *Effect of defects on the intrinsic strength and stiffness of graphene.* Nature Communications, 2014. **5**: p. 3186.
97. Kumar, A. and M. Khandelwal, *Amino acid mediated functionalization and reduction of graphene oxide - synthesis and the formation mechanism of nitrogen-doped graphene.* New Journal of Chemistry, 2014. **38**(8): p. 3457-3467.
98. Ma, Y., et al., *Extraordinary improvement of ablation resistance of carbon/phenolic composites reinforced with low loading of graphene oxide*. Vol. 167. 2018.
99. Plimpton, S., *Fast Parallel Algorithms for Short-Range Molecular Dynamics.* Journal of Computational Physics, 1995. **117**(1): p. 1-19.
100. Berens, P.H. and K.R. Wilson, *MOLECULAR-DYNAMICS AND SPECTRA .1. DIATOMIC ROTATION AND VIBRATION.* Journal of Chemical Physics, 1981. **74**(9): p. 4872-4882.
101. Guillot, B., *A MOLECULAR-DYNAMICS STUDY OF THE FAR INFRARED-SPECTRUM OF LIQUID WATER.* Journal of Chemical Physics, 1991. **95**(3): p. 1543-1551.
102. Bornhauser, P. and D. Bougeard, *Intensities of the vibrational spectra of siliceous zeolites by molecular dynamics calculations. I. Infrared spectra.* Journal of Physical Chemistry B, 2001. **105**(1): p. 36-41.
103. Gaigeot, M.P. and M. Sprik, *Ab initio molecular dynamics computation of the infrared spectrum of aqueous uracil.* Journal of Physical Chemistry B, 2003. **107**(38): p. 10344-10358.
104. Thomas, M., et al., *Computing vibrational spectra from ab initio molecular dynamics.* Physical Chemistry Chemical Physics, 2013. **15**(18): p. 6608-6622.
105. Braun, E. *Open Source Code: Calculating an IR Spectra from a LAMMPS Simulation*. 2016 [cited 2018 Oct. 25, 2018]; Available from: https://zenodo.org/record/154672#.W9HlQ6fMwlK.
106. Araujo, M.P., et al., *Tuning the surface chemistry of graphene flakes: new strategies for selective oxidation.* Rsc Advances, 2017. **7**(23): p. 14290-14301.
107. Bagri, A., et al., *Structural evolution during the reduction of chemically derived graphene oxide.* Nature Chemistry, 2010. **2**(7): p. 581-587.

108. Dimiev, A.M., L.B. Alemany, and J.M. Tour, *Graphene Oxide. Origin of Acidity, Its Instability in Water, and a New Dynamic Structural Model.* Acs Nano, 2013. **7**(1): p. 576-588.
109. Kumar, P.V., et al., *Scalable enhancement of graphene oxide properties by thermally driven phase transformation.* Nature Chemistry, 2014. **6**(2): p. 151-158.
110. Szabo, T., O. Berkesi, and I. Dekany, *DRIFT study of deuterium-exchanged graphite oxide.* Carbon, 2005. **43**(15): p. 3186-3189.

Chapter 4: Atomistic Computational Studies of Cellulose: Structure, Property and Process*

4.1 Introduction

Cellulose is the basic building block of algae, bacteria, plants and many other natural biomaterials. It is the most abundant and widespread natural resource to civilization, with an annual production of about 700 billion tons. Owing to properties such as renewability, sustainability, low cost, tunable mechanical strength, high biodegradability and excellent biocompatibility, cellulose has been widely used in biofuel productions,[1, 2] energy related applications,[3-6] biomedical engineering,[7-15] paper and construction industry.[16-20] To convert raw cellulose into fine chemicals and materials, various treatments have been proposed, which are classified into categories such as mechanical treatments including milling,[21, 22] grinding/refining,[23-25] high-pressure homogenizers,[26-29] cryocrushing,[27, 30, 31] and high intensity ultrasonic process;[32-34] chemical treatments[32, 35-43] through oxidizing agents, alkali, acid, and organic solvents; hydrolysis treatments[35, 44-64] via the utilization of dilute acid, concentrated acid, enzyme, and autohydrolysis; pyrolysis treatments[65-69] with steam, hydrothermolysis, or wet oxidation, and other electrical and biological treatments.[70-79]

Significant efforts and remarkable progresses have been achieved and summarized regarding fundamental understanding of cellulose structures,[4, 47, 80-85] the physical and chemical properties[3, 4, 47, 83, 84, 86-88] and corresponding characterization methods.[89-92] Reviews are also available for experimental studies of cellulose dissolution/interactions,[93, 94] cellulose degradation/conversion via enzymes,[95, 96], catalysis,[97-102] hydrolysis[99, 103-105] and pyrolysis processes,[104, 106] as well as numerous cellulose applications.[3, 4, 15, 82, 85, 87,

*Qiao, Q., C. Liu, X. Li, and L. Huang, Atomistic Computational Studies of Cellulose: Structure, Property and Process. Manuscript submitted for publication.

88, 91, 107-112] From the theoretical point of view, reports are available regarding model developments of cellulose microfibril and plant cell wall,[113] mathematical models for cellulose plant growth,[114] computational studies of the decomposition of lignocellulosic materials (cellulose, hemicellulose and lignin) via catalyzes, enzyme, pyrolysis and dissolution methods,[115, 116] and computational NMR predictions of carbohydrate materials.[117] Despite the knowledge, a molecular level understanding of how cellulose structure transforms under different treatments and how its property could be fine-tuned accordingly, is still incomplete.

It is also worth noting that producing cellulose-based advanced materials via subtle treatment strategies, instead of breaking cellulose bond and structure harshly, has been brought to a new horizon in the past decade. The effective manipulation of inherent structure and hydrogen bonding (HB) networks can significantly facilitate cellulose utilization. For example, Song and co-workers demonstrated a subtle two-step treatment to obtain advanced materials from cellulose resources. They processed natural wood to firstly remove lignin and hemicellulose, followed by a mechanical compressing to fine-tune properties of the remaining cellulose. The transformed wood, mostly the structurally manipulated cellulose, is mechanically more than 10 times stronger than steel.[36] Similar strategies have been also adopted to produce compressible carbon sponges and activated carbon with a high surface area.[37, 118-121]

While cellulose utilization depends critically on the effective and selective modification of characteristic structures, this comprehensive review examines existing atomistic computational studies of cellulose, revealing the structural-lead property evolution and constructing the relationship of cellulose martials, treatment conditions and atomistic modeling techniques. In particular, we outline the state-of-the-art understanding of cellulose structures, and discuss in details cellulose interactions, dissolutions and decompositions via computational methods of

quantum mechanics (QM), *ab initio* density functional theory (DFT) calculation, *ab initio* molecular dynamics (AIMD), molecular dynamics (MD) and reactive molecular dynamics (RxMD) simulations. In addition, cellulose characterizations, beneficial to validate and support computational results, are also briefly summarized. We anticipate this overview provides a clear theoretical insight to complex structures and competing interactions of cellulose, which could shed a light on fundamental understandings of similar systems of biomolecules, polymers and surfactants.

4.2 Structure and Computational Model of Cellulose

Cellulose is a linear polysaccharide of repeating D-glucose units, $(C_6H_{10}O_5)_n$. Depending on cellulose resources, the degree of polymerization (DP), which is the number of anhydroglucose units, varies from 10,000 to 15,000.[84] Natural cellulose has a complex structure, with coexisting crystalline and amorphous regions. Different cellulose polymorphs have been also reported under different conditions. Over the past decades, unit cell parameters and crystallinity of cellulose polymorphs have been investigated by X-ray (XRD), electron and neutron diffraction techniques.[122] In general, cellulose crystalline allomorphs are classified into the following categories[123]: cellulose I, also known as native cellulose, including cellulose Iα and Iβ; cellulose II; cellulose III, which includes cellulose III_I and III_{II}; cellulose IV, including IV_I and IV_{II}. Table 5 summarizes unit cell parameter of cellulose polymorphs from available experimental and computational studies. It is worth noting that cellulose IV_I is slightly distorted from cellulose I, not a genuine allomorph.[124, 125] Despite the lattice and conformation difference, as shown in Figure 13 (a), all cellulose polymorphs are composed of glucose units that are bonded with β-1,4-glycosidic linkages. The hydroxyl groups interact with each other and form intra- and inter HBs,

stabilizing the parallel chain conformation and maintaining cellulose structures and properties. Figure 13 (b) illustrates a characteristic HB network of cellulose Iβ, and Figure 13 (c) demonstrates the interconversions between different cellulose polymorphs.

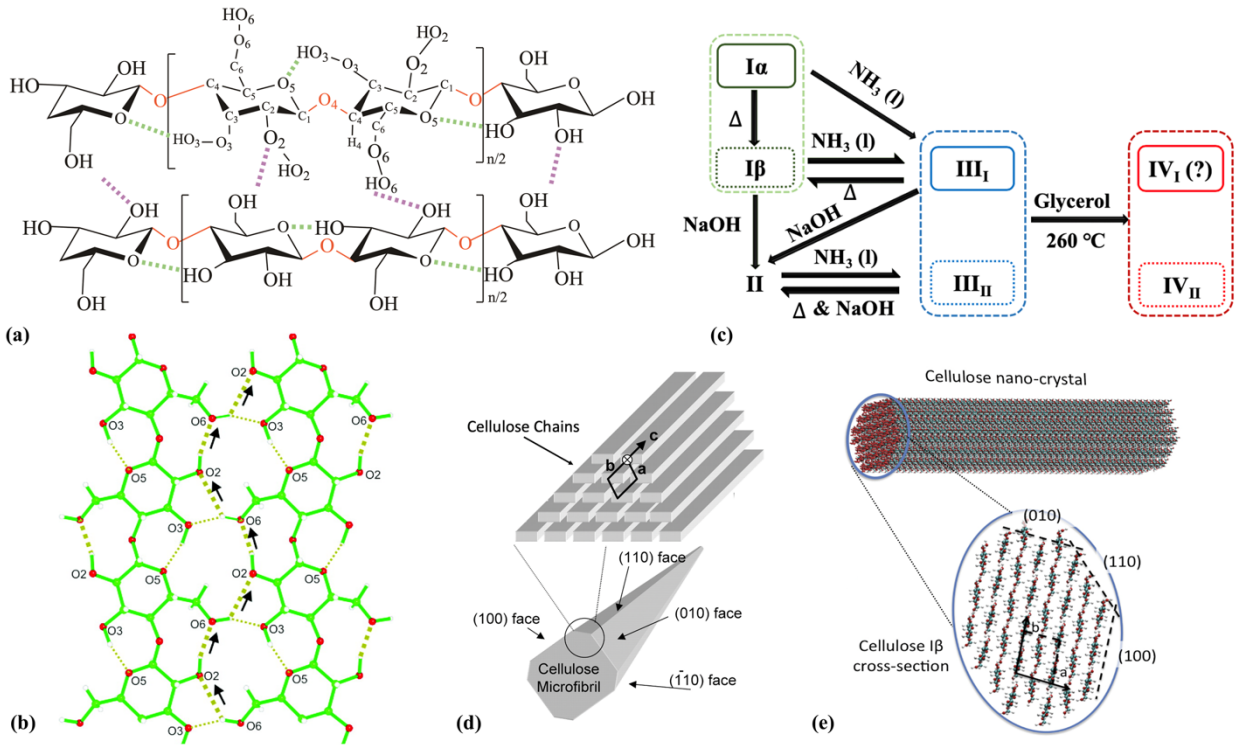

Figure 13. (a) A representative structure of cellulose with intra- and intra-hydrogen bonds, with the typical structural angles, φ= O5-C1-O4-C4 , and ψ=C1-O4-C4-C5; (b) The proposed cooperative hydrogen bonds network in cellulose Iβ from Nishiyama[126] (thick dotted lines) and the O6-H···O3 linkage (thin dotted lines); (c) Interconversions between cellulose polymorphs; (d) cellulose Iα[127] and (e) Iβ microfibril[128] with different exposed surfaces. Reproduced with permission from refs 126, 127 and 128. Copyright 2008 American Chemical Society, 2003 National Academy of Sciences and 2019 Elsevier, respectively.

As the native form of cellulose, cellulose I has two crystal phases, namely, cellulose Iα and Iβ. The two phases coexist in cellulose fiber and their ratio varies according to different cellulose resources. It is reported that cellulose Iα is predominant in bacteria and algae, while cellulose Iβ

dominates in plants such as wood and cotton.[129, 130] Nishiyama et al. reported XRD and neutron fiber diffraction results of lattice parameter, atomic coordinates and HB patterns of cellulose Iα[131] and Iβ.[132] Cellulose Iα is a triclinic structure while cellulose Iβ is monoclinic. Details of unit cell parameters are available in Table 5 and Table 6, which are widely referenced to construct computational cellulose models. Langan and co-workers studied cellulose II lattice parameters via XRD and neutron fiber diffractions.[133, 134] Compared with cellulose I, cellulose II has antiparallel chains and the HB patterns are significantly different. When cellulose I is treated by NaOH solutions, it could be converted into cellulose II.[135],[136]

Cellulose III can be obtained by liquid ammonia treatment[137, 138]: III_I and III_{II} are resulted from cellulose I and cellulose II, respectively. The reversible interconversion is dominated by thermal or hydrothermal treatments.[139] Two sets of lattice parameters of cellulose III_I are available: the two-chain model from Sarko[140] and the one-chain monoclinic unit by Wada.[141] According to molecular simulation results of Ford and co-workers,[142] Wada's model is energetically more favorable. As for cellulose III_{II}, the structural detail is still under debate.[143] For example, Sarko et al.[140] suggested that cellulose III_I and III_{II} share the same lattice parameter, but Wada and co-workers[144] argued that cellulose III_{II} is a disordered phase of cellulose III_I or other cellulose crystals. Cellulose IV was firstly identified by Hutino and Sakurada[145] in their XRD study of heat treated cellulose I with glycerol at 260 ℃. A detailed summary of the preparation and products of cellulose IV is available from Kulshreshtha.[146] Recent studies from Wada et al.[124] argued that cellulose IV_I is more of a distorted form of cellulose I rather than a genuine allomorph. Later, Newman[125] performed XRD simulations of cellulose IV_I and IV_{II} and confirmed that: (a) cellulose IV_I is a distorted form of cellulose Iβ; (b) little is previously known about cellulose IV_{II} but it is distinctly different from cellulose Iβ. More

details and discussions on cellulose allomorphs and their structural difference are available in the reference.[122, 123, 147-149]

It is worth noting that cellulose microfibrils are also widely used as cellulose models. In nature, cellulose chains form crystalline microfibrils with either a triclinic (cellulose Iα) or a monoclinic (cellulose Iβ) geometry.[128, 150] The surface of cellulose microfibrils could be elucidated from experiments. For example, the triclinic (1 0 0)/monoclinic (1 1 0) surface, the monoclinic (1 $\bar{1}$ 0) surface, and the triclinic (1 1 0)/monoclinic (2 0 0) surface have been identified from native cellulose forms.[127, 151, 152] Example of cellulose Iα and Iβ microfibrils are illustrated in Figure 13 (d) and (e), respectively.

Table 5. Calculated unit cell parameters of cellulose polymorphs from published computational studies.

	Method	a (Å)	b (Å)	c (Å)	α (°)	β (°)	γ (°)	T(K)	Ref.
Iα	LDA	5.71	6.48	10.24	118.6	115.1	81	0	Li et al.[153]
Iα	PBE	6.38	7.03	10.54	115.4	113.2	76	0	Li et al.[153]
Iα	DFT (PBE-D2)	5.97	6.63	10.47	116.9	114.3	80.7	0	Li et al.[153]
Iα	MD (CHARMM)	6.57	5.87	10.42	115	113	91	EM[a]	Reiling[154] and Marhofer et al.[155]
Iα	MD (CHARMM)	7.09	6.31	10.42	115	113	91	300	Reiling[154] and Marhofer et al.[155]
Iα	MM (COMPASS)	5.51	7.02	10.27	119	112	82	EM[a]	Eichhorn et al.[156]
Iα	MM (COMPASS)	6.78	5.66	10.42	119	113	81	EM[a]	Eichhorn et al.[156]
Iα	MM (COMPASS)[b]	5.76	7.1	10.44	118	118	82	EM[a]	Eichhorn et al.[156]
Iα	MM (COMPASS)[b]	7.11	5.69	10.45	118	117	82	EM[a]	Eichhorn et al.[156]
Iα	MD (GLYCAM06)	6.89	5.83	10.75	120.4	110.6	81.7	300	Maurer et al.[157]
Iα	MD (GROMOS)	6.661	6.241	10.47	114.9	113.3	78.66	300	Chen et al.[158]
Iα	MD (Opt. GROMOS)	6.481	5.954	10.48	116.3	114	81.43	300	Chen et al.[158]
Iα	Packing	6.3	6.9	10.36	113	121	76	EM[a]	Viëtor et al.[159]

Iβ	LDA	7.41	7.94	10.24	90	90	96.2	0	Li et al.[153]
Iβ	DFT (PBE)	-[c]	8.27	10.54	90	90	94.7	0	Li et al.[153]
Iβ	DFT (PBE-D2)	7.85	8.18	10.47	90	90	96.6	0	Li et al.[153]
Iβ	DFT (PBE)	8.7	8.23	10.46	90	90	95.5	0	Bučko et al.[160]
Iβ	DFT (PBE-D2)	7.65	8.14	10.39	90	90	96.8	0	Bučko et al.[160]
Iβ	DFT-D2	7.78	8.2	10.38	90	90	96.5	0	Lee et al.[161]
Iβ	DFT (PBE-D2)	7.54	8.14	10.39	90	90	96.4	0	Lee et al.[162]
Iβ	DFT (PBE-D2)	7.53	8.4	10.35	90	90	100	0	Lee et al.[162]
Iβ	DFT (PBE-D2)	7.56	8.13	10.39	90	90	96.7	0	Dri et al.[163]
Iβ	MM (COMPASS)	7.56	8.05	10.43	90	90	98	EM[a]	Eichhorn et al.[156]
Iβ	MM (COMPASS)	8.14	8.03	10.44	91	76	89	EM[a]	Eichhorn et al.[156]
Iβ	MM (COMPASS)[b]	7.43	8.53	10.48	94	92	99	EM[a]	Eichhorn et al.[156]
Iβ	MM (COMPASS)[b]	7.44	8.5	10.49	91	91	99	EM[a]	Eichhorn et al.[156]
Iβ	MD (GROMOS)	7.6	8.1	10.4	90	90	84	300	Kroon-Batenburg et al.[164]
Iβ	MD (GROMOS)	7.6	8.1	10.4	90	90	96	300	Kroon-Batenburg et al.[164]
Iβ	MD (GROMOS)	8.37 ± 0.002	8.168± 0.002	10.523± 0.002	89.97± 0.02	89.97± 0.03	90.92± 0.03	300	Bergenstråhle et al.[165]
Iβ	MD (GROMOS)	9.005± 0.0055	8.659± 0.0069	10.470± 0.0002	77.62± 0.36/103.17± 1.17	78.30± 1.11/101.41± 0.45	88.30 ± 3.04	500	Bergenstråhle et al.[165]
Iβ	MD (GROMOS)	8.34	8.17	10.5	90	90	90	300	Chen et al.[166]
Iβ	MM (GROMOS)	7.681	8.027	10.387	90	90	92.8	0	Molnar et al.[167]
Iβ	MD (GROMOS)	8.42	8.14	10.43	90	90	92.9	300	Chen et al.[158]
Iβ	MD (Opt. GROMOS)	7.799	8.089	10.44	89.99	90	94.17	300	Chen et al.[158]
Iβ	MD (CHARMM)	8.02	8.12	10.39	90	90	97.5	EM[a]	Reiling[154] and Marhofer et al.[155]
Iβ	MD (CHARMM)	8.13	8.03	10.39	90	90	97.5	300	Reiling[154] and Marhofer et al.[155]
Iβ	MD (CHARMM)	8.47	8.11	10.51	90	90	90	300	Matthews et al.[168]
Iβ	MD (CHARMM)	7.96	8.35	10.44	90	90	98.3	300	Matthews et al.[169]
Iβ	MD (GLYCAM06)	7.74	8.24	10.8	90	90	97.6	300	Djahedi et al.[170]
Iβ	MM (CVFF1)	7.652	8.136	10.615	90	90	96.8	EM[a]	Yao et al.[171]

Iβ	MM (CVFF2)	7.787	8.201	10.388	90	90	96.2	EM[a]	Yao et al.[171]
Iβ	MM (CVFF3)	8.188	7.898	10.607	90	90	95.1	EM[a]	Yao et al.[171]
Iβ	MD (ReaxFF)[d]	8.549	8.922	10.814	89.99	90.03	99.77	300	Dri et al.[172]
Iβ	MD (ReaxFF)[d]	8.731	8.989	10.736	90.02	90	106.24	300	Dri et al.[172]
Iβ	MD (ReaxFF)[d]	8.214	8.85	10.76	90.07	90.19	103.94	300	Dri et al.[172]
Iβ	MD (ReaxFF)[d]	8.394	8.33	10.536	103.8	86.26	88.12	300	Dri et al.[172]
Iβ	MD (ReaxFF)[d]	7.802	8.552	10.615	89.7	90.14	100.09	300	Dri et al.[172]
Iβ	MD (ReaxFF)[d]	8.101	7.997	10.466	83.26	87.36	92.06	300	Dri et al.[172]
Iβ	MD (ReaxFF)[d]	7.377	7.718	10.557	90.03	90.02	88.61	300	Dri et al.[172]
Iβ	MD (ReaxFF)[d]	7.32	7.816	10.552	89.09	90.06	91.31	300	Dri et al.[172]
Iβ	MD (ReaxFF)[d]	7.32	7.816	10.552	89.09	90.06	91.31	300	Dri et al.[172]
Iβ	MD (GLYCAM06)	8.026	7.869	10.617	90.01	90.01	94.48	300	Dri et al.[172]
Iβ	MD (COMPASS)	7.8	8.2	10.3	88.3	88.7	92.1	300	Dri et al.[172]
Iβ	MD (ReaxFF)	7.786±0.016	8.203±0.017	10.382±0.062	90±0.01	90±0.01	90.88±0.74	300	Qiao et al.[173]
Iβ	MD (ReaxFF)	7.861±0.038	8.282±0.04	10.482±0.152	90±0.69	90±0.76	89.28±0.72	500	Qiao et al.[173]
Iβ	MD (ReaxFF)	7.876±0.029	8.298±0.031	10.503±0.116	90±19.64	90±18.34	86.02±0.54	800	Qiao et al.[173]
Iβ	MD (ReaxFF)	7.908±0.021	8.332±0.022	10.54±0.084	90±13.60	90±6.98	83.82±2.17	1000	Qiao et al.[173]
Iβ	MD (ReaxFF)	7.996±0.042	8.425±0.444	10.663±0.167	90±4.88	90±5.20	70.04±3.84	1100	Qiao et al.[173]
Iβ	MD (GLYCAM06)	7.9	8.4	10.75	85.1	90.2	102.2	300	Maurer et al.[157]
Iβ	MD (GLYCAM06)	7.63	8.23	10.8	89.99	89.99	97.17	298	Zhang et al.[174]
Iβ	MD (GLYCAM06)	8.11	8.28	10.78	90	89.96	98.33	500	Zhang et al.[174]
Iβ	MD (GLYCAM06)	7.62	8.23	10.8	89.69	90.2	97.32	298	Zhang et al.[174]
Iβ	MD (GLYCAM06)	7.61	8.2	10.76	90.27	90.45	94.2	298	Zhang et al.[174]
Iβ	MD (PCFF)	7.6	8.74	10.46	90.4	92.3	103.5	300	Mazeau et al.[175]
Iβ	MD (PCFF)	8.11	8.56	10.72	90	89.99	95.32	300	Mazeau[176]
Iβ	MD (PCFF)	7.81	8.51	10.78	90	90	92.08	300	Mazeau[176]
Iβ	MD (PCFF)	7.7	8.5	10.69	89.86	89.97	89.31	300	Mazeau[176]
Iβ	MD (PCFF)	7.91	8.53	10.74	89.67	89.9	93.73	300	Mazeau[176]
Iβ	MD (PCFF)	7.71	8.7	10.67	90	90	102.13	300	Mazeau[176]
Iβ	MD (PCFF)	8.11	8.56	10.72	90	90	95.31	300	Mazeau[176]
Iβ	MD (PCFF)	7.98	8.25	10.79	90.23	89.91	87.19	300	Mazeau[176]

Iβ	MD (PCFF)	7.95	8.77	10.57	90	90	100.67	300	Mazeau[176]
Iβ	MD (PCFF)	7.67	8.51	10.6	89.78	90.26	94.33	300	Mazeau[176]
Iβ	MD (PCFF)	6.82	9.48	10.48	90.03	90.6	91.74	300	Mazeau[176]
Iβ	MD (Custom)	8.06	8.51	10.4	90.1	90.6	96.6	300	Neyertz et al.[177]
Iβ	Packing (MM3)	7.5	8.7	10.36	90	90	94.1	EM[a]	Viëtor et al.[159]
II	CPMD	7.8	9.31	10.74	90	90	116.6	298	Ganster et al.[178]
II	MD (GROMOS)	8.058	9.38	10.41	90.1	90.05	112.7	300	Chen et al.[158]
II	MD (Opt. GROMOS)	8.146	8.628	10.39	90.02	90.01	114	300	Chen et al.[158]
II	MD (GLYCAM06)	8.4	8.92	10.75	90	90	109.8	300	Djahedi et al.[170]
II	MD (GLYCAM06)	8.02	9.32	10.77	90.2	91.6	121.5	300	Zhang et al.[174]
II	MD (GLYCAM06)	8.3	8.77	10.73	89.7	91.2	117.1	300	Zhang et al.[174]
II	MM (COMPASS)	6.93	10.22	10.38	90	90	120	EM[a]	Eichhorn et al.[156]
II	MM (COMPASS)[b]	7.44	10.86	10.41	90	90	127	EM[a]	Eichhorn et al.[156]
II	MD (CHARMM)	8.14	9.06	10.34	90	90	114	EM[a]	Marhofer et al.[155]
II	MD (CHARMM)	8.25	8.92	10.34	90	90	114	300	Marhofer et al.[155]
II	MD (CHARMM)	8.02	9.03	10.34	90	90	115.3	EM[a]	Marhofer et al.[155]
II	MD (CHARMM)	7.92	9.01	10.34	90	90	115.3	300	Marhofer et al.[155]
II	MD (GROMOS)	8.1	9	10.3	90	90	120	300	Kroon-Batenburg et al.[164]
II	MD (GROMOS)	8.1	8.9	10.3	90	90	119	300	Kroon-Batenburg et al.[164]
III_I	MD (GLYCAM06)	4.42	8.09	10.76	90	90	93.3	300	Djahedi et al.[170]
III	MD (GROMOS)	5.008	8.192	10.06	89.99	89.99	111.9	300	Chen et al.[158]
III	MD (Opt. GROMOS)	4.715	8.203	10	90	89.97	111.9	300	Chen et al.[158]

[a] Energy minimization.
[b] Without the hydrogen bonds in the simulations
[c] Not binding
[d] Different versions of ReaxFF force field were tested.

Table 6. Measured unit cell parameters of cellulose polymorphs from published studies.

	Method	a (Å)	b (Å)	c (Å)	α (°)	β (°)	γ (°)	T (K)	Ref.
I	XRD	8.17	7.86	10.38	90	90	97	-	Gardner et al.[179]
Iα	Electron diffraction	6.74	5.93	10.36	117	113	81	293	Sugiyama et al.[180]

Iα	XRD & NFD	6.717	5.962	10.4	118.08	114.8	80.37	293	Nishiyama et al.[131]
Iβ	XRD & NFD	7.784	8.201	10.38	90	90	96.5	293	Nishiyama et al.[132]
Iβ	XRD SM	7.85	8.27	10.38	90	90	96.3	-	Finkenstadt et al.[181]
Iβ	XRD GB	7.82	8.16	10.32	90	90	97.5	-	
Iβ	XRD	7.78	8.19	10.34	90	90	96.5	-	Woodcock et al.[182]
Iβ	XRD	7.88	8.32	10.39	90	90	95.9	-	Okano et al.[183]
Iβ	XRD	7.85	8.14	10.34	90	90	96.6	-	Sarko et al.[184]
Iβ	Electron diffraction	7.94	8.39	10.58	90	90	98	173.15~233.15	Honjo et al.[185]
Iβ	Electron diffraction	8.01	8.17	10.36	90	90	97.3	293	Sugiyama et al.[180]
Iβ	XRD	7.71	8.34	10.37	90	90	97.6	-	Takahashi et al.[186]
Iβ	XRD	7.9	8.35	10.3	90	90	96	-	Meyer et al.[187]
Iβ	XRD	7.76	8.19	10.38	90	90	96.51	100	Langan et al.[188]
Iβ	XRD	7.83	8.19	10.38	90	90	96.55	298	Langan et al.[188]
Iβ	XRD & NFD	7.64	8.18	10.37	90	90	96.54	15	Nishiyama et al.[126]
Iβ	XRD & NFD	7.76	8.2	10.37	90	90	96.62	295	
Iβ[a]	XRD	8.1	8	10.3	90	90	95	-	Thomas et al.[189]
Iβ[b]	XRD	7.88	8.3	10.36	90	90	94.5	-	Lee et al.[161]
II	NFD	8.01	9.04	10.36	90	90	117.1	-	Langan et al.[133]
II	XRD	8.01	9.03	10.31	90	90	117.1	-	Langan et al.[134]
II	XRD	8.01	9.04	10.36	90	90	117.1	-	Kolpak et al.[190]
II	XRD	8.02	8.99	10.36	90	90	116.6	-	Kolpak et al.[191]
II	Synchrotron X-ray	8.01	9.02	10.34	90	90	117.11	100	Langan et al.[188]
II	Synchrotron X-ray	8.03	9.04	10.35	90	90	117.11	298	
II	XRD	7.96	9.09	10.31	90	90	117.3	-	Stipanovic et al.[192]
II	XRD	7.92	9.08	10.34	90	90	117.3	-	Wellard[193]
III_I	XRD and NFD	4.45	7.85	10.31	90	90	105.1	-	Wada et al.[141]

[a] Annealed Celery collenchyma (Cellulose Iβ)
[b] Celery collenchyma (Cellulose Iβ)

4.3 Molecular Mechanics Studies of Cellulose

Considering the relative complex structure of cellulose and the expensive computational cost of QM methods, Molecular dynamics (MD) has become the method of choice to study cellulose at the atomic scale. MD simulations provide the dynamics of atoms through Newton's

equations of motion. The equations are discretized in time and integrated to obtain trajectories, that is, the positions and velocities of atoms as functions of time. The trajectory records the system evolution at specific temperature and pressure conditions, and can be analyzed to obtain structural, dynamical, thermal, and mechanical properties of the system. In recent years, MD simulations of cellulose systems have been performed with reliable interatomic interactions. The results have been validated through detailed comparison with experimental measurements and QM calculations. The emergence of supercomputers and highly efficient parallel algorithms also significant boost atomistic aspects of cellulose systems. In the past decade, massively parallel computers delivering petaflop (10^{15} floating point operations per second) performance have become available. When combined with highly efficient, linearly scaling parallel algorithms, MD simulations can handle systems of 10^9 atoms and archive timescales on the order of milliseconds. Figure 14 shows the distribution of about 330 MD studies of cellulose systems, from the twist and chirality configurational changes of cellulose crystals, the structural conversions between cellulose polymorphs, the HB network patterns to the thermal stability of cellulose in gaseous and aqueous solutions. A great deal of research interest (~ 34% of the total 330 papers) is about the behavior of cellulose in water, alkaline and organic solutions and environment friendly ILs. This is due to the fact that cellulose is normally processed in solutions. A fundamental understanding of structural and property change of cellulose in solutions could promote cellulose conversion and optimize the industry process. For the same reason, it has been a hot research topic on the interaction, adsorption, and interfacial properties of cellulose when mixed with other molecules or solvents. In the native form, cellulose is surrounded by hemicellulose, lignin and water. Thus, the interfaces between water and cellulose microfibrils, and the exposure of hydrophilic/hydrophobic surface will certainly matter. Understanding cellulose/enzyme interaction is also critical. This is because the

cellulose degradation via enzymic hydrolysis is still one of the most widely adopted treatment in industry. Due to the complex structure of enzyme and protein, MD becomes the affordable atomistic computational method for this purpose. In this section, we also summarize computational studies to improve cellulose properties via nanocomposites. It is also known that interatomic potential, also known as force field, is the essential input to MD simulations. The degree to which the results of MD simulation represent the properties of real materials is determined by how reliable the force field is. Over the years, a number of force fields have been adopted and reported to provide accurate descriptions to certain cellulose properties. Yet, developing and parameterizing better force fields require more future efforts.

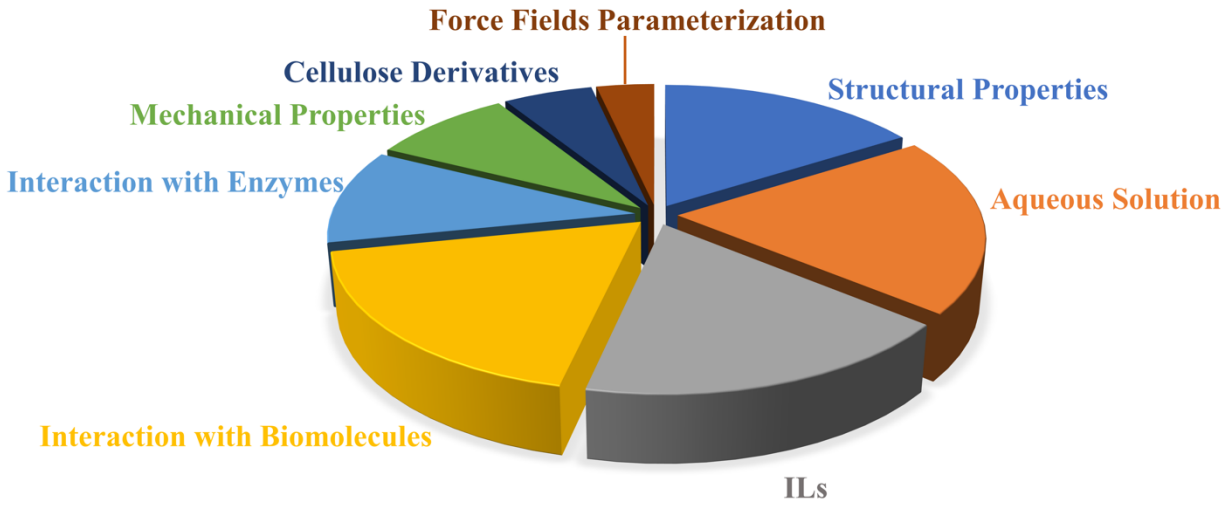

Figure 14 . The analysis and topic distribution of 330 MD studies of cellulose.

4.3.1 Force Fields for Cellulose Systems

The accuracy of force fields is critical to the quality of cellulose MD simulations, from the calculation of unit cell parameters,[158, 194] see also Table 5, to the energy and conformation analysis of cellulose.[195] Despite different force fields predict slightly different unit cell

parameters to a same cellulose polymorph, most MD calculations produce satisfactory results, which are comparable to experimental XRD measurements. For cellulose MD studies, it is critical to benchmark the adopted force field and make sure the calculations generate correct results. Figure 15 shows the analysis regarding the choice of force fields for 330 cellulose MD studies. As the distribution shows, the CHARMM force field is most recommended for cellulose/enzyme systems. For the study of structure, interaction and adsorption of cellulose, GROMOS, CHARMM and GLYCAM06 are popular. AMMBER is widely adopted for the behavior of cellulose in aqueous and ionic liquid solutions, while GLYCAM06 and OPLS-AA force fields are popular for the study of cellulose dissolution in ILs. Other force fields such as CSFF[195-198], CVFF,[171, 199] MM2,[200-203] MM3,[142, 204] CLAYFF,[205] CFF91[206], as well as specially customized force fields[177, 207-211] are also reported for cellulose composites and various calculations of cellulose properties. For example, Yong et al.[171] tested COMPASS, Deriding, UFF, CVFF and PCFF force fields for cellulose unit cell, and concluded that CVFF force field has the best prediction compared with experiments. On the other hand, Bazooyar et al.[212] reported that, compared with Deriding and UFF, COMPASS force field is more suitable for the study of cellulose dissolution: it could successfully predict the preferred *syn* conformation of cellobiose in water. The MD simulations also agree with *ab initio* DFT method. Interestingly, Wang et al.[213] also reported that COMPASS force field is the most proper force field for mechanical properties and solubility studies of amorphous cellulose (DP $\geq$ 10). Similarly, the simulation of cellulose Iβ microfibrils at high temperatures has been benchmarked with three force fields, namely CHARMM, GLYCAM06 and GROMOS.[169, 174, 214-217] Those studies show that CHARMM and GLYCAM06 provide consistent results with experimental data.

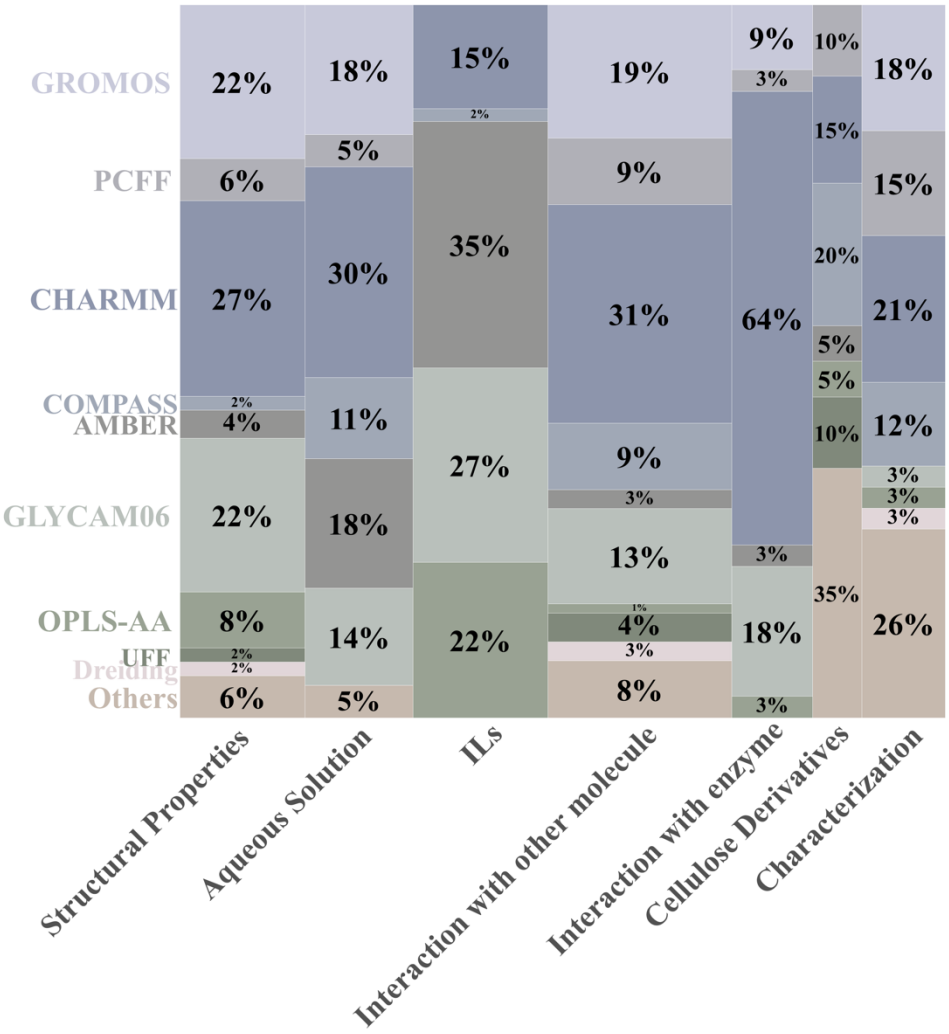

Figure 15. The analysis of 330 cellulose MD studies and the choice of force fields.

4.3.2 Cellulose Model and System Size

The choice of cellulose model and the system size are important to MD simulations. Subject to available computational resources, it is wise to always run test calculations and maintain a balance between the system size and the accessible trajectory. For cellulose systems involving macromolecules and complex structures such as enzymes and proteins, a trajectory time of milliseconds is required to capture the dynamics of the system.[218] Recent progresses in GPU-based calculations bring positive perspectives of calculating cellulose systems at larger spatial and

temporal scales. To most current MD studies, cellulose crystalline models with 18, 24 and 36 chains are commonly adopted for cellulose microfibrils. It has been justified that models with 18 and 24 cellulose chains could reproduce structural characteristics of native cellulose from wide-angle X-ray scattering (WAXS), small-angle neutron scattering (SANS) and solid-state nuclear magnetic resonance (ssNMR).[189, 219] Therefore, it is popular to use 18~24 chains to represent cellulose microfibrils with different shapes of cross-sections, such as square, hexagonal and others[113, 220-223] Cellulose models with 36 chains and large DP values were adopted to study the recalcitrant crystalline core of plant cell wall microfibrils,[224] as well as other cellulose microfibrils.[165, 168, 169, 174, 217, 225-231]

Figure 16 shows a summary of typical number of chains and DP values for cellulose MD studies reviewed in this section. A large cellulose model is consisted of 144 chains and a DP value of 400, but such system is computationally very expensive. Most models use 2~36 chains and 2~40 DP, which are appropriate for small cellulose crystals and microfibrils. It is worth pointing out that cellulose with small DP values is soluble in water. Therefore, the study of cellulose in aqueous solutions usually use 1~2 for the DP of cellulose models. As for the study of cellulose allomorphs interconversion, longer cellulose chains are preferable. When it comes to complex systems (ILs, enzymes and proteins), usually a simple cellulose model, one chain with 1~20 DP, will be appropriate. For cellulose property calculations, such as elastic modulus, XRD, IR and NMR, various cellulose models have been adopted, with a range of 1~40 in chains and DP values.

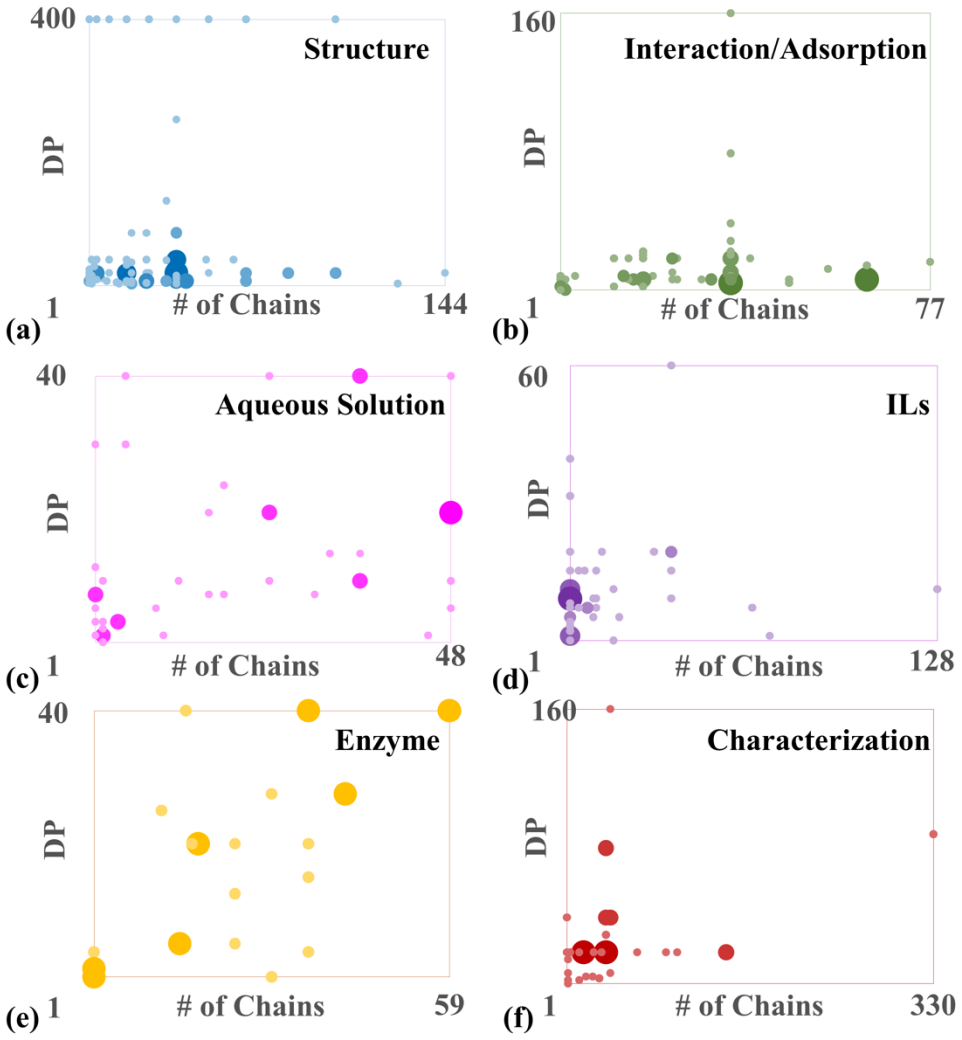

Figure 16. A summary of typical number of chains and DP values for cellulose models via MD simulations. The size of the dots represents the frequency, while the colors are just to better distinguish the six cellulose properties of interest.

4.3.3 Structural Properties of Cellulose

Using the experimental input of cellulose structural information, for instance, the lattice parameter and atomic coordinates from XRD and neutron fiber diffraction experiments[122-125, 131-134, 140, 141, 144-149], MD simulations have been designed to capture the crystalline/amorphous structural changes[175, 232-235], the allomorphs interconversions[216,

236], the HBs network[176, 230, 237], and the thermal properties of cellulose systems.[165, 166, 174, 207, 217, 238-241]

Heiner et al.[242] adopted GROMOS87 force field and performed MD simulations to study cellulose Iα and Iβ. They found that cellulose Iβ is structurally more stable than Iα, which agrees with experimental results,[243] with more interchain HBs observed in cellulose Iβ. Their calculated ^{13}C NMR shift is due to the dihedral angle of C-6, and the OH-stretching region from the calculated IR plots can be used to estimate the number of different HBs in the cellulose system. Kroon-Batenburg et al.[164] studies the crystalline cellulose Iβ and II via GROMOS force field. They reported that the cellulose Iβ structure agrees with the previous parallel-down model.[179] Cellulose layers are parallel and hydrophobic, with all the OH groups in *tg* conformation. Two intramolecular HBs that paralleled to the 1-4-β bond and two intralayer HBs were identified in the cellulose Iβ units, forming the HB networking.

The HB network is critical to maintain cellulose crystal structures. Therefore, the fundamental understanding of HBs could help to design better processes to stabilize or breakdown cellulose materials. Mazeau et al.[176] performed MD simulations to study the HB network of cellulose Iβ crystal. Similarly, Agarwal et al.[244] calculated the infrared radiation (IR) of cellulose Iβ HB network. The results agreed with experimental measurements,[132] revealing a predominant intrachain HBs at 300-400 K and a weaker interchain HB network at 450-500 K. Those MD simulations conclude that it is easier to form a 3-D HB network at high temperatures, which in return promotes the structural stability of cellulose Iβ, as previously discussed by other studies.[165, 173, 217, 245, 246] Chen et al.[247] studied the HB patterns of cellulose II and III_I, and also calculated the fiber diffraction patterns of both cellulose models, which are consistent with experiments.[133, 141] Djahedi et al.[248] demonstrated how the HBs and covalent bonds

affect the stiffness of cellulose Iβ. Their MD simulation results revealed that the HBs contribute only about 12% to cellulose stiffness, but the HB network could significantly influence the modulus. For example, the HB network helps to stabilize cellulose Iβ structure during the deformation process, which eventually leads to a higher axial modulus.

Besides the study of pristine cellulose structures, MD simulations have been also applied in the study of cellulose polymorph interconversions. Hardy et al.[236] studied the interconversion between cellulose Iα and Iβ via CHARMM force field. The transition from metastable Iα to stable Iβ was reported to start from the chain torsional rotation and the breakdown of HB network. Based on the MD simulation results, they also proposed a break-slip model to describe the transition process. Bregado et al.[216] performed MD simulations with CHARMM force field to study the amorphization of cellulose Iα and Iβ under various temperatures. By the of analysis of HBs, calculated IR, lateral order index, radial distribution functions (g(r)), XRD and distribution of dihedral angle, they found that paracrystalline structures were similar in the temperature range of 380 to 700 K. Figure 17 (a) showed an example of calculated g(r) for crystalline, paracrystalline and amorphous cellulose. Their results also revealed that both cellulose Iα and Iβ became completely amorphous with lower DP, while paracrystalline core were observed in the structures with the increasing of degree of polymerization. Kulasinski et al.[249] investigated the conversions between crystalline, paracrystalline and amorphous cellulose. They proposed that paracrystalline cellulose is the intermediate from crystal to amorphous phase. The structure obtained from their quenching simulation protocol exhibits similar isotropic amorphous properties of experimental reports. Also, the crystal to amorphous phase transition was identified to occur at 450~550 K.

The thermal stability of cellulose has been also investigated via MD simulations. Bergenstråhle et al.[165] estimated lattice parameter changes of cellulose Iβ at high temperatures

via GROMOS 45a4 force field. A structural transition was observed at 450 K when the origin chains rotated around the helix axis and hydroxymethyl groups were transferred to a different conformation, as also discussed by Matthews.[217] Similarly, Zhang et al.[174] studied the thermal response of cellulose Iβ crystal via GROMOS 45a4 and GLYCAM06 force fields. They observed similar structural transition[165] in the temperature range of 475-500 K. They also reported that GLYCAM06 force field provides more consistent results with experiments at high temperatures. Tang et al.[238, 240, 241] improved the thermal stability of insulation paper cellulose by grafting polysiloxane. They found that a mass fraction of 6.5% polysiloxane can improve the thermal stability by 50 K[238, 240] in gaseous conditions and 60 K in micro-water environment.[241] They also reported a better thermal stability of the 5% nano-SiO_2-doped insulation paper cellulose.[239] As illustrated in Figure 17 (b), Diaz et al. [250] performed experiments and MD simulations to understand the thermal conductivity of cellulose Iβ nanocrystals (CNCs). They reported a thermal conductivity range of ~0.72-5.7 W m^{-1} K^{-1} for a single CNCs and ~0.22−0.53 W m^{-1} K^{-1} for CNCs films. The film thermal conductivity was reported to depend both on the DP of CNCs and the directions between heat flow and cellulose chain axis.

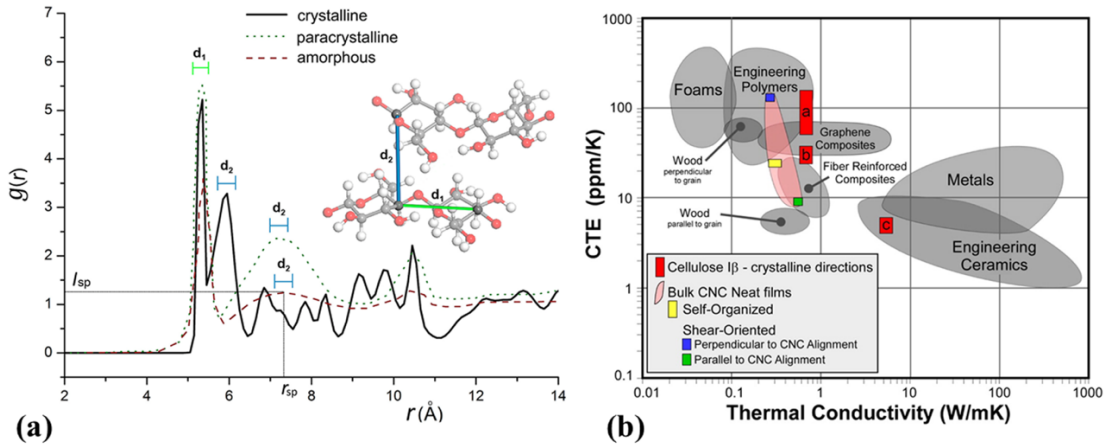

Figure 17. (a) An illustration of g(r) of C_4-C_4 pair for crystalline cellulose Iβ (DP=10) at 298 K. The d_1 and d_2 distances indicated the positions of the two first peaks along the r-axis. Inside this figure two cellulose chains are represented, in which an arbitrary C_4 atom (in dark gray color) connects by sticks with other nearest C_4 atoms. The sticks of d_1 and d_2 represent the symbolize distances rather than bonds between C4 atoms. The green stick connects C4 atoms where their distances contribute to the first peak of g(r) that located at d_1, whereas the blue stick those contributing to the second peak of g(r) that located at d_2. Profiles of this function for paracrystalline (green dotted line) and amorphous cellulose (wine dashed line) were extracted from Kulasinski and co-workers.[249] I_{sp} and r_{sp} stand for the intensity and distance of the second peak maximum in g(r), respectively;[216] (b) The Ashby plot of thermal response of cellulose Iβ (simulation results) and bulk CNC (experimental measurement) compared with other materials.[250] Reproduced with permission from refs 216 and 250. Copyright 2019 Elsevier B.V. and 2014 American Chemical Society.

4.4 RxMD Simulations of Cellulose

ReaxFF force field was initially developed by van Duin in 2001[251] to describe complex and large-scale reactive systems that contain many hundreds to several thousands of atoms. Due to the advantages that electronic/reaction details and large time/space scale computations can be achieved simultaneously, RxMD based on reactive force field (ReaxFF) has gained more and more attention for computational studies of complex systems, such as protein/DNA,[252, 253]

membrane fuel cell systems,[254] and very complicated coal structure and properties.[255, 256] In order to describe a continuous interaction pathway and allow bond formation or breaking of the system, ReaxFF adopts the concept of bond order to monitor structural evolution and identify adsorption and chemical reactions. This is different from classical force fields where the structural topology is consisted of bonds, angles, dihedrals and improper angles. It is worth pointing out that ReaxFF based RxMD simulations are generally one order slower than MD simulations with classical force fields, which is partly due to the expensive charge calculation at each step via the electronegativity equalization method (EEM) to determine the bond order of each atom of the system.[257-259] Yet, with parallel supercomputers, trajectories of up to microseconds could be archived for complex systems such as cellulose. In literature, ReaxFF based RxMD simulations are specialized in predicting structural evolution, tracing intermediates, and analyzing final products,[173, 260, 261]and are priority choices for reactive adsorption, dissociation and complex reactions.[262-264] More details of ReaxFF are available from recent reviews.[265-267]

During the past decade, ReaxFF force field parameters have been developed for cellulose, hemicellulose, lignin systems,[255, 267-271] and successfully described similar systems, such as complex long-chain polymers[272-274], coal and biomass materials.[255, 256] Despite the capability of handling large and complex systems, for most reported RxMD simulations of cellulose systems, the size of simulation box is usually on the order of 10 nm, which is still much smaller than the experimental sample of 50~500 nm.[84] In addition, we note that the quality of RxMD simulations defends exclusively on whether or not the ReaxFF force field has been parameterized for the system and investigated properties. For instance, Dri and co-workers[172] evaluated three sets of ReaxFF parameters[267, 270, 271] and compared with two classical force fields (COMPASS[275] and GLYCAM[276]) in the prediction of lattice parameters, elastic-

thermal behavior, and the anisotropy of cellulose Iβ. They concluded that the predictability of ReaxFF varies: the one developed by Chenoweth[267] is the best for reproducing lattice parameters of cellulose Iβ; the ReaxFF parameters from Rahaman[271] have the most accuracy for Young's Modulus along the chain direction. However, all three ReaxFF sets failed to predict the Young's Modulus in the transverse direction. When performing RxMD simulations with ReaxFF force field, one should benchmark the choice of system size and morphology, screen adsorption and reaction conditions, and carefully validate RxMD results with experimental findings and QM calculations if possible.

4.4.1 Structural and Mechanical Properties of Cellulose

Diaz and co-workers[277] adopted ReaxFF force field to study the coefficient of thermal expansion of self-organized and shear oriented cellulose Iβ nanocrystals. Instead of using one or two cellulose chains in QM calculations, RxMD can easily handle systems with tens of cellulose chains. Starting from experimental XRD results and reported unit cell parameters,[132] the elastic modulus of crystalline cellulose Iβ was reported to be 7.0 ± 1.7, 28.8 ± 2.9 and 139.5 ± 3.5 GPa along x, y and z directions.[278] RxMD simulations also predicted the transverse elastic modulus to be 5.1 ± 0.7 GPa, which agrees well with experiments.[279] It is also encouraging that ReaxFF force field can capture elastic differences at three directions, which is due to the directional strain and the inhomogeneous HB network of cellulose structures. RxMD simulations of frictional sliding on cellulose Iβ (110), $(1\bar{1}0)$ and (200) surfaces are also reported.[280] The model was consisted of two cellulose surfaces, with the bottom cellulose substrate fixed and the top cellulose surface mobile. The results reveal that the sliding velocity of the top cellulose surface has a negligible effect on friction, whereas the orientation of the contacting cellulose surfaces, the magnitude of normal load and the number of hydrogen bonds (N_{HB}) impact significant on the

friction between two cellulose surfaces. Other RxMD simulation was also reported for crystalline cellulose Iβ by the reactive empirical bond-order (REBO) potential.[281] The results showed that chain breakdown occurred in cellulose Iβ crystal, with an increasing number of free molecules of carbon, oxygen and hydrogen elements.[282] The damage of the cellulose structures results in the breakdown of glucose units and free molecules in the system, while the cross-linking and chain scission are less common.[283]

Other mechanical properties have been also reported by RxMD simulations. Our group recently reported the evolution of structure and mechanical properties of crystalline cellulose Iβ via isolated pyrolysis treatments from 300-1300 K.[173] The system was composed of 8 cellulose chains, each with 12 glucose monomers. Periodic boundary conditions were applied at all directions to mimic the bulk behavior of cellulose Iβ. Simulation results reveal that cellulose Iβ generally maintains the crystalline structure at temperatures below 1000 K, with noticeable corrugation and twist of the chains and the evolution of the HB network. The predicted Young's modulus is comparable to experiments and other computational studies. RxMD simulations also well captured the trend that Young's modulus decreases at temperature increase. It is also important to note that mechanical properties are sensitive to the adopted strain rate in those RxMD simulations. Wu and co-workers performed similar RxMD simulations for mechanical properties of crystal cellulose Iβ.[284] The simulation results reveal the highly anisotropic nature of cellulose Iβ, including elastic modulus, the Poisson's ratio, the yield and ultimate stress and strain.

4.4.2 Cellulose Decomposition

The pyrolysis of amorphous cellulose was investigated via RxMD for temperatures from 500 to 1400 K.[285] The cellulose was modelled by six long-chains that contained 60 units of 1,4-β-D-glucopyranoses ($C_{2160}H_{3612}O_{1800}$), in a cubic simulation box of 30.45 Å. GPU-enabled ReaxFF

MD (GMD-Reax) simulations were performed to investigate initial reactions of the pyrolysis process. The pyrolysis products identified from simulation trajectories are mainly glycolaldehyde, levoglucosan and water, agreeing well with experiments from temperatures of 673-1073K. The decomposition of amorphous cellulose was also reported as a function of the degrees of polymerization, DP = 8, 16, 32 and 64.[286] At the high temperature range of 1400 to 2000 K, the simulation revealed the breaking of 1−4-β bonds, which eventually leads to the decomposition of amorphous cellulose, producing products of glycolaldehyde, water, formaldehyde and formic acid. Similarly, Atmani et al. [287] performed RxMD simulations to investigate the decomposition of cellulose into kerogen. When cellulose Iβ was heated from 423 to 3502 K, the formation of kerogen and maturation were observed. Similar structural features were identified between formed kerogen and experimental mature type III kerogen. Those studies suggest that ReaxFF satisfactorily captures the nature of cellulose pyrolysis process.

Besides the dry pyrolysis where cellulose is the only initial species, the decomposition of cellulose/water mixtures have been also reported.[288] The simulation system was composed of water and 8 amorphous cellulose chains, each with 10 glucose units. Both water content (33 wt% and 66wt%) and temperature (1250 to 2000 K) were controllable parameters. The results demonstrated that water could enhance the decomposition of cellulose chains and increase the oxygenation of products. Also, higher temperatures seem to result in lower oxygenating effects of water. The co-pyrolysis process of seaweed polysaccharides and cellulose was also investigated.[289] By increasing the temperature from 300 K to 1273 K, main products of furans were reported of *Enteromorpha clathrata* (EN) polysaccharides pyrolysis, while acid esters were predominant in the pyrolysis of *Sargassum fusiforme* (SA). The calculations also revealed

synergetic effect of cellulose and seaweed polysaccharides, a significantly increase of conversion and production rates.

4.4.3 Cellulose Composite

Cellulose is widely used in biohybrid materials because of its sustainability, biocompatibility and easy operating features. The hydroxyl groups make cellulose easy to form intra- and intermolecular HBs with other materials. For example, Hu et al.[290] investigated the synergistic effect between graphene oxide (GO) and NFC fibers. The strength, toughness and Young's modulus could be significantly improved via interactions in the hybrid GO-NFC microfibril. NFCs enhance the binding between GO sheets by weaving and wrapping GO sheets together. Meanwhile, GO sheets also bridge NFCs together to improve the mechanical properties. In addition, Ca^{+} cations at the interface of NFC and GO can further enhance the binding of the composite. Mao et al.[291] constructed a sandwich model with monolayer GO between CNC crystals to evaluate the suppression of hydrophobic facet of the cellulose-GO nanocomposite. It was discussed that the HBs between OH groups of cellulose and functional groups of GO result in the suppression of hydrophobic (2 0 0) facet of CNCs, while the hydrophilic (1 1 0)/(1 $\bar{1}$ 0) surfaces remain intact. Such finding could lead to new strategies to modify cellulose-based composites for surface and interface applications. Zhu and co-workers[292] carried out a complex RxMD study, with (2,2,6,6-tetramethylpiperidine-1-oxylradical)-mediated oxidized cellulose nanofibrils (TOCNFs) and graphene oxide. Their simulation system was composed of 16 crystalline cellulose Iβ chains, each with 16 D-glucose units, several GO sheets, water, Cu^{2+} and $SO4^{2-}$. Such hybrid TOCNFs-GO membrane demonstrated excellent mechanical properties, great adsorption capability, metal capture ability and recyclability. The self-assembly process, the metal capture

and cluster formation of the TOCNFs-GO membrane were captured and satisfactorily described by ReaxFF force field, see Figure 18 for the spatial distribution functions of copper and sulfur atoms surrounding the TOCNF+GO model surface at high concentration.

Other complex cellulose composites have been reported by RxMD studies. For example, Beste[293, 294] reported RxMD simulations of lignin conversions in the softwood, with temperatures up to 4000 K. The 5-5 linkage was identified as the weakest linker during the cyclization and dehydrogenation process. Chen et al.[295] assessed four different versions of ReaxFF[267-270] in the study of pyrolysis and combustion of cellulose, hemicellulose and lignin mixtures.

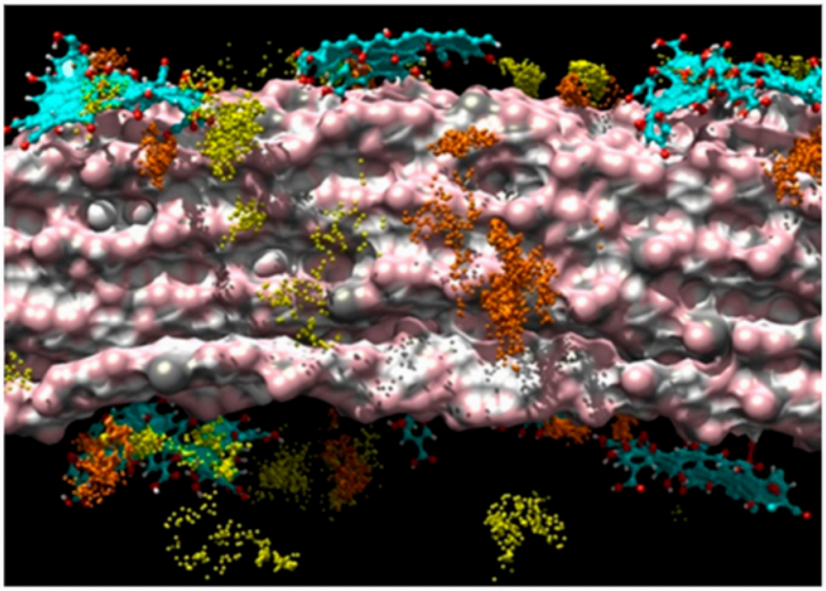

Figure 18. Spatial distribution functions of copper (orange) and sulfur (yellow) atoms surrounding the TOCNF+GO model at high concentration. The orange and yellow regions represent density contours 2 times larger than the average solvent density. TOCNF (solvent-accessible surface where the oxygens are light pink) and GO molecules (cyan sticks with red oxygens) are average conformations (reconstructed).[292] Reproduced with permission from ref. 292. Copyright 2018 American Chemical Society.

4.5 Mechanical Properties of Cellulose

The elastic modulus is one of the mostly studied mechanical properties of cellulose based materials and composites due to their excellent mechanical strength.[84] In general, the elastic modulus is calculated by the equation:

$$E = \frac{Stress}{Strain}$$

where stress is the force divided by the area and strain is the ratio of change caused by the stress. Young's modulus, shear modulus and bulk modulus based on different measurements of stress, strain and directions. As one of the commonly measured one, Young's modulus is used to describe mechanical properties about the resistance to deform along one direction where opposing force are applied. Materials with good stiffness commonly have a large Young's modulus. Experimentally, Young's modulus could be measured by XRD[296] or Raman spectroscopy[297]. From the computational point of view, several methods have been proposed to calculate Young's modulus:

(1) The calculation can be carried out to elongated (or decreased) the simulation box (z_0) by a small increment Δz (maximum 5% of the chain length)[206] along the axis of the applied stress, then the whole simulation box is re-optimized. The stress (σ) can be obtained by derivative of the function between the minimum potential energy and the axial length from the system[154, 156, 298], and the E_A is then the slope of the stress vs. strain ($\varepsilon=\Delta z/z_0$) curve.[172, 299, 300] A similar energy density method calculated E_A via twice the slope of energy density and the square of strain.[206]

(2) The stress can be defined as native value of pressure along the corresponding direction, the elastic modulus is then calculated by $E_A = \sigma/\varepsilon$. Instead of elongating simulation box by small increment,[165] the stress can also be changed directly with a constant pressure rate (e.g. 200bar/ps) with NPT ensemble[177].

(3) A alternative way is to allow the continuous elongation of simulation box along the direction where the stress is applied, with a defined strain rate in NPT system.[173, 301-306] The system is re-optimized in NPT ensemble in order to allow the dimensional changes due to Passion's effect.[173, 284]

(4) The elastic modulus also can be calculated by full elastic constant matrices based on the continuum concept of elasticity.[156, 178, 210, 307-309] The calculations can be performed via simulations tools in Materials Studio package.[156, 307-309] The energy minimization allows the changes of both atomic coordinates and unit cell parameters, which leads to no constant-area assumption.

A summary of the predicted Young's modulus (E_A) of cellulose polymorphs from simulation studies are listed in Table 7. Table 8 has the E_A values measured from experiments for the comparison, where E_A is the elastic modulus in the axial direction. The value of calculated E_A varies significantly in Table 7. The difference in the prediction of Young's modulus is mainly due to (1) the aforementioned elastic modulus calculation methods; (2) force fields;[171, 172, 206] (3) the HBs in cellulose model;[156, 204, 211, 248, 278, 300] (4) the number of cellulose chains and chain length of cellulose model;[206, 300] (5) with or without periodic boundary conditions for cellulose model;[206, 284] (6) any defects included in cellulose model.[167] Therefore, it is important to construct cellulose model in order to obtain accurate elastic modulus. Generally speaking, there are several approaches to construct cellulose model for the calculation of elastic modulus. First one is one-unit cell model with periodic boundary conditions, which is perfect for simulating infinite crystalline structures[297, 298], however, the accuracy of this method is highly dependent on the measurements of the original unit cell. The second method is super cell model with finite dimensions, which is appropriate for paracrystalline materials, while it might suffer

from the drawback of finite-size effects.[206] Cellulose system that consisting of super cell model with periodic boundary conditions is the third method that widely used. Although this approach precludes the surface properties, it can overcome the size limitation to study the bulk properties of cellulose, and avoid unreasonable response of the surface chains to the strain and interactions with neighboring atoms.[173, 284] In the literature, computational studies of cellulose mechanical properties have been reported by quantum mechanics, molecular mechanics and molecular dynamics simulations using both classic and reactive force fields.

Quantum mechanics. Quantum mechanics methods have been used to determine elastic modulus of cellulose and provide useful information for experiment. For example, Santiago Cintrón et al.[204] investigated the Young's modulus of 1,4'-*O*-dimethyl-*β*-cellobioside (DMCB), and an analogue, 2,3,6,20',3',6'-hexadeoxy-1,4'-*O*- dimethyl-b-cellobioside (DODMCB). The results indicated that HBs play an important role in the prediction of elastic modulus. The comparison between system with multiple chains and a single chain showed no difference in the elastic modulus value, which indicated that the interchain HBs have little effect on the mechanical property, while intrachain HBs significantly affect the stiffness of cellulose chains. Also, cellulose model with higher DP (20~40) showed an increased value of Young's modulus. Dri et al.[163] performed DFT calculations to evaluate the anisotropy of the elastic properties of crystalline cellulose Iβ. The 3D color contour plots in Figure 13 (c) indicated the anisotropy of the Young's modulus, with reported Young's modulus of surface (2 0 0), (0 0 1) and (0 1 0) is 206, 98 and 19 GPa, respectively.

Molecular mechanics. Molecular mechanics requires less time and has a high accuracy in the deformation calculations,[156, 171, 211, 310-313] Unlike the quasi-harmonic approximation[314], AIMD[178, 315] and MD[155, 316, 317], it calculated the elastic modulus

via minimum energy structure at very low temperature (~0 K), and the accuracy is highly dependent on the initial orientation of the structure.[156, 206] The elastic modulus of cellulose I, II, III_I, III_{II}, and IV has been reported as 138, 88, 87, 58, 75 GPa respectively,[318] which suggested the significant difference of these cellulose allomorphs. Eichhorn et al.[156, 297] investigated how the elastic modulus calculation method, HBs and cellulose structures affect the prediction of mechanical properties. They proposed that there is no difference for the modulus calculation methods between using COMPASS force field and full elastic constant matrices. While the removal of HBs in the system affects the stiffness calculations. Their results also showed that cellulose Iα and Iβ has similar stiffness and cellulose I is stable than cellulose II based the stiffness values. The calculated elastic modulus of cellulose Iβ via super cell model is reported by Tanaka and co-workers.[206] The best system size is 4×4×10 unit-cell size from their study. They also found that the second-generation force fields are more suitable for the cellulose optimization compared with first-generation ones. The deformation of amorphous cellulose was also studied,[313] and HBs formed between amorphous cellulose was reported to cause the yield of 7-8% strain and poor recovery of amorphous cellulose. Petridis et al.[319] found that an increasing hydration in cellulose materials can significantly change the mechanical and dynamical properties of cellulose. Cellulose model with 20% hydration is more rigid than dry one because of the smaller distance between cellulose chains and HBs formed between cellulose and water molecules. The shear resistance of CNCs is investigated by Molnar and co-workers.[167] It is found that the shear behavior is sensitive to noncovalent interactions and local structural changes such as deformation, translations and rotations. Furthermore, compared with perfect CNCs, the yield strength and dilatancy greatly decreased in the CNC models with defects (e.g. dislocations) on the cellulose chains.

Molecular dynamics. MD simulation provides a possible way to estimate the mechanical behavior of cellulose in a continuous way for non-zero temperatures.[177, 249, 320-322] Brickmann et al.[155] found that cellulose I and II with parallel chains showed comparable Young's modulus with experiments, which indicated that cellulose II model with parallel chains is more reasonable than that with antiparallel chains. Wohlert and co-workers[317] reported that the temperature dependence between Young's modulus and temperature is -0.05 GPa/K at room temperature for cellulose. In addition, a dependence was observed between Young's modulus and the number of chains in the system via CHARMM force field, whereas no dependence was found with GROMOS force field. Djahedi et al.[170] found that HBs affect the calculations of mechanical properties for cellulose via the synergies between different energy contributions such as covalent bonds, angles, dihedrals, electrostatic forces, dispersion and steric forces. The shear behavior of cellulose is also studied via MD simulations. Zhang and co-workers[323] studied the effect of shear loading on plant cell model with sandwich structures of cellulose on both sides and hemicellulose in the middle. They proposed that the shear strength can be controlled by optimizing the HBs formed between cellulose and hemicellulose interfaces. Moreover, the shear behavior between cellulose Iβ interfaces is affected by both surface energy and the energy along the shear direction.[316] The interfaces with weaker interactions present a stuck-slip deformation behavior due to the large energy barrier between cellulose chains, while interfaces with stronger interactions showed a continuous sliding process. Meanwhile, the study of mechanical properties of modified cellulose materials has also attracted great interest due to the large numbers of application in paper and energy related fields.[238, 308, 309, 324, 325] Wang et al.[307] found that the chain length of cellulose Iβ significantly influence the mechanical properties of insulation paper. The Young's modulus decreased with shorter chains and chains with higher fracture degree (FD). The number

of HBs in the system decreases with the increasing of FD, which reduces the mechanical strength of the insulation paper. The incorporation of insulation paper with melamine, SiO_2 and water showed strong mechanical strength, breakdown strength, high DP and low water content compared with original ones.[326]

Reactive molecular dynamics. Allowing the bond formation and breaking in ReaxFF makes it a potential simulation tool to study the tensile deformation of cellulose. The accuracy and predictability of ReaxFF in describing the mechanical properties of cellulose have been reported recently.[172] Wu et al.[278, 284] performed RxMD method to evaluate the elastic modulus of cellulose with different strain rates. They reported that the elastic behavior of cellulose is anisotropic. The increased strain rate results in a higher value of yield and ultimate stress. For the optimal strain rate of 10^{-3}/ps, the calculated Young's modulus, yield stress and ultimate stress along the stress direction are 113.5, 5.4 and 6.0 GPa, respectively, agreeing well with experiments in Table 8. Our group[173] used ReaxFF to investigate the Young's modulus of cellulose at different temperature with a constant strain rate of 10^{-4}/fs. The Young's modulus decreased with the temperature increase. The values of Young's modulus are 113.24, 99.03, 95.67 and 94.34 GPa for 300, 500, 800 and 1000 K, respectively.

Table 7. Calculated Young's modulus from published computational studies for cellulose and its derivatives.

	Method	E_A (GPa)	Ref.
I	MM (Custom)[d]	57	Treloar et al.[327]
I[180]	MM (Custom)	167.5	Tashiro et al.[210]
I[180]	MD (CHARMM)	162[a]	Marhofer et al.[155]
I[180]	MD (CHARMM)	128	Marhofer et al.[155]
I[180]	MM (Custom)	172.9	Tashiro et al.[211]
I[180]	MM (Custom)[d]	70.8	Tashiro et al.[211]
Iα[180]	MD (Custom)	128.7	Neyertz et al.[177]
Iα[131]	MM (COMPASS)	155[b]	Eichhorn et al.[156]

Iα[131]	MM (COMPASS)	152[c]	Eichhorn et al.[156]
Iα[131]	MM (COMPASS)[d]	114[b]	Eichhorn et al.[156]
Iα[131]	MM (COMPASS)[d]	118[c]	Eichhorn et al.[156]
Iα[131]	CG	138.3	Poma et al.[328]
Iα[329]	MM (COMPASS)	136[b]	Eichhorn et al.[156]
Iα[329]	MM (COMPASS)	66[c]	Eichhorn et al.[156]
Iα[329]	MM (COMPASS)[d]	117[b]	Eichhorn et al.[156]
Iα[329]	MM (COMPASS)[d]	52[c]	Eichhorn et al.[156]
Iβ[181]	MM (COMPASS)	116[b]	Eichhorn et al.[156]
Iβ[181]	MM (COMPASS)	104[c]	Eichhorn et al.[156]
Iβ[181]	MM (COMPASS)[d]	124[b]	Eichhorn et al.[156]
Iβ[181]	MM (COMPASS)[d]	125[c]	Eichhorn et al.[156]
Iβ[181]	MM (COMPASS)	124~125	Tanaka et al.[206]
Iβ[180]	MM (COMPASS)	172.9	Tashiro et al.[211]
Iβ[180]	MM & MD (CHARMM)	148	Reiling et al.[154]
Iβ[180]	MM & MD (GROMOS)	136 ± 6	Kroon-Batenburg et al.[164]
Iβ[132]	MM (COMPASS)	149[b]	Eichhorn et al.[156]
Iβ[132]	MM (COMPASS)	150[c]	Eichhorn et al.[156]
Iβ[132]	MM (COMPASS)[d]	127[b]	Eichhorn et al.[156]
Iβ[132]	MM (COMPASS)[d]	125[c]	Eichhorn et al.[156]
Iβ[132]	MD (GROMOS)	156	Bergenstrahle et al.[165]
Iβ[132]	QM (B3LYP/6- 311G**+)	99.7	Santiago Cintrón et al.[204]
Iβ[132]	QM (B3LYP/6- 311G**+)[d]	33	Santiago Cintrón et al.[204]
Iβ[132]	MM (MM3)	85.2 (DP=2)	Santiago Cintrón et al.[204]
Iβ[132]	MM (MM3)	142.7~147.5 (DP=20~40)	Santiago Cintrón et al.[204]
Iβ[132]	MM (MM3)[d]	37.6	Santiago Cintrón et al.[204]
Iβ[132]	QM[e]	206	Dri et al.[163]
Iβ[132]	MD (GROMOS) & FEM	100.5	Chen et al.[320]
Iβ[132]	MD (GLYCAM)	138	Djahedi et al.[170]
Iβ[132]	MD (ReaxFF)	139.5	Wu et al.[278]
Iβ[132]	MD (ReaxFF)[d]	120.3	Wu et al.[278]
Iβ[132]	MD (ReaxFF)	107.8~113.5	Wu et al. [284]
Iβ[132]	MD (ReaxFF, Mattsson)	124.5	Dri et al.[172]
Iβ[132]	MD (ReaxFF, Chenoweth)	117.2	Dri et al.[172]
Iβ[132]	MD (ReaxFF, Rahaman)	192.2	Dri et al.[172]
Iβ[132]	MD (COMPASS)	209.6	Dri et al.[172]
Iβ[132]	MD (GLYCAM)	129.4	Dri et al.[172]
Iβ[132]	MD (ReaxFF)	113.24	Qiao et al.[173]
Iβ[132]	MD (ReaxFF)	99.03 (500 K)	Qiao et al.[173]
Iβ[132]	MD (ReaxFF)	95.67 (800 K)	Qiao et al.[173]
Iβ[132]	MD (ReaxFF)	94.34 (1000 K)	Qiao et al.[173]
Iβ[132]	MM (CVFF1)	186	Yao et al.[171]
Iβ[132]	MM (CVFF2)	201.5	Yao et al.[171]
Iβ[132]	MM (CVFF3)	179.6	Yao et al.[171]
Iβ[132]	MD (AMBER)	161	Gupta et al.[299]
Iβ[132]	MM (COMPASS)	113 (single chain)	Wu et al. [300]
Iβ[132]	MM (COMPASS)	155	Wu et al. [300]
Iβ[132]	MM (GROMOS)	0.4~1.65 (shear stress)	Molnar et al.[167]

Iβ[132]	CG	135.4	Poma et al.[328]
Iβ[132]	CG	140~200	Shishehbor et al.[330]
Iβ[132]	CG/FEM	115~135 for (CNCs)	Shishehbor et al. [331]
Iβ[132]	CG/FEM	100~250	Shishehbor et al. [331]
Iβ[132]	MD (CHARMM)	20.1[τ]	Sinko et al.[316]
Iβ[132]	MD (PCFF)	37.63~104.34[c]	Wang et al. [307]
Iβ[132]	MD (PCFF)	11.23~12.23[c]	Wang et al. [308]
Iβ[132]	MD (PCFF)	12.74~14[c]	Zhu et al. [309]
Iβ	MD (Custom)	115.2	Neyertz et al.[177]
II[190]	MM (Custom)	162.1	Tashiro et al.[210]
II	MM (COMPASS)	98	Eichhorn et al.[297]
II[190]	MM & MD (GROMOS)	89 ± 4	Kroon-Batenburg et al.[164]
II[190]	CPMD	155	Gansteret al.[178]
II[190]	MD (CHARMM)	168[a, f]	Marhofer et al.[155]
II[190]	MD (CHARMM)	83[f]	Marhofer et al.[155]
II[190]	MD (CHARMM)	71[a, g]	Marhofer et al.[155]
II[190]	MD (CHARMM)	59[g]	Marhofer et al.[155]
II[133]	MM (COMPASS)	109[b]	Eichhorn et al.[156]
II[133]	MM (COMPASS)[d]	110[c]	Eichhorn et al.[156]
II[133]	MM (COMPASS)	101[b]	Eichhorn et al.[156]
II[133]	MM (COMPASS)[d]	92[c]	Eichhorn et al.[156]
II[332]	MM (COMPASS)	166[b]	Eichhorn et al.[156]
II[332]	MM (COMPASS)[d]	168[c]	Eichhorn et al.[156]
II[332]	MM (COMPASS)	106[b]	Eichhorn et al.[156]
II[332]	MM (COMPASS)[d]	107[c]	Eichhorn et al.[156]
II[134]	MD (GLYCAM)	112	Djahedi et al. [170]
III_I[141]	MD (GLYCAM)	101	Djahedi et al. [170]
C-Whiskers[k,] [333]	MM (COMPASS)	145	Sturcova et al.[298]
Amor-C[q]	MM (PCFF)	10.42 ± 1.08 (8.45)	Chen et al.[313]
MCC-H_2O	MD (ReaxFF)	13.45	Sahputra et al. [334]
Iβ[132]	MD (GROMOS)	33.5	Kulasinski et al.[249]
Amor-C-Air[h]	MD (PCFF)	19.8156 (450 K)	Wang et al. [324]
Amor-C-Air[h]	MD (PCFF)	21.0423 (460 K)	Wang et al. [324]
Amor-C-Air[h]	MD (PCFF)	17.8751 (470 K)	Wang et al. [324]
Amor-C-Air[h]	MD (PCFF)	18.2154 (480 K)	Wang et al. [324]
Amor-C-Air[h]	MD (PCFF)	17.0215 (490 K)	Wang et al. [324]
Amor-C-Air[h]	MD (PCFF)	16.8213 (500 K)	Wang et al. [324]
Amor-C-Air[h]	MD (PCFF)	15.8203 (510 K)	Wang et al. [324]
Amor-C-N_2[o]	MD (PCFF)	20.9467 (450 K)	Wang et al. [324]
Amor-C-N_2[o]	MD (PCFF)	21.6596 (460 K)	Wang et al. [324]
Amor-C-N_2[o]	MD (PCFF)	18.3133 (470 K)	Wang et al. [324]
Amor-C-N_2[o]	MD (PCFF)	19.9756 (480 K)	Wang et al. [324]
Amor-C-N_2[o]	MD (PCFF)	18.0819 (490 K)	Wang et al. [324]
Amor-C-N_2[o]	MD (PCFF)	19.0911 (500 K)	Wang et al. [324]
Amor-C-N_2[o]	MD (PCFF)	17.4743 (510 K)	Wang et al. [324]
C-H_2O[I]	MD (UFF)	15.8	Tang et al. [326]
CN-H_2O[m]	MD (UFF)	18.2	Tang et al. [326]
CAN-H_2O[n]	MD (UFF)	19.4	Tang et al. [326]
CA	FEM/FEA	0.1233	Stylianopoulos et al.[335]

BC	FEM/FEA	53.7~64.9	Gao et al. [336]
CNCs	FEM/FEA	29.78	Srinivasa et al.[337]
CFREL[l]	FEM/FEA	641.57×10^{-3}	Ahmad et al.[338]
C-GO[p]	FEM/FEA	355.2×10^{-3} (CA/GO=3%)	Naddeo et al.[339]
C-GO[p]	FEM/FEA	583.45×10^{-3} (CA/GO=90%)	Naddeo et al.[339]

[a] Energy minimization
[b] Stiffness
[c] Elastic constant
[d] Without the hydrogen bonds in the simulations
[e] Semi-empirical correction for van der Waals interactions
[f] Cellulose model with parallel chains
[g] Cellulose model with antiparallel chains
[h] Amorphous cellulose with air
[I] Cellulose modified by H_2O
[J] Commercial mechanical testing system
[k] Cellulose whiskers
[l] Cellulose fiber reinforced epoxy laminates
[m] Cellulose modified by SiO_2 and H_2O
[n] Cellulose modified by melamine, SiO_2 and water
[o] Amorphous cellulose with N_2
[p] Cellulose/GO composite
[q] Amorphous cellulose
[τ] Transverse modulus

Table 8. Measured Young's modulus from published studies for cellulose and its derivatives.

	Method	EA (GPa)	Ref.
I	XRD	134	Sakuradaet al.[340]
I	XRD	120~135	Matsuo et al.[296]
I	XRD	138	Nishino et al.[318]
Iβ	Inelastic X-ray scattering	220±50	Diddens et al.[341]
Iβ	Raman Spectroscopy	105	Rusli et al.[342]
Iβ	AFM	151	Iwamoto et al.[343]
Iβ	XRD	130	Nishino et al.[318]
Iβ	XRD	130~137	Sakuradaet al.[340]
Iβ	XRD	114	Ishikawa et al.[344]
II	XRD	88	Nishino et al.[318]
II	XRD	106~112	Matsuo et al.[296]
II	XRD	78	Langan et al.[133]
II	XRD	90	Marhofer et al.[155]
II	XRD	89	Ishikawa et al.[344]

II	XRD	70~90	Mann et al.[345]
III_I	XRD	87	Nishino et al.[318]
III_I	XRD	115~122	Ishikawat et al.[346]
III_I	XRD	115	Ishikawa et al.[344]
III_{II}	XRD	58	Nishino et al.[318]
IV	XRD	75	Nishino et al.[318]
C-Whiskers[b]	Raman Spectroscopy	143	Sturcova et al.[298]
Amor-C[a]	Exp.	8.45	Mark et al.[347]
MCC-H_2O	Exp.	9.2~11.1	Hancock et al.[348]
BC	Raman Spectroscopy	114	Hsieh et al.[349]
BC	Raman Spectroscopy	79~88	Tanpichai et al.[350]
CA	Exp.	3.5~12.4 $\times 10^{-3}$	Stylianopoulos et al.[335]
NFCF[c]	Compression testing	1.2 ~8.65	Sehaqui et al.[351]
NFCF[c]	Compression testing	1.2 ~8.65	Ali et al. [352]
NFCF[c]	Compression testing	1.2 ~8.65	Gordeyeva et al. [353]

[a] Amorphous cellulose
[b] Cellulose whiskers
[c] Nanofibrillar cellulose foams

4.6 Conclusion

Due to the severe worldwide energy and environmental problems, cellulose and its derivatives have become one of the widespread and valuable natural resource and will be continuously dominated in the biomass applications in the future. Previous research efforts have been mainly focused on traditional treatments of cellulose, such as conversion, degradation, dissolution and pyrolysis. With an increasing interest in manipulating subtle properties of native cellulose, using computational techniques to classify and construct the structure-property-process relationship of cellulose martials has been a hot topic for both academia and industry. Smarter and green treatment strategies would critically require effective and selective modifications of characteristic chemistry and structures, to achieve desirable properties.

Computational simulations at atomistic level, including quantum mechanics, molecular mechanics, molecular dynamics and reactive molecular dynamics, have provide powerful methods

and useful information in understanding the fundamental mechanism of cellulose conversion and utilization. In particular, those computational methods offer insights into the electrostatic and van der Waals interactions to the hydrogen bonding network, which plays an important role in structural and mechanical properties of cellulose. By modifying HBs between chains or at interface, cellulose exhibits enhanced mechanical strength and thermal stability. The HB network also affects the dissolution of cellulose in ionic liquids and other solvents. Moreover, the investigation of interactions, adsorptions and interfacial properties between cellulose and other molecules helps to understand cellulose structure, chemistry and property under various conditions. Like discussed in this review, QM calculations provide accurate reaction mechanism of cellulose decomposition, while QM/MM hybrid method and RxMD are able to proceed structural evolution of large and complex cellulose based system, which can further help in optimizing cellulose pyrolysis processes conditions. In this review, we outline the state-of-the-art understanding of cellulose structures, and discuss in details cellulose interactions, dissolutions and decompositions via computational methods of molecular dynamics (MD) and reactive molecular dynamics (RxMD) simulations. In addition, cellulose characterizations, beneficial to validate and support computational results, are also briefly summarized. The combination of simulation and experiment could facilitate the construction of the structure-property-process relationship and provide better guidelines to cellulose treatments at industrial level.

4.7 Reference

1. Rubin, E.M., *Genomics of cellulosic biofuels.* Nature, 2008. **454**(7206): p. 841-845.
2. Hill, J., et al., *Environmental, economic, and energetic costs and benefits of biodiesel and ethanol biofuels.* Proceedings of the National Academy of Sciences, 2006. **103**(30): p. 11206.
3. Thomas, B., et al., *Nanocellulose, a Versatile Green Platform: From Biosources to Materials and Their Applications.* Chemical Reviews, 2018. **118**(24): p. 11575-11625.

4. Zhu, H., et al., *Wood-Derived Materials for Green Electronics, Biological Devices, and Energy Applications.* Chemical Reviews, 2016. **116**(16): p. 9305-9374.
5. Muhd Julkapli, N. and S. Bagheri, *Nanocellulose as a green and sustainable emerging material in energy applications: a review.* Polymers for Advanced Technologies, 2017. **28**(12): p. 1583-1594.
6. Chen, H., et al., *Exploring Chemical, Mechanical, and Electrical Functionalities of Binders for Advanced Energy-Storage Devices.* Chemical Reviews, 2018. **118**(18): p. 8936-8982.
7. Jacob, J., et al., *Biopolymer based nanomaterials in drug delivery systems: A review.* Materials Today Chemistry, 2018. **9**: p. 43-55.
8. Löbmann, K. and A.J. Svagan, *Cellulose nanofibers as excipient for the delivery of poorly soluble drugs.* International Journal of Pharmaceutics, 2017. **533**(1): p. 285-297.
9. Chin, S.F., F.B. Jimmy, and S.C. Pang, *Size controlled fabrication of cellulose nanoparticles for drug delivery applications.* Journal of Drug Delivery Science and Technology, 2018. **43**: p. 262-266.
10. Treesuppharat, W., et al., *Synthesis and characterization of bacterial cellulose and gelatin-based hydrogel composites for drug-delivery systems.* Biotechnology Reports, 2017. **15**: p. 84-91.
11. Luo, H., et al., *Bacterial cellulose/graphene oxide nanocomposite as a novel drug delivery system.* Current Applied Physics, 2017. **17**(2): p. 249-254.
12. Abo-Elseoud, W.S., et al., *Chitosan nanoparticles/cellulose nanocrystals nanocomposites as a carrier system for the controlled release of repaglinide.* International Journal of Biological Macromolecules, 2018. **111**: p. 604-613.
13. Rahimi, M., et al., *Biocompatible magnetic tris(2-aminoethyl)amine functionalized nanocrystalline cellulose as a novel nanocarrier for anticancer drug delivery of methotrexate.* New Journal of Chemistry, 2017. **41**(5): p. 2160-2168.
14. Madhusudana Rao, K., A. Kumar, and S.S. Han, *Polysaccharide based bionanocomposite hydrogels reinforced with cellulose nanocrystals: Drug release and biocompatibility analyses.* International Journal of Biological Macromolecules, 2017. **101**: p. 165-171.
15. Sheikhi, A., et al., *Recent advances in nanoengineering cellulose for cargo delivery.* Journal of Controlled Release, 2019. **294**: p. 53-76.
16. Nogi, M., et al., *High thermal stability of optical transparency in cellulose nanofiber paper.* Applied Physics Letters, 2013. **102**(18): p. 181911.
17. Salajkova, M., et al., *Tough nanopaper structures based on cellulose nanofibers and carbon nanotubes.* Composites Science and Technology, 2013. **87**: p. 103-110.
18. Sun, X., et al., *Cellulose Nanofibers as a Modifier for Rheology, Curing and Mechanical Performance of Oil Well Cement.* Scientific Reports, 2016. **6**(1): p. 31654.
19. Li, F., E. Mascheroni, and L. Piergiovanni, *The Potential of NanoCellulose in the Packaging Field: A Review.* Packaging Technology and Science, 2015. **28**(6): p. 475-508.
20. Juntaro, J., et al., *Nanocellulose enhanced interfaces in truly green unidirectional fibre reinforced composites.* Composite Interfaces, 2007. **14**(7-9): p. 753-762.
21. Sun, Y. and J. Cheng, *Hydrolysis of lignocellulosic materials for ethanol production: a review.* Bioresource Technology, 2002. **83**(1): p. 1-11.
22. Millett, M.A., A.J. Baker, and L.D. Satter, *Physical And Chemical Pretreatments For Enhancing Cellulose Saccharification.* Biotechnology and Bioengineering, 1976(6): p. 125-153.

23. Iwamoto, S., A.N. Nakagaito, and H. Yano, *Nano-fibrillation of pulp fibers for the processing of transparent nanocomposites.* Applied Physics A, 2007. **89**(2): p. 461-466.
24. Bandera, D., et al., *Influence of mechanical treatments on the properties of cellulose nanofibers isolated from microcrystalline cellulose.* Reactive and Functional Polymers, 2014. **85**: p. 134-141.
25. Panthapulakkal, S. and M. Sain, *Preparation and Characterization of Cellulose Nanofibril Films from Wood Fibre and Their Thermoplastic Polycarbonate Composites.* International Journal of Polymer Science, 2012.
26. Zimmermann, T., N. Bordeanu, and E. Strub, *Properties of nanofibrillated cellulose from different raw materials and its reinforcement potential.* Carbohydrate Polymers, 2010. **79**(4): p. 1086-1093.
27. Dufresne, A., J.-Y. Cavaillé, and M.R. Vignon, *Mechanical behavior of sheets prepared from sugar beet cellulose microfibrils.* Journal of Applied Polymer Science, 1997. **64**(6): p. 1185-1194.
28. Stelte, W. and A.R. Sanadi, *Preparation and Characterization of Cellulose Nanofibers from Two Commercial Hardwood and Softwood Pulps.* Industrial & Engineering Chemistry Research, 2009. **48**(24): p. 11211-11219.
29. Leitner, J., et al., *Sugar beet cellulose nanofibril-reinforced composites.* Cellulose, 2007. **14**(5): p. 419-425.
30. Alemdar, A. and M. Sain, *Isolation and characterization of nanofibers from agricultural residues – Wheat straw and soy hulls.* Bioresource Technology, 2008. **99**(6): p. 1664-1671.
31. Chakraborty, A., M. Sain, and M. Kortschot, *Cellulose microfibrils: A novel method of preparation using high shear refining and cryocrushing*, in *Holzforschung*. 2005. p. 102.
32. Johnson, R.K., et al., *A new bio-based nanocomposite: fibrillated TEMPO-oxidized celluloses in hydroxypropylcellulose matrix.* Cellulose, 2009. **16**(2): p. 227-238.
33. Wang, S. and Q. Cheng, *A novel process to isolate fibrils from cellulose fibers by high-intensity ultrasonication, Part 1: Process optimization.* Journal of Applied Polymer Science, 2009. **113**(2): p. 1270-1275.
34. Frone, A.N., et al., *Preparation And Characterization Of Pva Composites With Cellulose Nanofibers Obtained By Ultrasonication.* Bioresources, 2011. **6**(1): p. 487-512.
35. Dong, X.M., J.-F. Revol, and D.G. Gray, *Effect of microcrystallite preparation conditions on the formation of colloid crystals of cellulose.* Cellulose, 1998. **5**(1): p. 19-32.
36. Song, J., et al., *Processing bulk natural wood into a high-performance structural material.* Nature, 2018. **554**(7691): p. 224-228.
37. Chen, C., et al., *Scalable and Sustainable Approach toward Highly Compressible, Anisotropic, Lamellar Carbon Sponge.* Chem, 2018. **4**(3): p. 544-554.
38. Trifol, J., et al., *Chemically extracted nanocellulose from sisal fibres by a simple and industrially relevant process.* Cellulose, 2017. **24**(1): p. 107-118.
39. Bhatnagar, A. and M. Sain, *Processing of Cellulose Nanofiber-reinforced Composites.* Journal of Reinforced Plastics and Composites, 2005. **24**(12): p. 1259-1268.
40. Rånby, B.G., *Fibrous macromolecular systems. Cellulose and muscle. The colloidal properties of cellulose micelles.* Discussions of the Faraday Society, 1951. **11**(0): p. 158-164.
41. Saito, T., et al., *Homogeneous Suspensions of Individualized Microfibrils from TEMPO-Catalyzed Oxidation of Native Cellulose.* Biomacromolecules, 2006. **7**(6): p. 1687-1691.

42. Saito, T., et al., *Individualization of Nano-Sized Plant Cellulose Fibrils by Direct Surface Carboxylation Using TEMPO Catalyst under Neutral Conditions.* Biomacromolecules, 2009. **10**(7): p. 1992-1996.
43. Wu, Q., et al., *A High Strength Nanocomposite Based on Microcrystalline Cellulose and Polyurethane.* Biomacromolecules, 2007. **8**(12): p. 3687-3692.
44. Broder, J.D., et al., *Biofuels system economics.* World Resource Review, 1995. **7**(4): p. 560-569.
45. Iranmahboob, J., F. Nadim, and S. Monemi, *Optimizing acid-hydrolysis: a critical step for production of ethanol from mixed wood chips.* Biomass and Bioenergy, 2002. **22**(5): p. 401-404.
46. Hubbe, M.A., et al., *Cellulosic Nanocomposites: A Review.* Bioresources, 2008. **3**(3): p. 929-980.
47. Habibi, Y., L.A. Lucia, and O.J. Rojas, *Cellulose Nanocrystals: Chemistry, Self-Assembly, and Applications.* Chemical Reviews, 2010. **110**(6): p. 3479-3500.
48. Wang, B. and M. Sain, *Isolation of nanofibers from soybean source and their reinforcing capability on synthetic polymers.* Composites Science and Technology, 2007. **67**(11): p. 2521-2527.
49. Filson, P.B. and B.E. Dawson-Andoh, *Sono-chemical preparation of cellulose nanocrystals from lignocellulose derived materials.* Bioresource Technology, 2009. **100**(7): p. 2259-2264.
50. Elazzouzi-Hafraoui, S., et al., *The Shape and Size Distribution of Crystalline Nanoparticles Prepared by Acid Hydrolysis of Native Cellulose.* Biomacromolecules, 2008. **9**(1): p. 57-65.
51. Beck-Candanedo, S., M. Roman, and D.G. Gray, *Effect of Reaction Conditions on the Properties and Behavior of Wood Cellulose Nanocrystal Suspensions.* Biomacromolecules, 2005. **6**(2): p. 1048-1054.
52. Bondeson, D., A. Mathew, and K. Oksman, *Optimization of the isolation of nanocrystals from microcrystalline celluloseby acid hydrolysis.* Cellulose, 2006. **13**(2): p. 171.
53. Karim, Z., et al., *Necessity of enzymatic hydrolysis for production and functionalization of nanocelluloses.* Critical Reviews in Biotechnology, 2017. **37**(3): p. 355-370.
54. Henriksson, M., et al., *An environmentally friendly method for enzyme-assisted preparation of microfibrillated cellulose (MFC) nanofibers.* European Polymer Journal, 2007. **43**(8): p. 3434-3441.
55. Pääkkö, M., et al., *Enzymatic Hydrolysis Combined with Mechanical Shearing and High-Pressure Homogenization for Nanoscale Cellulose Fibrils and Strong Gels.* Biomacromolecules, 2007. **8**(6): p. 1934-1941.
56. Tibolla, H., F.M. Pelissari, and F.C. Menegalli, *Cellulose nanofibers produced from banana peel by chemical and enzymatic treatment.* LWT - Food Science and Technology, 2014. **59**(2, Part 2): p. 1311-1318.
57. Chung, D., et al., *Cellulosic ethanol production via consolidated bioprocessing at 75 °C by engineered Caldicellulosiruptor bescii.* Biotechnology for Biofuels, 2015. **8**(1): p. 163.
58. Yarbrough, J.M., et al., *Multifunctional Cellulolytic Enzymes Outperform Processive Fungal Cellulases for Coproduction of Nanocellulose and Biofuels.* ACS Nano, 2017. **11**(3): p. 3101-3109.
59. Camarero Espinosa, S., et al., *Isolation of Thermally Stable Cellulose Nanocrystals by Phosphoric Acid Hydrolysis.* Biomacromolecules, 2013. **14**(4): p. 1223-1230.

60. Reid, M.S., M. Villalobos, and E.D. Cranston, *Benchmarking Cellulose Nanocrystals: From the Laboratory to Industrial Production.* Langmuir, 2017. **33**(7): p. 1583-1598.
61. Battista, O.A., *Hydrolysis and Crystallization of Cellulose.* Industrial & Engineering Chemistry, 1950. **42**(3): p. 502-507.
62. Lee, S.-Y., et al., *Nanocellulose reinforced PVA composite films: Effects of acid treatment and filler loading.* Fibers and Polymers, 2009. **10**(1): p. 77-82.
63. Filpponen, I. and D.S. Argyropoulos, *Regular Linking of Cellulose Nanocrystals via Click Chemistry: Synthesis and Formation of Cellulose Nanoplatelet Gels.* Biomacromolecules, 2010. **11**(4): p. 1060-1066.
64. Liu, D., et al., *Starch composites reinforced by bamboo cellulosic crystals.* Bioresource Technology, 2010. **101**(7): p. 2529-2536.
65. Chen, L., et al., *Unveiling Mesopore Evolution in Carbonized Wood: Interfacial Separation, Migration, and Degradation of Lignin Phase.* ACS Sustainable Chemistry & Engineering, 2015. **3**(10): p. 2489-2495.
66. Shafizadeh, F. and A.G.W. Bradbury, *Thermal degradation of cellulose in air and nitrogen at low temperatures.* Journal of Applied Polymer Science, 1979. **23**(5): p. 1431-1442.
67. Melo, E. and J.F. Kennedy, *Cellulose hydrolysis (biotechnology monographs, Vol. 3) edited by L.-T. Fan, M. M. Gharpuray and Y.-H. Lee, Springer-Verlag, Berlin, Heidelberg, New York, London, Paris and Tokyo, 1987. pp. viii + 198, price DM168.00. ISBN 3-540-17671-3.* British Polymer Journal, 1988. **20**(6): p. 532-532.
68. Kilzer, F.J. and A. Broido, *Speculations on the nature of cellulose pyrolysis.* Pyrodynamics, 1965. **2**: p. 151-163.
69. Zwart, R.W.R., H. Boerrigter, and A. van der Drift, *The Impact of Biomass Pretreatment on the Feasibility of Overseas Biomass Conversion to Fischer−Tropsch Products.* Energy & Fuels, 2006. **20**(5): p. 2192-2197.
70. Galbe, M. and G. Zacchi, *Pretreatment of Lignocellulosic Materials for Efficient Bioethanol Production*, in *Biofuels*, L. Olsson, Editor. 2007, Springer Berlin Heidelberg: Berlin, Heidelberg. p. 41-65.
71. Ballesteros, I., et al., *Ethanol production from steam-explosion pretreated wheat straw.* Applied Biochemistry and Biotechnology, 2006. **130**(1): p. 496-508.
72. Okano, K., et al., *Conversion of Japanese red cedar (Cryptomeria japonica) into a feed for ruminants by white-rot basidiomycetes.* Animal Feed Science and Technology, 2005. **120**(3): p. 235-243.
73. Lee, J.W., et al., *Biological pretreatment of softwood Pinus densiflora by three white rot fungi.* Journal of Microbiology, 2007. **45**(6): p. 485-491.
74. Hatakka, A.I., *Pretreatment of wheat straw by white-rot fungi for enzymic saccharification of cellulose.* European journal of applied microbiology and biotechnology, 1983. **18**(6): p. 350-357.
75. Ander, P. and K.-E. Eriksson, *Selective Degradation of Wood Components by White-Rot Fungi.* Physiologia Plantarum, 1977. **41**(4): p. 239-248.
76. Akin, D.E., et al., *Alterations in structure, chemistry, and biodegradability of grass lignocellulose treated with the white rot fungi Ceriporiopsis subvermispora and Cyathus stercoreus.* Applied and Environmental Microbiology, 1995. **61**(4): p. 1591.
77. Boominathan, K. and C.A. Reddy, *cAMP-mediated differential regulation of lignin peroxidase and manganese-dependent peroxidase production in the white-rot*

basidiomycete Phanerochaete chrysosporium. Proceedings of the National Academy of Sciences, 1992. **89**(12): p. 5586.
78. Singh, P., et al., *Biological pretreatment of sugarcane trash for its conversion to fermentable sugars.* World Journal of Microbiology and Biotechnology, 2008. **24**(5): p. 667-673.
79. Kumar, A.K. and S. Sharma, *Recent updates on different methods of pretreatment of lignocellulosic feedstocks: a review.* Bioresources and Bioprocessing, 2017. **4**(1): p. 7.
80. Gray, H.L. and C.J. Staud, *Recent advances in cellulose and starch chemistry.* Chemical Reviews, 1927. **4**(4): p. 355-373.
81. Iguchi, M., S. Yamanaka, and A. Budhiono, *Bacterial cellulose—a masterpiece of nature's arts.* Journal of Materials Science, 2000. **35**(2): p. 261-270.
82. Kontturi, E., T. Tammelin, and M. Österberg, *Cellulose—model films and the fundamental approach.* Chemical Society Reviews, 2006. **35**(12): p. 1287-1304.
83. Habibi, Y., *Key advances in the chemical modification of nanocelluloses.* Chemical Society Reviews, 2014. **43**(5): p. 1519-1542.
84. Moon, R.J., et al., *Cellulose nanomaterials review: structure, properties and nanocomposites.* Chemical Society Reviews, 2011. **40**(7): p. 3941-3994.
85. Wu, Z.-Y., et al., *Bacterial Cellulose: A Robust Platform for Design of Three Dimensional Carbon-Based Functional Nanomaterials.* Accounts of Chemical Research, 2016. **49**(1): p. 96-105.
86. Klemm, D., et al., *Cellulose: Fascinating Biopolymer and Sustainable Raw Material.* Angewandte Chemie International Edition, 2005. **44**(22): p. 3358-3393.
87. Roy, D., et al., *Cellulose modification by polymer grafting: a review.* Chemical Society Reviews, 2009. **38**(7): p. 2046-2064.
88. Joubert, F., et al., *The preparation of graft copolymers of cellulose and cellulose derivatives using ATRP under homogeneous reaction conditions.* Chemical Society Reviews, 2014. **43**(20): p. 7217-7235.
89. Sisson, W.A., *X-ray studies regarding the structure and behavior of native cellulose membranes.* Chemical Reviews, 1940. **26**(2): p. 187-201.
90. Heinze, T. and A. Koschella, *Carboxymethyl Ethers of Cellulose and Starch – A Review.* Macromolecular Symposia, 2005. **223**(1): p. 13-40.
91. Gericke, M., J. Trygg, and P. Fardim, *Functional Cellulose Beads: Preparation, Characterization, and Applications.* Chemical Reviews, 2013. **113**(7): p. 4812-4836.
92. Foster, E.J., et al., *Current characterization methods for cellulose nanomaterials.* Chemical Society Reviews, 2018. **47**(8): p. 2609-2679.
93. Pinkert, A., et al., *Ionic Liquids and Their Interaction with Cellulose.* Chemical Reviews, 2009. **109**(12): p. 6712-6728.
94. Wang, H., G. Gurau, and R.D. Rogers, *Ionic liquid processing of cellulose.* Chemical Society Reviews, 2012. **41**(4): p. 1519-1537.
95. Schwarz, W., *The cellulosome and cellulose degradation by anaerobic bacteria.* Applied Microbiology and Biotechnology, 2001. **56**(5): p. 634-649.
96. Pérez, J., et al., *Biodegradation and biological treatments of cellulose, hemicellulose and lignin: an overview.* International Microbiology, 2002. **5**(2): p. 53-63.
97. Wang, A. and T. Zhang, *One-Pot Conversion of Cellulose to Ethylene Glycol with Multifunctional Tungsten-Based Catalysts.* Accounts of Chemical Research, 2013. **46**(7): p. 1377-1386.

98. Barta, K. and P.C. Ford, *Catalytic Conversion of Nonfood Woody Biomass Solids to Organic Liquids.* Accounts of Chemical Research, 2014. **47**(5): p. 1503-1512.
99. Esposito, D. and M. Antonietti, *Redefining biorefinery: the search for unconventional building blocks for materials.* Chemical Society Reviews, 2015. **44**(16): p. 5821-5835.
100. Zhang, X., K. Wilson, and A.F. Lee, *Heterogeneously Catalyzed Hydrothermal Processing of C5–C6 Sugars.* Chemical Reviews, 2016. **116**(19): p. 12328-12368.
101. Zhang, Z., J. Song, and B. Han, *Catalytic Transformation of Lignocellulose into Chemicals and Fuel Products in Ionic Liquids.* Chemical Reviews, 2017. **117**(10): p. 6834-6880.
102. Shrotri, A., H. Kobayashi, and A. Fukuoka, *Cellulose Depolymerization over Heterogeneous Catalysts.* Accounts of Chemical Research, 2018. **51**(3): p. 761-768.
103. Lynd, L.R., et al., *Microbial Cellulose Utilization: Fundamentals and Biotechnology.* Microbiology and Molecular Biology Reviews, 2002. **66**(3): p. 506.
104. Kumar, P., et al., *Methods for Pretreatment of Lignocellulosic Biomass for Efficient Hydrolysis and Biofuel Production.* Industrial & Engineering Chemistry Research, 2009. **48**(8): p. 3713-3729.
105. Chen, H., et al., *A review on the pretreatment of lignocellulose for high-value chemicals.* Fuel Processing Technology, 2017. **160**: p. 196-206.
106. Liu, C., et al., *Catalytic fast pyrolysis of lignocellulosic biomass.* Chemical Society Reviews, 2014. **43**(22): p. 7594-7623.
107. Arora, P. and Z. Zhang, *Battery Separators.* Chemical Reviews, 2004. **104**(10): p. 4419-4462.
108. Ummartyotin, S. and H. Manuspiya, *A critical review on cellulose: From fundamental to an approach on sensor technology.* Renewable and Sustainable Energy Reviews, 2015. **41**: p. 402-412.
109. Lavoine, N. and L. Bergström, *Nanocellulose-based foams and aerogels: processing, properties, and applications.* Journal of Materials Chemistry A, 2017. **5**(31): p. 16105-16117.
110. Chen, W., et al., *Nanocellulose: a promising nanomaterial for advanced electrochemical energy storage.* Chemical Society Reviews, 2018. **47**(8): p. 2837-2872.
111. Chen, C. and L. Hu, *Nanocellulose toward Advanced Energy Storage Devices: Structure and Electrochemistry.* Accounts of Chemical Research, 2018. **51**(12): p. 3154-3165.
112. Zhou, S., et al., *Cladophora Cellulose: Unique Biopolymer Nanofibrils for Emerging Energy, Environmental, and Life Science Applications.* Accounts of Chemical Research, 2019. **52**(8): p. 2232-2243.
113. Cosgrove, D.J., *Re-constructing our models of cellulose and primary cell wall assembly.* Current Opinion in Plant Biology, 2014. **22**: p. 122-131.
114. Smithers, E.T., J.X. Luo, and R.J. Dyson, *Mathematical principles and models of plant growth mechanics: from cell wall dynamics to tissue morphogenesis.* Journal of Experimental Botany, 2019. **70**(14): p. 3587-3599.
115. Zhang, Y.Q., et al., *Recent progress in theoretical and computational studies on the utilization of lignocellulosic materials.* Green Chemistry, 2019. **21**(1): p. 9-35.
116. Beckham, G.T., et al., *Towards a molecular-level theory of carbohydrate processivity in glycoside hydrolases.* Current Opinion in Biotechnology, 2014. **27**: p. 96-106.
117. Toukach, F.V. and V.P. Ananikov, *Recent advances in computational predictions of NMR parameters for the structure elucidation of carbohydrates: methods and limitations.* Chemical Society Reviews, 2013. **42**(21): p. 8376-8415.

118. Guan, H., Z. Cheng, and X. Wang, *Highly Compressible Wood Sponges with a Spring-like Lamellar Structure as Effective and Reusable Oil Absorbents.* ACS Nano, 2018. **12**(10): p. 10365-10373.
119. Fu, Q., et al., *Wood Nanotechnology for Strong, Mesoporous, and Hydrophobic Biocomposites for Selective Separation of Oil/Water Mixtures.* ACS Nano, 2018. **12**(3): p. 2222-2230.
120. Vidiella del Blanco, M., E.J. Fischer, and E. Cabane, *Underwater Superoleophobic Wood Cross Sections for Efficient Oil/Water Separation.* Advanced Materials Interfaces, 2017. **4**(21): p. 1700584.
121. Keplinger, T., X. Wang, and I. Burgert, *Nanofibrillated cellulose composites and wood derived scaffolds for functional materials.* Journal of Materials Chemistry A, 2019. **7**(7): p. 2981-2992.
122. Rongpipi, S., et al., *Progress and Opportunities in the Characterization of Cellulose – An Important Regulator of Cell Wall Growth and Mechanics.* Frontiers in Plant Science, 2019. **9**(1894).
123. O'Sullivan, A.C., *Cellulose: the structure slowly unravels.* Cellulose, 1997. **4**(3): p. 173-207.
124. Wada, M., L. Heux, and J. Sugiyama, *Polymorphism of Cellulose I Family: Reinvestigation of Cellulose IVI.* Biomacromolecules, 2004. **5**(4): p. 1385-1391.
125. Newman, R.H., *Simulation of X-ray diffractograms relevant to the purported polymorphs cellulose IVI and IVII.* Cellulose, 2008. **15**(6): p. 769-778.
126. Nishiyama, Y., et al., *Neutron Crystallography, Molecular Dynamics, and Quantum Mechanics Studies of the Nature of Hydrogen Bonding in Cellulose Iβ.* Biomacromolecules, 2008. **9**(11): p. 3133-3140.
127. Lehtiö, J., et al., *The binding specificity and affinity determinants of family 1 and family 3 cellulose binding modules.* Proceedings of the National Academy of Sciences, 2003. **100**(2): p. 484.
128. Malaspina, D.C. and J. Faraudo, *Molecular insight into the wetting behavior and amphiphilic character of cellulose nanocrystals.* Advances in Colloid and Interface Science, 2019. **267**: p. 15-25.
129. Sugiyama, J., J. Persson, and H. Chanzy, *Combined infrared and electron diffraction study of the polymorphism of native celluloses.* Macromolecules, 1991. **24**(9): p. 2461-2466.
130. Horii, F., A. Hirai, and R. Kitamaru, *CP/MAS carbon-13 NMR spectra of the crystalline components of native celluloses.* Macromolecules, 1987. **20**(9): p. 2117-2120.
131. Nishiyama, Y., et al., *Crystal structure and hydrogen bonding system in cellulose 1(alpha), from synchrotron X-ray and neutron fiber diffraction.* Journal of the American Chemical Society, 2003. **125**(47): p. 14300-14306.
132. Nishiyama, Y., P. Langan, and H. Chanzy, *Crystal structure and hydrogen-bonding system in cellulose 1 beta from synchrotron X-ray and neutron fiber diffraction.* Journal of the American Chemical Society, 2002. **124**(31): p. 9074-9082.
133. Langan, P., Y. Nishiyama, and H. Chanzy, *A revised structure and hydrogen-bonding system in cellulose II from a neutron fiber diffraction analysis.* Journal of the American Chemical Society, 1999. **121**(43): p. 9940-9946.
134. Langan, P., Y. Nishiyama, and H. Chanzy, *X-ray Structure of Mercerized Cellulose II at 1 Å Resolution.* Biomacromolecules, 2001. **2**(2): p. 410-416.

135. Kim, N.-H., et al., *Molecular Directionality in Cellulose Polymorphs.* Biomacromolecules, 2006. **7**(1): p. 274-280.
136. Yokota, S., et al., *Cellulose I Nanolayers Designed by Self-Assembly of its Thiosemicarbazone on a Gold Substrate.* Advanced Materials, 2007. **19**(20): p. 3368-3370.
137. Barry, A.J., F.C. Peterson, and A.J. King, *x-Ray Studies of Reactions of Cellulose in Non-Aqueous Systems. I. Interaction of Cellulose and Liquid Ammonia1.* Journal of the American Chemical Society, 1936. **58**(2): p. 333-337.
138. Clark, G.L. and E.A. Parker, *An X-ray Diffraction Study of the Action of Liquid Ammonia on Cellulose and Its Derivatives.* The Journal of Physical Chemistry, 1937. **41**(6): p. 777-786.
139. Wada, M., et al., *Improved Structural Data of Cellulose IIII Prepared in Supercritical Ammonia.* Macromolecules, 2001. **34**(5): p. 1237-1243.
140. Sarko, A., J. Southwick, and J. Hayashi, *Packing Analysis of Carbohydrates and Polysaccharides. 7. Crystal Structure of Cellulose IIII and Its Relationship to Other Cellulose Polymorphs.* Macromolecules, 1976. **9**(5): p. 857-863.
141. Wada, M., et al., *Cellulose IIII Crystal Structure and Hydrogen Bonding by Synchrotron X-ray and Neutron Fiber Diffraction.* Macromolecules, 2004. **37**(23): p. 8548-8555.
142. Ford, Z.M., et al., *Determining the crystal structure of cellulose IIII by modeling.* Carbohydrate Research, 2005. **340**(5): p. 827-833.
143. Hori, R. and M. Wada, *The thermal expansion of cellulose II and IIIII crystals.* Cellulose, 2006. **13**(3): p. 281-290.
144. Wada, M., et al., *X-ray Crystallographic, Scanning Microprobe X-ray Diffraction, and Cross-Polarized/Magic Angle Spinning 13C NMR Studies of the Structure of Cellulose IIIII.* Biomacromolecules, 2009. **10**(2): p. 302-309.
145. Hutino, K. and I. Sakurada, *Über die Existenz einer vierten Modifikation der Cellulose.* Naturwissenschaften, 1940. **28**(36): p. 577-578.
146. Kulshreshtha, A.K., *2—A Review Of The Literature On The Formation Of Cellulose Iv, Its Structure, And Its Significance In The Technology Of Rayon Manufacture.* The Journal of The Textile Institute, 1979. **70**(1): p. 13-18.
147. Zugenmaier, P., *Conformation and packing of various crystalline cellulose fibers.* Progress in Polymer Science, 2001. **26**(9): p. 1341-1417.
148. Dri, F.L., et al., *Anisotropy and temperature dependence of structural, thermodynamic, and elastic properties of crystalline cellulose I-beta: a first-principles investigation.* Modelling and Simulation in Materials Science and Engineering, 2014. **22**(8).
149. Wada, M., Y. Nishiyama, and P. Langan, *X-ray Structure of Ammonia−Cellulose I: New Insights into the Conversion of Cellulose I to Cellulose IIII.* Macromolecules, 2006. **39**(8): p. 2947-2952.
150. Nishiyama, Y., *Structure and properties of the cellulose microfibril.* Journal of Wood Science, 2009. **55**(4): p. 241-249.
151. Kuutti, L., et al., *Identification and surface structure of crystalline cellulose studied by atomic force microscopy.* Journal of Microscopy, 1995. **178**(1): p. 1-6.
152. Baker, A.A., et al., *New Insight into Cellulose Structure by Atomic Force Microscopy Shows the Iα Crystal Phase at Near-Atomic Resolution.* Biophysical Journal, 2000. **79**(2): p. 1139-1145.

153. Li, Y., M. Lin, and J.W. Davenport, *Ab Initio Studies of Cellulose I: Crystal Structure, Intermolecular Forces, and Interactions with Water.* The Journal of Physical Chemistry C, 2011. **115**(23): p. 11533-11539.
154. Reiling, S. and J. Brickmann, *Theoretical investigations on the structure and physical properties of cellulose.* Macromolecular Theory and Simulations, 1995. **4**(4): p. 725-743.
155. Marhofer, R.J., S. Reiling, and J. Brickmann, *Computer simulations of crystal structures and elastic properties of cellulose.* Berichte Der Bunsen-Gesellschaft-Physical Chemistry Chemical Physics, 1996. **100**(8): p. 1350-1354.
156. Eichhorn, S.J. and G.R. Davies, *Modelling the crystalline deformation of native and regenerated cellulose.* Cellulose, 2006. **13**(3): p. 291-307.
157. Maurer, R.J., A.F. Sax, and V. Ribitsch, *Molecular simulation of surface reorganization and wetting in crystalline cellulose I and II.* Cellulose, 2013. **20**(1): p. 25-42.
158. Chen, P., Y. Nishiyama, and K. Mazeau, *Atomic partial charges and one Lennard-Jones parameter crucial to model cellulose allomorphs.* Cellulose, 2014. **21**(4): p. 2207-2217.
159. Vietor, R.J., et al., *A priori crystal structure prediction of native celluloses.* Biopolymers, 2000. **54**(5): p. 342-354.
160. Bučko, T., et al., *Improved Description of the Structure of Molecular and Layered Crystals: Ab Initio DFT Calculations with van der Waals Corrections.* The Journal of Physical Chemistry A, 2010. **114**(43): p. 11814-11824.
161. Lee, C.M., et al., *Hydrogen-Bonding Network and OH Stretch Vibration of Cellulose: Comparison of Computational Modeling with Polarized IR and SFG Spectra.* Journal of Physical Chemistry B, 2015. **119**(49): p. 15138-15149.
162. Lee, C.M., et al., *Sum-Frequency-Generation Vibration Spectroscopy and Density Functional Theory Calculations with Dispersion Corrections (DFT-D2) for Cellulose Iα and Iβ.* The Journal of Physical Chemistry B, 2013. **117**(22): p. 6681-6692.
163. Dri, F.L., et al., *Anisotropy of the elastic properties of crystalline cellulose I-beta from first principles density functional theory with Van der Waals interactions.* Cellulose, 2013. **20**(6): p. 2703-2718.
164. Kroon-Batenburg, L.M.J. and J. Kroon, *The crystal and molecular structures of cellulose I and II.* Glycoconjugate Journal, 1997. **14**(5): p. 677-690.
165. Bergenstrahle, M., L.A. Berglund, and K. Mazeau, *Thermal response in crystalline I beta cellulose: A molecular dynamics study.* Journal of Physical Chemistry B, 2007. **111**(30): p. 9138-9145.
166. Chen, P., Y. Nishiyama, and K. Mazeau, *Torsional Entropy at the Origin of the Reversible Temperature-Induced Phase Transition of Cellulose.* Macromolecules, 2012. **45**(1): p. 362-368.
167. Molnar, G., et al., *Cellulose crystals plastify by localized shear.* Proceedings of the National Academy of Sciences of the United States of America, 2018. **115**(28): p. 7260-7265.
168. Matthews, J.F., et al., *Computer simulation studies of microcrystalline cellulose I beta.* Carbohydrate Research, 2006. **341**(1): p. 138-152.
169. Matthews, J.F., et al., *Comparison of Cellulose I beta Simulations with Three Carbohydrate Force Fields.* Journal of Chemical Theory and Computation, 2012. **8**(2): p. 735-748.

170. Djahedi, C., L.A. Berglund, and J. Wohlert, *Molecular deformation mechanisms in cellulose allomorphs and the role of hydrogen bonds.* Carbohydrate Polymers, 2015. **130**: p. 175-182.
171. Yao, Y.T., K.L. Alderson, and A. Alderson, *Modeling of negative Poisson's ratio (auxetic) crystalline cellulose I-beta.* Cellulose, 2016. **23**(6): p. 3429-3448.
172. Dri, F.L., et al., *Evaluation of reactive force fields for prediction of the thermo-mechanical properties of cellulose I-beta.* Computational Materials Science, 2015. **109**: p. 330-340.
173. Qiao, Q., X. Li, and L. Huang, *Crystalline Cellulose under Pyrolysis Conditions: The Structure–Property Evolution via Reactive Molecular Dynamics Simulations.* Journal of Chemical & Engineering Data, 2020. **65**(2): p. 360-372.
174. Zhang, Q.O., et al., *A molecular dynamics study of the thermal response of crystalline cellulose I beta.* Cellulose, 2011. **18**(2): p. 207-221.
175. Mazeau, K. and L. Heux, *Molecular dynamics simulations of bulk native crystalline and amorphous structures of cellulose.* Journal of Physical Chemistry B, 2003. **107**(10): p. 2394-2403.
176. Mazeau, K., *Structural micro-heterogeneities of crystalline I beta-cellulose.* Cellulose, 2005. **12**(4): p. 339-349.
177. Neyertz, S., et al., *A new all-atom force field for crystalline cellulose I.* Journal of Applied Polymer Science, 2000. **78**(11): p. 1939-1946.
178. Ganster, J. and J. Blackwell, *NpH-MD-simulations of the elastic moduli of cellulose II at room temperature.* Journal of Molecular Modeling, 1996. **2**(9): p. 278-285.
179. Gardner, K.H. and J. Blackwell, *The structure of native cellulose.* Biopolymers, 1974. **13**(10): p. 1975-2001.
180. Sugiyama, J., R. Vuong, and H. Chanzy, *Electron diffraction study on the two crystalline phases occurring in native cellulose from an algal cell wall.* Macromolecules, 1991. **24**(14): p. 4168-4175.
181. Finkenstadt, V.L. and R.P. Millane, *Crystal Structure of Valonia Cellulose Iβ.* Macromolecules, 1998. **31**(22): p. 7776-7783.
182. Woodcock, C. and A. Sarko, *Packing Analysis of Carbohydrates and Polysaccharides. 11. Molecular and Crystal Structure of Native Ramie Cellulose.* Macromolecules, 1980. **13**(5): p. 1183-1187.
183. Okano, T. and A. Koyanagi, *Structural variation of native cellulose related to its source.* Biopolymers, 1986. **25**(5): p. 851-861.
184. Sarko, A. and R. Muggli, *Packing Analysis of Carbohydrates and Polysaccharides. III. Valonia Cellulose and Cellulose II.* Macromolecules, 1974. **7**(4): p. 486-494.
185. Honjo, G. and M. Watanabe, *Examination of Cellulose Fibre by the Low-Temperature Specimen Method of Electron Diffraction and Electron Microscopy.* Nature, 1958. **181**(4605): p. 326-328.
186. Takahashi, Y. and H. Matsunaga, *Crystal structure of native cellulose.* Macromolecules, 1991. **24**(13): p. 3968-3969.
187. Meyer, K.H. and L. Misch, *Positions des atomes dans le nouveau modèle spatial de la cellulose.* Helvetica Chimica Acta, 1937. **20**(1): p. 232-244.
188. Langan, P., et al., *Synchrotron X-ray structures of cellulose Iβ and regenerated cellulose II at ambient temperature and 100 K.* Cellulose, 2005. **12**(6): p. 551-562.
189. Thomas, L.H., et al., *Structure of Cellulose Microfibrils in Primary Cell Walls from Collenchyma.* Plant Physiology, 2013. **161**(1): p. 465.

190. Kolpak, F.J. and J. Blackwell, *Determination of the Structure of Cellulose II.* Macromolecules, 1976. **9**(2): p. 273-278.
191. Kolpak, F.J., M. Weih, and J. Blackwell, *Mercerization of cellulose: 1. Determination of the structure of Mercerized cotton.* Polymer, 1978. **19**(2): p. 123-131.
192. Stipanovic, A.J. and A. Sarko, *Packing Analysis of Carbohydrates and Polysaccharides. 6. Molecular and Crystal Structure of Regenerated Cellulose II.* Macromolecules, 1976. **9**(5): p. 851-857.
193. Wellard, H.J., *Variation in the lattice spacing of cellulose.* Journal of Polymer Science, 1954. **13**(71): p. 471-476.
194. Wohlert, J., *Vapor Pressures and Heats of Sublimation of Crystalline β-Cellobiose from Classical Molecular Dynamics Simulations with Quantum Mechanical Corrections.* The Journal of Physical Chemistry B, 2014. **118**(20): p. 5365-5373.
195. Bergenstrahle, M., et al., *Simulation studies of the insolubility of cellulose.* Carbohydrate Research, 2010. **345**(14): p. 2060-2066.
196. Miyamoto, H., U. Schnupf, and J.W. Brady, *Water Structuring over the Hydrophobic Surface of Cellulose.* Journal of Agricultural and Food Chemistry, 2014. **62**(46): p. 11017-11023.
197. Tolmachev, D.A. and N.V. Lukasheva, *Study of the process of mineralization of nanofibrils of native bacterial cellulose in solutions of mineral ions: Modeling via the method of molecular dynamics.* Polymer Science Series A, 2014. **56**(4): p. 545-557.
198. Lukasheva, N.V. and D.A. Tolmachev, *Cellulose Nanofibrils and Mechanism of their Mineralization in Biomimetic Synthesis of Hydroxyapatite/Native Bacterial Cellulose Nanocomposites: Molecular Dynamics Simulations.* Langmuir, 2016. **32**(1): p. 125-134.
199. Kasat, R.B., et al., *Effect of the solute molecular structure on its enantioresolution on cellulose tris(3,5-dimethylphenylcarbamate).* Journal of Chromatography B-Analytical Technologies in the Biomedical and Life Sciences, 2008. **875**(1): p. 81-92.
200. Prusskii, A.I. and L.A. Aleshina, *Computer simulation of the atomic structure of regenerated cellulose.* Polymer Science Series A, 2016. **58**(3): p. 386-398.
201. Zhmud, B.V., E. Poptoshev, and R.J. Pugh, *Role of hydration and conformational changes in adsorption dynamics of ethyl(hydroxyethyl)cellulose at the air/solution interface.* Langmuir, 1998. **14**(13): p. 3620-3624.
202. Majidi, R., H.R. Taghiyari, and M. Ekhlasi, *Adsorption Patterns of Helium on Carbon and Cellulose Nanotubes: Molecular Dynamics Simulations.* Nano, 2017. **12**(3).
203. Majidi, R., H.R. Taghiyari, and D. Abdolmaleki, *Molecular Dynamics Simulation Evaluating the Hydrophilicity of Nanowollastonite on Cellulose.* Journal of Structural Chemistry, 2019. **60**(9): p. 1520-1527.
204. Santiago Cintrón, M., G.P. Johnson, and A.D. French, *Young's modulus calculations for cellulose Iβ by MM3 and quantum mechanics.* Cellulose, 2011. **18**(3): p. 505-516.
205. Yang, Y.M., et al., *Can carboxymethyl cellulose molecules bind swelling montmorillonite layers in Water?* Colloids and Surfaces a-Physicochemical and Engineering Aspects, 2018. **553**: p. 515-519.
206. Tanaka, F. and T. Iwata, *Estimation of the elastic modulus of cellulose crystal by molecular mechanics simulation.* Cellulose, 2006. **13**(5): p. 509-517.
207. Queyroy, S., F. Muller-Plathe, and D. Brown, *Molecular dynamics Simulations of cellulose oligomers: Conformational analysis.* Macromolecular Theory and Simulations, 2004. **13**(5): p. 427-440.

208. Dou, Y.B., et al., *Transparent, Flexible Films Based on Layered Double Hydroxide/Cellulose Acetate with Excellent Oxygen Barrier Property.* Advanced Functional Materials, 2014. **24**(4): p. 514-521.
209. Uto, T., et al., *Molecular dynamics simulations of theoretical cellulose nanotube models.* Carbohydrate Polymers, 2018. **190**: p. 331-338.
210. Tashiro, K. and M. Kobayashi, *Theoretical evaluation of three-dimensional elastic constants of native and regenerated celluloses: role of hydrogen bonds.* Polymer, 1991. **32**(8): p. 1516-1526.
211. Tashiro, K. and M. Kobayashi, *Calculation of crystallite modulus of native cellulose.* Polymer Bulletin, 1985. **14**(3): p. 213-218.
212. Bazooyar, F., F.A. Momany, and K. Bolton, *Validating empirical force fields for molecular-level simulation of cellulose dissolution.* Computational and Theoretical Chemistry, 2012. **984**: p. 119-127.
213. Wang, X.B., et al., *Selection of Optimal Polymerization Degree and Force Field in the Molecular Dynamics Simulation of Insulating Paper Cellulose.* Energies, 2017. **10**(9).
214. Murillo, J.D., et al., *Biomass Pyrolysis Kinetics: A Review Of Molecular-Scale Modeling Contributions.* Brazilian Journal of Chemical Engineering, 2017. **34**: p. 1-18.
215. Hadden, J.A., A.D. French, and R.J. Woods, *Unraveling Cellulose Microfibrils: A Twisted Tale.* Biopolymers, 2013. **99**(10): p. 746-756.
216. Bregado, J.L., et al., *Amorphous paracrystalline structures from native crystalline cellulose: A molecular dynamics protocol.* Fluid Phase Equilibria, 2019. **491**: p. 56-76.
217. Matthews, J.F., et al., *High-Temperature Behavior of Cellulose I.* Journal of Physical Chemistry B, 2011. **115**(10): p. 2155-2166.
218. Hollingsworth, S.A. and R.O. Dror, *Molecular Dynamics Simulation for All.* Neuron, 2018. **99**(6): p. 1129-1143.
219. Fernandes, A.N., et al., *Nanostructure of cellulose microfibrils in spruce wood.* Proceedings of the National Academy of Sciences, 2011. **108**(47): p. E1195.
220. Oehme, D.P., H. Yang, and J.D. Kubicki, *An evaluation of the structures of cellulose generated by the CHARMM force field: comparisons to in planta cellulose.* Cellulose, 2018. **25**(7): p. 3755-3777.
221. Oehme, D.P., et al., *Gaining insight into cell wall cellulose macrofibril organisation by simulating microfibril adsorption.* Cellulose, 2015. **22**(6): p. 3501-3520.
222. Yu, L., et al., *The Patterned Structure of Galactoglucomannan Suggests It May Bind to Cellulose in Seed Mucilage.* Plant Physiology, 2018. **178**(3): p. 1011-1026.
223. Kubicki, J.D., et al., *The Shape of Native Plant Cellulose Microfibrils.* Scientific Reports, 2018. **8**: p. 8.
224. Domin, D., et al., *Breaking down cellulose fibrils with a mid-infrared laser.* Cellulose, 2018. **25**(10): p. 5553-5568.
225. Ding, S.-Y. and M.E. Himmel, *The Maize Primary Cell Wall Microfibril: A New Model Derived from Direct Visualization.* Journal of Agricultural and Food Chemistry, 2006. **54**(3): p. 597-606.
226. Mazeau, K., *Structural Micro-heterogeneities of Crystalline Iβ-cellulose.* Cellulose, 2005. **12**(4): p. 339-349.
227. Matthews, J.F., M.E. Himmel, and M.F. Crowley, *Conversion of cellulose Iα to Iβ via a high temperature intermediate (I-HT) and other cellulose phase transformations.* Cellulose, 2012. **19**(1): p. 297-306.

228. Gross, A.S. and J.W. Chu, *On the Molecular Origins of Biomass Recalcitrance: The Interaction Network and Solvation Structures of Cellulose Microfibrils.* Journal of Physical Chemistry B, 2010. **114**(42): p. 13333-13341.
229. Gross, A.S., A.T. Bell, and J.W. Chu, *Thermodynamics of Cellulose Solvation in Water and the Ionic Liquid 1-Butyl-3-Methylimidazolim Chloride.* Journal of Physical Chemistry B, 2011. **115**(46): p. 13433-13440.
230. Chen, P., et al., *Diversity of potential hydrogen bonds in cellulose I revealed by molecular dynamics simulation.* Cellulose, 2014. **21**(2): p. 897-908.
231. Oehme, D.P., et al., *Unique Aspects of the Structure and Dynamics of Elementary Iβ Cellulose Microfibrils Revealed by Computational Simulations.* Plant Physiology, 2015. **168**(1): p. 3.
232. Hardy, B.J. and A. Sarko, *Conformational analysis and molecular dynamics simulation of cellobiose and larger cellooligomers.* Journal of Computational Chemistry, 1993. **14**(7): p. 831-847.
233. Heiner, A.P. and O. Teleman, *Structural reporter parameters for the characterisation of crystalline cellulose.* Pure and Applied Chemistry, 1996. **68**(11): p. 2187-2192.
234. KroonBatenburg, L.M.J., B. Bouma, and J. Kroon, *Stability of cellulose structures studied by MD simulations. Could mercerized cellulose II be parallel?* Macromolecules, 1996. **29**(17): p. 5695-5699.
235. Tanaka, F. and N. Fukui, *Molecular motion of an isolated single chain cellulose molecule.* Sen-I Gakkaishi, 2004. **60**(9): p. 261-265.
236. Hardy, B.J. and A. Sarko, *Molecular dynamics simulations and diffraction-based analysis of the native cellulose fibre: Structural modelling of the I-alpha and I-beta phases and their interconversion.* Polymer, 1996. **37**(10): p. 1833-1839.
237. Cai, L., Y. Liu, and H.J. Liang, *Impact of hydrogen bonding on inclusion layer of urea to cellulose: Study of molecular dynamics simulation.* Polymer, 2012. **53**(5): p. 1124-1130.
238. Tang, C., et al., *Thermal Stability of Modified Insulation Paper Cellulose Based on Molecular Dynamics Simulation.* Energies, 2017. **10**(3).
239. Zhang, S., et al., *Thermal stability and dielectric properties of nano-SiO2-doped cellulose.* Applied Physics Letters, 2017. **111**(1): p. 4.
240. Zhang, S., et al., *Improvement of thermal stability of insulation paper cellulose by modified polysiloxane grafting.* Applied Physics Letters, 2016. **109**(17): p. 4.
241. Wang, X.B., et al., *Thermal stability improvement of polysiloxane-grafted insulating paper cellulose in micro-water environment.* Aip Advances, 2018. **8**(10): p. 9.
242. Heiner, A.P., J. Sugiyama, and O. Teleman, *Crystalline cellulose I-alpha and I-beta studied by molecular-dynamics simulation.* Carbohydrate Research, 1995. **273**(2): p. 207-223.
243. Belton, P.S., et al., *High-resolution solid-state carbon-13 nuclear magnetic resonance spectroscopy of tunicin, an animal cellulose.* Macromolecules, 1989. **22**(4): p. 1615-1617.
244. Agarwal, V., et al., *Simulating infrared spectra and hydrogen bonding in cellulose I beta at elevated temperatures.* Journal of Chemical Physics, 2011. **135**(13): p. 13.
245. Matthews, J.F., et al., *Computer simulation studies of microcrystalline cellulose Iβ.* Carbohydrate Research, 2006. **341**(1): p. 138-152.
246. Yui, T., et al., *Swelling behavior of the cellulose I beta crystal models by molecular dynamics.* Carbohydrate Research, 2006. **341**(15): p. 2521-2530.

247. Chen, P., et al., *Alternative hydrogen bond models of cellulose II and IIII based on molecular force-fields and density functional theory.* Cellulose, 2015. **22**(3): p. 1485-1493.
248. Djahedi, C., et al., *Role of hydrogen bonding in cellulose deformation: the leverage effect analyzed by molecular modeling.* Cellulose, 2016. **23**(4): p. 2315-2323.
249. Kulasinski, K., et al., *A comparative molecular dynamics study of crystalline, paracrystalline and amorphous states of cellulose.* Cellulose, 2014. **21**(3): p. 1103-1116.
250. Diaz, J.A., et al., *Thermal Conductivity in Nanostructured Films: From Single Cellulose Nanocrystals to Bulk Films.* Biomacromolecules, 2014. **15**(11): p. 4096-4101.
251. van Duin, A.C.T., et al., *ReaxFF: A reactive force field for hydrocarbons.* Journal of Physical Chemistry A, 2001. **105**(41): p. 9396-9409.
252. Monti, S., et al., *Exploring the conformational and reactive dynamics of biomolecules in solution using an extended version of the glycine reactive force field.* Physical Chemistry Chemical Physics, 2013. **15**(36): p. 15062-15077.
253. Zhang, W.W. and A.C.T. van Duin, *Improvement of the ReaxFF Description for Functionalized Hydrocarbon/Water Weak Interactions in the Condensed Phase.* Journal of Physical Chemistry B, 2018. **122**(14): p. 4083-4092.
254. Zhang, W.W. and A.C.T. van Duin, *ReaxFF Reactive Molecular Dynamics Simulation of Functionalized Poly(phenylene oxide) Anion Exchange Membrane.* Journal of Physical Chemistry C, 2015. **119**(49): p. 27727-27736.
255. Castro-Marcano, F., et al., *Combustion of an Illinois No. 6 coal char simulated using an atomistic char representation and the ReaxFF reactive force field.* Combustion and Flame, 2012. **159**(3): p. 1272-1285.
256. Zhang, J.L., et al., *The effect of supercritical water on coal pyrolysis and hydrogen production: A combined ReaxFF and DFT study.* Fuel, 2013. **108**: p. 682-690.
257. Russo, M.F. and A.C.T. van Duin, *Atomistic-scale simulations of chemical reactions: Bridging from quantum chemistry to engineering.* Nuclear Instruments & Methods in Physics Research Section B-Beam Interactions with Materials and Atoms, 2011. **269**(14): p. 1549-1554.
258. Mortier, W.J., S.K. Ghosh, and S. Shankar, *Electronegativity equalization method for the calculation of atomic charges in molecules.* Journal of the American Chemical Society, 1986. **108**(15): p. 4315-4320.
259. Janssens, G.O.A., et al., *COMPARISON OF CLUSTER AND INFINITE CRYSTAL CALCULATIONS ON ZEOLITES WITH THE ELECTRONEGATIVITY EQUALIZATION METHOD (EEM).* Journal of Physical Chemistry, 1995. **99**(10): p. 3251-3258.
260. Huang, L.L., et al., *Controllable atomistic graphene oxide model and its application in hydrogen sulfide removal.* Journal of Chemical Physics, 2013. **139**(19).
261. Bagri, A., et al., *Structural evolution during the reduction of chemically derived graphene oxide.* Nature Chemistry, 2010. **2**(7): p. 581-587.
262. Senftle, T.P., et al., *The ReaxFF reactive force-field: development, applications and future directions.* 2016. **2**: p. 15011.
263. Liang, T., et al., *Reactive Potentials for Advanced Atomistic Simulations.* Annual Review of Materials Research, Vol 43, 2013. **43**: p. 109-129.
264. Li, P. and K.M. Merz, *Metal Ion Modeling Using Classical Mechanics.* Chemical Reviews, 2017. **117**(3): p. 1564-1686.

265. Agrawalla, S. and A.C.T. van Duin, *Development and Application of a ReaxFF Reactive Force Field for Hydrogen Combustion.* Journal of Physical Chemistry A, 2011. **115**(6): p. 960-972.
266. Chenoweth, K., et al., *Development and application of a ReaxFF reactive force field for oxidative dehydrogenation on vanadium oxide catalysts.* Journal of Physical Chemistry C, 2008. **112**(37): p. 14645-14654.
267. Chenoweth, K., A.C.T. van Duin, and W.A. Goddard, *ReaxFF reactive force field for molecular dynamics simulations of hydrocarbon oxidation.* Journal of Physical Chemistry A, 2008. **112**(5): p. 1040-1053.
268. Strachan, A., et al., *Shock waves in high-energy materials: The initial chemical events in nitramine RDX.* Physical Review Letters, 2003. **91**(9).
269. Budzien, J., A.P. Thompson, and S.V. Zybin, *Reactive Molecular Dynamics Simulations of Shock Through a Single Crystal of Pentaerythritol Tetranitrate.* Journal of Physical Chemistry B, 2009. **113**(40): p. 13142-13151.
270. Mattsson, T.R., et al., *First-principles and classical molecular dynamics simulation of shocked polymers.* Physical Review B, 2010. **81**(5).
271. Rahaman, O., et al., *Development of a ReaxFF Reactive Force Field for Glycine and Application to Solvent Effect and Tautomerization.* Journal of Physical Chemistry B, 2011. **115**(2): p. 249-261.
272. Chenoweth, K., et al., *Simulations on the thermal decomposition of a poly(dimethylsiloxane) polymer using the ReaxFF reactive force field.* Journal of the American Chemical Society, 2005. **127**(19): p. 7192-7202.
273. Leininger, J.P., C. Minot, and F. Lorant, *Two theoretical simulations of hydrocarbons thermal cracking: Reactive force field and density functional calculations.* Journal of Molecular Structure-Theochem, 2008. **852**(1-3): p. 62-70.
274. Liu, X.L., et al., *Study of high density polyethylene (HDPE) pyrolysis with reactive molecular dynamics.* Polymer Degradation and Stability, 2014. **104**: p. 62-70.
275. Sun, H., *COMPASS: An ab initio force-field optimized for condensed-phase applications - Overview with details on alkane and benzene compounds.* Journal of Physical Chemistry B, 1998. **102**(38): p. 7338-7364.
276. Kirschner, K.N., et al., *GLYCAM06: A generalizable Biomolecular force field. Carbohydrates.* Journal of Computational Chemistry, 2008. **29**(4): p. 622-655.
277. Diaz, J.A., et al., *Thermal Expansion of Self-Organized and Shear-Oriented Cellulose Nanocrystal Films.* Biomacromolecules, 2013. **14**(8): p. 2900-2908.
278. Wu, X.W., R.J. Moon, and A. Martini, *Crystalline cellulose elastic modulus predicted by atomistic models of uniform deformation and nanoscale indentation.* Cellulose, 2013. **20**(1): p. 43-55.
279. Wagner, R., et al., *Uncertainty quantification in nanomechanical measurements using the atomic force microscope.* Nanotechnology, 2011. **22**(45): p. 455703.
280. Wu, X.W., R.J. Moon, and A. Martini, *Atomistic Simulation of Frictional Sliding Between Cellulose I beta Nanocrystals.* Tribology Letters, 2013. **52**(3): p. 395-405.
281. Ni, B., K.-H. Lee, and S.B. Sinnott, *A reactive empirical bond order (REBO) potential for hydrocarbon–oxygen interactions.* Journal of Physics: Condensed Matter, 2004. **16**(41): p. 7261-7275.
282. Polvi, J., et al., *Primary Radiation Defect Production in Polyethylene and Cellulose.* Journal of Physical Chemistry B, 2012. **116**(47): p. 13932-13938.

283. Polvi, J. and K. Nordlund, *Low-energy irradiation effects in cellulose.* Journal of Applied Physics, 2014. **115**(2): p. 8.
284. Wu, X.W., R.J. Moon, and A. Martini, *Tensile strength of I beta crystalline cellulose predicted by molecular dynamics simulation.* Cellulose, 2014. **21**(4): p. 2233-2245.
285. Zheng, M., et al., *Initial reaction mechanisms of cellulose pyrolysis revealed by ReaxFF molecular dynamics.* Fuel, 2016. **177**: p. 130-141.
286. Paajanen, A. and J. Vaari, *High-temperature decomposition of the cellulose molecule: a stochastic molecular dynamics study.* Cellulose, 2017. **24**(7): p. 2713-2725.
287. Atmani, L., et al., *From cellulose to kerogen: molecular simulation of a geological process.* Chemical Science, 2017. **8**(12): p. 8325-8335.
288. Rismiller, S.C., et al., *Water assisted liquefaction of lignocellulose biomass by ReaxFF based molecular dynamic simulations.* Fuel, 2018. **215**: p. 835-843.
289. Wang, S., et al., *Co-pyrolysis mechanism of seaweed polysaccharides and cellulose based on macroscopic experiments and molecular simulations.* Bioresource Technology, 2017. **228**: p. 305-314.
290. Li, Y.Y., et al., *Hybridizing wood cellulose and graphene oxide toward high-performance fibers.* Npg Asia Materials, 2015. **7**: p. 10.
291. Mao, Q., et al., *Interface Strain Induced Hydrophobic Facet Suppression in Cellulose Nanocomposite Embedded with Highly Oxidized Monolayer Graphene Oxide.* Advanced Materials Interfaces, 2017. **4**(23): p. 11.
292. Zhu, C.T., S. Monti, and A.P. Mathew, *Cellulose Nanofiber-Graphene Oxide Biohybrids: Disclosing the Self-Assembly and Copper-Ion Adsorption Using Advanced Microscopy and ReaxFF Simulations.* Acs Nano, 2018. **12**(7): p. 7028-7038.
293. Beste, A., *ReaxFF Study of the Oxidation of Lignin Model Compounds for the Most Common Linkages in Softwood in View of Carbon Fiber Production.* Journal of Physical Chemistry A, 2014. **118**(5): p. 803-814.
294. Beste, A., *ReaxFF Study of the Oxidation of Softwood Lignin in View of Carbon Fiber Production.* Energy & Fuels, 2014. **28**(11): p. 7007-7013.
295. Chen, C., et al., *Reactive Molecular Dynamics Simulations of Biomass Pyrolysis and Combustion under Various Oxidative and Humidity Environments.* Industrial & Engineering Chemistry Research, 2017. **56**(43): p. 12276-12288.
296. Matsuo, M., et al., *Effect of orientation distribution and crystallinity on the measurement by x-ray diffraction of the crystal lattice moduli of cellulose I and II.* Macromolecules, 1990. **23**(13): p. 3266-3275.
297. Eichhorn, S.J., R.J. Young, and G.R. Davies, *Modeling Crystal and Molecular Deformation in Regenerated Cellulose Fibers.* Biomacromolecules, 2005. **6**(1): p. 507-513.
298. Sturcova, A., G.R. Davies, and S.J. Eichhorn, *Elastic modulus and stress-transfer properties of tunicate cellulose whiskers.* Biomacromolecules, 2005. **6**(2): p. 1055-1061.
299. Gupta, K.M., Z.Q. Hu, and J.W. Jiang, *Mechanistic understanding of interactions between cellulose and ionic liquids: A molecular simulation study.* Polymer, 2011. **52**(25): p. 5904-5911.
300. Wu, X.W., R.J. Moon, and A. Martini, *Calculation of single chain cellulose elasticity using fully atomistic modeling.* Tappi Journal, 2011. **10**(4): p. 37-42.
301. Plimpton, S., *Fast Parallel Algorithms for Short-Range Molecular Dynamics.* Journal of Computational Physics, 1995. **117**(1): p. 1-19.

302. Mishin, Y., et al., *Interatomic potentials for monoatomic metals from experimental data and ab initio calculations.* Physical Review B, 1999. **59**(5): p. 3393-3407.
303. Spearot, D.E., et al., *Tensile strength of 〈100〉 and 〈110〉 tilt bicrystal copper interfaces.* Acta Materialia, 2007. **55**(2): p. 705-714.
304. Tschopp, M.A., D.E. Spearot, and D.L. McDowell, *Atomistic simulations of homogeneous dislocation nucleation in single crystal copper.* Modelling and Simulation in Materials Science and Engineering, 2007. **15**(7): p. 693-709.
305. Tschopp, M.A. and D.L. McDowell, *Influence of single crystal orientation on homogeneous dislocation nucleation under uniaxial loading.* Journal of the Mechanics and Physics of Solids, 2008. **56**(5): p. 1806-1830.
306. Hossain, D., et al., *Molecular dynamics simulations of deformation mechanisms of amorphous polyethylene.* Polymer, 2010. **51**(25): p. 6071-6083.
307. Wang, Y.Y., et al., *The Relationship Between Dp, Fracture Degree And Mechanical Strength Of Cellulose I-Beta In Insulation Paper By Molecular Dynamic Simulations.* International Journal of Modern Physics B, 2013. **27**(31).
308. Wang, Y.Y., et al., *Influence Of Moisture On Mechanical Properties Of Cellulose Insulation Paper.* International Journal of Modern Physics B, 2014. **28**(7).
309. Zhu, M.Z., et al., *Mechanical property of hydrous amorphous cellulose studied by molecular dynamics.* Russian Journal of Physical Chemistry B, 2016. **10**(3): p. 524-530.
310. Kroonbatenburg, L.M.J., J. Kroon, and M.G. Northolt, *Chain Modulus And Intramolecular Hydrogen-Bonding In Native And Regenerated Cellulose Fibers.* Polymer Communications, 1986. **27**(10): p. 290-292.
311. Fan, C.F. and S.L. Hsu, *Application of the molecular simulation technique to generate the structure of an aromatic polysulfone system.* Macromolecules, 1991. **24**(23): p. 6244-6249.
312. Fan, C.F., et al., *Molecular Modeling of Polycarbonate. 1. Force Field, Static Structure, and Mechanical Properties.* Macromolecules, 1994. **27**(9): p. 2383-2391.
313. Chen, W., G.C. Lickfield, and C.Q. Yang, *Molecular modeling of cellulose in amorphous state. Part I: model building and plastic deformation study.* Polymer, 2004. **45**(3): p. 1063-1071.
314. Lacks, D.J. and G.C. Rutledge, *Simulation of the temperature dependence of mechanical properties of polyethylene.* The Journal of Physical Chemistry, 1994. **98**(4): p. 1222-1231.
315. Parrinello, M. and A. Rahman, *Strain fluctuations and elastic constants.* The Journal of Chemical Physics, 1982. **76**(5): p. 2662-2666.
316. Sinko, R., et al., *Dimensions of Biological Cellulose Nanocrystals Maximize Fracture Strength.* Acs Macro Letters, 2014. **3**(1): p. 64-69.
317. Wohlert, J., M. Bergenstrahle-Wohlert, and L.A. Berglund, *Deformation of cellulose nanocrystals: entropy, internal energy and temperature dependence.* Cellulose, 2012. **19**(6): p. 1821-1836.
318. Nishino, T., K. Takano, and K. Nakamae, *Elastic modulus of the crystalline regions of cellulose polymorphs.* Journal of Polymer Science Part B: Polymer Physics, 1995. **33**(11): p. 1647-1651.
319. Petridis, L., et al., *Hydration Control of the Mechanical and Dynamical Properties of Cellulose.* Biomacromolecules, 2014. **15**(11): p. 4152-4159.
320. Chen, P., et al., *Linear, non-linear and plastic bending deformation of cellulose nanocrystals.* Physical Chemistry Chemical Physics, 2016. **18**(29): p. 19880-19887.

321. Chen, P., et al., *I alpha to I beta mechano-conversion and amorphization in native cellulose simulated by crystal bending.* Cellulose, 2018. **25**(8): p. 4345-4355.
322. Sahputra, I.H., A. Alexiadis, and M.J. Adams, *Temperature dependence of the Young's modulus of polymers calculated using a hybrid molecular mechanics–molecular dynamics method.* Journal of Physics: Condensed Matter, 2018. **30**(35): p. 355901.
323. Zhang, N., et al., *Cellulose-hemicellulose interaction in wood secondary cell-wall.* Modelling and Simulation in Materials Science and Engineering, 2015. **23**(8): p. 15.
324. Wang, W., Y.T. Wang, and X.N. Li, *Molecular Dynamics Study on Mechanical Properties of Cellulose with Air/Nitrogen Diffusion Behavior.* Bioresources, 2018. **13**(4): p. 7900-7910.
325. Tang, C., et al., *Molecular Simulation and Experimental Analysis of Al2O3-Nanoparticle-Modified Insulation Paper Cellulose.* Ieee Transactions on Dielectrics and Electrical Insulation, 2017. **24**(2): p. 1018-1026.
326. Tang, C., et al., *Enhanced mechanical properties and thermal stability of cellulose insulation paper achieved by doping with melamine-grafted nano-SiO2.* Cellulose, 2018. **25**(6): p. 3619-3633.
327. Treloar, L.R.G., *Calculations of elastic moduli of polymer crystals: II. Terylene.* Polymer, 1960. **1**: p. 279-289.
328. Poma, A.B., M. Chwastyk, and M. Cieplak, *Elastic moduli of biological fibers in a coarse-grained model: crystalline cellulose and beta-amyloids.* Physical Chemistry Chemical Physics, 2017. **19**(41): p. 28195-28206.
329. Aabloo, A. and A.D. French, *Preliminary potential energy calculations of cellulose iα crystal structure.* Macromolecular Theory and Simulations, 1994. **3**(1): p. 185-191.
330. Shishehbor, M. and P.D. Zavattieri, *Effects of interface properties on the mechanical properties of bio-inspired cellulose nanocrystal (CNC)-based materials.* Journal of the Mechanics and Physics of Solids, 2019. **124**: p. 871-896.
331. Shishehbor, M., et al., *A continuum-based structural modeling approach for cellulose nanocrystals (CNCs).* Journal of the Mechanics and Physics of Solids, 2018. **111**: p. 308-332.
332. Sternberg, U., et al., *Crystal Structure Refinements of Cellulose Polymorphs using Solid State 13C Chemical Shifts.* Cellulose, 2003. **10**(3): p. 189-199.
333. Cael, J.J., et al., *Infrared and Raman spectroscopy of carbohydrates. Paper V. Normal coordinate analysis of cellulose I.* The Journal of Chemical Physics, 1975. **62**(3): p. 1145-1153.
334. Sahputra, I.H., A. Alexiadis, and M.J. Adams, *Effects of Moisture on the Mechanical Properties of Microcrystalline Cellulose and the Mobility of the Water Molecules as Studied by the Hybrid Molecular Mechanics-Molecular Dynamics Simulation Method.* Journal of Polymer Science Part B-Polymer Physics, 2019. **57**(8): p. 454-464.
335. Stylianopoulos, T., et al., *Tensile mechanical properties and hydraulic permeabilities of electrospun cellulose acetate fiber meshes.* Journal of Biomedical Materials Research Part B-Applied Biomaterials, 2012. **100B**(8): p. 2222-2230.
336. Gao, X., et al., *Assessing stiffness of nanofibres in bacterial cellulose hydrogels: Numerical-experimental framework.* Materials Science & Engineering C-Materials for Biological Applications, 2017. **77**: p. 9-18.

337. Srinivasa, P., A. Kulachenko, and F. Karlberg, *Material properties of the cell walls in nanofibrillar cellulose foams from finite element modelling of tomography scans.* Cellulose, 2017. **24**(2): p. 519-533.
338. Ahmad, F. and P.K. Bajpai, *Evaluation of stiffness in a cellulose fiber reinforced epoxy laminates for structural applications: Experimental and finite element analysis.* Defence Technology, 2018. **14**(4): p. 278-286.
339. Naddeo, F., et al., *Finite element multiscale modelling of elastic behavior of cellulose acetate-Graphene oxide nanocomposites, produced using a SC-CO2 assisted technique.* Journal of Supercritical Fluids, 2018. **140**: p. 248-257.
340. Sakurada, I., Y. Nukushina, and T. Ito, *Experimental determination of the elastic modulus of crystalline regions in oriented polymers.* Journal of Polymer Science, 1962. **57**(165): p. 651-660.
341. Diddens, I., et al., *Anisotropic Elastic Properties of Cellulose Measured Using Inelastic X-ray Scattering.* Macromolecules, 2008. **41**(24): p. 9755-9759.
342. Rusli, R. and S.J. Eichhorn, *Determination of the stiffness of cellulose nanowhiskers and the fiber-matrix interface in a nanocomposite using Raman spectroscopy.* Applied Physics Letters, 2008. **93**(3): p. 033111.
343. Iwamoto, S., et al., *Elastic Modulus of Single Cellulose Microfibrils from Tunicate Measured by Atomic Force Microscopy.* Biomacromolecules, 2009. **10**(9): p. 2571-2576.
344. Ishikawa, A., T. Okano, and J. Sugiyama, *Fine structure and tensile properties of ramie fibres in the crystalline form of cellulose I, II, IIII and IVI.* Polymer, 1997. **38**(2): p. 463-468.
345. Mann, J. and L. Roldan-Gonzalez, *X-ray measurements of the elastic modulus of cellulose crystals.* Polymer, 1962. **3**: p. 549-553.
346. Ishikawat, A., S. Kuga, and T. Okano, *Determination of parameters in mechanical model for cellulose III fibre.* Polymer, 1998. **39**(10): p. 1875-1878.
347. Mark, H.F., *Encyclopedia of polymer science and technology—plastics, resins, rubbers, fibers*. Vol. 3. 1982, New York: Wiley.
348. Hancock, B.C., S.-D. Clas, and K. Christensen, *Micro-scale measurement of the mechanical properties of compressed pharmaceutical powders. 1: The elasticity and fracture behavior of microcrystalline cellulose.* International Journal of Pharmaceutics, 2000. **209**(1): p. 27-35.
349. Hsieh, Y.C., et al., *An estimation of the Young's modulus of bacterial cellulose filaments.* Cellulose, 2008. **15**(4): p. 507-513.
350. Tanpichai, S., et al., *Effective Young's Modulus of Bacterial and Microfibrillated Cellulose Fibrils in Fibrous Networks.* Biomacromolecules, 2012. **13**(5): p. 1340-1349.
351. Sehaqui, H., et al., *Mechanical performance tailoring of tough ultra-high porosity foams prepared from cellulose I nanofiber suspensions.* Soft Matter, 2010. **6**(8): p. 1824-1832.
352. Ali, Z.M. and L.J. Gibson, *The structure and mechanics of nanofibrillar cellulose foams.* Soft Matter, 2013. **9**(5): p. 1580-1588.
353. Gordeyeva, K.S., et al., *Stabilizing nanocellulose-nonionic surfactant composite foams by delayed Ca-induced gelation.* Journal of Colloid and Interface Science, 2016. **472**: p. 44-51.

Chapter 5: Crystalline Cellulose: The Structure-Property Evolution under Pyrolysis Conditions*

5.1 Introduction

Cellulose exists in algae, bacteria and other natural biomaterials as a basic building block. It is also a primary component of cell walls of green plants, along with hemicellulose and lignin. Cellulose-based materials have been widely used in many applications, for example, biofuel productions[1, 2], paper manufactory[3, 4], construction industry[5-7], energy related fields[8-11], drug delivery[12-17], biomedical therapy[18-20], to just name a few. The unique properties of nontoxicity, good biocompatibility, high biodegradability, high water adsorption and great mechanical properties make cellulose one of the most promising candidates to address the increasing challenges in environmental, ecological and energy fields.

Chemically, cellulose is a polysaccharide that consists of a linear chain of thousands of repeating D-glucose units, which are interlinked with β-1,4-linkages. Hydroxyl groups of cellulose chains and the inter/intra hydrogen bonding (HB) networks are dominating structural factors to cellulose properties. The utilization of cellulose-based materials largely depends on the effective manipulation of cellulose HB networks. Accordingly, various treatments have been proposed to process raw cellulose materials, which could be classified as the following categories: (1) mechanical treatments such as milling[21, 22], grinding/refining[23-25], high-pressure homogenizers[26-29], cryocrushing[27, 30, 31], and high intensity ultrasonic treatments[32-34]; (2) hydrolysis treatments[35-56] via the application of dilute acid, concentrated acid, enzyme or autohydrolysis; (3) pyrolysis treatments[57-61] through the steam, hydrothermolysis or wet

*Qiao, Q., X. Li, and L. Huang, *Crystalline Cellulose under Pyrolysis Conditions: The Structure–Property Evolution via Reactive Molecular Dynamics Simulations.* Journal of Chemical & Engineering Data, 2020. **65**(2): p. 360-372.

oxidation; (4) chemical treatments[32, 42, 62-69] from oxidizing agents, alkali, acid and organic solvents; (5) electrical, biological and other treatments[70-79].

Most recently, producing cellulose based advanced materials via subtle treatment strategies has been brought to a new horizon. Exciting progresses include the milestone work of Hu[62] and co-workers where they processed natural wood chemically to remove lignin, followed by a mechanical compressing to fine tune the remaining cellulose structures into crumple and interlock. The transformed wood, mostly composed of structurally manipulated cellulose, is mechanically more than 10 times stronger than steel[62]. Selectively removing hemicellulose and lignin has witnessed other promising progresses, including compressible carbon sponges and high surface area activated carbon for chemical and biosensor development, and water/oil separations[63, 80-83]. Making use of the inherent structural and chemical properties is key to producing cellulose based advanced materials and maximizing their performance. It is worth noting that available results seem to suggest that having a proper amount of lignin is beneficial. The hypothesis is that the leftover lignin helps to bind cellulose fibers when further processed.

On the other hand, despite the importance and recent promising progress of the field, the theoretical understanding of cellulose based materials and their fundamental structure-property relationship are still far from complete. There is a pressing need to develop molecule level understandings of cellulose based materials and how their structure and property evolve under various treatments. To date, the majority theoretical research efforts are from *ab initio* density functional theory (DFT) and classical force field based molecular dynamics (MD) simulations of crystalline cellulose structures and corresponding electronic properties[84-89]. The breakdown of cellulose under solution (such as water, acid or ionic liquid environments) or pyrolysis conditions has been also studied computationally. For example, classical MD simulations were used to

simulate the surface of cellulose Iβ and its interactions with water.[90]. Matthews and co-workers used molecular mechanics (MM) simulations to study the crystalline cellulose configuration changes with water surrounding around[91]. They found that cellulose unit was expanded and twisted, and that the formation of adjacent water layer on the cellulose surface might delay the transitions of enzymes and further result in a slower hydrolysis rate in enzymes-catalyzed hydrolysis approach[91]. They also found[92] that the twisting between cellulose chains results in the formation of a 3D hydrogen bond network inside hydrate cellulose Iβ microfibrils under high temperature (~500 K). *Ab initio* and MD simulations have been also used to understand the dissolution mechanism of cellulose in aqueous solutions. Janesko et al.[93] applied DTF calculations to study the interaction between cellulose and charged ions in ionic liquids (ILs). Singh and co-workers[94] carried out *ab initio* molecular dynamics (AIMD) simulations to study the dissolution of cellulose Iβ monomers in ILs. They found that the breaking of hydrogen bond network was the key factor for cellulose dissolution. Similarly, Liu et al.[95] found in their MD simulations that the strong hydrogen bonding between anion and cellobiose could significantly impact cellulose dissolution. Moreover, other researchers[96-98] have also reported that the changes of interchain and intrachain hydrogen bond network lead to cellulose dissolution in ILs.

When it comes to pyrolysis treatments, BergenstråhleLars et al.[99] reported via classical MD simulations that cellulose Iβ crystal changed its structure when the temperature was above 450 K . Assary et al.[100] and Mayes et al.[101] performed DFT calculations to study the fast pyrolysis of cellulose. They both observed cellobiose depolymerization, epoxide formation and the production of Levoglucosan (LGA). Agarwal et al.[102] performed both AIMD and Car-Parrinello molecular dynamics (CPMD) simulations to study cellulose decomposition pathways. They found that the cellulose decomposition to liquid intermediates started around 260 ºC and

LGA was produced from the fast pyrolysis between 400 to 600 ºC, agreeing well with the results of Assary and Mayes. The authors also used classical MD to simulate the IR of cellulose Iβ crystal at 300~500 K.[103] The IR agreed with that of experiments and high temperatures can weaken cellulose intrachain hydrogen bonds, eventually leading to the formation of a 3-D hydrogen bonding network.

In recent years, reactive force field (ReaxFF) based MD simulation (RxMD) has gained more and more attention from the cellulose research community. It is mainly due to the advantages that electronic/reaction details and large time/space scale computations can be achieved simultaneously in RxMD simulations. A number of RxMD simulations have been reported for cellulose, hemicellulose, lignin and their mixtures. For example, Beste and co-workers[104] reported a RxMD study of the conversion of lignin at various temperatures, and they found that the 5-5 linkage was the weakest linker during the cyclization and dehydrogenation. Zheng and co-workers[105] studied the pyrolysis process of amorphous cellulose at temperatures from 500 to 1400 K. The reported pyrolysis products agree well with available experiments, which also confirms that the applied ReaxFF force field provides an accurate description of cellulose pyrolysis processes. Meanwhile, Paajanen et al.[106] studied the amorphous cellulose decomposition from 1400 to 2000 K. They observed that the breaking of 1-4-β bonds eventually leads to the cellulose decomposition, and that the decomposition products are mainly glycolaldehyde, water, formaldehyde and formic acid, which agreed with experimental results.

In this work, a series of RxMD simulations have been performed to reveal the structural evolution of crystalline cellulose Iβ via pyrolysis treatments under an isolated condition. By varying the pyrolysis temperature, the change of cellulose crystallinity, the variation of inter/intra HB networks, the reaction and distribution of C, O and H elements have been recorded and

analyzed. In addition, the pyrolysis treated cellulose and its mechanical properties were also discussed in terms of Young's modulus and the yield tensile stress. Despite the pyrolysis process was modeled under an isolated condition, that is, no contribution was considered from oxygen and water of the air, this work demonstrates a general computational protocol to study cellulose systems under reactive conditions. Furthermore, the constructed structure-property relationship could shed light on how to select pyrolysis conditions and achieve desirable structural, chemical and mechanical properties of engineered cellulose-based materials. The article is organized as following: Section 5.2 presents a brief introduction to the ReaxFF reactive force field, a simulation protocol and a list of computational characterizations. Section 5.3 contains the calculation results and discussions of structural evolution of crystalline cellulose Iβ as a function of time, the characterizations of inter/intra HB networks, and the mechanical properties of processed cellulose. Conclusions are finally provided in Section 5.4.

5.2 Crystalline Cellulose Model and Simulation Details

5.2.1 Crystalline Cellulose

The initial cellulose Iβ crystal was generated by the cellulose builder from Gomes and co-workers[107, 108], with the lattice parameters[108] of 7.784 Å, 8.201 Å, 10.380 Å, 90°, 90°, 96.550° from experimental XRD and neutron fiber diffraction results at 293 K. In our RxMD simulations, a 2×2×6 supercell was constructed which produces a triclinic simulation box of 15.568 ×16.402 × 62.280 Å. In this work, benchmark calculations on larger systems have been performed at the initial stage of this research. Quantitively similar results were obtained about properties such as the hydrogen bonding network and the Young's modulus. Also, we followed the choice of simulation box size and used a similar total number of atoms in the cellulose

model[105, 106, 109, 110]. Figure 19 (a) shows characteristic covalent bonds of crystalline cellulose, namely, the bonds of the glucose unit that hold the ring structure, and the 1-4-β bonds that connect glucose units. It is expected that at elevated temperatures, either the glucose ring structure or the 1-4-β bond would break down. Besides covalent bonds, the HB networking is also critical to cellulose properties. As shown in Figure 19 (b), hydrogen bonds (green dashed lines) come from both inter and intra cellulose chains. As temperature increases, the crystallinity of cellulose structure decreases, consequently producing a change of the inter and intra HB networks, which significantly affects mechanical properties of the pyrolysis treated cellulose.

5.2.2. ReaxFF Reactive Force Field and RxMD Simulation

Proposed by van Duin and co-workers in 2001, ReaxFF reactive force field has been actively developed to describe complex and large-scale reactive systems, which could contain hundreds to several thousands of atoms[111]. So far, ReaxFF has been applied to describe complex systems such as protein/DNA[112, 113], membrane fuel cell system[114] and very complex coal structure and properties[115]. ReaxFF has become a choice for multi-scale modeling of systems with adsorption, dissociation and complicated reactions[116-118]. Unlike traditional definitions of bonds, angles and dihedrals of classical force fields, a concept of bond order[119-123] has been developed in ReaxFF to calculate atomic connections and system energies in order to describe the continuous bond formation and breaking and mimic the reaction pathway in the systems[111]. These advantages make ReaxFF an useful tool in predicting structural evolution, tracing intermediates and analyzing final products[124, 125]. Recently, ReaxFF has been successfully used for the study of the mechanism of pyrolysis process of cellulose, hemicellulose, lignin and their derivatives[104-106, 109, 126, 127]. Generally speaking, ReaxFF is one order slower than

the non-reactive force fields, the most expensive calculations part of ReaxFF has been the charge calculations that comes from electronegativity equalization method (EEM) by Mortier and co-workers[128-130]. However, with the help of parallel calculations, a time scale of microseconds trajectory could be archived[117]. More details of ReaxFF are available from recent reviews[131-133]. The ReaxFF parameters used in this work have successfully described cellulose systems[106, 109].

All RxMD simulations were performed by the LAMMPS package. The isothermal-isobaric (NPT) ensemble was applied where the pressure was maintained at 1 atm. The temperature was controlled via the temperature-programmed protocol, changing from 300 K slowly to targeted final temperatures (500, 800, 1000, 1100, 1200, 1300 K). The Berendsen method with a temperature damping coefficient of 100 fs was applied to maintain the system temperature. Initial velocity was assigned according to the Boltzmann distribution. A timestep of 0.25 fs was adopted in all calculations. Each of the RxMD simulations in this work has a trajectory of at least 10 ns. For the cellulose decomposition distribution analysis, longer simulations have been performed for 60 ns for 1200 and 1300 K. For the Young's modulus analysis, after the 10-ns trajectory, additional calculation of 1 ns was carried out to collect the data at a smaller timestep (0.05 fs). Other calculations were performed at a timestep of 0.25 fs. It is worth nothing that identifying the true equilibrium state is always important and challenging for molecule simulations. Technically, the equilibrium state is justified via various analyses such as the total energy of the system, the root-mean-square deviation of atomic positions, diffusion coefficients, *etc*. Zheng and co-workers[105] have summarized that cellulose is thermally stable in the temperature range of 673-1073 K (experimentally) and 500-1400 K (computationally). The wide temperature range is mainly due to different cellulose resources and the treatment conditions (isolated, vacuum, with a mixture of

gases or liquids). Our work shows that cellulose is generally stable up to 1000 K, which qualitatively agrees with other computational studies. In addition, we have tested the calculations for different timescales, from 25 ns up to 100 ns. No qualitative difference was observed. However, it is worth nothing that the choice of simulation time depends critically on the property of interest, for example, to gain cellulose dissociation kinetics, longer calculations are recommended.

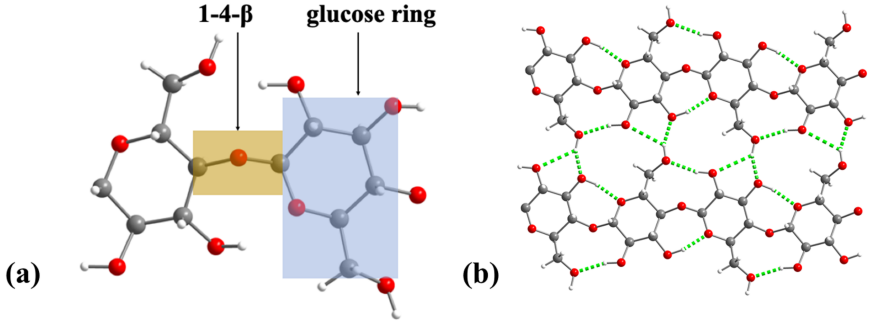

Figure 19. Initial configurations of the Iβ crystalline cellulose; (a) two characteristic covalent bonds in a single cellulose chain; (b) the hydrogen bonding network from two parallel cellulose chains.

5.2.3. Monitored Properties from RxMD Simulation

(a) Hydrogen Bonding Network

The HB networking has been widely used to describe structural changes of crystalline cellulose Iβ, and is considered as a packing indictor when linear cellulose chains roll into highly ordered structures[108, 134-138]. In this work, the HB criteria proposed by Nishiyama and co-workers[108] were adopted:

$$R_L^{O\cdots H} < R^{O\cdots H} < R_H^{O\cdots H};\ \ \theta^{O\cdots HO} < \theta_C^{O\cdots HO}$$

where $R^{O\cdots H}$ is the distance between the HB acceptor (O) and the HB donor (H). The low and high thresholds are 1.7 Å and 2.6 Å, respectively. $\theta^{O\cdots HO}$ represents the angle O···O–H for the HB formation where the threshold angle is 110°.

(b) Computational X-ray Diffraction

X-ray diffraction (XRD) patterns are sensitive to spacings between layers or rows of atoms and are capable of determining the orientation of a single crystal or grain. XRD has been utilized to identify crystal structures, measure the size, shape and internal stress of small crystalline regions. It is also a primary tool for determination of nano-crystallite orientation in polymers. In this work, XRD plots were calculated to monitor the structural evolution of crystalline cellulose: the peak positions are determined by the lattice parameters, while the peak intensities are from the motif. XRD calculations were carried out by the Mercury and Diamond software, more information is available from the software manual[139, 140].

(c) Young's Modulus

Young's modulus defines the relationship between stress (force per unit area) and strain (proportional deformation) in the linear elasticity regime of a uniaxial deformation[141]. A larger Young's Modulus suggests a better stiffness of a material. Young's modulus could be experimentally determined via X-ray diffraction[142] or Raman spectroscopy[143]. Computationally, several methods have been proposed to calculate this elastic modulus[143-146]. One method is to enlarge the simulation box length repeatedly by a small amount, along the axis where the stress is applied. The simulation system is then reoptimized at each new fixed cell unit[110, 146]. Another method is to allow the simulation box to elongate continuously at a defined

strain rate for a uniaxial tensile deformation. Several articles have adopted the second method to estimate the Young's modulus for amorphous polymers and metals[147-152].

This work also uses the second method to monitor the uniaxial tensile deformation at three different strain rates. In those simulations, the tensile stress is the negative value of pressure along the corresponding direction. The strain is then calculated by the amount of the length change for that direction. Young's modulus (E) is the ratio of tensile stress ($\sigma(\varepsilon)$) and strain ε, $E = \sigma(\epsilon)/\epsilon$. From the stress-strain diagram, the point of yielding is estimated by the offset yield method, also known as 0.2% offset yield strength. As shown in the following section, the yield strength is obtained by drawing through the point of the horizontal axis of ε = 0.2%, a line parallel to the initial straight-line portion of the stress-strain diagram.

5.3 Results and Discussions

5.3.1 Cellulose Configuration under Different Temperatures

As shown in Figure 20, the temperature effect on cellulose configuration has been monitored. Figure 20 (a) displays the final configurations from different temperatures, whereas the hydrogen bonding network of cellulose chains is illustrated by green dashed lines. In Figure 20 (b) and (c), the cellulose has been treated by 300 K and 1100 K, respectively. The structure gets corrugated and twisted due to the pyrolysis process, which in turn could modify the hydrogen bonding network. Both traditional and ReaxFF force fields provide similar descriptions to cellulose conformation and its hydrogen bonding network. We analyzed and compared cellulose unit cell predicted from this work and reported experimental and computational data from the literature. Nishiyama and co-worker[108] reported atomistic coordinates of cellulose crystal via XRD and neturon fiber diffraction at room temperature (293 K), which is adopted as the starting structure in

this work. Matthews and co-workers[91, 92] used CHARMM force field to discuss cellulose structures. Bergenstråhle[99] observed similar cellulose structural changes via GROMOS, PCFF, MM3 and CHARMM force fields. In Table 1 of the Supporting Information, the equilibrium unit cell parameters are listed from experiments and different computational studies, including this work.

Compared with results from traditional force fields[89, 92, 99, 153-155], ReaxFF described the cellulose structure similar to that of experimental value at 293 K[108]. It is worth noting that the unit cell angle γ is smaller than the experimental result, which is probably due to the underestimation of cellulose chain-chain dispersion interactions via the ReaxFF force field. A smaller γ value is also reported from calculations with traditional force fields at 300 K[92, 99]. In our calculations, when temperature increased to 500 K, larger unit cell parameters were observed, also similar to results from traditional force fields[99]. As discussed in the literature[92, 99], the change of unit cell shape (α and β angles) indicates the inter-chain sliding of cellulose crystal. When the temperature increased from 500 K to 1100 K in this work, the unit cell change became more significant, suggesting the increasing distance between cellulose chains. Such configurational change eventually leads to the structural collapse of cellulose at high temperatures, around 1100 K according to RxMD simulations in this work. In RxMD calculations, the cellulose structure was stable up to 1000 K. At 1100 K, cellulose was stable for a few nanoseconds but then it gradually decomposed. Even though cellulose is not thermally stable at 1100 K, the observed stability transition is important. When the temperature was beyond 1200 K, the cellulose structure quickly decomposed. Reaction products such as H_2, CO, H_2O and very little CO_2 were observed, as shown in the supplementary materials. These pyrolysis products were also reported by previous work[105, 109].

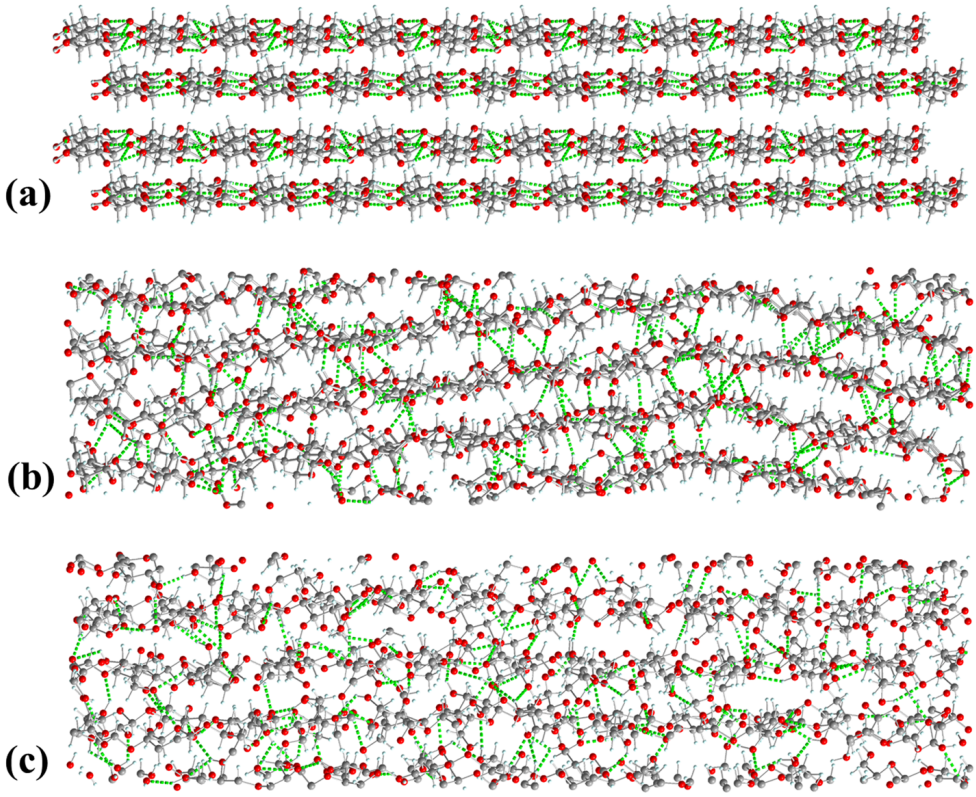

Figure 20. Cellulose configuration changes at different temperatures: (a) initial cellulose crystalline structure (exp. 293 K)[108]; (b) cellulose structure at 300 K; (c) intermediate cellulose structure at 1100 K. When the temperature is higher than 1200 K, the cellulose structure will decompose. The hydrogen bonding network is shown in green dashed lines.

5.3.2 XRD of Cellulose Structures

XRD is a useful method to identify crystalline, semi crystalline and amorphous structures. Here we calculated XRD to qualitatively determine the crystalline phase of cellulose under pyrolysis conditions. Since the initial cellulose crystal was built up based on experimental XRD data[108], we used its XRD here to represent experimental XRD results from Nishiyama and co-workers. The green region represents the peak ranges of experimental XRD results that reported by other authors[156-158]. Cellulose structure at 300 K, 1000 K and 1100K were used to study

the structure phase change under different pyrolysis temperatures. As shown in Figure 21, cellulose structures at 300 K and 1000 K have similar XRD patterns as that of the experimental results (exp.[108]), for both peak position and peak intensity. This suggests that Iβ crystalline cellulose has a relatively good thermal stability. When the temperature increases to 1100 K, there is a noticeable XRD peak shift when we calculated the XRD of cellulose intermediate crystalline structure. From 300 K to 1000 K, the calculations revealed cellulose structural changes, such as the corrugations and the twists of cellulose chains. But the chains were generally still parallel to each other, and the distance between chains did not change too much. Therefore, no significant XRD peak shifting was observed between the initial crystalline cellulose and cellulose at temperatures from 300 K to 1000 K. When temperature was further increased to 1100 K, an obvious increase in cellulose chain-chain distance was happening. In addition, the twist of individual cellulose chains was more significant. Both contributed to the shift of XRD peaks from this temperature (1100 K) and up. It is also worth noting that the increased chain-chain distance reduced the total number of HBs between cellulose chains and eventually led to the collapse of cellulose structure. At 1200 K and above, XRD results showed an amorphous cellulose structure, suggesting the structural collapse at those higher pyrolysis temperatures.

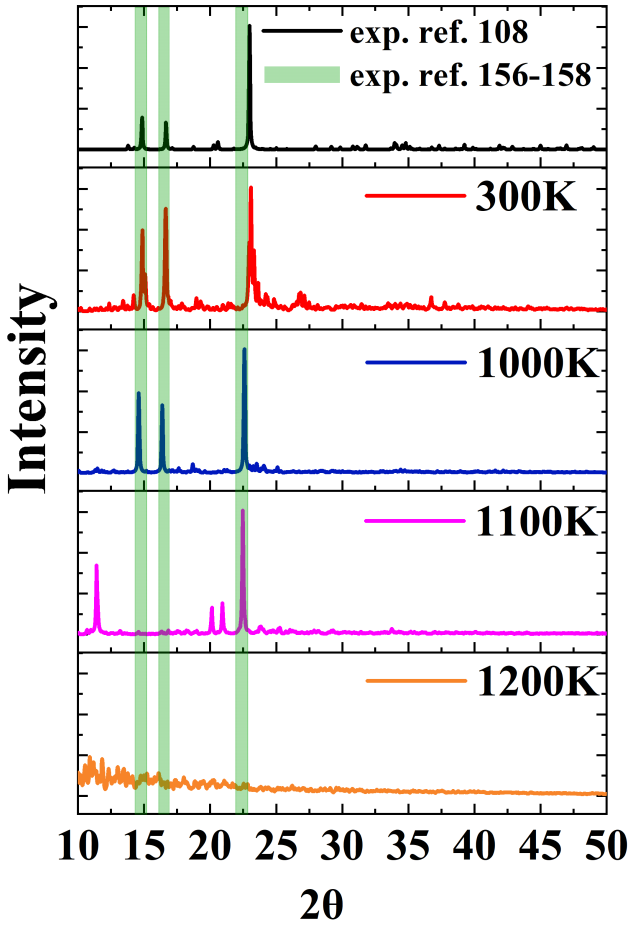

Figure 21. XRD of cellulose structures at different pyrolysis temperatures.

5.3.3 Cellulose Decomposition and Element Distribution Analysis

Under pyrolysis temperatures of 1200 and 1300 K, the crystalline cellulose structure could fully decompose. The categories of pyrolysis products have already been studied and one of the classifications[109] was adopted in this work: (a) organic gas composites which contains 1-4 carbon atoms; (b) light tar which contains 5-13 carbon atoms; (c) heavy tar which contains 14−39 carbon atoms; (d) char which contains more than 40 carbon atoms. As shown in Figure 22 (a), cellulose started to decompose into tar or heavy tar at the beginning of the simulations. After the crystalline structure was decomposed, several light tar products were detected, as well as light gas

molecules such as CH_4 and CO. RxMD simulations with the same ReaxFF force field have been performed to understand the pyrolysis decomposition of cellulose, hemicellulose and lignin[105, 106, 109, 159]. From experimental point of view, pyrolysis temperatures could be divided into[160]: (1) 550-950 K (slow pyrolysis); (2) 850-1250 K (fast pyrolysis); (3) 1050-1300 K (flash pyrolysis). We adopted the concept and qualitatively treated temperatures from 500 to 800 K as slow pyrolysis, 800 to 1000 K as medium pyrolysis, and temperature 1100 K and above as fast pyrolysis. It is also worth noting that cellulose pyrolysis at high temperatures have been investigated via ReaxFF force field[105, 109] In this work, we mainly focus on cellulose structural evolution under low and medium pyrolysis temperatures. Cellulose decomposition products depend on the pyrolysis setting, that is, the initial cellulose structure (crystalline vs. amorphous), the pyrolysis temperature (medium vs. high), and the pyrolysis atmosphere (isolated vs. ambient with CO_2, O_2 or H_2O). For the isolated condition and under a high temperature (> 1200 K), we observed that cellulose shall decompose completely into light products of H_2, CO, H_2O and very little CO_2 after a sufficient long RxMD calculation (~ 60 ns).

From the materials perspective, it is desirable that the pyrolysis process only produces necessary changes to structural and chemical properties cellulose and maintains the maximum use of the elements of cellulose. If a large amount of gas-phase species, such as CO_2, CO, CH_4, H_2, H_2O, shall be released during the pyrolysis process, the efficiency of converting cheap biomaterials to cellulose based advanced materials would be rather low. For the isolated pyrolysis conditions in this work, the calculations reveal that the release of CO_2 is negligible, see Figure 22 (b), and that CO and H_2 are the dominating gas-phase species. It is worth noting that gas-phase H_2O is released during the early stage of the pyrolysis process. At the studied high temperatures, those vapor water can further interact with cellulose and produce more CO and H_2.

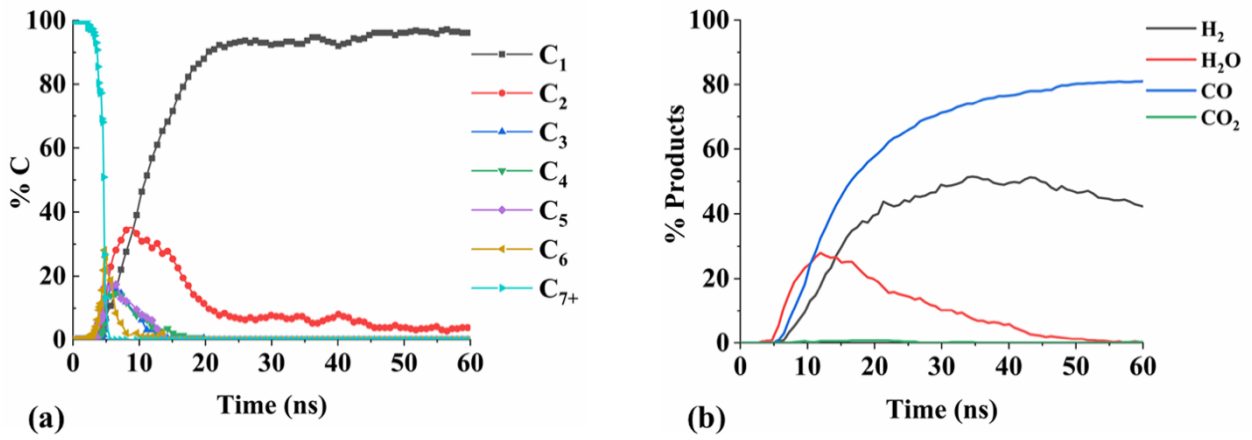

Figure 22. The analysis of cellulose decomposition at 1200 K: (a) the redistribution of carbon elements; C_1, C_2 to C_{7+} denotes decomposition products having 1 carbon atom, 2 carbon atoms, 7 or more carbon atoms, respectively. (b) light gas-phase molecules during the isolated pyrolysis process.

5.3.4 Cellulose Hydrogen Bonding Network

The cellulose configuration in Figure 20 shows that the corrugation and twist can lead the linear cellulose chains to a more complex three-dimensional hydrogen bonding network. To further monitor this change, the two types of hydrogen bonds have been distinguished, namely, the intra-chain HB that are formed between hydroxyl groups of same cellulose chains; the inter-chain HB that are formed between hydroxyl groups from different cellulose chains. The percentage of hydrogen bond intactness is defined as the number of intra (or inter)-HBs over the total number of HBs. Figure 23 (a) shows the numerical analysis of the two hydrogen bonds where more inter-chain HBs exist in those studied pyrolysis conditions. While for the pristine initial cellulose crystal, the majority is the intra-chain HBs. In addition, comparing the initial model and cellulose at 300 and 1000 K, the total number of HBs is 292, 247±10 and 183±11, respectively. This indicates that the studied Iβ cellulose is thermally stable from 300 K to 1000 K.

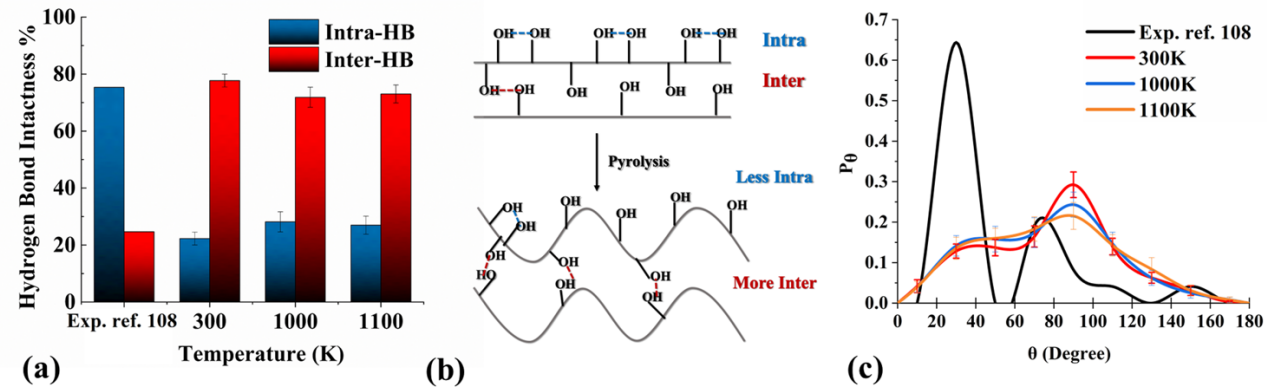

Figure 23. (a) The intra-chain HB and inter-chain HB distributions at different pyrolysis temperatures; (b) A schematic illustration of the inter- and intra-HB network change due to pyrolysis temperature; (c) The HB angular distribution, which is through the analysis of the angle formed between the HB bond and the positive Z axis.

A scheme in Figure 23 (b) illustrates the comparison of hydrogen bonding network between the pristine Iβ cellulose crystal and the cellulose after the pyrolysis treatment. In the initial crystal state, all cellulose chains are linear and highly ordered, with most hydroxyl groups on a cellulose chain pointing to the same directions. As a result, it is easier to form intra-chain HBs than inter-chain HBs due to the structural hindrance. On the contrary, under pyrolysis treatments, the corrugation and twist of cellulose chains prevent the formation of intra HBs but promote those inter HBs. At finite temperatures, cellulose chains rotate, twist and corrugate to form a 3-dimentional hydrogen bonding (HB) network. Figure 23 (a) reveals a significant difference between experiment (XRD and neutron fiber diffraction data) and RxMD simualtions. This is likely due to the fact that in RxMD simualtions, all hydrogen atoms are expressed explicitly. Their intections contribute significantly to the HB network. However, XRD and neutron diffraction experiments cannot determine exact locations of hydrogen atoms, which might lead to the incorrect

description of the HB network. This explains the overestimated intra HB and the preferential HB angular distribution in Figure 23 (c): peak postions aound 30º, 70º, 150º. The HB angular distribution is through the analysis of the angle formed between the HB bond and the positive Z axis. In this wrok, the RxMD results show that inter HB bonds are ciritial to the 3D network. It is also the main reason why cellulose is stable even at high temperarures (for example, 1000 K in this work). The 3D HB network and its change due to temperature have been investigated also by classical force fields, with qualitatively similar results[91, 92, 99, 161]. It is worth mentioning that the total number of hydrogen bonds shall decrease under even higher pyrolysis temperatures. This is because the distance between cellulose chains was slightly gets enlarged under higher temperatures, and eventually those inter-chain HBs would disappear.

5.3.5 The Breakdown of Cellulose Structures

In order to gain the fundamental insight when and how the cellulose structure breaks down, the two characteristic covalent bonds of Figure 20 (a) have been monitored, and the definition of bond intactness is defined as following: (1) for 1-4-β bond, the oxygen atom remains connected with the exact same two carbon atoms during the pyrolysis process; (2) for the glucose ring structure, all bonds from the ring structure are monitored, as well as the C-OH and C-CH_2OH groups that are connected with the ring structure. Each carbon in the glucose unit shall remain bonded with the neighboring atoms during the pyrolysis process; In this work, the bond intactness is evaluated as a function of interatomic distance, to monitor the type, the breaking and formation of bonds via ReaxFF[162]. With the bond order information, the intactness of a molecule or structure is further evaluated to see whether and for how long atoms of the molecule/structure remain connected.

For the studied conditions, both 1-4-β and glucose ring bonds remain intact for the temperature range of 300 K to 1000 K. When the temperature increased to 1200 K, 1-4-β bonds started to break down within 2 ns, and by the end of the 5 ns in the trajectory, all 1-4-β bonds were decomposed, as shown in the inset of Figure 24 (a). Meanwhile, the breakdown of glucose ring structures was also detected at 1200 K. Compared with the 1-4-β bond, the decompose of glucose ring was slightly delayed, and it took until the 7.5 ns in the trajectory to break all glucose rings. This suggests that the glucose ring is more thermally stable than the 1-4-β structure. At 1300 K, the breakdown was expedited: within 2 ns, all 1-4-β were decomposed; while the complete breakdown of glucose rings was achieved within 5 ns. But no temperature range is identified where 1-4-β bonds are decomposed and the glucose rings remain intact. It is probably due to the dangling bonds of broken 1-4-β structures, which can further induce the breakdown of glucose rings. Under different conditions, that is, instead of isolated pyrolysis, with liquid or gas mediated pyrolysis processes, the 1-4-β bond breakdown does not spontaneously lead to the decomposition of glucose rings. Thus, the cellulose structure could be modified selectively, by removing only those 1-4-β bonds. It is also interesting to note the collective contributions from the 3-D HB network. At 1200 or 1300 K, where both 1-4-β bonds and cellulose rings were decomposing, the 3-D hydrogen bonding network was still able to hold together partial crystalline cellulose chains. It is worth point out that the dissociation energies for characteristic structural changes are: 0.2 ~ 40 kcal/mol for the hydrogen bonded (HB) network; 51 ~ 76 kcal/mol for the glycosidic (1-4-ß) bond cleavage; 78 ~ 191 kcal/mol for the glucose ring dissociation[163-165]. In our calculations, when temperature was increasing from 300 K, the first structural change was from the 3-D HB network. At 1100 K, the thermo energy was able to further break down 1-4-ß bonds and induce partial structural collapse of cellulose. In addition, the total number of HB also decreased at 1100 K,

which is another evidence to cellulose structural collapse. The simulation results also revealed that it is challenging to identify a temperature region where glucose rings stay intact but H-bonding network and 1-4-ß bonds are broken. This is probably due to the fact that 1-4-ß bonds and glucose rings alternate to form cellulose structures, see Figure 20. When 1-4-ß bonds start to break down, the neighboring glucose rings become unsaturated and could easily interact with molecules or other parts of the partially collapsed cellulose. Between the covalent and the HB bonds, is it possible to selectively remove the HB network and keep covalent bonds intact? More theoretical and experimental efforts are needed to validate the two hypotheses.

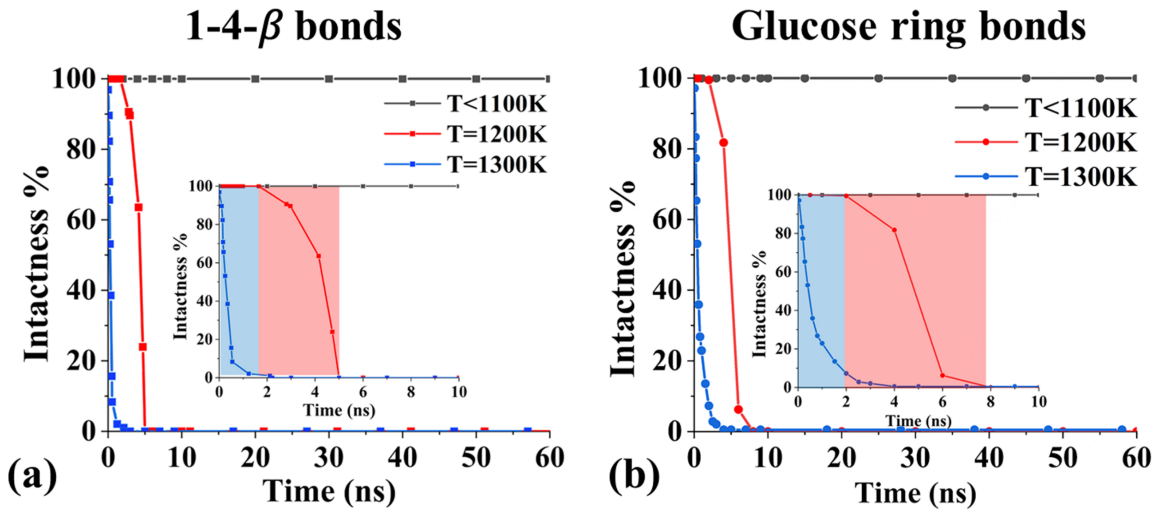

Figure 24. The intactness analysis of cellulose covalent bonds: (a) the 1-4-β bond; (b) the glucose ring. The red and blue regions respectively correspond to the time scales that 1-4-β bonds and glucose rings are detectable during the RxMD simulation.

5.3.6 Young's Modulus Analysis

The configurational change of cellulose leads to the HB network variation, which inevitably affects cellulose mechanical properties. In this work, the uniaxial tensile deformation along the z direction has been calculated to evaluate the Young's modulus of cellulose. The

deformation was carried out at 300 K at three different strain rates, namely, 10^{-3} /s, 10^{-4} /s and 10^{-5} /s. During the calculation, the stress (pressure) was only considered along the z direction, and the pressure of x and y directions were kept zero. A timestep of 0.05 fs was applied and a total of 1 ns RxMD calculation was performed for each case. A smaller timestep here was employed to avoid the error in calculating atoms motions or any unstable structures. The Young's modulus was averaged using the data from the last 10% of the simulation trajectory. At 300 K, the calculated Young's modulus was about 113.24±3.85 GPa (see Figure 25 (a)) at the strain rate of 10^{-4} /s, which agreed well with other calculations[110]. From the literature, the Young's modulus of cellulose has been reported to be 110-220±50 GPa experimentally[142, 166-169], or in the range of 110~173 GPa by computational studies[99, 110, 143, 144, 146, 153, 155, 170, 171]. The relatively small Young's modulus is probably coming from the adopted ReaxFF force field and the Iβ crystalline cellulose structure. In Figure 25 (b) we plotted the deformation curves for temperature from 300 K to 1000 K with a strain rate of 10-4 /s. We observed a Young's modulus of 99.03±2.16 GPa, 95.67±3.65 GPa and 94.34±3.08 GPa at 500, 800 and 1000K, respectively. When temperature increases, the Young's modulus would decrease. This is because cellulose can deform easily at higher temperatures, leading to the drop of Young's modulus.

In addition, as shown in Figure 25 (c), at the strain rate of 10^{-4} /s, via the aforementioned proportional limit method, the yield stress was determined to be about 8.75 GPa, which is in an excellent agreement with experimental and other modeling results[110, 172, 173].

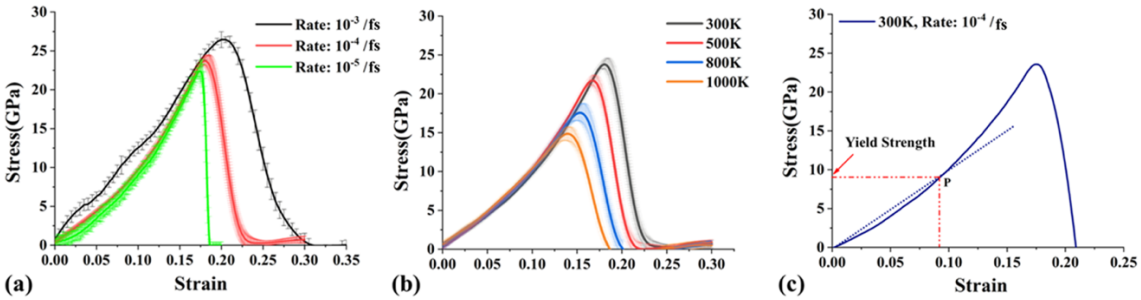

Figure 25. (a) The stress-strain diagram of cellulose at 300 K, strain rate of 10^{-3} /fs is in black, strain rate of 10^{-4} /fs is in red and train rate of 10^{-5} /fs is in green, respectively; (b) The stress-strain diagram of cellulose at 300, 500, 800 and 1000 K. The strain rate is kept at 10-4 /s; (c) The determination of cellulose yield stress at the strain rate of 10-4 /s and 300 K.

5.4 Conclusion

While classical force field has been adopted to study cellulose properties and cellulose interaction with other materials, chemical reaction and thermal decomposition of cellulose are beyond the reach. In this work, via ReaxFF based reactive molecular dynamics (RxMD) simulations, we observed bond breaking and structural change of cellulose at elevated temperatures. By changing the pyrolysis temperature from 300 K to 1300 K, we are able to the analyze the overall configuration, the covalent bonds of 1-4-β and glucose ring units, the inter- and intra-hydrogen bonding networks, and the element distributions systematically. XRD and Young's modulus have been also computed to compare with available experimental and previous modeling results. Key results include: (a) cellulose is able to hold the general crystalline structure for temperatures up to 1000 K. The good thermal stability is assisted by the interchange of inter- and intra-chain HB networks. (b) when the pyrolysis temperature is beyond 1200 K, both 1-4-β bonds and glucose ring units will decompose. Light gas-phase molecules, such as CO and H_2, are detected as major decomposition products. (c) Through the analysis of XRD, Young's modulus and elements distribution, we show that the ReaxFF reactive force field is capable of describing

both stable and dissociative properties of cellulose under isolated pyrolysis processes. Ultimately, this work provides an atomic level fundamental understanding of cellulose structural evolution via pyrolysis treatments. More studies where cellulose under real pyrolysis conditions, that is, instead of isolated conditions but via liquid or gas mediated pyrolysis processes, are worth pursuing. Moreover, the detailed mechanism of how cellulose, hemicellulose and lignin respond differently to pyrolysis treatments could lead to a subtle manipulation and a successful conversion of biomass into advanced functional materials.

5.5 Reference

1. Rubin, E.M., *Genomics of cellulosic biofuels.* Nature, 2008. **454**: p. 841.
2. Hill, J., et al., *Environmental, economic, and energetic costs and benefits of biodiesel and ethanol biofuels.* Proceedings of the National Academy of Sciences, 2006. **103**(30): p. 11206.
3. Nogi, M., et al., *High thermal stability of optical transparency in cellulose nanofiber paper.* Applied Physics Letters, 2013. **102**(18): p. 181911.
4. Salajkova, M., et al., *Tough nanopaper structures based on cellulose nanofibers and carbon nanotubes.* Composites Science and Technology, 2013. **87**: p. 103-110.
5. Sun, X., et al., *Cellulose Nanofibers as a Modifier for Rheology, Curing and Mechanical Performance of Oil Well Cement.* Scientific Reports, 2016. **6**: p. 31654.
6. Li, F., E. Mascheroni, and L. Piergiovanni, *The Potential of NanoCellulose in the Packaging Field: A Review.* Packaging Technology and Science, 2015. **28**(6): p. 475-508.
7. Juntaro, J., et al., *Nanocellulose enhanced interfaces in truly green unidirectional fibre reinforced composites.* Composite Interfaces, 2007. **14**(7-9): p. 753-762.
8. Thomas, B., et al., *Nanocellulose, a Versatile Green Platform: From Biosources to Materials and Their Applications.* Chemical Reviews, 2018. **118**(24): p. 11575-11625.
9. Zhu, H., et al., *Wood-Derived Materials for Green Electronics, Biological Devices, and Energy Applications.* Chemical Reviews, 2016. **116**(16): p. 9305-9374.
10. Muhd Julkapli, N. and S. Bagheri, *Nanocellulose as a green and sustainable emerging material in energy applications: a review.* Polymers for Advanced Technologies, 2017. **28**(12): p. 1583-1594.
11. Chen, H., et al., *Exploring Chemical, Mechanical, and Electrical Functionalities of Binders for Advanced Energy-Storage Devices.* Chemical Reviews, 2018. **118**(18): p. 8936-8982.
12. Jacob, J., et al., *Biopolymer based nanomaterials in drug delivery systems: A review.* Materials Today Chemistry, 2018. **9**: p. 43-55.
13. Löbmann, K. and A.J. Svagan, *Cellulose nanofibers as excipient for the delivery of poorly soluble drugs.* International Journal of Pharmaceutics, 2017. **533**(1): p. 285-297.

14. Chin, S.F., F.B. Jimmy, and S.C. Pang, *Size controlled fabrication of cellulose nanoparticles for drug delivery applications.* Journal of Drug Delivery Science and Technology, 2018. **43**: p. 262-266.
15. Treesuppharat, W., et al., *Synthesis and characterization of bacterial cellulose and gelatin-based hydrogel composites for drug-delivery systems.* Biotechnology Reports, 2017. **15**: p. 84-91.
16. Luo, H., et al., *Bacterial cellulose/graphene oxide nanocomposite as a novel drug delivery system.* Current Applied Physics, 2017. **17**(2): p. 249-254.
17. Abo-Elseoud, W.S., et al., *Chitosan nanoparticles/cellulose nanocrystals nanocomposites as a carrier system for the controlled release of repaglinide.* International Journal of Biological Macromolecules, 2018. **111**: p. 604-613.
18. Rahimi, M., et al., *Biocompatible magnetic tris(2-aminoethyl)amine functionalized nanocrystalline cellulose as a novel nanocarrier for anticancer drug delivery of methotrexate.* New Journal of Chemistry, 2017. **41**(5): p. 2160-2168.
19. Madhusudana Rao, K., A. Kumar, and S.S. Han, *Polysaccharide based bionanocomposite hydrogels reinforced with cellulose nanocrystals: Drug release and biocompatibility analyses.* International Journal of Biological Macromolecules, 2017. **101**: p. 165-171.
20. Sheikhi, A., et al., *Recent advances in nanoengineering cellulose for cargo delivery.* Journal of Controlled Release, 2019. **294**: p. 53-76.
21. Sun, Y. and J. Cheng, *Hydrolysis of lignocellulosic materials for ethanol production: a review.* Bioresource Technology, 2002. **83**(1): p. 1-11.
22. Millett, M.A., A.J. Baker, and L.D. Satter, *Physical and chemical pretreatments for enhancing cellulose saccharification.* Biotechnology and bioengineering symposium, 1976(6): p. 125-153.
23. Iwamoto, S., A.N. Nakagaito, and H. Yano, *Nano-fibrillation of pulp fibers for the processing of transparent nanocomposites.* Applied Physics A, 2007. **89**(2): p. 461-466.
24. Bandera, D., et al., *Influence of mechanical treatments on the properties of cellulose nanofibers isolated from microcrystalline cellulose.* Reactive and Functional Polymers, 2014. **85**: p. 134-141.
25. Panthapulakkal, S. and M. Sain, *Preparation and Characterization of Cellulose Nanofibril Films from Wood Fibre and Their Thermoplastic Polycarbonate Composites.* International Journal of Polymer Science, 2012. **2012**: p. 6.
26. Zimmermann, T., N. Bordeanu, and E. Strub, *Properties of nanofibrillated cellulose from different raw materials and its reinforcement potential.* Carbohydrate Polymers, 2010. **79**(4): p. 1086-1093.
27. Dufresne, A., J.-Y. Cavaillé, and M.R. Vignon, *Mechanical behavior of sheets prepared from sugar beet cellulose microfibrils.* Journal of Applied Polymer Science, 1997. **64**(6): p. 1185-1194.
28. Stelte, W. and A.R. Sanadi, *Preparation and Characterization of Cellulose Nanofibers from Two Commercial Hardwood and Softwood Pulps.* Industrial & Engineering Chemistry Research, 2009. **48**(24): p. 11211-11219.
29. Leitner, J., et al., *Sugar beet cellulose nanofibril-reinforced composites.* Cellulose, 2007. **14**(5): p. 419-425.
30. Alemdar, A. and M. Sain, *Isolation and characterization of nanofibers from agricultural residues – Wheat straw and soy hulls.* Bioresource Technology, 2008. **99**(6): p. 1664-1671.

31. Chakraborty, A., M. Sain, and M. Kortschot, *Cellulose microfibrils: A novel method of preparation using high shear refining and cryocrushing*, in *Holzforschung*. 2005. p. 102.
32. Johnson, R.K., et al., *A new bio-based nanocomposite: fibrillated TEMPO-oxidized celluloses in hydroxypropylcellulose matrix.* Cellulose, 2009. **16**(2): p. 227-238.
33. Wang, S. and Q. Cheng, *A novel process to isolate fibrils from cellulose fibers by high-intensity ultrasonication, Part 1: Process optimization.* Journal of Applied Polymer Science, 2009. **113**(2): p. 1270-1275.
34. Frone, A.N., et al., *Preparation and characterization of PVA composites with cellulose nanofibers obtained by unltrasonication.* BioResources; Vol 6, No 1 (2011), 2011.
35. Broder, J.D., et al., *Biofuels system economics.* World Resource Review, 1995. **7**(4): p. 560-569.
36. Iranmahboob, J., F. Nadim, and S. Monemi, *Optimizing acid-hydrolysis: a critical step for production of ethanol from mixed wood chips.* Biomass and Bioenergy, 2002. **22**(5): p. 401-404.
37. Hubbe, M.A., et al., *Cellulose nanocomposites: a review.* BioResources; Vol 3, No 3 (2008), 2008.
38. Habibi, Y., L.A. Lucia, and O.J. Rojas, *Cellulose Nanocrystals: Chemistry, Self-Assembly, and Applications.* Chemical Reviews, 2010. **110**(6): p. 3479-3500.
39. Wang, B. and M. Sain, *Isolation of nanofibers from soybean source and their reinforcing capability on synthetic polymers.* Composites Science and Technology, 2007. **67**(11): p. 2521-2527.
40. Filson, P.B. and B.E. Dawson-Andoh, *Sono-chemical preparation of cellulose nanocrystals from lignocellulose derived materials.* Bioresource Technology, 2009. **100**(7): p. 2259-2264.
41. Elazzouzi-Hafraoui, S., et al., *The Shape and Size Distribution of Crystalline Nanoparticles Prepared by Acid Hydrolysis of Native Cellulose.* Biomacromolecules, 2008. **9**(1): p. 57-65.
42. Dong, X.M., J.-F. Revol, and D.G. Gray, *Effect of microcrystallite preparation conditions on the formation of colloid crystals of cellulose.* Cellulose, 1998. **5**(1): p. 19-32.
43. Beck-Candanedo, S., M. Roman, and D.G. Gray, *Effect of Reaction Conditions on the Properties and Behavior of Wood Cellulose Nanocrystal Suspensions.* Biomacromolecules, 2005. **6**(2): p. 1048-1054.
44. Bondeson, D., A. Mathew, and K. Oksman, *Optimization of the isolation of nanocrystals from microcrystalline celluloseby acid hydrolysis.* Cellulose, 2006. **13**(2): p. 171.
45. Karim, Z., et al., *Necessity of enzymatic hydrolysis for production and functionalization of nanocelluloses.* Critical Reviews in Biotechnology, 2017. **37**(3): p. 355-370.
46. Henriksson, M., et al., *An environmentally friendly method for enzyme-assisted preparation of microfibrillated cellulose (MFC) nanofibers.* European Polymer Journal, 2007. **43**(8): p. 3434-3441.
47. Pääkkö, M., et al., *Enzymatic Hydrolysis Combined with Mechanical Shearing and High-Pressure Homogenization for Nanoscale Cellulose Fibrils and Strong Gels.* Biomacromolecules, 2007. **8**(6): p. 1934-1941.
48. Tibolla, H., F.M. Pelissari, and F.C. Menegalli, *Cellulose nanofibers produced from banana peel by chemical and enzymatic treatment.* LWT - Food Science and Technology, 2014. **59**(2, Part 2): p. 1311-1318.

49. Chung, D., et al., *Cellulosic ethanol production via consolidated bioprocessing at 75 °C by engineered Caldicellulosiruptor bescii.* Biotechnology for Biofuels, 2015. **8**(1): p. 163.
50. Yarbrough, J.M., et al., *Multifunctional Cellulolytic Enzymes Outperform Processive Fungal Cellulases for Coproduction of Nanocellulose and Biofuels.* ACS Nano, 2017. **11**(3): p. 3101-3109.
51. Camarero Espinosa, S., et al., *Isolation of Thermally Stable Cellulose Nanocrystals by Phosphoric Acid Hydrolysis.* Biomacromolecules, 2013. **14**(4): p. 1223-1230.
52. Reid, M.S., M. Villalobos, and E.D. Cranston, *Benchmarking Cellulose Nanocrystals: From the Laboratory to Industrial Production.* Langmuir, 2017. **33**(7): p. 1583-1598.
53. Battista, O.A., *Hydrolysis and Crystallization of Cellulose.* Industrial & Engineering Chemistry, 1950. **42**(3): p. 502-507.
54. Lee, S.-Y., et al., *Nanocellulose reinforced PVA composite films: Effects of acid treatment and filler loading.* Fibers and Polymers, 2009. **10**(1): p. 77-82.
55. Filpponen, I. and D.S. Argyropoulos, *Regular Linking of Cellulose Nanocrystals via Click Chemistry: Synthesis and Formation of Cellulose Nanoplatelet Gels.* Biomacromolecules, 2010. **11**(4): p. 1060-1066.
56. Liu, D., et al., *Starch composites reinforced by bamboo cellulosic crystals.* Bioresource Technology, 2010. **101**(7): p. 2529-2536.
57. Chen, L., et al., *Unveiling Mesopore Evolution in Carbonized Wood: Interfacial Separation, Migration, and Degradation of Lignin Phase.* ACS Sustainable Chemistry & Engineering, 2015. **3**(10): p. 2489-2495.
58. Kilzer, F.J. and A. Broido, *Speculations on the nature of cellulose pyrolysis.* Pyrodynamics. 2: 151-163, 1965. **2**: p. 151-163.
59. Shafizadeh, F. and A.G.W. Bradbury, *Thermal degradation of cellulose in air and nitrogen at low temperatures.* Journal of Applied Polymer Science, 1979. **23**(5): p. 1431-1442.
60. Melo, E. and J.F. Kennedy, *Cellulose hydrolysis (biotechnology monographs, Vol. 3) edited by L.-T. Fan, M. M. Gharpuray and Y.-H. Lee, Springer-Verlag, Berlin, Heidelberg, New York, London, Paris and Tokyo, 1987. pp. viii + 198, price DM168.00. ISBN 3-540-17671-3.* British Polymer Journal, 1988. **20**(6): p. 532-532.
61. Zwart, R.W.R., H. Boerrigter, and A. van der Drift, *The Impact of Biomass Pretreatment on the Feasibility of Overseas Biomass Conversion to Fischer−Tropsch Products.* Energy & Fuels, 2006. **20**(5): p. 2192-2197.
62. Song, J., et al., *Processing bulk natural wood into a high-performance structural material.* Nature, 2018. **554**: p. 224.
63. Chen, C., et al., *Scalable and Sustainable Approach toward Highly Compressible, Anisotropic, Lamellar Carbon Sponge.* Chem, 2018. **4**(3): p. 544-554.
64. Trifol, J., et al., *Chemically extracted nanocellulose from sisal fibres by a simple and industrially relevant process.* Cellulose, 2017. **24**(1): p. 107-118.
65. Bhatnagar, A. and M. Sain, *Processing of Cellulose Nanofiber-reinforced Composites.* Journal of Reinforced Plastics and Composites, 2005. **24**(12): p. 1259-1268.
66. Rånby, B.G., *Fibrous macromolecular systems. Cellulose and muscle. The colloidal properties of cellulose micelles.* Discussions of the Faraday Society, 1951. **11**(0): p. 158-164.
67. Saito, T., et al., *Homogeneous Suspensions of Individualized Microfibrils from TEMPO-Catalyzed Oxidation of Native Cellulose.* Biomacromolecules, 2006. **7**(6): p. 1687-1691.

68. Saito, T., et al., *Individualization of Nano-Sized Plant Cellulose Fibrils by Direct Surface Carboxylation Using TEMPO Catalyst under Neutral Conditions.* Biomacromolecules, 2009. **10**(7): p. 1992-1996.
69. Wu, Q., et al., *A High Strength Nanocomposite Based on Microcrystalline Cellulose and Polyurethane.* Biomacromolecules, 2007. **8**(12): p. 3687-3692.
70. Galbe, M. and G. Zacchi, *Pretreatment of Lignocellulosic Materials for Efficient Bioethanol Production*, in *Biofuels*, L. Olsson, Editor. 2007, Springer Berlin Heidelberg: Berlin, Heidelberg. p. 41-65.
71. Ballesteros, I., et al., *Ethanol production from steam-explosion pretreated wheat straw.* Applied Biochemistry and Biotechnology, 2006. **130**(1): p. 496-508.
72. Okano, K., et al., *Conversion of Japanese red cedar (Cryptomeria japonica) into a feed for ruminants by white-rot basidiomycetes.* Animal Feed Science and Technology, 2005. **120**(3): p. 235-243.
73. Lee, J.-W., et al., *Biological pretreatment of softwood Pinus densiflora by three white rot fungi.* Journal of microbiology, 2007. **45 6**: p. 485-91.
74. Hatakka, A.I., *Pretreatment of wheat straw by white-rot fungi for enzymic saccharification of cellulose.* European journal of applied microbiology and biotechnology, 1983. **18**(6): p. 350-357.
75. Ander, P. and K.-E. Eriksson, *Selective Degradation of Wood Components by White-Rot Fungi.* Physiologia Plantarum, 1977. **41**(4): p. 239-248.
76. Akin, D.E., et al., *Alterations in structure, chemistry, and biodegradability of grass lignocellulose treated with the white rot fungi Ceriporiopsis subvermispora and Cyathus stercoreus.* Applied and environmental microbiology, 1995. **61**(4): p. 1591-1598.
77. Boominathan, K. and C.A. Reddy, *cAMP-mediated differential regulation of lignin peroxidase and manganese-dependent peroxidase production in the white-rot basidiomycete Phanerochaete chrysosporium.* Proceedings of the National Academy of Sciences, 1992. **89**(12): p. 5586.
78. Singh, P., et al., *Biological pretreatment of sugarcane trash for its conversion to fermentable sugars.* World Journal of Microbiology and Biotechnology, 2008. **24**(5): p. 667-673.
79. Kumar, A.K. and S. Sharma, *Recent updates on different methods of pretreatment of lignocellulosic feedstocks: a review.* Bioresources and Bioprocessing, 2017. **4**(1): p. 7.
80. Guan, H., Z. Cheng, and X. Wang, *Highly Compressible Wood Sponges with a Spring-like Lamellar Structure as Effective and Reusable Oil Absorbents.* ACS Nano, 2018. **12**(10): p. 10365-10373.
81. Fu, Q., et al., *Wood Nanotechnology for Strong, Mesoporous, and Hydrophobic Biocomposites for Selective Separation of Oil/Water Mixtures.* ACS Nano, 2018. **12**(3): p. 2222-2230.
82. Vidiella del Blanco, M., E.J. Fischer, and E. Cabane, *Underwater Superoleophobic Wood Cross Sections for Efficient Oil/Water Separation.* Advanced Materials Interfaces, 2017. **4**(21): p. 1700584.
83. Keplinger, T., X. Wang, and I. Burgert, *Nanofibrillated cellulose composites and wood derived scaffolds for functional materials.* Journal of Materials Chemistry A, 2019. **7**(7): p. 2981-2992.
84. Qian, X., et al., *Atomic and Electronic Structures of Molecular Crystalline Cellulose Iβ: A First-Principles Investigation.* Macromolecules, 2005. **38**(25): p. 10580-10589.

85. Qian, X., *The effect of cooperativity on hydrogen bonding interactions in native cellulose Iβ from ab initio molecular dynamics simulations.* Molecular Simulation, 2008. **34**(2): p. 183-191.
86. Li, Y., M. Lin, and J.W. Davenport, *Ab Initio Studies of Cellulose I: Crystal Structure, Intermolecular Forces, and Interactions with Water.* The Journal of Physical Chemistry C, 2011. **115**(23): p. 11533-11539.
87. Ishikawa, T., et al., *Ab initio studies on the structure of and atomic interactions in cellulose IIII crystals.* Carbohydrate Research, 2015. **417**: p. 72-77.
88. Bučko, T., et al., *Ab Initio Study of Structure and Interconversion of Native Cellulose Phases.* The Journal of Physical Chemistry A, 2011. **115**(35): p. 10097-10105.
89. Mazeau, K. and L. Heux, *Molecular dynamics simulations of bulk native crystalline and amorphous structures of cellulose.* Journal of Physical Chemistry B, 2003. **107**(10): p. 2394-2403.
90. Mazeau, K. and A. Rivet, *Wetting the (110) and (100) Surfaces of Iβ Cellulose Studied by Molecular Dynamics.* Biomacromolecules, 2008. **9**(4): p. 1352-1354.
91. Matthews, J.F., et al., *Computer simulation studies of microcrystalline cellulose Iβ.* Carbohydrate Research, 2006. **341**(1): p. 138-152.
92. Matthews, J.F., et al., *High-Temperature Behavior of Cellulose I.* The Journal of Physical Chemistry B, 2011. **115**(10): p. 2155-2166.
93. Janesko, B.G., *Modeling interactions between lignocellulose and ionic liquids using DFT-D.* Physical Chemistry Chemical Physics, 2011. **13**(23): p. 11393-11401.
94. Payal, R.S. and S. Balasubramanian, *Dissolution of cellulose in ionic liquids: an ab initio molecular dynamics simulation study.* Physical Chemistry Chemical Physics, 2014. **16**(33): p. 17458-17465.
95. Liu, H., et al., *Understanding the Interactions of Cellulose with Ionic Liquids: A Molecular Dynamics Study.* The Journal of Physical Chemistry B, 2010. **114**(12): p. 4293-4301.
96. Zhao, Y.L., et al., *Effects of Cationic Structure on Cellulose Dissolution in Ionic Liquids: A Molecular Dynamics Study.* Chemphyschem, 2012. **13**(13): p. 3126-3133.
97. Zhao, Y., et al., *Effects of anionic structure on the dissolution of cellulose in ionic liquids revealed by molecular simulation.* Carbohydrate Polymers, 2013. **94**(2): p. 723-730.
98. Rabideau, B.D., A. Agarwal, and A.E. Ismail, *Observed Mechanism for the Breakup of Small Bundles of Cellulose I alpha and I beta in Ionic Liquids from Molecular Dynamics Simulations.* Journal of Physical Chemistry B, 2013. **117**(13): p. 3469-3479.
99. Bergenstråhle, M., L.A. Berglund, and K. Mazeau, *Thermal Response in Crystalline Iβ Cellulose: A Molecular Dynamics Study.* The Journal of Physical Chemistry B, 2007. **111**(30): p. 9138-9145.
100. Assary, R.S. and L.A. Curtiss, *Thermochemistry and Reaction Barriers for the Formation of Levoglucosenone from Cellobiose.* ChemCatChem, 2012. **4**(2): p. 200-205.
101. Mayes, H.B. and L.J. Broadbelt, *Unraveling the Reactions that Unravel Cellulose.* The Journal of Physical Chemistry A, 2012. **116**(26): p. 7098-7106.
102. Agarwal, V., et al., *Ab Initio Dynamics of Cellulose Pyrolysis: Nascent Decomposition Pathways at 327 and 600 °C.* Journal of the American Chemical Society, 2012. **134**(36): p. 14958-14972.
103. Agarwal, V., et al., *Simulating infrared spectra and hydrogen bonding in cellulose Iβ at elevated temperatures.* The Journal of Chemical Physics, 2011. **135**(13): p. 134506.

104. Beste, A., *ReaxFF Study of the Oxidation of Softwood Lignin in View of Carbon Fiber Production.* Energy & Fuels, 2014. **28**(11): p. 7007-7013.
105. Zheng, M., et al., *Initial reaction mechanisms of cellulose pyrolysis revealed by ReaxFF molecular dynamics.* Fuel, 2016. **177**: p. 130-141.
106. Paajanen, A. and J. Vaari, *High-temperature decomposition of the cellulose molecule: a stochastic molecular dynamics study.* Cellulose, 2017. **24**(7): p. 2713-2725.
107. Gomes, T.C.F. and M.S. Skaf, *Cellulose-Builder: A toolkit for building crystalline structures of cellulose.* Journal of Computational Chemistry, 2012. **33**(14): p. 1338-1346.
108. Nishiyama, Y., P. Langan, and H. Chanzy, *Crystal Structure and Hydrogen-Bonding System in Cellulose Iβ from Synchrotron X-ray and Neutron Fiber Diffraction.* Journal of the American Chemical Society, 2002. **124**(31): p. 9074-9082.
109. Chen, C., et al., *Reactive Molecular Dynamics Simulations of Biomass Pyrolysis and Combustion under Various Oxidative and Humidity Environments.* Industrial & Engineering Chemistry Research, 2017. **56**(43): p. 12276-12288.
110. Wu, X., R.J. Moon, and A. Martini, *Tensile strength of Iβ crystalline cellulose predicted by molecular dynamics simulation.* Cellulose, 2014. **21**(4): p. 2233-2245.
111. van Duin, A.C.T., et al., *ReaxFF: A reactive force field for hydrocarbons.* Journal of Physical Chemistry A, 2001. **105**(41): p. 9396-9409.
112. Monti, S., et al., *Exploring the conformational and reactive dynamics of biomolecules in solution using an extended version of the glycine reactive force field.* Physical Chemistry Chemical Physics, 2013. **15**(36): p. 15062-15077.
113. Zhang, W. and A.C.T. van Duin, *Improvement of the ReaxFF Description for Functionalized Hydrocarbon/Water Weak Interactions in the Condensed Phase.* The Journal of Physical Chemistry B, 2018. **122**(14): p. 4083-4092.
114. Zhang, W. and A.C.T. van Duin, *ReaxFF Reactive Molecular Dynamics Simulation of Functionalized Poly(phenylene oxide) Anion Exchange Membrane.* The Journal of Physical Chemistry C, 2015. **119**(49): p. 27727-27736.
115. Castro-Marcano, F., et al., *Pyrolysis of a large-scale molecular model for Illinois no. 6 coal using the ReaxFF reactive force field.* Journal of Analytical and Applied Pyrolysis, 2014. **109**: p. 79-89.
116. Senftle, T.P., et al., *The ReaxFF reactive force-field: development, applications and future directions.* 2016. **2**: p. 15011.
117. Liang, T., et al., *Reactive Potentials for Advanced Atomistic Simulations.* Annual Review of Materials Research, Vol 43, 2013. **43**: p. 109-129.
118. Li, P. and K.M. Merz, *Metal Ion Modeling Using Classical Mechanics.* Chemical Reviews, 2017. **117**(3): p. 1564-1686.
119. Abell, G.C., *Empirical chemical pseudopotential theory of molecular and metallic bonding.* Physical Review B, 1985. **31**(10): p. 6184-6196.
120. Tersoff, J., *New empirical model for the structural properties of silicon.* Physical Review Letters, 1986. **56**(6): p. 632-635.
121. Tersoff, J., *New empirical approach for the structure and energy of covalent systems.* Physical Review B, 1988. **37**(12): p. 6991-7000.
122. Tersoff, J., *Empirical Interatomic Potential for Carbon, with Applications to Amorphous Carbon.* Physical Review Letters, 1988. **61**(25): p. 2879-2882.
123. Tersoff, J., *Modeling solid-state chemistry: Interatomic potentials for multicomponent systems.* Physical Review B, 1989. **39**(8): p. 5566-5568.

124. Qiao, Q., et al., *Graphene oxide model with desirable structural and chemical properties.* Carbon, 2019. **143**: p. 566-577.
125. Huang, L., et al., *Controllable atomistic graphene oxide model and its application in hydrogen sulfide removal.* The Journal of Chemical Physics, 2013. **139**(19): p. 194707.
126. Zhang, T., et al., *Initial Mechanisms for an Overall Behavior of Lignin Pyrolysis through Large-Scale ReaxFF Molecular Dynamics Simulations.* Energy & Fuels, 2016. **30**(4): p. 3140-3150.
127. Zhang, T., X. Li, and L. Guo, *Initial Reactivity of Linkages and Monomer Rings in Lignin Pyrolysis Revealed by ReaxFF Molecular Dynamics.* Langmuir, 2017. **33**(42): p. 11646-11657.
128. Russo, M.F. and A.C.T. van Duin, *Atomistic-scale simulations of chemical reactions: Bridging from quantum chemistry to engineering.* Nuclear Instruments & Methods in Physics Research Section B-Beam Interactions with Materials and Atoms, 2011. **269**(14): p. 1549-1554.
129. Mortier, W.J., S.K. Ghosh, and S. Shankar, *Electronegativity equalization method for the calculation of atomic charges in molecules.* Journal of the American Chemical Society, 1986. **108**(15): p. 4315-4320.
130. Janssens, G.O.A., et al., *Comparison of cluster and infinite crystal calculations on zeolites with electronegativity equalization method (EEM).* Journal of Physical Chemistry, 1995. **99**(10): p. 3251-3258.
131. Agrawalla, S. and A.C.T. van Duin, *Development and Application of a ReaxFF Reactive Force Field for Hydrogen Combustion.* Journal of Physical Chemistry A, 2011. **115**(6): p. 960-972.
132. Chenoweth, K., et al., *Development and application of a ReaxFF reactive force field for oxidative dehydrogenation on vanadium oxide catalysts.* Journal of Physical Chemistry C, 2008. **112**(37): p. 14645-14654.
133. Chenoweth, K., A.C.T. van Duin, and W.A. Goddard, *ReaxFF reactive force field for molecular dynamics simulations of hydrocarbon oxidation.* Journal of Physical Chemistry A, 2008. **112**(5): p. 1040-1053.
134. Djahedi, C., L.A. Berglund, and J. Wohlert, *Molecular deformation mechanisms in cellulose allomorphs and the role of hydrogen bonds.* Carbohydrate Polymers, 2015. **130**: p. 175-182.
135. Djahedi, C., et al., *Role of hydrogen bonding in cellulose deformation: the leverage effect analyzed by molecular modeling.* Cellulose, 2016. **23**(4): p. 2315-2323.
136. Lee, C.M., et al., *Hydrogen-Bonding Network and OH Stretch Vibration of Cellulose: Comparison of Computational Modeling with Polarized IR and SFG Spectra.* The Journal of Physical Chemistry B, 2015. **119**(49): p. 15138-15149.
137. Araujo, C., et al., *Hydrogen Bond Dynamics of Cellulose through Inelastic Neutron Scattering Spectroscopy.* Biomacromolecules, 2018. **19**(4): p. 1305-1313.
138. Altaner, C.M., et al., *How Cellulose Stretches: Synergism between Covalent and Hydrogen Bonding.* Biomacromolecules, 2014. **15**(3): p. 791-798.
139. Mercury. *Mercury User Guide and Tutorials*. 2019 [cited 2019 Aug/25/2019]; Available from: https://www.ccdc.cam.ac.uk/support-and-resources/CCDCResources/Mercury_UserGuide.pdf.
140. Diamond. *Diamond, Crystal and Molecular Structure Visualization*. 2019 [cited 2019 Aug/25/2019]; Available from: https://www.crystalimpact.com/download/diamond/tutorial.pdf.

141. Truesdell, C., *The rational mechanics of flexible or elastic bodies 1638-1788 ; introduction to Leonhardi Euleri opera omnia Vol. X et XI seriei secundae*. 1960, Turici: Orell F¸ssli.
142. Matsuo, M., et al., *Effect of orientation distribution and crystallinity on the measurement by x-ray diffraction of the crystal lattice moduli of cellulose I and II.* Macromolecules, 1990. **23**(13): p. 3266-3275.
143. Eichhorn, S.J., R.J. Young, and G.R. Davies, *Modeling Crystal and Molecular Deformation in Regenerated Cellulose Fibers.* Biomacromolecules, 2005. **6**(1): p. 507-513.
144. Tanaka, F. and T. Iwata, *Estimation of the Elastic Modulus of Cellulose Crystal by Molecular Mechanics Simulation.* Cellulose, 2006. **13**(5): p. 509-517.
145. Šturcová, A., G.R. Davies, and S.J. Eichhorn, *Elastic Modulus and Stress-Transfer Properties of Tunicate Cellulose Whiskers.* Biomacromolecules, 2005. **6**(2): p. 1055-1061.
146. Eichhorn, S.J. and G.R. Davies, *Modelling the crystalline deformation of native and regenerated cellulose.* Cellulose, 2006. **13**(3): p. 291-307.
147. Hossain, D., et al., *Molecular dynamics simulations of deformation mechanisms of amorphous polyethylene.* Polymer, 2010. **51**(25): p. 6071-6083.
148. Plimpton, S., *Fast Parallel Algorithms for Short-Range Molecular Dynamics.* Journal of Computational Physics, 1995. **117**(1): p. 1-19.
149. Spearot, D.E., et al., *Tensile strength of ⟨100⟩ and ⟨110⟩ tilt bicrystal copper interfaces.* Acta Materialia, 2007. **55**(2): p. 705-714.
150. Tschopp, M.A., D.E. Spearot, and D.L. McDowell, *Atomistic simulations of homogeneous dislocation nucleation in single crystal copper.* Modelling and Simulation in Materials Science and Engineering, 2007. **15**(7): p. 693-709.
151. Tschopp, M.A. and D.L. McDowell, *Influence of single crystal orientation on homogeneous dislocation nucleation under uniaxial loading.* Journal of the Mechanics and Physics of Solids, 2008. **56**(5): p. 1806-1830.
152. Mishin, Y., et al., *Interatomic potentials for monoatomic metals from experimental data and ab initio calculations.* Physical Review B, 1999. **59**(5): p. 3393-3407.
153. Kroon-Batenburg, L.M.J. and J. Kroon, *The crystal and molecular structures of cellulose I and II.* Glycoconjugate Journal, 1997. **14**(5): p. 677-690.
154. Viëtor, R.J., et al., *A priori crystal structure prediction of native celluloses.* Biopolymers, 2000. **54**(5): p. 342-354.
155. Reiling, S. and J. Brickmann, *Theoretical investigations on the structure and physical properties of cellulose.* Macromolecular Theory and Simulations, 1995. **4**(4): p. 725-743.
156. Wada, M. and T. Okano, *Localization of Iα and Iβ phases in algal cellulose revealed by acid treatments.* Cellulose, 2001. **8**(3): p. 183-188.
157. Popescu, M.-C., et al., *Evaluation of morphological and chemical aspects of different wood species by spectroscopy and thermal methods.* Journal of Molecular Structure, 2011. **988**(1): p. 65-72.
158. Poletto, M., L.H. Ornaghi, and J.A. Zattera, *Native Cellulose: Structure, Characterization and Thermal Properties.* Materials, 2014. **7**(9).
159. Rismiller, S.C., et al., *Water assisted liquefaction of lignocellulose biomass by ReaxFF based molecular dynamic simulations.* Fuel, 2018. **215**: p. 835-843.
160. Jahirul, I.M., et al., *Biofuels Production through Biomass Pyrolysis —A Technological Review.* Energies, 2012. **5**(12).
161. Yui, T., et al., *Swelling behavior of the cellulose Iβ crystal models by molecular dynamics.* Carbohydrate Research, 2006. **341**(15): p. 2521-2530.

162. van Duin, A.C.T., et al., *ReaxFF: A Reactive Force Field for Hydrocarbons.* The Journal of Physical Chemistry A, 2001. **105**(41): p. 9396-9409.
163. Zhu, C., et al., *Energetics of cellulose and cyclodextrin glycosidic bond cleavage.* Reaction Chemistry & Engineering, 2017. **2**(2): p. 201-214.
164. Kimball, J.W. *The Energy Relationships in Cellular Respiration and Photosynthesis: the Balance Sheet*. 2019 [cited 2019 9/2/2019]; Available from: https://www.biology-pages.info/B/BalanceSheet.html.
165. Steiner, T., *The Hydrogen Bond in the Solid State.* Angewandte Chemie International Edition, 2002. **41**(1): p. 48-76.
166. Diddens, I., et al., *Anisotropic Elastic Properties of Cellulose Measured Using Inelastic X-ray Scattering.* Macromolecules, 2008. **41**(24): p. 9755-9759.
167. Nakamae, K., et al., *Experimental Determination of the Elastic Modulus of Crystalline Regions of Some Aromatic Polyamides, Aromatic Polyesters, and Aromatic Polyether Ketone.* Polymer Journal, 1987. **19**: p. 451.
168. Sakurada, I., Y. Nukushina, and T. Ito, *Experimental determination of the elastic modulus of crystalline regions in oriented polymers.* Journal of Polymer Science, 1962. **57**(165): p. 651-660.
169. Moon, R.J., et al., *Cellulose nanomaterials review: structure, properties and nanocomposites.* Chemical Society Reviews, 2011. **40**(7): p. 3941-3994.
170. Tashiro, K. and M. Kobayashi, *Calculation of crystallite modulus of native cellulose.* Polymer Bulletin, 1985. **14**(3): p. 213-218.
171. Neyertz, S., et al., *A new all-atom force field for crystalline cellulose I.* Journal of Applied Polymer Science, 2000. **78**(11): p. 1939-1946.
172. Saito, T., et al., *An Ultrastrong Nanofibrillar Biomaterial: The Strength of Single Cellulose Nanofibrils Revealed via Sonication-Induced Fragmentation.* Biomacromolecules, 2013. **14**(1): p. 248-253.
173. Mark, R.E., *Cell wall mechanics of tracheids*. 1967, New Haven, London: Yale Univ. Press.

Chapter 6: Cellulose-Graphene Oxide Composite and Model Development

6.1 Introduction

Graphene is a "wonder two-dimensional material" with excellent mechanical and physical properties [1-4], and attracts growing interest in research since it is first reported in 2004 [5]. The superior elastic modulus of graphene is ~1 TPa [3] which makes graphene "stronger than steel" and widely used in the application of reinforcement in polymer-based nanocomposites. The polymer-functionalized graphene showed great enhancement in the mechanical, thermal, electrical and optical properties [6-9].

Due to the accessibility of macro-scale production, interfacial modification, and better dispersibility, the graphene precursor, graphene oxide (GO) derivatives, has been considered as a promising candidate in polymer nanocomposites [10-14]. Because of its unusual electronic properties, wet-chemical processability, large-scale availability as monolayers, and low cost, GO has become one of the most widely utilized two-dimensional (2D) nanomaterials during the past decade [15-19]. The extensive applications of GO include composites [20], separation [21-23], catalysis [24, 25], sensing [26, 27], electronics [28, 29], energy storage [30, 31], biological and drug delivery [32-35]. The mechanical and fracture studies of GO itself is still ambiguous and conflicting since GO structure is highly dependent on the synthesis method, which results in the different concentration and distribution of functional groups (mainly hydroxyl, epoxide and carboxyl) [18, 36-39], and defects located on GO surface. Both the structural (defect, curvature) and chemical (functional groups) properties of GO significantly affect the mechanical behavior of

GO. For example, Cao et al. [40] studied mechanical properties of the monolayer GO membranes with20% degree of oxidation via the Density functional theory (DFT). It is showed that the brittle failure of GO occurred along the connecting oxidized carbon atoms on GO surface. On the contrary, Wei and co-workers [41] found that 70% oxidization monolayer GO exhibits ductile behavior via density functional-based tight binding (DFTB). They proposed that the mechanical strength can be fine-tuned by converting epoxide groups into more stable ether groups. Their reported elastic modulus (256.4 ± 28.2 GPa) is lower than the value (384 ± 31 GPa) proposed from Cao et al. [40], which indicated that the increasing of oxidation of GO might lead to the decrease of elastic modulus. More specifically, the hydroxyl groups are reported to cause brittle behavior, whereas the ductile failure occurred when the transformation of epoxide-to-ether groups is dominated on GO surface [42, 43]. Meng et al. [44] predicted the critical stress intensity factor of GO via a coarse-grain model with the degree of oxidation from 20% to 80%. Using reactive force field (ReaxFF), Verma et al. [45] proposed that the spatial distribution and concentration of hydroxyl and epoxide groups are critical for the ductile behavior of GO. Experimentally, Gao and co-workers[46] reported that the grip pressure, length and loading rate highly affect the measurement of GO mechanical properties. Sakorikar et al. [47] demonstrated that the thickness of reduced graphene oxide (rGO) determines the crack propagation process of rGO films. An increasing thickness results in the decrease of the crack density and the increase of crack width. Similarly, Cao et al. [48] found that the random distribution of functional groups between GO multiple layers prevents the growth of preexisting crack. Although efforts have been made from both experiments and simulation on the studies of functionalized GO materials, a better fundamental understanding of GO mechanical properties at atomistic level is still required.

As the basic building block of algae, bacteria and green plants, cellulose has a production of about 700 billion tons per year due to its renewability, sustainability, high biodegradability and excellent biocompatibility. Since it is the most abundant and cheapest natural biomaterials, cellulose has been widely used in biofuel productions [49, 50], biomedical engineering [51-59], energy related applications [60-63] and paper and construction industry [64-68]. Cellulose is a linear polysaccharide of repeating D-glucose units with a degree of polymerization (DP) from 10,000 to 15,000 [69]. The coexistence of both crystalline and amorphous regions, and the hydrogen bonds (HBs) network formed in cellulose chains make cellulose excellent mechanical properties.

Cellulose and its derivatives have been used to functionalize GO for GO/cellulose nanocomposites, and the prediction of mechanical properties is one of the important parts for the investigation of GO/cellulose composites. Effort has been made experimentally in order to evaluate the properties and applications of GO-cellulose composites [70, 71]. Kim et al. [72] proposed that a small amount GO in GO/cellulose films can greatly improve the Young's modulus of the composite by 31%, but the presence of GO results in brittle behavior of the GO/cellulose films. Luo and co-workers [73] found that the bacterial cellulose (BC)-GO nanocomposites with sophisticated three-dimensional (3D) porous structure showed enhanced Young's modulus (~36 MPa) compared with pure BC (~10 MPa). Li and co-workers [74] incorporated GO with nanofibrillated cellulose (NFC) fibers and reported that this hybrid fibers are stronger than the pure GO and NFC due to the synergistic effect of bonds between NFC fibers and GO sheets. A cellulose/rGO paper with tunable mechanical properties and high biocompatibility was reported by Peng et al. [75], which could be used in biomaterial scaffolds for biomedical and tissue engineering. A potential electrochemical film consisting of nanocrystalline cellulose acetate

(NCCA) and GO showed not only the enhancement of 61.92% in tensile strength compared with pure NCCA, but the electrical properties are greatly improved as well [76].

However, the measurement of mechanical properties from experiments might be inconsistent due to physical obstacle such as difficulties in controlling the layer number of GO, monitoring the dispersion state of GO composites and modifying the GO/cellulose interface [77-79]. To address this issue, computational tools such as molecular dynamics (MD) simulation provides alternative way to characterizing target composites without any synthesizing operations. Medhekar et al. and Compton et al. [80, 81] both performed RxMD to study the mechanical properties of multilayered GO composite paper. They concluded that the HBs network and water molecules influence the mechanical behavior of multilayered GO composite. The control of structural and mechanical properties of the GO composite can be achieved by adjusting the amounts of functional groups, adding extra H-bonding favorable polymers (e.g. polyvinyl alcohol) and changing the concentration of water between GO layers. Zhang and Jiang [82] performed MD simulations to understanding the mechanical behavior of graphene/GO paper composite. It is found that a large number of functional groups between graphene/GO layers increases the overall stiffness by increasing the number of HBs in the system. While the elastic modulus of single GO sheet decreased with more functional groups in the surface. Rahman et al. [83] reported that the Young's modulus of graphene/cellulose composites with 5% graphene are 100% higher than pure cellulose resin system.

Despite of the plenty computational studies aforementioned, there is barely no published work comparing the mechanical performance of monolayer GO and new cellulose-GO nanocomposites after incorporating amorphous cellulose chains on GO surface. In this work, a series of RxMD simulations have been carried out to reveal the mechanical properties of pure GO

and cellulose-GO nanocomposites. The GO model used in this work will be generated from previous work in order to predict both structural and chemical properties of GO with random distribution of multiple oxygen-containing functional groups, vacancy defects and curvature.[84] Two different cellulose-GO composites are constructed, namely, cellulose (monolayer)-GO model and cellulose (multilayer)-GO model. The tensile deformation, Young's modulus and yield strength of GO and cellulose-GO composites have been recorded and calculated under the temperature of 300, 500 800 K, with two strain rates of 10^{-4}/fs and 10^{-5}/fs. We hope the GO model with the simultaneously description to both structural and chemical properties, will provide a new fundamental understanding of the mechanical performance of GO and cellulose-GO composites, and could add some advancement to existing knowledge.

6.2 Cellulose-GO Composite Model and Simulation Protocol

6.2.1 Reactive Force Field

In 2001, van Duin and co-workers developed a ReaxFF reactive empirical force field with the bond-order concept that adopted from Tersoff [85]. Over the development of the last twenty years, ReaxFF has been successfully employed to describe the development and optimization of material properties as well as some large and multiscale modeling systems such as membrane fuel cell system[86], biological studies involving with protein/DNA [87, 88], and very complex coal structure and properties [89]. Instead of using the description of bond length, angle and dihedrals from classical force fields, the application of bond order allows the simulation of reaction pathway in the system due to the continuous bond formation and breaking. These advantages make ReaxFF a powerful computational tool in the study of structural evolution and chemical reactions. Generally, RaxFF is one order slower than the non-reactive MD simulations due to the expensive

charge calculations via electronegativity equalization method (EEM) proposed by Mortier and co-workers [90-92]. However, the simulation time of a microseconds trajectory can be reduced by the utilization of hardware and parallel calculations. Recently, ReaxFF has been reported to use extensively for the structural evolution of GO [80, 81, 93-101], biomass system including cellulose, hemicellulose, lignin and their derivatives [102-107]. More details of ReaxFF are available from recent reviews [108-110] and the website of the developers [111]. The ReaxFF parameters used in this work have successfully described cellulose systems [106, 107].

6.2.2 Cellulose-GO Model and RxMD Simulation

The pure GO sheet is generated via the RxMD simulations from Chapter 3, with trigger temperature of 1000 K, initial functionalization density of 50 % and ratios of hydroxyl and epoxy of 1:1 (50%GO, (1:1), T_{tri}=1000 K), and cellulose chains are adopted from Chapter 5. In Figure 26 (a) and (b) are the top and side view about the vacancy distribution and curvature of GO sheet. A total of 14 cellulose chains were set to parallel to both GO sides and each other in order to represent a cellulose-GO monolayer model, as shown in Figure 26 (c) and (d). While in Figure 26 (e) and (f), each GO side is built up with 20 amorphous cellulose chains to represent a cellulose-GO multilayer model.

The RxMD calculations were carried out via the LAMMPS software package with the ReaxFF implemented as an external library [112]. The isothermal–isobaric (NPT) ensemble at a low initial temperature and 1 atm were applied for each simulation to relax the initial structure to an appropriate volume and reduce stresses from the GO basal plane. Then the annealing process was performed from the low temperature to the target temperature (300, 500 and 800 K). The Berendsen method with the damping constant 100 fs was applied to maintain the temperature of

the system and the initial velocity is generated by the Boltzmann distribution. A timestep of 0.25 fs is used throughout the calculations. All the calculations have at least a 10-ns trajectory to reach the equilibrium. For the calculation of Young's modulus, additional 1 ns was employed after 10 ns equilibrium calculations, with a smaller timestep of 0.05 fs for data collection. In this work, the equilibrium state is justified via the change of total energy.

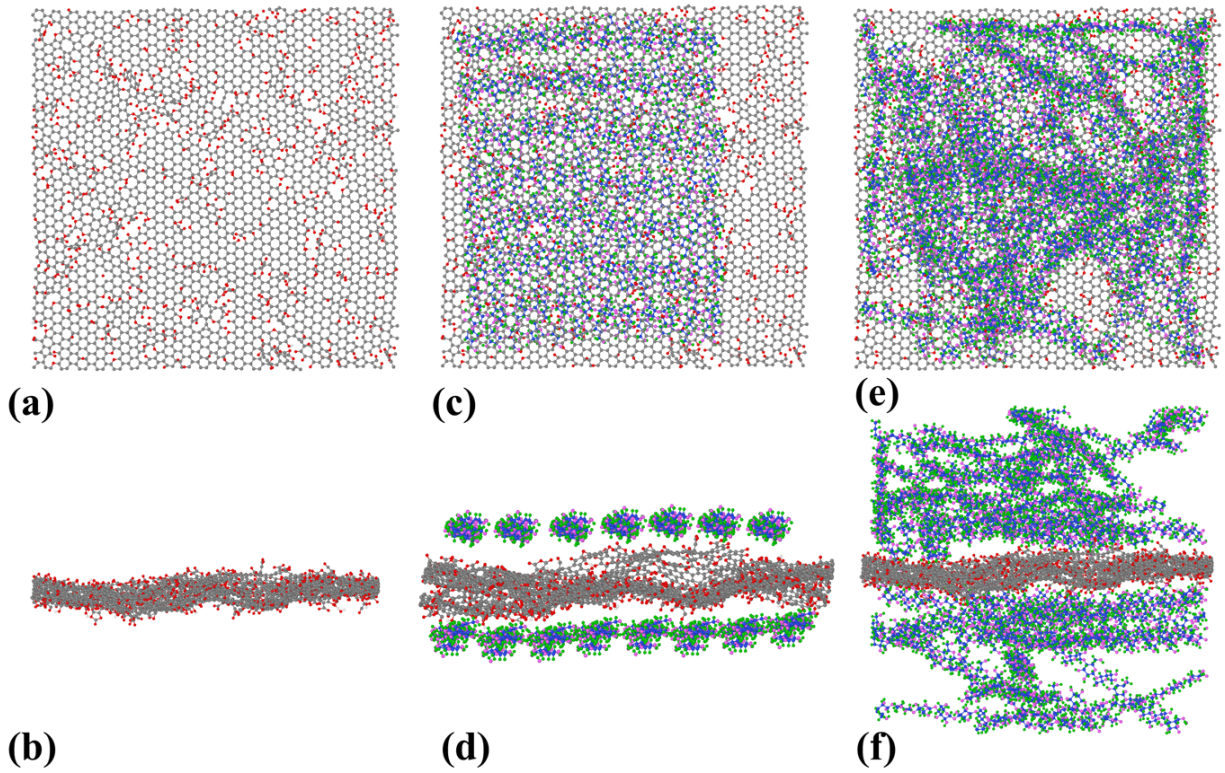

Figure 26. The (a) top view and (b) side view of GO sheet that generated by the initial pure 50%GO, (1:1), T_{tri}=1000 K model; The (c) top view and (d) side view of cellulose(monolayer)-GO model, with 7 paralleled cellulose chains on each GO side; The (e) top view and (f) side view of cellulose(multilayer)-GO model, with 20 amorphous cellulose chains on each GO side. The carbon, oxygen and hydrogen atoms in GO and cellulose are in different colors. In GO: grey, red and white are carbon, oxygen and hydrogen atoms, respectively. In cellulose: blue, pink and green are carbon atoms, carbon, oxygen and hydrogen atoms, respectively.

6.2.3. The Simulation of Tensile Deformation

Several methods have been proposed to perform the tensile deformation process and calculate Young's modulus:

(1) The calculation can be carried out to elongated (or decreased) the simulation box (z_0) by a small increment Δz (maximum 5% of the chain length) [113] along the axis of the applied stress, then the whole simulation box is re-optimized. The stress (σ) can be obtained by derivative of the function between the minimum potential energy and the axial length from the system[114-116], and the E_A is then the slope of the stress vs. strain ($\varepsilon=\Delta z/z_0$) curve [117-119]. A similar energy density method calculated E_A via twice the slope of energy density and the square of strain.[113]

(2) The stress can be defined as native value of pressure along the corresponding direction, the elastic modulus is then calculated by $E_A = \sigma/\varepsilon$. Instead of elongating simulation box by small increment,[120] the stress can also be changed directly with a constant pressure rate (e.g. 200bar/ps) with NPT ensemble[121].

(3) Alternative way is to allow the continuous elongation of simulation box along the direction where the stress is applied, with a defined strain rate in NPT system [112, 122-127] The system is re-optimized in NPT ensemble in order to allow the dimensional changes due to Passion's effect [127, 128].

(4) The elastic modulus can also be calculated by full elastic constant matrices based on the continuum concept of elasticity [116, 129-133]. The calculations can be performed via simulations tools in Materials Studio package [116, 131-133]. The energy minimization allows the changes of both atomic coordinates and unit cell parameters, which leads to no constant-area assumption.

In this work we use the (3) method to monitor the uniaxial tensile deformation at two different strain rates for three temperatures. It is worth noting that the application of periodic boundary conditions [113, 128] also affect the elastic modulus value from computational studies. A widely used method is the one-unit cell model with periodic boundary conditions, which is perfect for simulating infinite crystalline structures [115, 134], however, the accuracy of this method is highly dependent on the measurements of the original unit cell. Another method is super cell model with finite dimensions, which is appropriate for paracrystalline materials, while it might suffer from the drawback of finite-size effects [113]. Systems that consisting of super cell model with periodic boundary conditions are also widely used in the calculations of elastic modulus. Although this approach precludes the surface properties, it can overcome the size limitation to study the bulk properties of cellulose, and avoid unreasonable response of the surface chains to the strain and interactions with neighboring atoms [128, 135]. Here we adopted the third method using super cell model with periodic boundary conditions. And similar with previous study [127], the 0.2% offset yield strength is used to estimate the yielding strength of pure GO and GO-cellulose composites.

6.3 Results and Discussions

6.3.1 Mechanical Properties of Pure GO

As aforementioned in the introduction session, the degree of oxidation, different type of functional groups, defects and number of layers can significantly affect the mechanical behavior of GO. Here in the Table 9 we listed the detailed structural and chemistry information about the monolayer GO sheet used in this work. Also, the mechanical behavior of GO and cellulose-GO composites with different strain rates and temperatures are summarized in Table 10. The effect

of temperature and strain rate on the mechanical performance will be described separately in the following sessions.

Table 9. The structural and chemistry properties of GO sheet

Degree of Oxidation	C/O Ratio	Pore Range	Pore Density
30.08%	4.47	0.2-0.5nm	4.31%

Table 10. The mechanical behavior of GO and cellulose-GO composites under various conditions.

	GO			
	10^{-4} /fs		10^{-5} /fs	
	Armchair[a]	Zigzag[b]	Armchair[a]	Zigzag[b]
100 K	Ductile	Brittle	Ductile	Brittle
300 K	Ductile	Brittle	Ductile	Brittle
500 K	Brittle	Brittle	Ductile	Brittle
800 K	Brittle	Brittle	Ductile	Brittle

[a] along the X direction, as shown in Figure 26 (a).
[b] along the Y direction, as shown in Figure 26 (a).

6.3.1.1 Ductile vs. Brittle Behavior of GO

The anisotropic mechanical behavior was observed for pure GO along different deformation directions at various temperatures (see Table 10). For example, Figure 27 showed that with a constant strain rate of 10^{-5} /fs at 500 K, GO exhibits obviously ductile behavior along the armchair direction, whereas when performed tensile deformation along zigzag direction, a brittle behavior occurred for the same GO system. While the ultimate strength is almost the same (3.67 and 3.91 GPa for armchair and zigzag direction) as shown in Figure 27. And the calculated Young's modulus (the slopes) from both directions showed little difference. Similar results were also recorded for GO systems at 100 K, 300 K and 800 K.

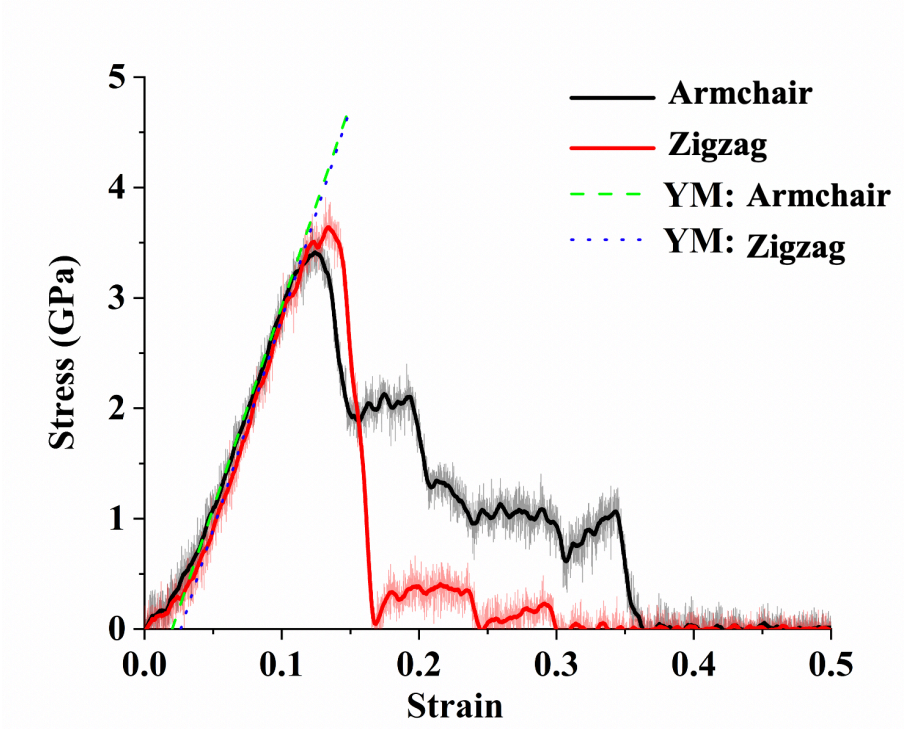

Figure 27. The stress-strain diagram of GO at 500 K, strain rate of 10^{-5} /fs is employed, the tensile deformation along armchair direction is in black and tensile deformation along zigzag direction is in red, the slope of deformation curve along armchair direction is in green dashed line and the slope of deformation curve along zigzag direction is in blue dotted line, respectively;

6.3.1.2 The Mechanical Behavior of GO: Temperature Dependency

With a constant strain rate of 10^{-5} /fs, GO showed ductile behavior along the armchair direction and brittle behavior for zigzag direction for all temperatures, as showed in Figure 28 (a) and (b). The ultimate strength is decreasing when temperature increased for both directions. Similarly, the calculated Young's modulus decreased as temperature increased. A summary of the calculated Young's modulus can be found in Table 11.

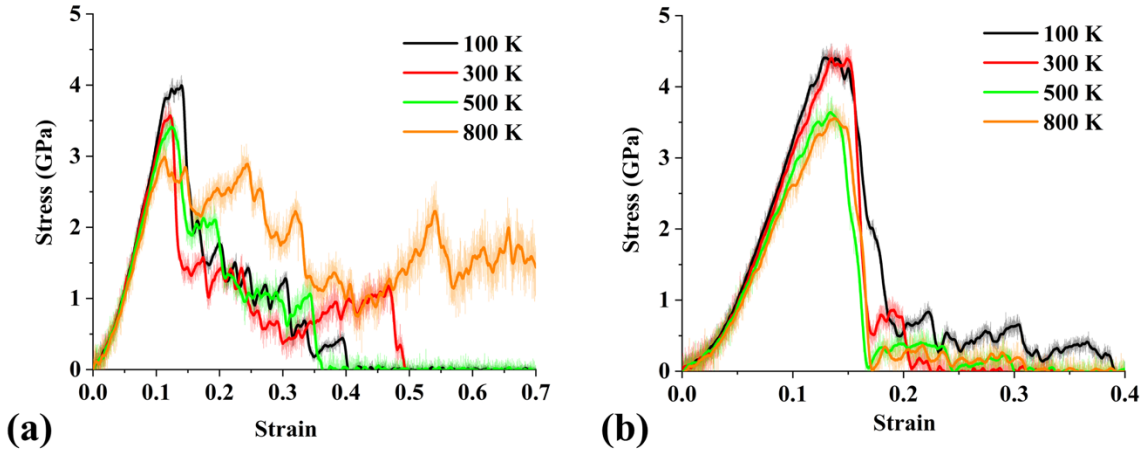

Figure 28. The stress-strain diagrams of GO with a constant strain rate of 10^{-5} /fs for (a) along armchair direction and (b) zigzag direction at various temperatures. The black, red, green and orange lines represent the temperature of 100 K, 300 K, 500 K and 800 K, respectively.

Table 11. The calculated Young's Modulus of GO and cellulose-GO composites under various conditions.

Temperature (K)	GO (GPa)
100	40.90654 ± 0.04519
300	37.93096 ± 0.08123
500	36.63569±0.04464
800	33.64642 ± 0.11716

6.3.1.3 The Mechanical Behavior of GO: Strain Rate Dependency

With a constant temperature at 800 K, we have performed tensile deformations with two strain rates, 10^{-4} /fs and 10^{-5} /fs. In Figure 29 we provided a strain-stress diagram that compared the deformation curves along armchair directions. Within the strain of 0~0.1 (elastic region), the snapshots are similar for both strain rates. When the strain is ~0.15 (plastic region), the GO system

with a smaller strain rate (10^{-5} /fs) showed larger pores on the GO surface with wrinkling. When the strain is ~0.2, both systems have large pores and channels for the further fracture.

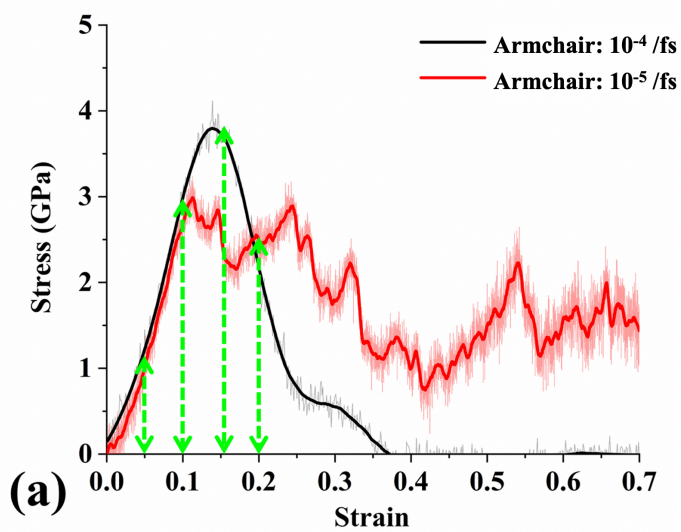

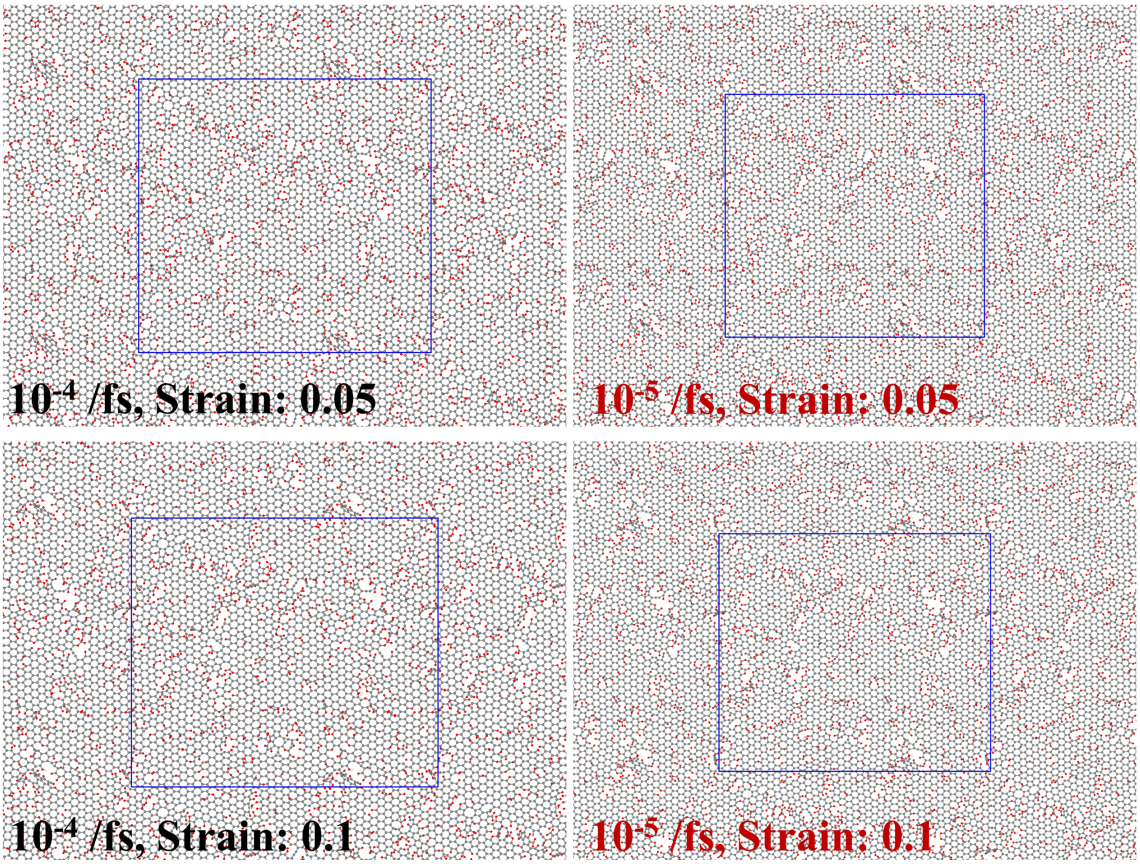

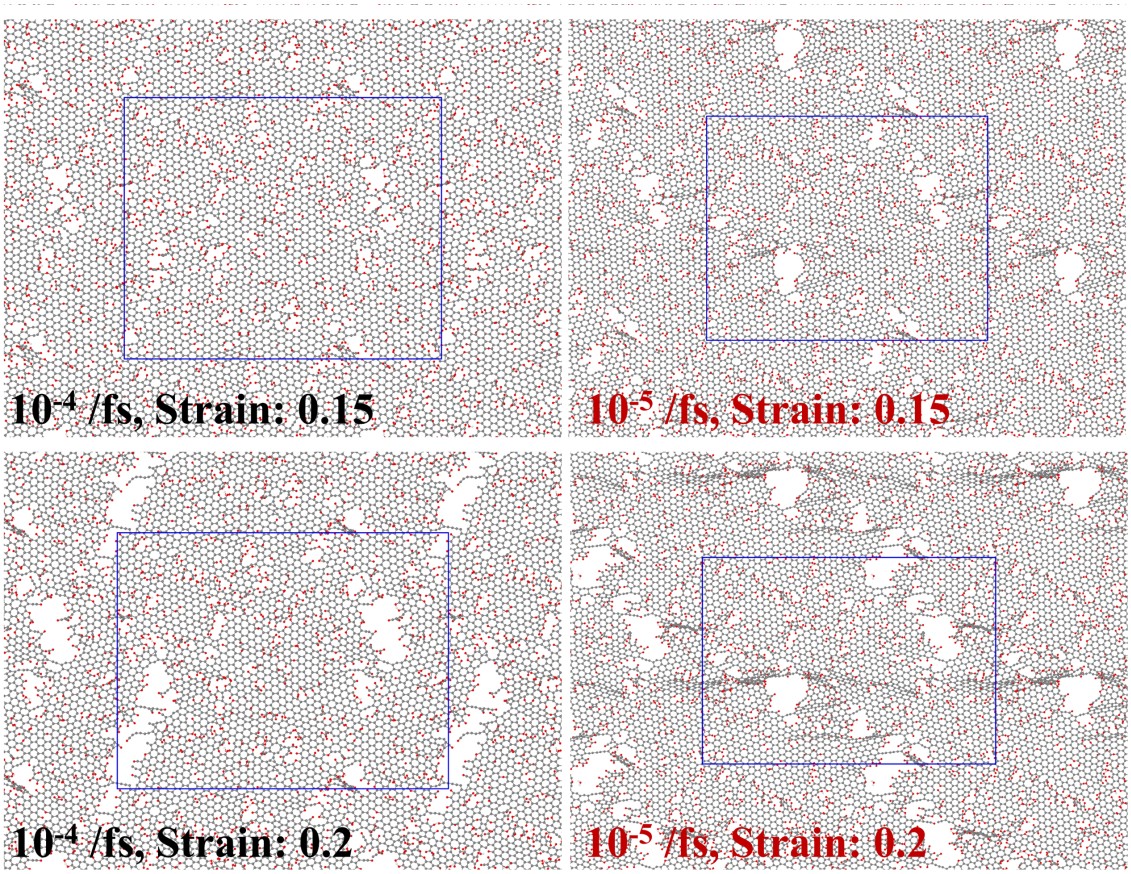

Figure 29. The stress-strain diagrams of GO at 800 K (a) with two constant strain rates of 10^{-4} /fs (black) and 10^{-5} /fs (red); (b-i) showed the snapshots of GO system with two strain rates at strain of 0.05, 0.1, 0.15 and 0.2, respectively.

6.3.1.4 The Fracture surface of GO

The fracture surface of GO systems with a constant strain rate of 10^{-4} /fs at 300 K are compared, see Figure 30. Along the deformation direction of armchair, GO deformation showed ductile behavior, and a coarse fracture surface was observed in Figure 30 (a) and (c), whereas for the zigzag direction, brittle behavior leads to a much smoother fracture surface, as shown in Figure 30 (b) and (c). In Figure 30 (d) we provided a coastline map using the fitting curve to illustrate the different configuration of GO surfaces. For the coarse GO surface generated by the ductile

behavior, the fitting curve has higher intensity and sharper shape. The fracture coastline of armchair can be as high as 20 Å. While for the GO surface obtained from brittle behavior, low intensity and wide shape are observed with a fracture coastline ~10 Å. This fracture surface difference is also reported by experiments for various materials.[136]

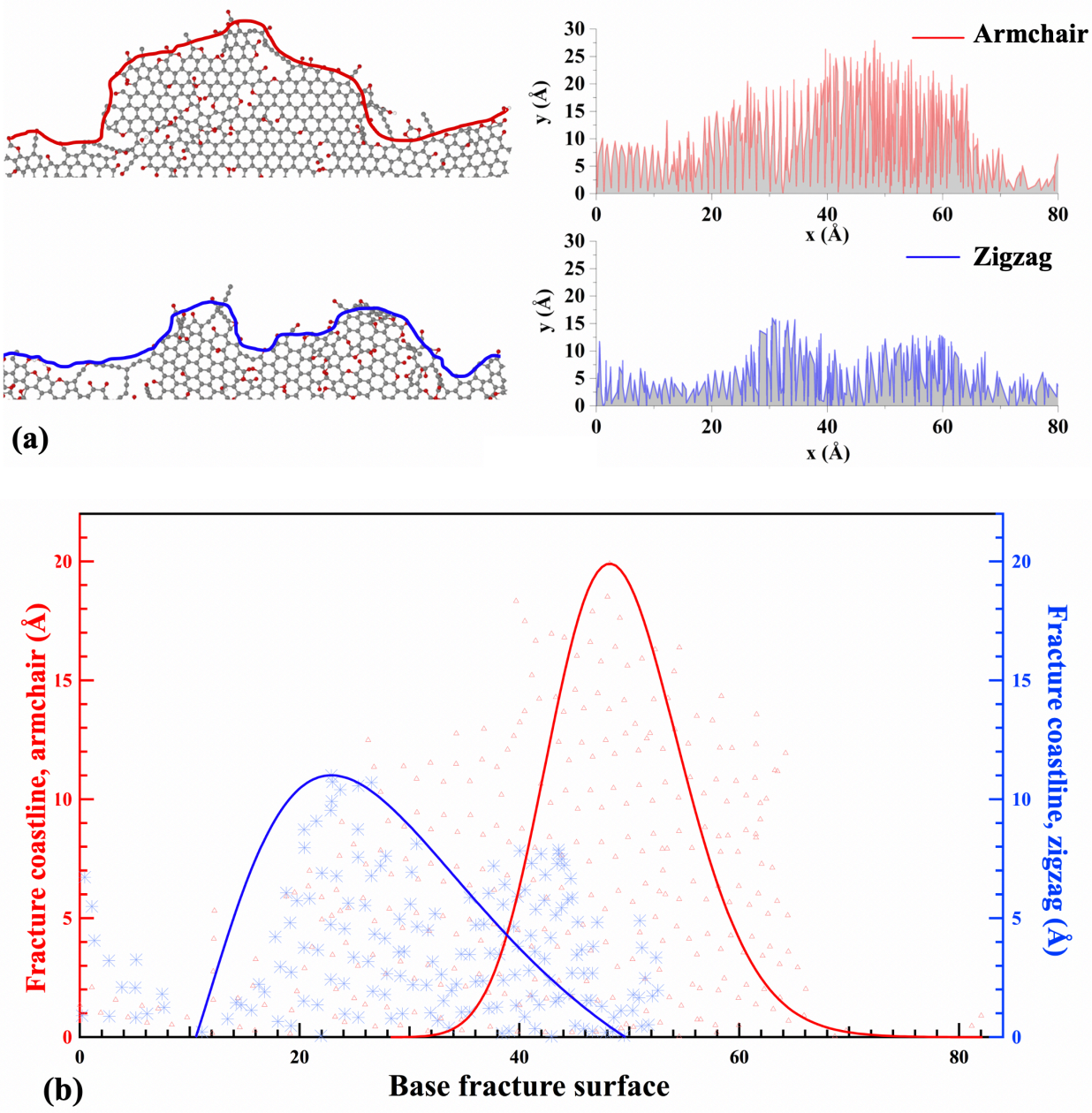

Figure 30. The snapshot of fracture surface of GO at 300 K for the deformation along (a) armchair and (b) zigzag direction with a constant strain rate of 10^{-4} /fs; (c) The comparison of fracture

surface of GO systems; (d) The coastline map of fracture surfaces of GO systems; The deformation along armchair direction is red and along zigzag direction is blue, respectively.

6.3.1.5 The Tensile Deformation process of GO

The tensile deformation process along armchair direction of GO with a constant strain rate of 10^{-5} /fs at 800 K is represented in Figure 31. GO exhibits ductile behavior during the whole deformation process. Under the strain of 0.1, GO surface showed little difference compared with initial GO sheet without applied strain (see Figure 26 (a)). For the strain of ~0.5 and above, GO is significantly wrinkled and corrugated with some small region of carbon atoms holding the whole sheet together. Figure 31 (g) is the side view of GO sheet at strain of 0.7, interestingly, the 2D GO sheet transferred to a 3D, tube-like materials with channels inside the materials. And the GO structure under this condition has larger Poisson's ration compared with other systems.

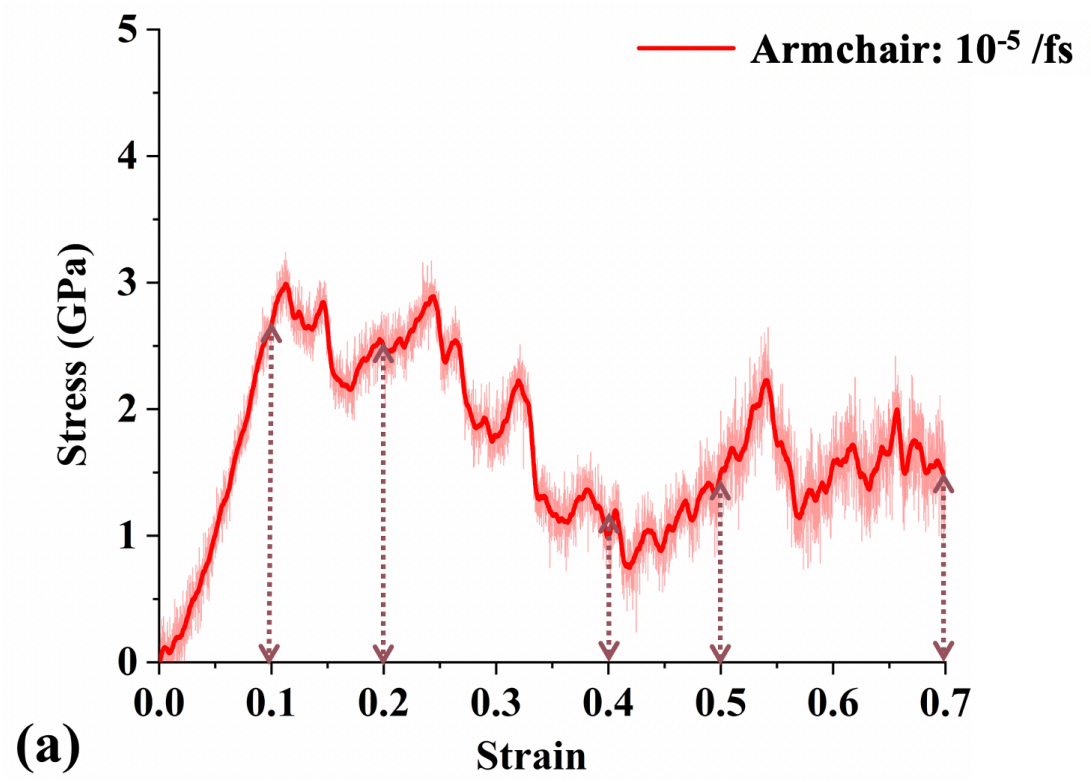

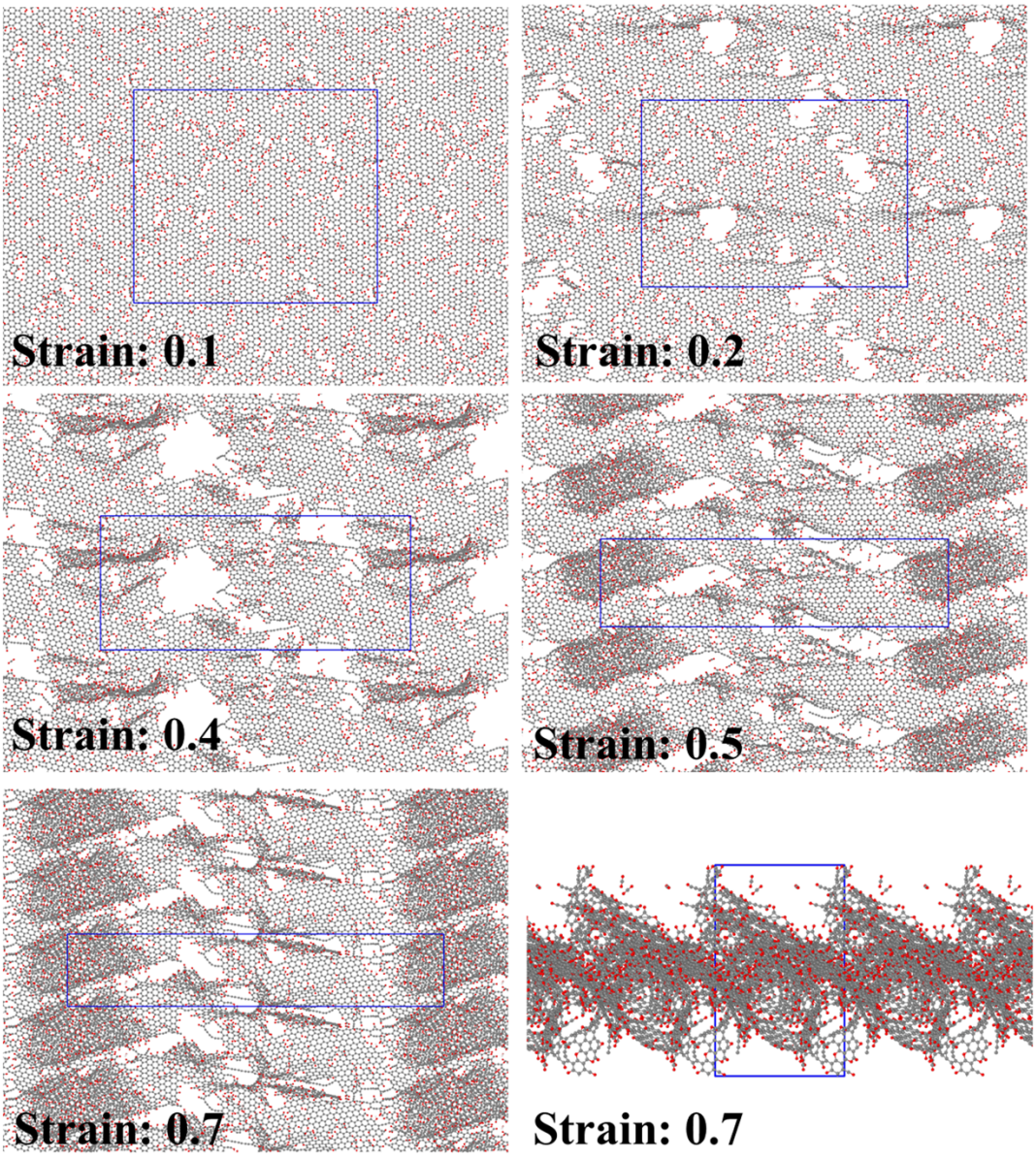

Figure 31. (a) The stress-strain diagram and (b-g) The snapshot of GO at 800 K for the deformation along armchair direction with a constant strain rate of 10^{-5} /fs at strain of 0.1, 0.2, 0.4, 0.5 and 0.7, respectively.

6.3.2 Mechanical behavior of Cellulose-GO composites

The comparison of mechanical behavior of GO, cellulose(monolayer)-GO and cellulose(multilayer)-GO systems are represented in Figure 32. With a constant strain rate of 10^{-5} /fs at 300 K, all three materials showed ductile behavior along both armchair and zigzag directions. The cellulose(monolayer)-GO composite has similar ultimate strength and Young's modulus compared with pure GO system. While for cellulose(multilayer)-GO system, the mechanical strength is greatly decreased. The Young's modulus for cellulose(multilayer)-GO composite is only 50% of the Young's modulus of cellulose(monolayer)-GO composite.

In Figure 33 (a) and (b), cellulose chains are well packed and attached on both side of the GO surface after 5 ns equilibrium. The fracture of cellulose(monolayer)-GO composite occurred at the defects that did not covered by cellulose chains, as shown in Figure 33 (c) and (e) for both armchair and zigzag directions. This is probably due to the interactions between the well packed cellulose chains and functional groups on GO surfaces. For the cellulose(multilayer)-GO composite, amorphous cellulose chains formed self-aggregation on both the GO surfaces. However, the fracture might occur under the amorphous cellulose chains, especially for zigzag directions, see Figure 34 (c) and (e).

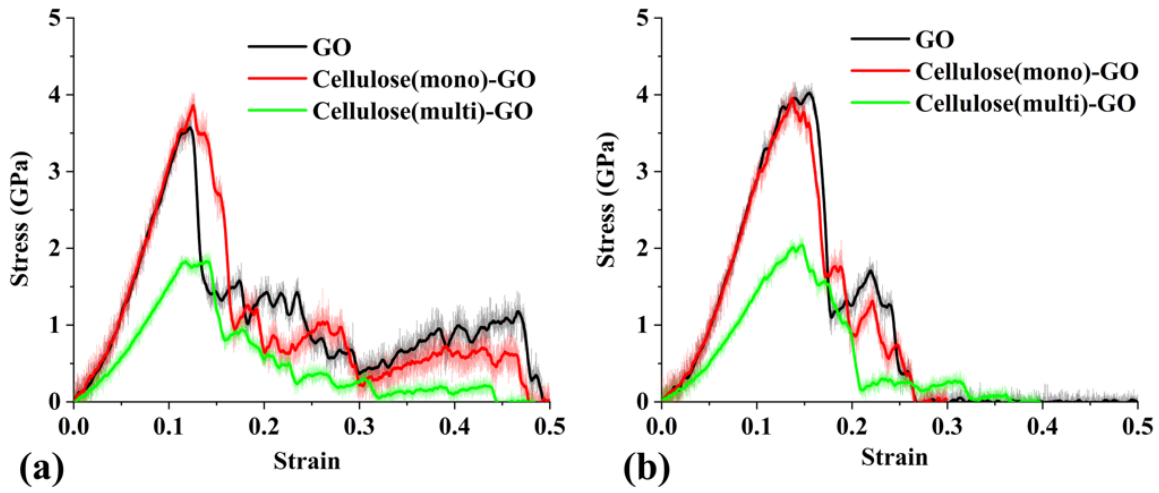

Figure 32. The stress-strain diagrams of GO, cellulose(monolayer)-GO and cellulose(multilayer)-GO system at 300 K with a constant strain rate of 10^{-5} /fs along (a) armchair and (b) zigzag direction. GO, cellulose(monolayer)-GO and cellulose(multilayer)-GO are in black, red and green, respectively.

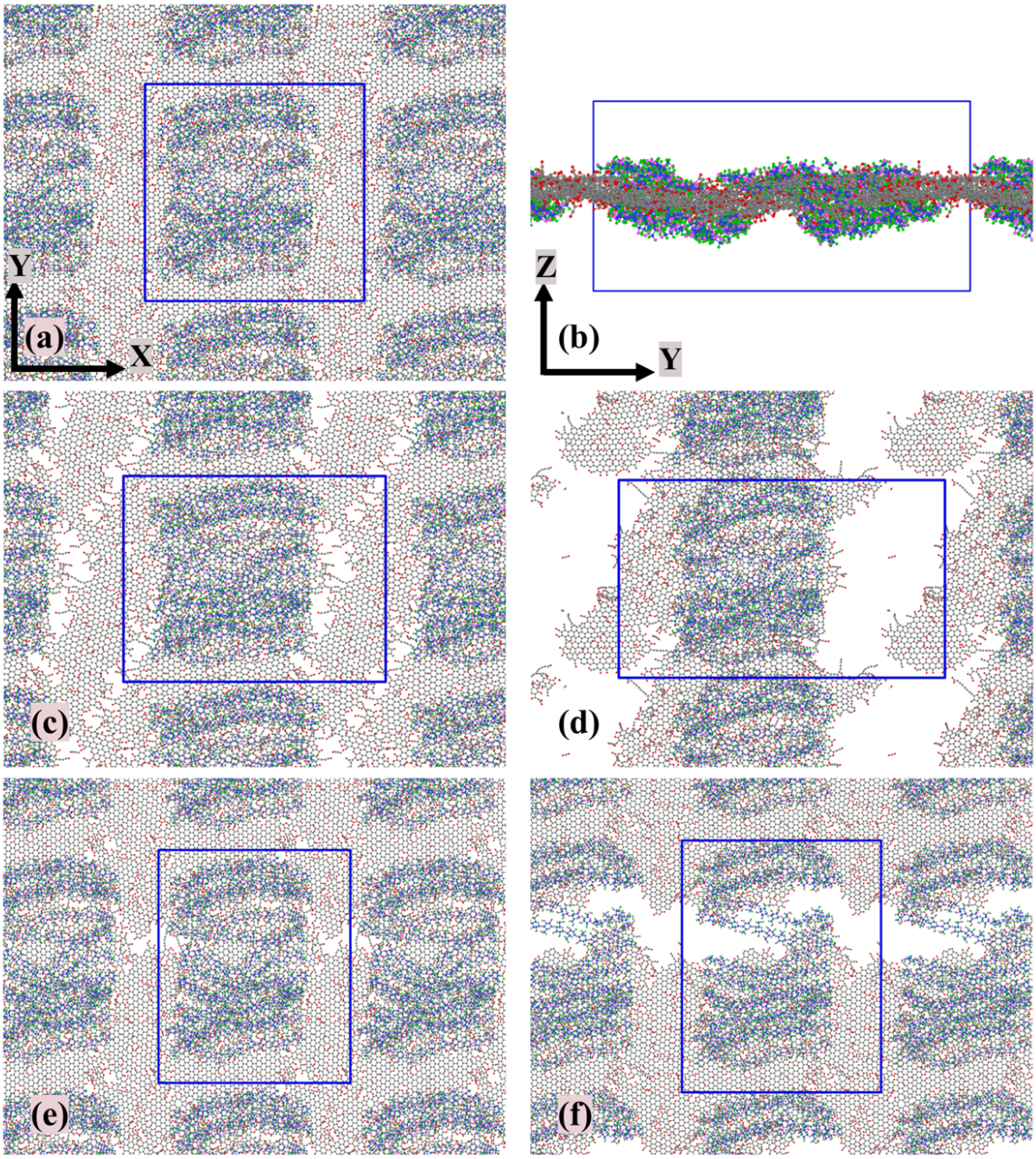

Figure 33. The snapshot of cellulose(monolayer)-GO composite at (a) starting state; (b) side view of the starting state; (c-d) deformation along armchair direction; (e-f) deformation along zigzag direction; The simulations were carried out with a constant strain rate of 10^{-5} /fs at 300 K.

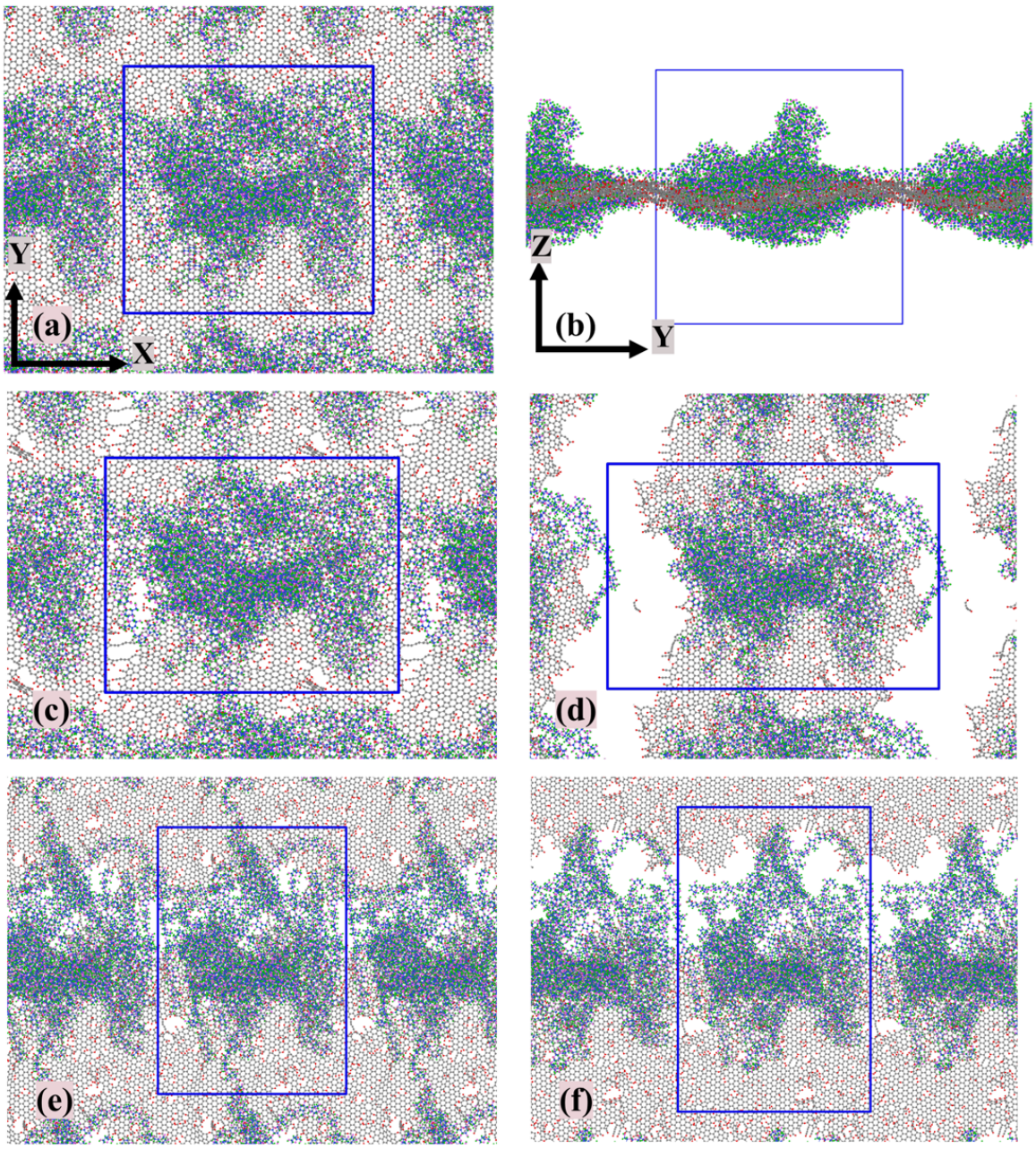

Figure 34. The snapshot of cellulose(multilayer)-GO composite at (a) starting state; (b) side view of the starting state; (c-d) deformation along armchair direction; (e-f) deformation along zigzag direction. The simulations were carried out with a constant strain rate of 10^{-5} /fs at 300 K.

6.4 Conclusion

With ReaxFF, we have carried out several RxMD simulations to investigate the model development of cellulose-GO composites and explore the mechanical behavior of pure GO, cellulose(monolayer)-GO and cellulose(multilayer)-GO composites. A temperature range from 100 K to 800 K and two strain rates of 10^{-4} /fs and 10^{-5} /fs were employed in the tensile deformation calculations. The main conclusions are:

(1) GO exhibits anisotropic mechanical behavior along armchair and zigzag directions. With a GO sheet of 30% carbon atoms oxidized, pore range of 0.2~0.5 nm and pore density of 4.31%, GO mostly showed ductile behavior along armchair directions and brittle behavior along zigzag directions. A coarse fracture surface of GO was observed while a much smoother one was found on GO system with brittle behavior.

(2) With a constant strain rate of 10^{-5} /fs, the ductile behavior was observed along the deformation direction of armchair for GO, whereas the zigzag direction is brittle. As temperature increased, the ultimate strength and Young's modulus of the GO system decreased.

(3) At temperature of 800 K, GO showed ductile behavior along armchair direction with a strain rate of 10^{-5} /fs. However, when strain rate increased to 10^{-4} /fs, GO is brittle along the armchair direction. The snapshots of two GO system with different strain rates showed no obvious difference with a strain rate ~0.1. When strain rate increased to 0.15, larger pores and wrinkled GO surface were observed in the GO system with strain rate of 10^{-5} /fs, and ductile behavior occurred in the system. At the strain of 0.7, GO system with strain rate of 10^{-5} /fs transformed from 2D flat structure into a 3D tube-like material with channels formed in the system.

(4) Compared with pure GO system, cellulose(monolayer)-GO composite presents similar mechanical properties whereas cellulose(multilayer)-GO composite has a 50% weaker mechanical strength.

The calculation and analysis of structural and mechanical properties are still on-going. More efforts will be needed to fully reveal the mechanism of how the defect and functional groups on GO surface affect the transition between ductile and brittle behavior. The mechanism of why the mechanical strength of cellulose(multilayer)-GO composites decreased are needed to be investigated. Additionally, how the number of cellulose layers influence the mechanical behavior is also interesting to study.

6.5 Reference

1. Geim, A.K. and K.S. Novoselov, *The rise of graphene.* Nature Materials, 2007. **6**(3): p. 183-191.
2. Geim, A.K., *Graphene: Status and Prospects.* Science, 2009. **324**(5934): p. 1530.
3. Lee, C., et al., *Measurement of the Elastic Properties and Intrinsic Strength of Monolayer Graphene.* Science, 2008. **321**(5887): p. 385.
4. Palermo, V., et al., *Nanoscale Mechanics of Graphene and Graphene Oxide in Composites: A Scientific and Technological Perspective.* Advanced Materials, 2016. **28**(29): p. 6232-6238.
5. Novoselov, K.S., et al., *Electric Field Effect in Atomically Thin Carbon Films.* Science, 2004. **306**(5696): p. 666.
6. Potts, J.R., et al., *Graphene-based polymer nanocomposites.* Polymer, 2011. **52**(1): p. 5-25.
7. Rafiee, M.A., et al., *Enhanced Mechanical Properties of Nanocomposites at Low Graphene Content.* ACS Nano, 2009. **3**(12): p. 3884-3890.
8. Song, W.-L., et al., *Polymeric nanocomposites with graphene sheets – Materials and device for superior thermal transport properties.* Polymer, 2012. **53**(18): p. 3910-3916.
9. Wu, J., et al., *Enhanced mechanical and gas barrier properties of rubber nanocomposites with surface functionalized graphene oxide at low content.* Polymer, 2013. **54**(7): p. 1930-1937.
10. Kim, J., L.J. Cote, and J. Huang, *Two Dimensional Soft Material: New Faces of Graphene Oxide.* Accounts of Chemical Research, 2012. **45**(8): p. 1356-1364.
11. Du, J. and H.-M. Cheng, *The Fabrication, Properties, and Uses of Graphene/Polymer Composites.* Macromolecular Chemistry and Physics, 2012. **213**(10-11): p. 1060-1077.
12. Young, R.J., et al., *The mechanics of graphene nanocomposites: A review.* Composites Science and Technology, 2012. **72**(12): p. 1459-1476.

13. Zhang, Y., et al., *What factors control the mechanical properties of poly (dimethylsiloxane) reinforced with nanosheets of 3-aminopropyltriethoxysilane modified graphene oxide?* Polymer, 2013. **54**(14): p. 3605-3611.
14. Li, Z., et al., *Control of the functionality of graphene oxide for its application in epoxy nanocomposites.* Polymer, 2013. **54**(23): p. 6437-6446.
15. Novoselov, K.S., et al., *Electric field effect in atomically thin carbon films.* Science, 2004. **306**(5696): p. 666-669.
16. Novoselov, K.S., et al., *Two-dimensional gas of massless Dirac fermions in graphene.* Nature, 2005. **438**(7065): p. 197-200.
17. Gao, W., *Graphene oxide: Reduction recipes, spectroscopy, and applications*. 2015: Springer International Publishing. 1-147.
18. Ayrat M. Dimiev, S.E., *Graphene Oxide: Fundamentals and Applications*. 2017, Chichester, West Sussex: John Wiley & Sons, Inc.
19. Gilje, S., et al., *A chemical route to graphene for device applications.* Nano Letters, 2007. **7**(11): p. 3394-3398.
20. Stankovich, S., et al., *Graphene-based composite materials.* Nature, 2006. **442**(7100): p. 282-286.
21. Joshi, R.K., et al., *Precise and Ultrafast Molecular Sieving Through Graphene Oxide Membranes.* Science, 2014. **343**(6172): p. 752-754.
22. Li, H., et al., *Ultrathin, Molecular-Sieving Graphene Oxide Membranes for Selective Hydrogen Separation.* Science, 2013. **342**(6154): p. 95-98.
23. Gao, W., et al., *Engineered Graphite Oxide Materials for Application in Water Purification.* Acs Applied Materials & Interfaces, 2011. **3**(6): p. 1821-1826.
24. Gao, W., et al., *Is reduced graphene oxide favorable for nonprecious metal oxygen-reduction catalysts?* Carbon, 2016. **102**: p. 346-356.
25. Song, Y.J., et al., *Graphene Oxide: Intrinsic Peroxidase Catalytic Activity and Its Application to Glucose Detection.* Advanced Materials, 2010. **22**(19): p. 2206-2210.
26. Zhou, M., Y.M. Zhai, and S.J. Dong, *Electrochemical Sensing and Biosensing Platform Based on Chemically Reduced Graphene Oxide.* Analytical Chemistry, 2009. **81**(14): p. 5603-5613.
27. Robinson, J.T., et al., *Reduced Graphene Oxide Molecular Sensors.* Nano Letters, 2008. **8**(10): p. 3137-3140.
28. Eda, G. and M. Chhowalla, *Chemically Derived Graphene Oxide: Towards Large-Area Thin-Film Electronics and Optoelectronics.* Advanced Materials, 2010. **22**(22): p. 2392-2415.
29. Eda, G., G. Fanchini, and M. Chhowalla, *Large-area ultrathin films of reduced graphene oxide as a transparent and flexible electronic material.* Nature Nanotechnology, 2008. **3**(5): p. 270-274.
30. Gao, W., et al., *Direct laser writing of micro-supercapacitors on hydrated graphite oxide films.* Nature Nanotechnology, 2011. **6**(8): p. 496-500.
31. Gao, W., et al., *Ozonated Graphene Oxide Film as a Proton-Exchange Membrane.* Angewandte Chemie-International Edition, 2014. **53**(14): p. 3588-3593.
32. Liu, Z., et al., *PEGylated nanographene oxide for delivery of water-insoluble cancer drugs.* Journal of the American Chemical Society, 2008. **130**(33): p. 10876-+.
33. Zhang, L.M., et al., *Functional Graphene Oxide as a Nanocarrier for Controlled Loading and Targeted Delivery of Mixed Anticancer Drugs.* Small, 2010. **6**(4): p. 537-544.

34. Rahmani, F., et al., *Molecular simulation insights on the in vacuo adsorption of amino acids on graphene oxide surfaces with varying surface oxygen densities.* Journal of Nanoparticle Research, 2016. **18**(11): p. 320.
35. Mahdavi, M., F. Rahmani, and S. Nouranian, *Molecular simulation of pH-dependent diffusion, loading, and release of doxorubicin in graphene and graphene oxide drug delivery systems.* Journal of Materials Chemistry B, 2016. **4**(46): p. 7441-7451.
36. A. Lerf, H.H., T. Riedl, M. Forster and J. Klinowski, *Solid State Ionics*. Vol. 101-103. 1997. 857-862.
37. He, H.Y., et al., *Solid-state NMR studies of the structure of graphite oxide.* Journal of Physical Chemistry, 1996. **100**(51): p. 19954-19958.
38. Lerf, A., et al., *Structure of graphite oxide revisited.* Journal of Physical Chemistry B, 1998. **102**(23): p. 4477-4482.
39. Gao, W., et al., *New insights into the structure and reduction of graphite oxide.* Nature Chemistry, 2009. **1**(5): p. 403-408.
40. Cao, C., et al., *High strength measurement of monolayer graphene oxide.* Carbon, 2015. **81**: p. 497-504.
41. Wei, X., et al., *Plasticity and ductility in graphene oxide through a mechanochemically induced damage tolerance mechanism.* Nature Communications, 2015. **6**(1): p. 8029.
42. Soler-Crespo, R.A., et al., *Engineering the Mechanical Properties of Monolayer Graphene Oxide at the Atomic Level.* The Journal of Physical Chemistry Letters, 2016. **7**(14): p. 2702-2707.
43. Verma, A., A. Parashar, and M. Packirisamy, *Tailoring the failure morphology of 2D bicrystalline graphene oxide.* Journal of Applied Physics, 2018. **124**(1): p. 015102.
44. Meng, Z., et al., *A coarse-grained model for the mechanical behavior of graphene oxide.* Carbon, 2017. **117**: p. 476-487.
45. Verma, A. and A. Parashar, *Molecular dynamics based simulations to study the fracture strength of monolayer graphene oxide.* Nanotechnology, 2018. **29**(11): p. 115706.
46. Gao, E., et al., *Intrinsic mechanical properties of graphene oxide films: Strain characterization and the gripping effects.* Carbon, 2017. **118**: p. 467-474.
47. Sakorikar, T., et al., *Thickness-dependent Crack Propagation in Uniaxially Strained Conducting Graphene Oxide Films on Flexible Substrates.* Scientific Reports, 2017. **7**(1): p. 2598.
48. Cao, C., et al., *Nonlinear fracture toughness measurement and crack propagation resistance of functionalized graphene multilayers.* Science Advances, 2018. **4**(4): p. eaao7202.
49. Rubin, E.M., *Genomics of cellulosic biofuels.* Nature, 2008. **454**(7206): p. 841-845.
50. Hill, J., et al., *Environmental, economic, and energetic costs and benefits of biodiesel and ethanol biofuels.* Proceedings of the National Academy of Sciences, 2006. **103**(30): p. 11206.
51. Jacob, J., et al., *Biopolymer based nanomaterials in drug delivery systems: A review.* Materials Today Chemistry, 2018. **9**: p. 43-55.
52. Löbmann, K. and A.J. Svagan, *Cellulose nanofibers as excipient for the delivery of poorly soluble drugs.* International Journal of Pharmaceutics, 2017. **533**(1): p. 285-297.
53. Chin, S.F., F.B. Jimmy, and S.C. Pang, *Size controlled fabrication of cellulose nanoparticles for drug delivery applications.* Journal of Drug Delivery Science and Technology, 2018. **43**: p. 262-266.

54. Treesuppharat, W., et al., *Synthesis and characterization of bacterial cellulose and gelatin-based hydrogel composites for drug-delivery systems.* Biotechnology Reports, 2017. **15**: p. 84-91.
55. Luo, H., et al., *Bacterial cellulose/graphene oxide nanocomposite as a novel drug delivery system.* Current Applied Physics, 2017. **17**(2): p. 249-254.
56. Abo-Elseoud, W.S., et al., *Chitosan nanoparticles/cellulose nanocrystals nanocomposites as a carrier system for the controlled release of repaglinide.* International Journal of Biological Macromolecules, 2018. **111**: p. 604-613.
57. Rahimi, M., et al., *Biocompatible magnetic tris(2-aminoethyl)amine functionalized nanocrystalline cellulose as a novel nanocarrier for anticancer drug delivery of methotrexate.* New Journal of Chemistry, 2017. **41**(5): p. 2160-2168.
58. Madhusudana Rao, K., A. Kumar, and S.S. Han, *Polysaccharide based bionanocomposite hydrogels reinforced with cellulose nanocrystals: Drug release and biocompatibility analyses.* International Journal of Biological Macromolecules, 2017. **101**: p. 165-171.
59. Sheikhi, A., et al., *Recent advances in nanoengineering cellulose for cargo delivery.* Journal of Controlled Release, 2019. **294**: p. 53-76.
60. Thomas, B., et al., *Nanocellulose, a Versatile Green Platform: From Biosources to Materials and Their Applications.* Chemical Reviews, 2018. **118**(24): p. 11575-11625.
61. Zhu, H., et al., *Wood-Derived Materials for Green Electronics, Biological Devices, and Energy Applications.* Chemical Reviews, 2016. **116**(16): p. 9305-9374.
62. Muhd Julkapli, N. and S. Bagheri, *Nanocellulose as a green and sustainable emerging material in energy applications: a review.* Polymers for Advanced Technologies, 2017. **28**(12): p. 1583-1594.
63. Chen, H., et al., *Exploring Chemical, Mechanical, and Electrical Functionalities of Binders for Advanced Energy-Storage Devices.* Chemical Reviews, 2018. **118**(18): p. 8936-8982.
64. Nogi, M., et al., *High thermal stability of optical transparency in cellulose nanofiber paper.* Applied Physics Letters, 2013. **102**(18): p. 181911.
65. Salajkova, M., et al., *Tough nanopaper structures based on cellulose nanofibers and carbon nanotubes.* Composites Science and Technology, 2013. **87**: p. 103-110.
66. Sun, X., et al., *Cellulose Nanofibers as a Modifier for Rheology, Curing and Mechanical Performance of Oil Well Cement.* Scientific Reports, 2016. **6**(1): p. 31654.
67. Li, F., E. Mascheroni, and L. Piergiovanni, *The Potential of NanoCellulose in the Packaging Field: A Review.* Packaging Technology and Science, 2015. **28**(6): p. 475-508.
68. Juntaro, J., et al., *Nanocellulose enhanced interfaces in truly green unidirectional fibre reinforced composites.* Composite Interfaces, 2007. **14**(7-9): p. 753-762.
69. Moon, R.J., et al., *Cellulose nanomaterials review: structure, properties and nanocomposites.* Chemical Society Reviews, 2011. **40**(7): p. 3941-3994.
70. Shi, Y., et al., *Preparation of graphene oxide–cellulose acetate nanocomposite membrane for high-flux desalination.* Journal of Materials Science, 2017. **52**(22): p. 13296-13306.
71. Uddin, M.E., et al., *Preparation and enhanced mechanical properties of non-covalently-functionalized graphene oxide/cellulose acetate nanocomposites.* Composites Part B: Engineering, 2016. **90**: p. 223-231.
72. Kim, C.-J., et al., *Graphene oxide/cellulose composite using NMMO monohydrate.* Carbohydrate Polymers, 2011. **86**(2): p. 903-909.

73. Luo, H., et al., *Layer-by-Layer Assembled Bacterial Cellulose/Graphene Oxide Hydrogels with Extremely Enhanced Mechanical Properties.* Nano-Micro Letters, 2018. **10**(3): p. 42.
74. Li, Y.Y., et al., *Hybridizing wood cellulose and graphene oxide toward high-performance fibers.* Npg Asia Materials, 2015. **7**: p. 10.
75. Peng, H., et al., *Simultaneous Reduction and Surface Functionalization of Graphene Oxide by Natural Cellulose with the Assistance of the Ionic Liquid.* The Journal of Physical Chemistry C, 2012. **116**(30): p. 16294-16299.
76. Kabiri, R. and H. Namazi, *Nanocrystalline cellulose acetate (NCCA)/graphene oxide (GO) nanocomposites with enhanced mechanical properties and barrier against water vapor.* Cellulose, 2014. **21**(5): p. 3527-3539.
77. Wang, C., et al., *Preparation of amino-functionalized graphene oxide/polyimide composite films with improved mechanical, thermal and hydrophobic properties.* Applied Surface Science, 2016. **362**: p. 11-19.
78. Nguyen, T.D.H., et al., *Bridge length effect of new dinuclear constrained geometry catalysts on controlling the polymerization behaviors of ethylene/styrene copolymerization.* Polymer, 2011. **52**(2): p. 318-325.
79. Chae, H.-R., et al., *Graphene oxide-embedded thin-film composite reverse osmosis membrane with high flux, anti-biofouling, and chlorine resistance.* Journal of Membrane Science, 2015. **483**: p. 128-135.
80. Medhekar, N.V., et al., *Hydrogen Bond Networks in Graphene Oxide Composite Paper: Structure and Mechanical Properties.* Acs Nano, 2010. **4**(4): p. 2300-2306.
81. Compton, O.C., et al., *Tuning the Mechanical Properties of Graphene Oxide Paper and Its Associated Polymer Nanocomposites by Controlling Cooperative Intersheet Hydrogen Bonding.* ACS Nano, 2012. **6**(3): p. 2008-2019.
82. Zhang, J. and D. Jiang, *Molecular dynamics simulation of mechanical performance of graphene/graphene oxide paper based polymer composites.* Carbon, 2014. **67**: p. 784-791.
83. Rahman, R., J.T. Foster, and A. Haque, *Molecular Dynamics Simulation and Characterization of Graphene-Cellulose Nanocomposites.* Journal of Physical Chemistry A, 2013. **117**(25): p. 5344-5353.
84. Qiao, Q., et al., *Graphene oxide model with desirable structural and chemical properties.* Carbon, 2019. **143**: p. 566-577.
85. Tersoff, J., *CHEMICAL ORDER IN AMORPHOUS-SILICON CARBIDE.* Physical Review B, 1994. **49**(23): p. 16349-16352.
86. Zhang, W. and A.C.T. van Duin, *ReaxFF Reactive Molecular Dynamics Simulation of Functionalized Poly(phenylene oxide) Anion Exchange Membrane.* The Journal of Physical Chemistry C, 2015. **119**(49): p. 27727-27736.
87. Monti, S., et al., *Exploring the conformational and reactive dynamics of biomolecules in solution using an extended version of the glycine reactive force field.* Physical Chemistry Chemical Physics, 2013. **15**(36): p. 15062-15077.
88. Zhang, W. and A.C.T. van Duin, *Improvement of the ReaxFF Description for Functionalized Hydrocarbon/Water Weak Interactions in the Condensed Phase.* The Journal of Physical Chemistry B, 2018. **122**(14): p. 4083-4092.
89. Castro-Marcano, F., et al., *Pyrolysis of a large-scale molecular model for Illinois no. 6 coal using the ReaxFF reactive force field.* Journal of Analytical and Applied Pyrolysis, 2014. **109**: p. 79-89.

90. Russo, M.F. and A.C.T. van Duin, *Atomistic-scale simulations of chemical reactions: Bridging from quantum chemistry to engineering.* Nuclear Instruments & Methods in Physics Research Section B-Beam Interactions with Materials and Atoms, 2011. **269**(14): p. 1549-1554.
91. Mortier, W.J., S.K. Ghosh, and S. Shankar, *Electronegativity equalization method for the calculation of atomic charges in molecules.* Journal of the American Chemical Society, 1986. **108**(15): p. 4315-4320.
92. Janssens, G.O.A., et al., *Comparison of cluster and infinite crystal calculations on zeolites with electronegativity equalization method (EEM).* Journal of Physical Chemistry, 1995. **99**(10): p. 3251-3258.
93. Huang, L.L., et al., *Controllable atomistic graphene oxide model and its application in hydrogen sulfide removal.* Journal of Chemical Physics, 2013. **139**(19).
94. Bagri, A., et al., *Structural evolution during the reduction of chemically derived graphene oxide.* Nature Chemistry, 2010. **2**: p. 581.
95. Goverapet Srinivasan, S. and A.C.T. van Duin, *Molecular-Dynamics-Based Study of the Collisions of Hyperthermal Atomic Oxygen with Graphene Using the ReaxFF Reactive Force Field.* The Journal of Physical Chemistry A, 2011. **115**(46): p. 13269-13280.
96. Zandiatashbar, A., et al., *Effect of defects on the intrinsic strength and stiffness of graphene.* Nature Communications, 2014. **5**: p. 3186.
97. Kumar, A. and M. Khandelwal, *Amino acid mediated functionalization and reduction of graphene oxide - synthesis and the formation mechanism of nitrogen-doped graphene.* New Journal of Chemistry, 2014. **38**(8): p. 3457-3467.
98. Akarsh, V. and P. Avinash, *Molecular dynamics based simulations to study the fracture strength of monolayer graphene oxide.* Nanotechnology, 2018. **29**(11): p. 115706.
99. Rahmani, F., et al., *Confinement effects on the thermal stability of poly(ethylene oxide)/graphene nanocomposites: A reactive molecular dynamics simulation study.* Journal of Polymer Science Part B: Polymer Physics, 2017. **55**(13): p. 1026-1035.
100. Rahmani, F., et al., *Reactive Molecular Simulation of the Damage Mitigation Efficacy of POSS-, Graphene-, and Carbon Nanotube-Loaded Polyimide Coatings Exposed to Atomic Oxygen Bombardment.* ACS Applied Materials & Interfaces, 2017. **9**(14): p. 12802-12811.
101. Ma, Y., et al., *Extraordinary improvement of ablation resistance of carbon/phenolic composites reinforced with low loading of graphene oxide*. Vol. 167. 2018.
102. Beste, A., *ReaxFF Study of the Oxidation of Softwood Lignin in View of Carbon Fiber Production.* Energy & Fuels, 2014. **28**(11): p. 7007-7013.
103. Zhang, T., et al., *Initial Mechanisms for an Overall Behavior of Lignin Pyrolysis through Large-Scale ReaxFF Molecular Dynamics Simulations.* Energy & Fuels, 2016. **30**(4): p. 3140-3150.
104. Zheng, M., et al., *Initial reaction mechanisms of cellulose pyrolysis revealed by ReaxFF molecular dynamics.* Fuel, 2016. **177**: p. 130-141.
105. Zhang, T., X. Li, and L. Guo, *Initial Reactivity of Linkages and Monomer Rings in Lignin Pyrolysis Revealed by ReaxFF Molecular Dynamics.* Langmuir, 2017. **33**(42): p. 11646-11657.
106. Chen, C., et al., *Reactive Molecular Dynamics Simulations of Biomass Pyrolysis and Combustion under Various Oxidative and Humidity Environments.* Industrial & Engineering Chemistry Research, 2017. **56**(43): p. 12276-12288.

107. Paajanen, A. and J. Vaari, *High-temperature decomposition of the cellulose molecule: a stochastic molecular dynamics study.* Cellulose, 2017. **24**(7): p. 2713-2725.
108. Agrawalla, S. and A.C.T. van Duin, *Development and Application of a ReaxFF Reactive Force Field for Hydrogen Combustion.* Journal of Physical Chemistry A, 2011. **115**(6): p. 960-972.
109. Chenoweth, K., et al., *Development and application of a ReaxFF reactive force field for oxidative dehydrogenation on vanadium oxide catalysts.* Journal of Physical Chemistry C, 2008. **112**(37): p. 14645-14654.
110. Chenoweth, K., A.C.T. van Duin, and W.A. Goddard, *ReaxFF reactive force field for molecular dynamics simulations of hydrocarbon oxidation.* Journal of Physical Chemistry A, 2008. **112**(5): p. 1040-1053.
111. van Duin, A.C.T. *Home - Dr. Adri van Duin.* [cited 2020 Mar. 28, 2020]; Available from: https://www.engr.psu.edu/adri/.
112. Plimpton, S., *Fast Parallel Algorithms for Short-Range Molecular Dynamics.* Journal of Computational Physics, 1995. **117**(1): p. 1-19.
113. Tanaka, F. and T. Iwata, *Estimation of the elastic modulus of cellulose crystal by molecular mechanics simulation.* Cellulose, 2006. **13**(5): p. 509-517.
114. Reiling, S. and J. Brickmann, *Theoretical investigations on the structure and physical properties of cellulose.* Macromolecular Theory and Simulations, 1995. **4**(4): p. 725-743.
115. Sturcova, A., G.R. Davies, and S.J. Eichhorn, *Elastic modulus and stress-transfer properties of tunicate cellulose whiskers.* Biomacromolecules, 2005. **6**(2): p. 1055-1061.
116. Eichhorn, S.J. and G.R. Davies, *Modelling the crystalline deformation of native and regenerated cellulose.* Cellulose, 2006. **13**(3): p. 291-307.
117. Gupta, K.M., Z.Q. Hu, and J.W. Jiang, *Mechanistic understanding of interactions between cellulose and ionic liquids: A molecular simulation study.* Polymer, 2011. **52**(25): p. 5904-5911.
118. Wu, X.W., R.J. Moon, and A. Martini, *Calculation of single chain cellulose elasticity using fully atomistic modeling.* Tappi Journal, 2011. **10**(4): p. 37-42.
119. Dri, F.L., et al., *Evaluation of reactive force fields for prediction of the thermo-mechanical properties of cellulose I-beta.* Computational Materials Science, 2015. **109**: p. 330-340.
120. Bergenstrahle, M., L.A. Berglund, and K. Mazeau, *Thermal response in crystalline I beta cellulose: A molecular dynamics study.* Journal of Physical Chemistry B, 2007. **111**(30): p. 9138-9145.
121. Neyertz, S., et al., *A new all-atom force field for crystalline cellulose I.* Journal of Applied Polymer Science, 2000. **78**(11): p. 1939-1946.
122. Mishin, Y., et al., *Interatomic potentials for monoatomic metals from experimental data and ab initio calculations.* Physical Review B, 1999. **59**(5): p. 3393-3407.
123. Spearot, D.E., et al., *Tensile strength of 〈100〉 and 〈110〉 tilt bicrystal copper interfaces.* Acta Materialia, 2007. **55**(2): p. 705-714.
124. Tschopp, M.A., D.E. Spearot, and D.L. McDowell, *Atomistic simulations of homogeneous dislocation nucleation in single crystal copper.* Modelling and Simulation in Materials Science and Engineering, 2007. **15**(7): p. 693-709.
125. Tschopp, M.A. and D.L. McDowell, *Influence of single crystal orientation on homogeneous dislocation nucleation under uniaxial loading.* Journal of the Mechanics and Physics of Solids, 2008. **56**(5): p. 1806-1830.

126. Hossain, D., et al., *Molecular dynamics simulations of deformation mechanisms of amorphous polyethylene.* Polymer, 2010. **51**(25): p. 6071-6083.
127. Qiao, Q., X. Li, and L. Huang, *Crystalline Cellulose under Pyrolysis Conditions: The Structure–Property Evolution via Reactive Molecular Dynamics Simulations.* Journal of Chemical & Engineering Data, 2020. **65**(2): p. 360-372.
128. Wu, X.W., R.J. Moon, and A. Martini, *Tensile strength of I beta crystalline cellulose predicted by molecular dynamics simulation.* Cellulose, 2014. **21**(4): p. 2233-2245.
129. Tashiro, K. and M. Kobayashi, *Theoretical evaluation of three-dimensional elastic constants of native and regenerated celluloses: role of hydrogen bonds.* Polymer, 1991. **32**(8): p. 1516-1526.
130. Ganster, J. and J. Blackwell, *NpH-MD-simulations of the elastic moduli of cellulose II at room temperature.* Journal of Molecular Modeling, 1996. **2**(9): p. 278-285.
131. Wang, Y.Y., et al., *The Relationship Between Dp, Fracture Degree And Mechanical Strength Of Cellulose I-Beta In Insulation Paper By Molecular Dynamic Simulations.* International Journal of Modern Physics B, 2013. **27**(31).
132. Wang, Y.Y., et al., *Influence Of Moisture On Mechanical Properties Of Cellulose Insulation Paper.* International Journal of Modern Physics B, 2014. **28**(7).
133. Zhu, M.Z., et al., *Mechanical property of hydrous amorphous cellulose studied by molecular dynamics.* Russian Journal of Physical Chemistry B, 2016. **10**(3): p. 524-530.
134. Eichhorn, S.J., R.J. Young, and G.R. Davies, *Modeling crystal and molecular deformation in regenerated cellulose fibers.* Biomacromolecules, 2005. **6**(1): p. 507-513.
135. Qiao, Q., X. Li, and L. Huang, *Crystalline Cellulose under Pyrolysis Conditions: The Structure–Property Evolution via Reactive Molecular Dynamics Simulations.* Journal of Chemical & Engineering Data, 2019.
136. Hicks, J., *1 - Fundamentals of the strength of materials*, in *Welded Joint Design (Third Edition)*, J. Hicks, Editor. 1999, Woodhead Publishing. p. 1-16.

Chapter 7: Conclusions and Outlook

7.1 Conclusions

Numerous studies and applications have been published to investigate carbon-based materials due to the environment problem and energy shortage. Although remarkable efforts have been made in the utilization of carbon materials, a detailed fundamental understanding of the structure and properties of these materials is still remained unknown. To address the issue of lacking representative models that contained both structural and chemistry of carbon-based materials, and the mechanism of how structure changes affect the properties of these materials at atomistic level, is this thesis, we have been applying RxMD simulations and several simulated characterization techniques to study the complex structure and model development of GO, cellulose and cellulose-GO composites, as shown in Figure 35.

In Chapter 2, we have summarized a brief introduction of computational methods including QM, MM and ReaxFF. The introduction of calculated characterization technique is also introduced in this chapter. The model development of GO is discussed in Chapter 3 using RxMD, calculated FTIR and XPS. The recent atomistic studies about the structure, properties and process of cellulose are reviewed in Chapter 4, as well as the calculation of FTIR, XRD, NMR. According to Chapter 4, the structural evolution of crystalline cellulose under the isolated pyrolysis process via ReaxFF is reported in Chapter 5. The pyrolysis temperature, the change of cellulose crystallinity, the variation of inter/intra HB networks, the reaction and distribution of C, O and H elements and mechanical properties of cellulose crystal have been analyzed. Based on Chapter 3 (GO) and Chapter 5 (cellulose), we proposed a cellulose-GO nanocomposite model. The model development and mechanical behavior of pure GO and cellulose-GO nanocomposites are investigated.

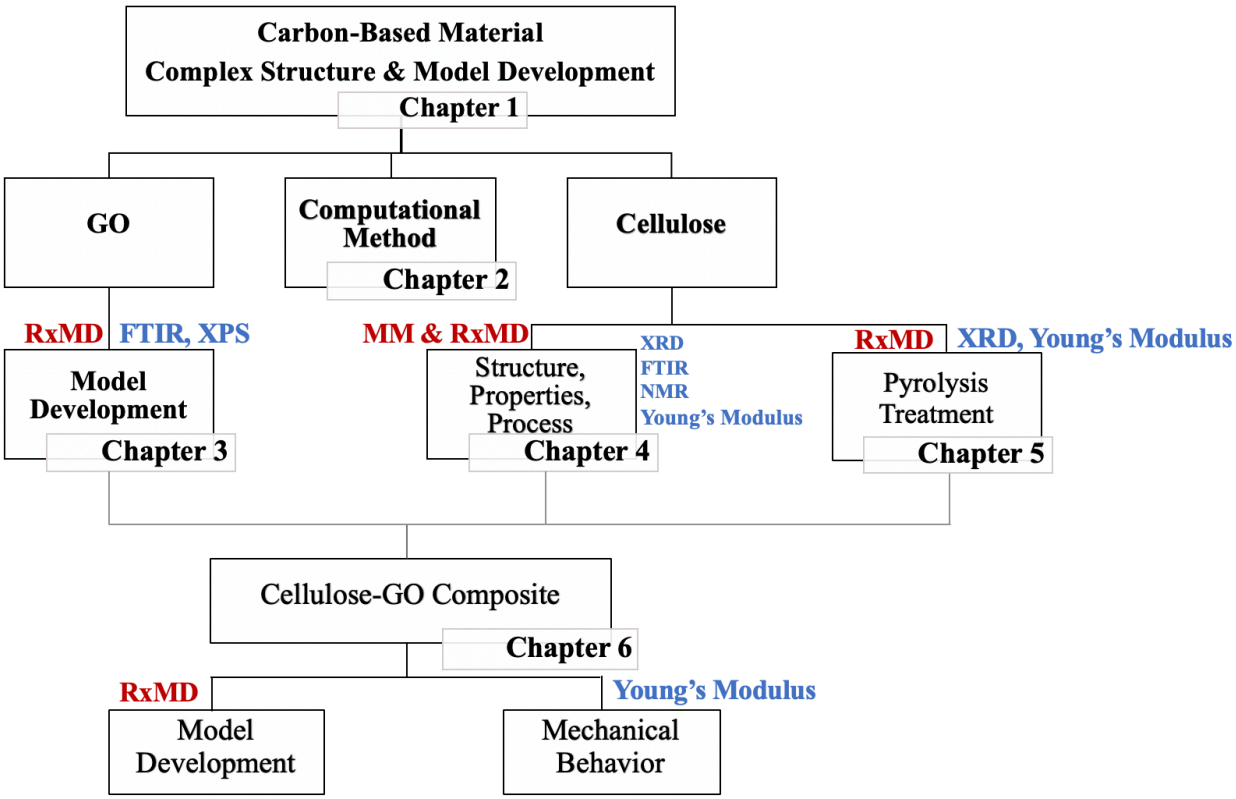

Figure 35. The tree of thesis outline with the color codes for words: black - the keyword for the topic and the chapter number; blue – the calculated characterization techniques; red – the computational method, respectively.

Finally, the results we obtained are conclude in this chapter, and future research plans about carbon-based material model development and properties studies has been given. The results can be summarized as following:

(1) With three critical controlling parameters, namely, the initial functionalization density, the ratio of hydroxyl/epoxy groups, the trigger annealing temperature T_{tri}, GO models proposed in this thesis have an overall C/O ratio in the range of 1.86 to 18.05, and vacancy defects as large as 1.7 nm. By comparing with GO sample from the modified Hummers method, the 70% GO (1:1) model from T=1500K is considered to be the best GO model, final model has a final functionalization density of 48.40%, C/O value about 2.93,

curvature for 0.9427 nm and vacancy sizes around 0.7-1.7 nm with a good agreement for both FTIR and XPS characteristics. While GO structures are very sensitive to experimental synthesis conditions, the studies in this thesis could provide a general protocol to generate atomic GO structures representative of experimental samples. The theoretical FTIR and XPS calculations are useful tools for GO model characterization, and can be adopted for computational studies of other two-dimensional materials and their composites.

(2) With an increasing interest in manipulating subtle properties of native cellulose, using computational techniques to classify and construct the structure-property-process relationship of cellulose martials has been a hot topic for both academia and industry. Computational simulations at atomistic level, including quantum mechanics, molecular mechanics, molecular dynamics and reactive molecular dynamics, have provide powerful methods and useful information in understanding the fundamental mechanism of cellulose conversion and utilization. For example, QM calculations provide accurate reaction mechanism of cellulose decomposition, while QM/MM hybrid method and RxMD are able to proceed structural evolution of large and complex cellulose based system, which can further help in optimizing cellulose pyrolysis processes conditions. In addition, cellulose characterizations, beneficial to validate and support computational results, are also briefly summarized. The combination of simulation and experiment could facilitate the construction of the structure-property-process relationship and provide better guidelines to cellulose treatments at industrial level.

(3) The structural evolution of crystalline cellulose under the pyrolysis process has been investigated via ReaxFF based reactive molecular dynamics (RxMD) simulations. By changing the pyrolysis temperature from 300 K to 1300 K, cellulose is able to hold the

general crystalline structure for temperatures up to 1000 K. The good thermal stability is assisted by the interchange of inter- and intra-chain HB networks. When the pyrolysis temperature is beyond 1200 K, both 1-4-β bonds and glucose ring units will decompose. Light gas-phase molecules, such as CO and H_2, are detected as major decomposition products. Through the analysis of XRD, Young's modulus and elements distribution, we show that the ReaxFF reactive force field is capable of describing both stable and dissociative properties of cellulose under isolated pyrolysis processes.

(4) With ReaxFF, we have carried out several RxMD simulations to investigate the model development of cellulose-GO composites and explore the mechanical behavior of pure GO, cellulose(monolayer)-GO and cellulose(multilayer)-GO composites. A temperature range from 100 K to 800 K and two strain rates of 10^{-4} /fs and 10^{-5} /fs were employed in the tensile deformation calculations. It is found that GO exhibits anisotropic mechanical behavior along armchair and zigzag directions. With a constant strain rate of 10^{-5} /fs, the ductile behavior was observed along the deformation direction of armchair for GO, whereas the zigzag direction is brittle. A coarse fracture surface of GO was observed while a much smoother one was found on GO system with brittle behavior. As temperature increased, the ultimate strength and Young's modulus of the GO system decreased for the system with constant strain rates. At temperature of 800 K, GO showed ductile behavior along armchair direction with a strain rate of 10^{-5} /fs. However, when strain rate increased to 10^{-4} /fs, GO is brittle along the armchair direction. The snapshots of these two GO systems with different strain rates showed no obvious difference with a strain rate ~0.1. When the strain rate increased to 0.15, larger pores and wrinkled GO surface were observed in the GO system with strain rate of 10^{-5} /fs, and ductile behavior occurred in the system.

At the strain of 0.7, GO system with strain rate of 10^{-5} /fs transformed from 2D flat structure into a 3D tube-like material with channels formed in the system. Compared with pure GO system, cellulose(monolayer)-GO composite presents similar mechanical properties whereas cellulose(multilayer)-GO composite has a 50% weaker mechanical strength.

7.2 Outlook

In this thesis we studied monolayer GO, its model development and corresponding nanocomposites. It would be interesting to further develop the mechanical properties of pure monolayer GO model. A better understanding of how the distribution of functional groups and defects affect the ductile and brittle mechanical behavior of pure GO could help in controlling the properties of GO materials and provide some insight into the manufactories. In addition, other simulated characterization technique can be carried out for GO materials. For example, the fatigue calculations of GO. The mechanical fatigue occurs with lower stress compared with the ultimate fracture strength, which can be used to evaluate the long-term dynamic reliability of materials. And besides the mechanical behavior, the functional groups and defects on GO can also be used to fine tune the fatigue behavior. Moreover, the investigation of mechanical properties of GO materials, such as the fracture behavior, fatigue behavior, and crack propagation, can also shed some light on other 2D materials. On the other hand, studies with modified GO materials also attract more and more interest from people. For example, Janus GO, with two distinct surfaces with different chemical structures and properties, can be used as stabilizers in emulsions, catalysts in chemical reactions, water repellent in textile fibers and sensor in biological systems. It would be also important to investigate the graphite oxide system, which is system that containing multiple

layers GO sheets. Because of the defects on the surface and multilayer structures, graphite oxide ca be used as a potential membrane material in water purification and separation processes.

Meanwhile, more efforts could be made on the study of mechanical behavior of cellulose-GO composites. In our research, we only consider the cellulose-GO material with amorphous cellulose chains on GO surface and the interactions of HBs in the system. More calculations can be carried out with (a) temperature-programmed RxMD simulations in order to have covalent bonds between cellulose and GO, which might lead to a great increase of the mechanical strength for the cellulose-GO composite; (b) using crystalline cellulose chains instead of amorphous ones on GO surface to build up a different cellulose-GO model, the mechanical behavior might be different compared with current model; (c) the analysis of how defect and functional groups affect the fracture behavior should be useful, and the detailed mechanism of deformation should be investigated and compared with pure GO cellulose systems.

Another promoting research topic is the manipulation of natural cellulose based materials. In this thesis we studied crystalline cellulose under the isolated pyrolysis process, which is the very first step investigation about how pure six-carbon surge (glucose) behave under isolated pyrolysis conditions. More studies where cellulose under real pyrolysis conditions, that is, instead of isolated conditions but via liquid or gas mediated pyrolysis processes, are worth pursuing. Moreover, the detailed mechanism of how cellulose, hemicellulose and lignin respond differently to pyrolysis treatments (see Figure 36) could lead to a subtle manipulation and a successful conversion of biomass into advanced functional materials. Aditionally, other treatment method, such as chemical treatment, could be studied to combine with the pyrolysis process.

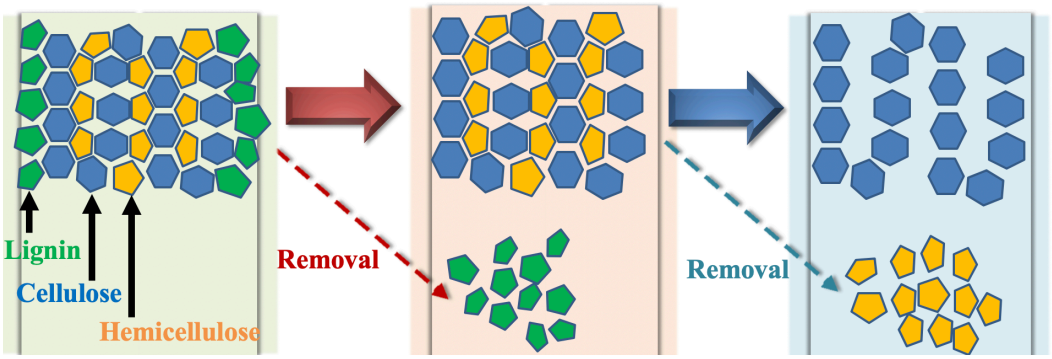

Figure 36. An illustration of manipulating natural cellulose material with the removal of hemicellulose and lignin.